NUMERICAL STUDY ON DROPLET BREAKUP DYNAMICS IN MICROCHANNELS

Saikat Biswas

NUMERICAL STUDY ON DROPLET BREAKUP DYNAMICS IN MICROCHANNELS

THESIS

Submitted in Partial Fulfillment of the

Requirements for the Degree of

Doctor of Philosophy

in

Engineering

by

Saikat Biswas

(166107025)

Under the Guidance of

Prof. Tapas K Mandal

And

Dr. Partho Sarathi Gooh Pattader

Department of Chemical Engineering

Indian Institute of Technology Guwahati

July, 2022

DEDICATED TO MY PARENTS

INDIAN INSTITUTE OF TECHNOLOGY GUWAHATI

GUWAHATI - 781039, ASSAM, INDIA

DEPARTMENT OF CHEMICAL ENGINEERING

CERTIFICATE

This is to certify that the thesis entitled **"*Numerical study on droplet breakup dynamics in microchannels*"** submitted by **Saikat Biswas** in fulfillment of the requirement of the *Degree of Doctor of Philosophy in Engineering*, is a record of bonafide research work carried out by him, in the Department of Chemical Engineering, Indian Institute of Technology, Guwahati, under our guidance and supervision. In our opinion, the thesis has reached the standard fulfilling the requirements of the Ph.D. degree as prescribed in the regulations of this institute.

(Prof. Tapas K Mandal)

Professor

Department of Chemical Engineering

Indian Institute of Technology Guwahati

Guwahati-781039, India

Email: tapasche@iitg.ac.in

(Prof. Partho S G Pattader)

Associate Professor

Department of Chemical Engineering

Indian Institute of Technology Guwahati

Guwahati-781039, India

Email: psgp@iitg.ac.in

ACKNOWLEDGEMENT

Words fail to express my sincere gratitude to my thesis supervisors Prof. Tapas K Mandal and Dr. Partho S G Pattader for their encouragement, patience, insightful advice, guidance and sustained interest in successful completion of my dissertation. In addition, their philosophical guidance has built up a momentum inside me.

I wish to acknowledge my respectful thanks to Prof. Bishnupada Mandal and Prof. Anugrah Singh, former HODs, and Prof. Kaustubha Mohanty, present-HOD for extending all the necessary facilities for carrying-out my research work. I am also grateful to all the professors in the department for their sincere cooperation.

I would like to thanks DST – FIST, Department of Chemical Engineering, IIT Guwahati for providing me the necessary computational facility.

I am thankful to my dad and mom, who have not only supported me in the completion of my Ph.D. but also have stood by me throughout my life. They have patiently supported me at all instances in my research work. I am also thankful to all my family members for their encouragement and support.

Date:

Place: IIT Guwahati (Saikat Biswas)

PREFACE

Preface

Numerical study on droplet breakup dynamics in microchannels

1. Introduction

Droplet-based microfluidics in immiscible fluids is one of the emerging fields in recent years due to its wide application in medicine, food, drug delivery, single-cell RNA/DNA sequencing, droplet digital PCR, diagnostic tests, tissue engineering, and cell therapy. This approach may regulate cell size and monodispersity while eliminating the need to immunize medicines during cell culture. They can quickly isolate cells from the external environment. Microdroplets can be created using two methods: I) Active technique II) and the Passive technique. In the active technique, the droplet is generated using external forces like electrical, magnetic forces, or thermal energies. The passive techniques include the geometry of the channel and the flow hydrodynamics. There are several configurations through which micro droplets can be created, such as T-junction, co-flow, flow-focusing, and some variations. Shear force is used in these geometries in order for droplets to be broken down. A variety of flow regimes may be seen, such as squeezing, dripping, jetting, and continuous regimes. Researchers have employed multiphase numerical simulation to forecast the different flow regimes based on flow hydrodynamics. Momentum and continuity are used as governing equations to determine the interface in the multiphase numerical simulation. Multiphase flow may be modeled using a variety of approaches, including the volume of fluid (VOF) model, the level set method (LS), the phase-field method, and the lattice Boltzmann method.

Droplets can be utilized as miniature reactors. For the reaction reproducibility and consistency, they allow accurate control over any reagent quantity. Hence, this dissertation

reports some techniques through which we can get two or more daughter droplets from a single mother droplet. Also, it reports droplet bifurcation and multi-furcation mechanism and many parametric studies on the droplet breakup process. The inside physics of dripping and jetting flow using velocity vectors in a flow-focusing device is also discussed. The effect of oil-water viscosity ratio, surface tension, and wettability on dripping and jetting flow are observed. The point-wise objectives of the thesis are as follows:

I. A computational study on phase velocity mediated droplet splitting and its mechanism at T-junction microchannel

II. Influence of microchannel geometry on droplet dynamics: a computational study

III. Numerical appraisal on liquid-liquid two-phase flow in a flow-focusing system

a. 2D simulation of dripping and jetting flow in a flow-focusing geometry

b. 3D simulation of dripping and jetting phenomena in a flow-focusing geometry

IV. Two-dimensional numerical simulation of droplet splitting in multi-furcating microchannel

A brief discussion on each objective is presented in the subsequent sections (3-6). Finally, a summary of the dissertation and the future scopes are also provided at the end of section 6.

2. Methodology

2.1 CFD Methodology

Computational Fluid Dynamics (CFD) is the simulation of fluid engineering systems using modelling (mathematical physical problem formulation) and numerical methods

(discretization methods, solvers, numerical parameters, and grid generation, among other things). Figure 1 depicts the procedure.

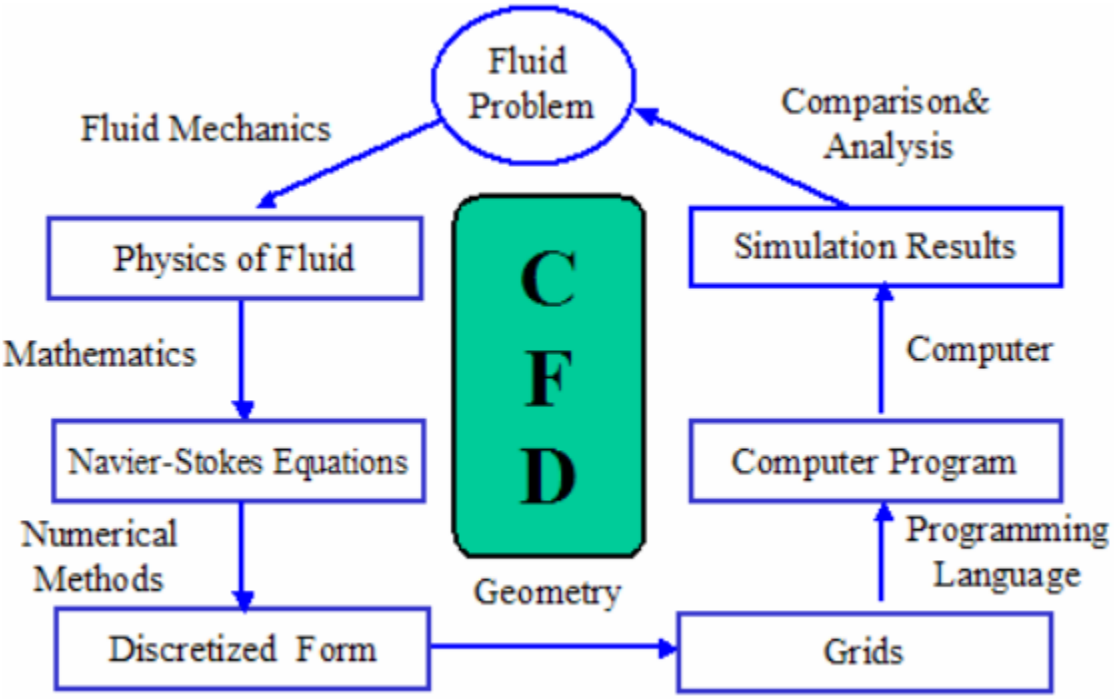

Figure 1. Process of Computational Fluid Dynamics

To begin with, we have a fluid problem. To solve this problem, we must first grasp the physical properties of fluids through the use of Fluid Mechanics. Then we may use mathematical equations to reflect these physical properties. CFD's governing equation is the Navier-Stokes Equation. Because the Navier-Stokes Equation is analytical, it will be discretized by a computer. There are several numerical discretization methods, including Finite Difference, Finite Element, and Finite Volume. As a result, because our discretization is dependent on them, we must also divide our entire problem area into multiple little parts. There are several apps available on the market to tackle CFD challenges, such as ANSYS FLUENT, COMSOL, and others. Workstations or supercomputers are frequently utilized to run the programs. Finally, the results

of our simulation are visible. We may compare and contrast the results of the simulation with those of experiments and real-world challenges. If the results are inadequate to solve the issue, the technique must be repeated until a satisfying solution is identified. This is how the CFD technique works.

The VOF (Volume of fluid) model, available in CFD solver ANSYS FLUENT, has been used for capturing the interface between the phases.

2.2 The Volume of Fluid (VOF) approach

In the VOF method, continuity equation and momentum balance equations are solved, followed by a volume fraction equation. All the equations are taken from ANSYS FLUENT theory guide with minor modification of nomenclature and discussed below.

Continuity equation:

$$\frac{\partial \rho}{\partial t} + \nabla \cdot (\rho \mathbf{u}) = 0 \tag{2.1}$$

Momentum conservation equation:

$$\frac{\partial (\rho u)}{\partial t} + \nabla \cdot (\rho u \mathbf{u}) = \nabla \cdot (\mu \nabla u) - \nabla p + \rho g + F_s \tag{2.2}$$

In Eqs. (2.1) and (2.2), u is the velocity. α_w and α_o are the volume fraction of water and oil phase respectively and obey the relation ($\alpha_w + \alpha_o = 1$) and lie between 0 and 1 in each computational cell. The fluid properties of the mixed-phase are computed as follows

$$\rho = \alpha_w \rho_w + (1 - \alpha_w) \rho_o \tag{2.3}$$

$$\mu = \alpha_w \mu_w + (1 - \alpha_w)\mu_o \tag{2.4}$$

The volume fraction equation is given below

$$\frac{\partial \alpha_i}{\partial t} + u.\nabla \alpha_i = 0 \tag{2.5}$$

In Eq. (2.5), subscript *i* denotes the *i*th phase: water (w) or oil (o).

The surface tension force (F_s) by continuum surface force (CSF) used in Eq. (2.2) was calculated as

$$F_s = \sigma \left[\frac{\rho k \hat{n}}{\left(\frac{1}{2}\right)(\rho_w + \rho_o)} \right] \tag{2.6}$$

Where σ is the coefficient of surface tension, $\hat{n}$ the surface normal, and k the local surface curvature, which is calculated as

$$k = \nabla.\hat{n} \tag{2.7}$$

Where $\hat{n} = n/|n|$ and $n = \nabla.\alpha_i$.

The fluid presumed contact angle with the wall is utilized to alter the surface normal in cells near the wall. The curvature of the surface near the wall is adjusted as a result of this so-called dynamic boundary condition.

If θ_{wl} is the contact angle at the wall, then the surface normal at the live cell next to the wall is

$$\hat{n} = \hat{n}_{wl} \cos\theta_{wl} + \hat{t}_{wl} \sin\theta_{wl} \tag{2.8}$$

Where $\hat{n}_{wl}$ and $\hat{t}_{wl}$ are the unit vectors normal and tangential to the wall, respectively. The local curvature of the surface is determined by combining this contact angle with the typically

calculated surface normal one cell away from the wall, and this curvature is utilized to change the body force term in the surface tension calculation.

In executing the VOF method, α_i and P are initially given in each computational cell center, and u is given at cell surfaces. ρ and μ at the interface can be determined by Eqs. (2.3) and (2.4) respectively. k and F_s are determined by Eqs. (2.7) and (2.6) respectively. Subsequently, the continuity (Eq. (2.1)) and momentum equation (Eq. (2.2)) are solved through a hydrodynamic scheme. The volume fraction equation is solved using a geo-reconstruction interpolation technique to achieve the highest accuracy. Importantly it is noted that the tracking of the interface between two phases is associated with this solution.

3. Objective – I: A computational study on phase velocity mediated droplet splitting and its mechanism at T-junction microchannel

In this study, 2D numerical simulations were conducted to reveal the breakup and non-breakup mechanism of a droplet in a horizontal microfluidic T-junction using oil-water volume fraction contours, pressure profile, velocity profile, and vorticity profile. The numerical simulation is validated with experimental results taken from the literature. Two types of droplet breakup regimes, namely tunnel-breakup and obstructed breakup along with a non-breakup regime with the alternate movement of droplets were found. The tunnel breakup is mainly due to the formation of vortex flow in front of the droplets whereas the breakup at obstruction is induced by the formation of high upstream pressure in the main channel. Interestingly, a pressure swing phenomenon is identified, which drives the droplets in the horizontal microfluidic T-junction's alternating arms. Depending on the phase velocities, numerous mixed phenomena

were also observed when the droplets flowed through the horizontal T-junction microchannel. A flow pattern map is presented to guide the on-demand requirement of the flow behavior based on two dimensionless numbers, namely capillary number and mixture Reynolds number. In pressure drop analysis, the drift flux model provides a better prediction than the homogeneous model. The pressure swing phenomena in the alternate movement of droplets through the T-junction of the microchannel is depicted in Figure 2.

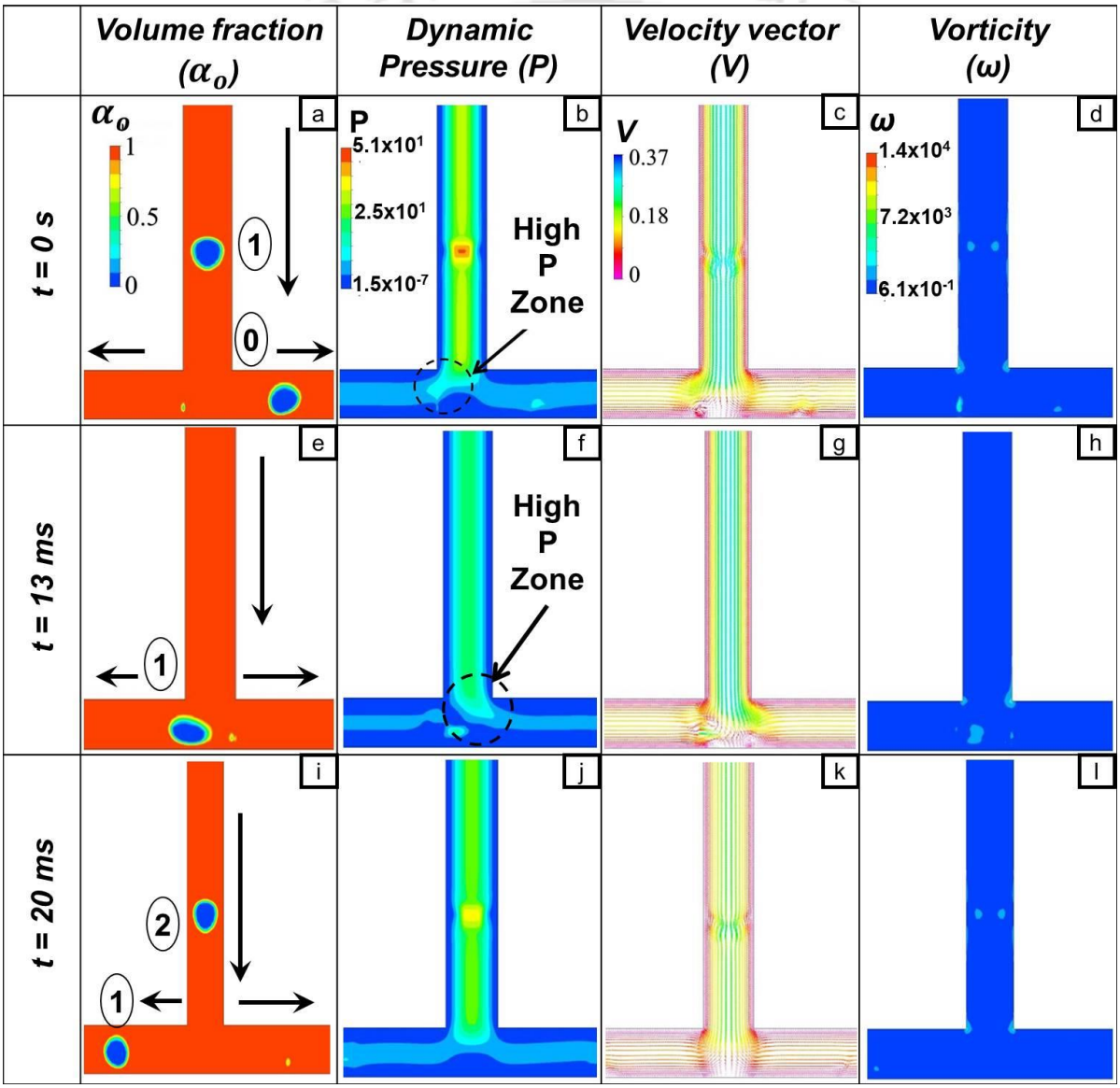

Figure 2. Volume fraction contour of mineral oil-water, Dynamic pressure field contour, Velocity vectors and Vorticity data during alternate movement of droplets at T-junction of the microchannel.

4. Objective – II: Influence of microchannel geometry on droplet dynamics: a computational study

In this study, the effect of width ratio (branch channel width/main channel width) on droplet breakup dynamics in a horizontal microfluidic T-junction using oil-water volume fraction contours, pressure profile, and velocity profile has been investigated using 2D simulation. Simulations have been also conducted to reveal the effect of branch arm length ratio (right arm length/left arm length) on droplet breakup dynamics. The numerical simulation is validated with experimental results taken from the literature. Two types of breakup regimes, along with a non-breakup regime, have been found. The breakup regimes are tunnel breakup, and obstructed breakup, and the non-breakup regime is the alternate movement of droplets. The tunnel breakup and the obstructed breakup are mainly due to the pressure difference in the branch channel and the direction of the velocity vectors towards the branch's exit. The pressure swing phenomenon is the reason behind the alternate movement of the droplets. Breakup with tunnel is found in WR = 0.75, 0.5, breakup with obstruction is found in WR = 0.25 and alternate movement is found in WR = 1 for Vw = 0.01 m/s, Vo = 0.18 m/s. It has been found that breakup tendency increases as we decrease the width ratio (1, 0.75, 0.5, and 0.25) and increase the arm length ratio (0.4, 0.6, and 0.9). Droplet breakup conditions have been studied. Mixed flow patterns have been displayed with the help of a flow pattern map for the width ratio = 1, 0.75, 0.5, and 0.25. Prediction of simulated pressure gradient has also been made with the help of the Lockhart and

Martinelli approach and Dimensional analysis for width ratio = 1. Some representative results on the effect of width ratio (1, 0.75, 0.5, 0.25) on droplet breakup has been represented in Figure 3.

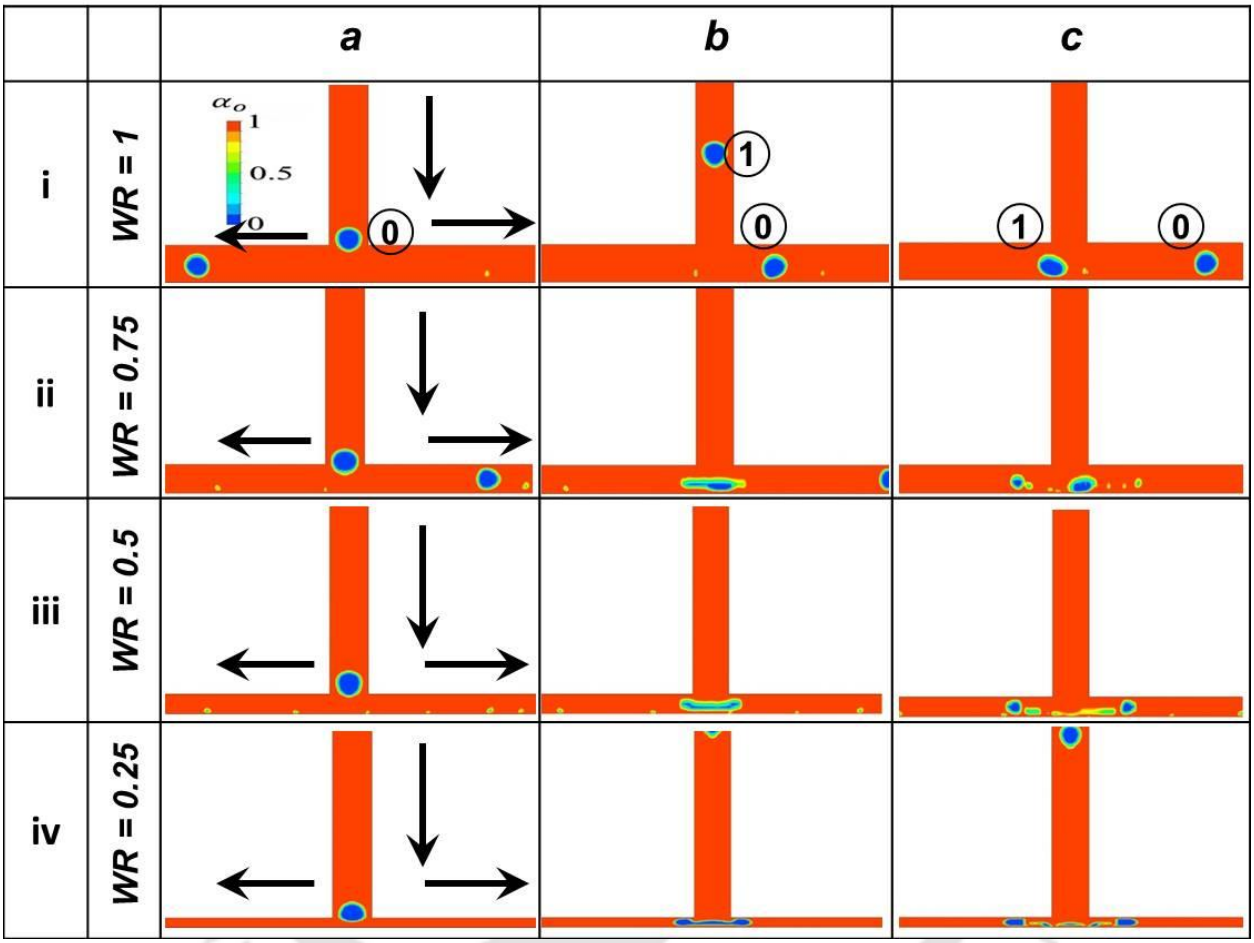

Figure 3. The width ratio alters the two-phase flow morphology. Red and blue colors represent the volume fraction contour of oil and water, respectively. Three columns refer to three different locations of the droplets in the microchannel along with the time of progression at a constant phase flow rate (V_w = 0.01 m/s, V_o = 0.18 m/s).

5. Objective – III: Numerical appraisal on liquid-liquid two-phase flow in a flow-focusing system

a. 2D simulation of dripping and jetting flow in a flow-focusing geometry

2D simulations have investigated flow regimes in a flow-focusing geometry by changing the dispersed phase and continuous phase velocities. The dispersed phase is the Polydimethylsiloxane (PDMS), and the continuous phase is the water. Simulations have been performed in a range of oil-water viscosity ratios $\left(\frac{\mu_o}{\mu_w}\right)$ from 3-50, and interfacial tension ranges from 0.0118-0.002 N/m. The walls of the microchannel are considered to be PMMA surfaces. An oil droplet's contact angle (θ) on the PMMA surface in the presence of water is 140°. Our study observed two types of flow regimes, namely dripping and jetting, by changing the dispersed phase and continuous phase velocities. The sequential time steps of void fraction contour have been presented to explore the droplet formation mechanism. The droplet pinch-off and jet growth time have been calculated for the dripping and jetting regimes, respectively. The outcomes are summarized in the form of a flow pattern map at a viscosity ratio of 12 and interfacial tension of 0.0118 N/m, which shows the transition boundary between dripping and jetting phenomena. The simulated transition boundary gives good agreement with the analytical solution available in the literature. The effect of oil-water viscosity ratio and interfacial tension on droplet size is also investigated. Moreover, the effect of oil-water viscosity ratio and interfacial tension on jet growth time has also been investigated. These findings will help to understand the different flow regimes and their transition in a flow focusing geometry and will

directly apply to microfluidic platform-based devices. Velocity vectors in Figure 4 represent the inside physics of jetting flow at $\frac{\mu_o}{\mu_w} = 12$, $\sigma = 0.0118$ N/m, $\theta = 140°$.

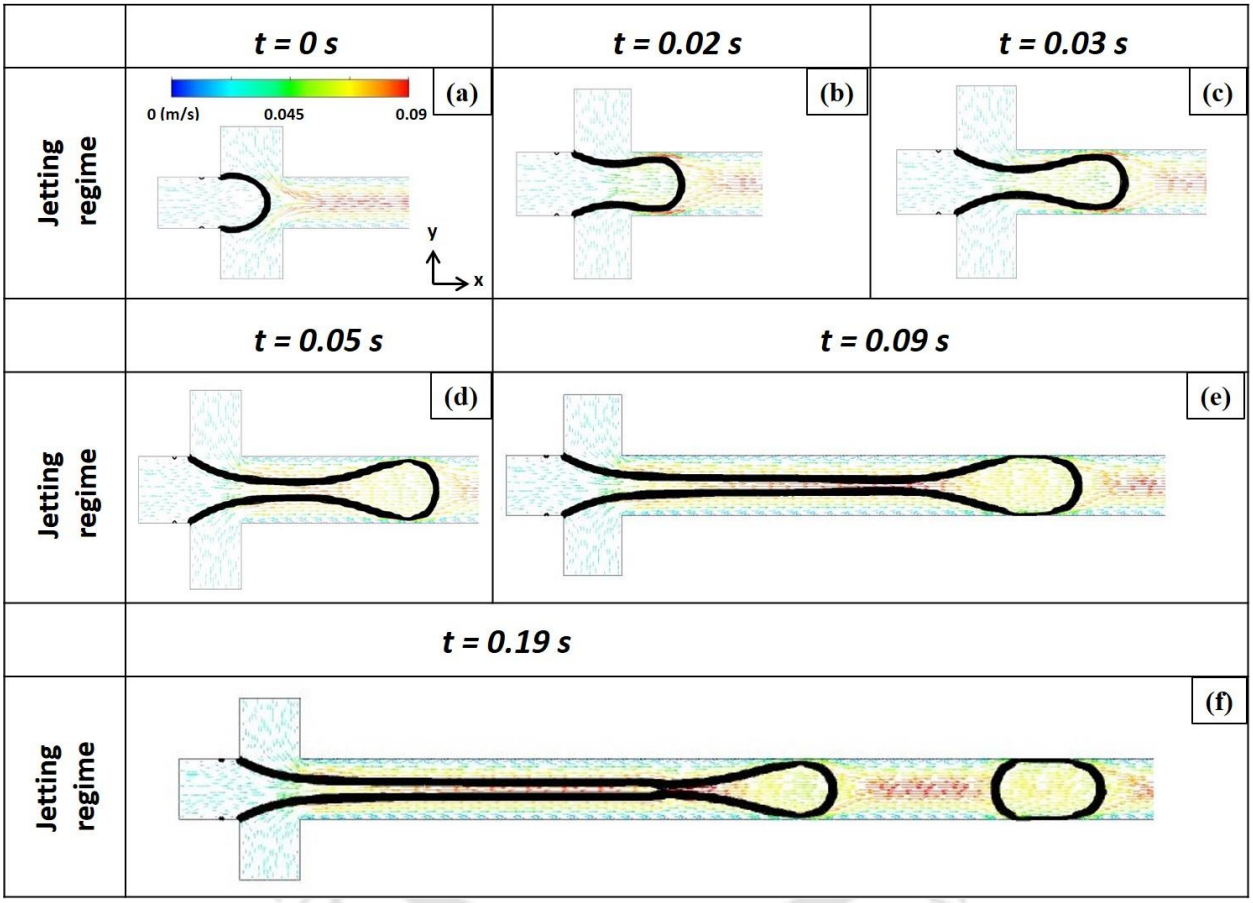

Figure 4. Velocity vectors at different time steps to explain the inside physics of jetting flow at $\frac{\mu_o}{\mu_w} = 12$, $\sigma = 0.0118$ N/m, $\theta = 140°$

b. 3D simulation of dripping and jetting phenomena in a flow-focusing geometry

3D simulations have been performed on a flow-focusing geometry using the VOF method to study the effect of viscosity, surface tension, wettability, and geometry on droplet generation for the dripping regime. Here the dispersed phase is the PDMS oil (polydimethylsiloxane), and the continuous phase is the water. Simulations were performed at different oil-to-water viscosity ratios $\left(\frac{\mu_o}{\mu_w}\right)$ of 3, 12, 27, and 50. The interfacial tension between PDMS oil and water is 0.0118 N/m. It has been reduced to 0.008 N/m, 0.005 N/m, and 0.002 N/m, and simulations were performed. The walls of the microchannel are considered to be PMMA surfaces. The contact angle of an oil droplet on the PMMA surface in the presence of water is 140°. The effect of wettability was shown at various contact angles (angle created by water droplet on the PMMA surface in the presence of oil) of 0°, 40°, 90°, 135° and 180°. Frequency of droplet (1/s), non-dimensional droplet length (L/W_c), droplet volume (nL), and droplet velocity (m/s) have been calculated for each of the cases. A flow pattern map has been developed to identify the dripping and jetting regimes. A comparison between normal geometry and two constricted geometries (having different orifice lengths) based on the frequency of droplet, non-dimensional droplet length, droplet volume, and droplet velocity has been made for both dripping and jetting regimes. Prediction of simulated non-dimensional droplet length has also been made using dimensional analysis. An Iso-surface visualization of the dripping regime at different oil-water viscosity ratios is represented in Figure 5.

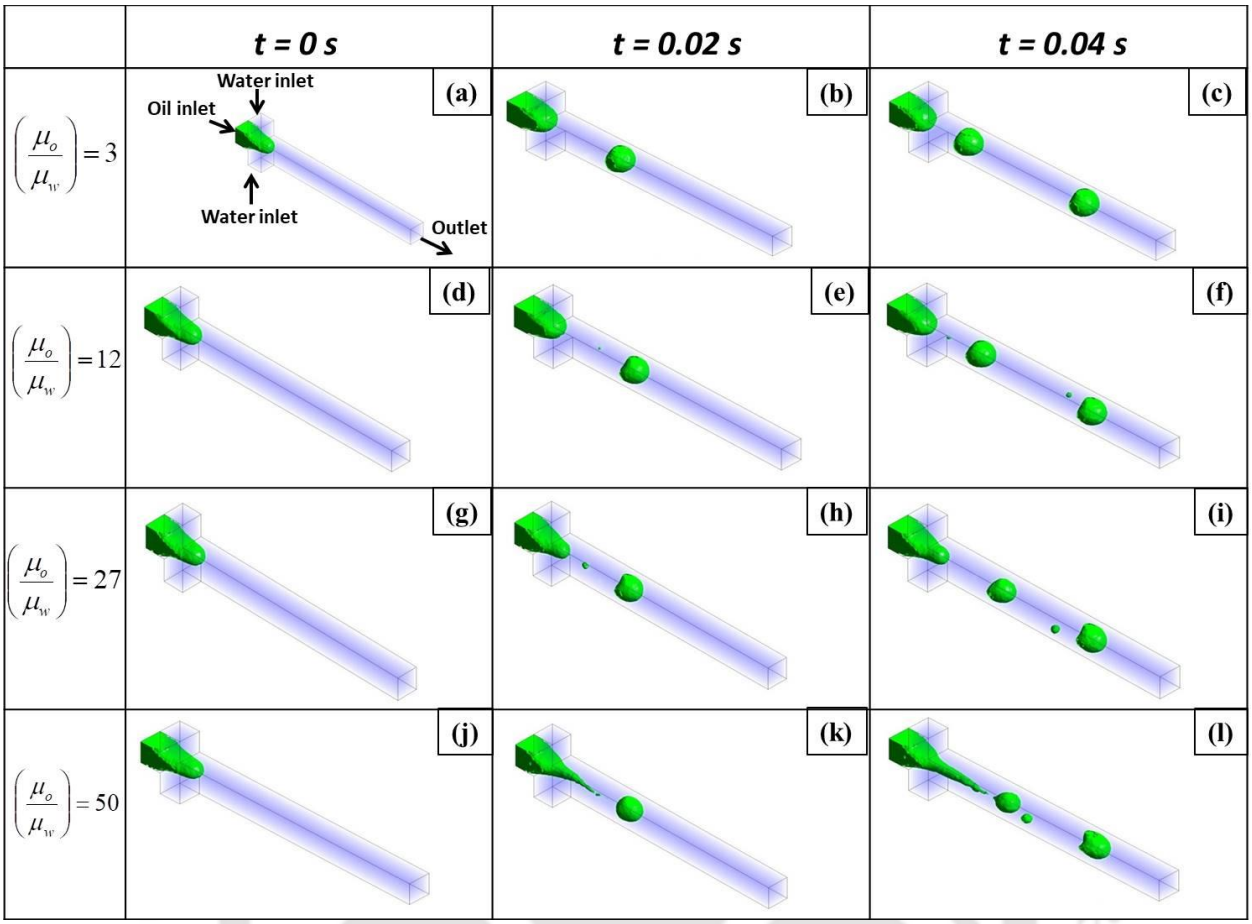

Figure 5. Time variation of Iso-surface visualization of dripping regime at different oil-water viscosity ratio

6. Objective – IV: Two-dimensional numerical simulation of droplet splitting in multi-furcating microchannel

Multiple splitting of droplets through multi-furcating microchannel, consisting of five outlets, is investigated using 2D simulation. For all five multi-furcating branches, a width ratio of 0.25 (branch channel width/main channel width) is used since multiple splitting occurs at this ratio. The values of the dispersed phase velocity at which the droplets multi-furcate across the five arms of the microchannel are determined. The mechanism of droplet multi-furcation is explained. Oil fraction data were collected for five velocity combinations, with the continuous phase velocity set to greater than 0.16 m/s, causing droplets to multi-furcate along the micro channel's five arms and is compared with the homogenous model. The droplet length distribution in the branch channels with various angles (0º, ±40º, and ±90º branch channels) is performed. The droplet frequency (counts per unit time) in the branch channels (0º, ±40º, and ±90º) is determined. Variation in the area distribution ratio with the capillary number was also observed. In this study a method for droplet splitting is proposed and our findings can be used in droplet-based biological assays. Mechanism of multi-furcation of droplets through multi-furcating channel has been explained with the help of volume fraction contour, dynamic pressure, velocity vector and vorticity in Figure 6.

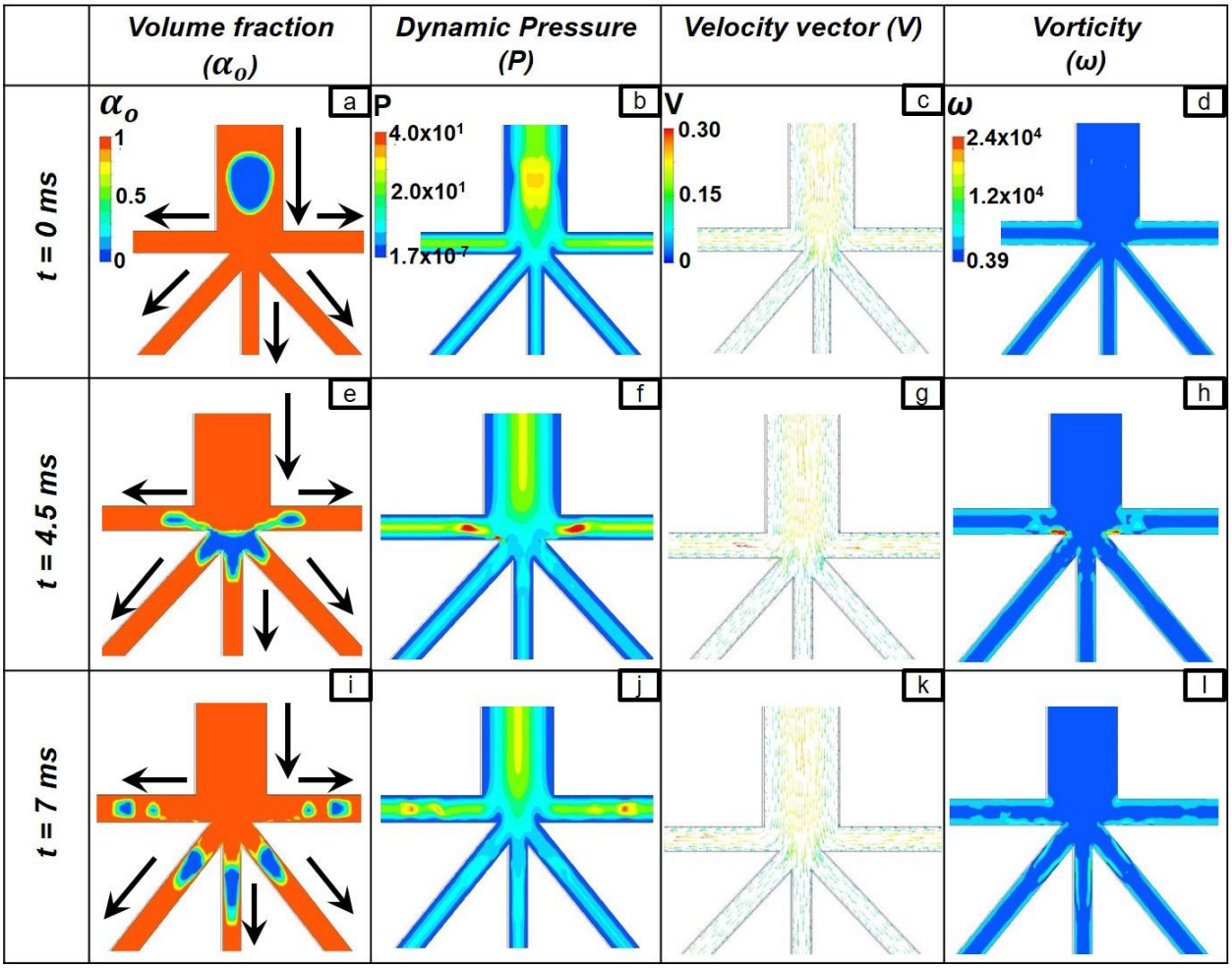

Figure 6. Pictorial representation of insight physics of a multi-furcation phenomena at V_w = 0.002 m/s and V_o = 0.16 m/s. 2nd column -volume fraction contour; 3rd column -dynamic pressure; 4th column -velocity vectors; and 5th column -vorticity

Summary

The detailed conclusions of the individual technical chapters are elaborated below.

- In the third chapter (first technical chapter), two types of droplet breakup regimes, namely tunnel-breakup and obstructed breakup and one non-breakup regime, alternate movement has been observed. New flow morphology, namely mixed flow pattern, transient in nature, has also been observed in a wide range of phase velocities. It has been found that pressure swing phenomena at the T-junction have instigated the movement of the droplets in alternate directions. The formation of vortex flow at the front ends of the droplets is one of the critical reasons for droplet breakup with tunnel. On the other hand, the resultant effect of larger droplet volume, upstream pressure buildup, and vortex flow are found to be responsible for droplet bifurcation with obstruction. The results show that the drift flux model gives a higher accuracy in pressure drop prediction.

- In the fourth chapter (second technical chapter), the tunnel breakup and the obstructed breakup are mainly due to the pressure difference in the branch channel and the direction of the velocity vectors which are toward the branch's exit, and the pressure swing phenomenon is the reason behind the alternate movement of the droplets. It has been found that breakup tendency increases as we decrease the width ratio (1, 0.75, 0.5, and 0.25) and increase the arm length ratio (0.4, 0.6, and 0.9).

- In the 5.a. chapter (third technical chapter), a mechanism on dripping and jetting phenomena also has been discussed. A flow pattern map has been presented identifying the dripping and

jetting regimes. It has been observed that the dripping is restricted to low to moderate weber numbers of the dispersed phase and low to high capillary numbers of the continuous phase. At the same time, the jetting regime is limited to low to high capillary numbers of continuous phases and moderate to high weber number of the dispersed phase. The transition between dripping and jetting has been confirmed through the calculation of the effective capillary number of the interface. The droplet size decreases with an increase in oil-water viscosity ratio and with a decrease in interfacial tension. The time scale of jet growth increases with an increase in oil-water viscosity ratio and a decrease in interfacial tension.

- In the 5.b. chapter (fourth technical chapter), It has been observed that the droplet became smaller in size with an increase in the oil-water viscosity ratio. The frequency increases with an increase in the oil-water viscosity ratio. On the other hand, droplets became larger with the increase in the interfacial tension. The droplet is not generated at 0.002 N/m (i.e., 0 Hz frequency) as a continuous oil thread is observed. In the present simulation, droplets onset at the interfacial tension of 0.005 N/m and frequency at this condition is 60 Hz. Then, it decreases continuously with an increase in the interfacial tension. Droplet velocity decreases with an increase in the interfacial tension. The effect of wettability was studied by changing wettability angles (θ) (angle created by water droplet on the PMMA surface in the presence of oil) from 0º-180º. For θ < = 90º, water is the continuous phase in which droplets of PDMS were formed. For θ > 90, the water became the dispersed phase in the continuous oil medium. At θ = 135° and 180º, the channel becomes super hydrophobic, which gives an annular flow configuration in the channel. Here, the oil phase warps the channel surface, and the water phase turns into a continuous thread flowing through the centre of the channel.

Wettability also influences the non-dimensional droplet length (L/W_c). The highest value of L/W_c and droplet volumes are 1.25 and 220 nL, respectively, at $\theta = 100°$. The frequency increases from 18-36 Hz for a change of θ from 0°-90° respectively, and then it decreases due to a change of θ from 90°-180°. It is important to note that a water thread is formed beyond $\theta = 135°$. That is why droplet frequency is considered 0 Hz. The droplet velocity increases from 0.045-0.050 m/s for change in θ from 0°-80° and then it decreases from 0.050-0.020 for the θ ranging from 80°-180°. Prediction of non-dimensional droplet length was made with the help of dimensional analysis in a flow-focusing geometry.

- In the sixth chapter (fifth technical chapter), the critical value of the dispersed phase and continuous phase velocities at which the droplets multi-furcate across the five arms of the microchannel is $V_w = 0.0001$ m/s and $V_o = 0.16$ m/s respectively. The mechanism for droplet multi-furcation is explained. A percentage deviation of 16.48 is found between the simulated oil fraction data and the homogenous model. The droplet length distribution in the branch channels (0^o, $\pm 40^o$, and $\pm 90^o$ branch channels) was found. It was observed that the dimensionless droplet length (l) increases first up to a certain flow rate ratio (0.62), then decreases. The frequency of droplet generation increases with an increase in capillary number. Variations in the area distribution ratio with the capillary number have also been reported.

Future scopes:

The works presented in the technical chapters further open up a wide range of future scopes in the relevant working fields, some of which are referred below.

- Experiments or simulation on droplet breakup can be done for non-Newtonian fluids.
- Air can be used instead of oil, and experiments/simulations can be done on droplet breakup.
- The effect of mass transfer or heat transfer on droplet breakup dynamics can be observed through simulation, experiment, or both.
- Experiments or simulations on droplet breakup can be done for more complex geometry.

ABSTRACT

Droplets can be used as mini-reactors. They provide precise control over any reagent amount, which improves reaction repeatability and uniformity. The small droplets decrease exposure to potentially hazardous chemicals. The food industry, diagnostic testing, cosmetics, supra-magnetic nanoparticle production, medication delivery, and drug discovery all use homogeneous droplets. Droplets are often formed by mechanical agitation. However, mechanical mixing produces droplets of varying sizes. This might jeopardize process controllability. Microfluidics, the study of fluid dynamics at the micro to the nanoscale, enables the control of droplet size and quantity. With hundreds to thousands of droplets formed each second, the throughput of droplet formation rises. Droplets can be formed using i) Active method ii) Passive method. The passive method includes various ways, such as T-junction, co-flow, flow-focusing, and some variants. On the other hand, additional energy such as alternating or direct current is applied in the case of active splitting. In this work, an interest was felt in doing the numerical study on droplet breakup dynamics in microchannels using the passive method with the help of CFD. The objectives of the present work are as follows:

I. A computational study on phase velocity mediated droplet splitting and its mechanism at T-junction microchannel

II. Influence of microchannel geometry on droplet breakup dynamics: a computational study

III. Numerical appraisal on liquid-liquid two-phase flow in a flow-focusing system

IIIa. 2D simulation of dripping and jetting flow in a flow-focusing geometry

IIIb. 3D simulation of dripping and jetting phenomena in a flow-focusing geometry

IV. Two-dimensional numerical simulation of droplet splitting in multi-furcating microchannel

A computational fluid dynamics study has been performed to reveal the inside physics of the droplet breakup mechanism when droplets pass through the T-junction of a microchannel. Two types of droplet breakup regimes, namely tunnel-breakup and obstructed breakup, and one non-breakup regime, including the alternate movement, have been observed. A new flow morphology, namely a mixed flow pattern, transient in nature, has also been observed in a wide range of phase velocities. The effect of width ratio (branch channel/ main channel) and arm length ratio (right arm length/ left arm length) on droplet splitting were investigated. It has been found that breakup tendency increases as we decrease the width ratio (1, 0.75, 0.5, and 0.25) and increase the arm length ratio (0.4, 0.6, and 0.9). Four flow pattern maps were developed based on the various mixed flow patterns for four different width ratios. A flow pattern map has been presented identifying the dripping and jetting regimes. The droplet size decreases with an increase in oil-water viscosity ratio and with a decrease in interfacial tension. The time scale of jet growth increases with an increase in oil-water viscosity ratio and a decrease in interfacial tension. The effect of oil-water viscosity ratio, surface tension, and wettability on dripping and jetting flow has been observed using 3D simulation. It has been observed that the droplet became smaller in size with an increase in the oil-water viscosity ratio. The frequency increases with an increase in the oil-water viscosity ratio. On the other hand, droplets became larger with the increase in the interfacial tension. The droplet is not generated at 0.002 N/m (i.e., 0 Hz frequency) as a continuous oil thread is observed. In the present simulation, droplets onset at the

interfacial tension of 0.005 N/m and frequency at this condition is 60 Hz. Then, it decreases continuously with an increase in the interfacial tension. Droplet velocity decreases with an increase in the interfacial tension. The effect of wettability was studied by changing wettability angles (θ) (angle created by water droplet on the PMMA surface in the presence of oil) from 0º-180º. For $\theta \leq 90^{\circ}$, water is the continuous phase in which droplets of PDMS were formed. For $\theta > 90°$, the water became the dispersed phase in the continuous oil medium. Prediction of non-dimensional droplet length was made with the help of dimensional analysis in a flow-focusing geometry. In the last objective, the multi-furcation of droplets through a multi-furcating channel was observed using 2D simulation. The critical value of the dispersed phase and continuous phase velocities at which the droplets multi-furcate across the five arms of the microchannel is $V_w = 0.0001$ m/s and $V_o = 0.16$ m/s, respectively. It was observed that the dimensionless droplet length (l) increases first up to a certain flow rate ratio (0.62), then decreases. The frequency of droplet generation increases with an increase in capillary number.

LIST OF CONTENTS

NOMENCLATURE

Subscripts

tp is the two phase

g is the gas

l is the liquid

m is the mixture

w is the water phase

Latin Capital Letters

D is the pipe diameter, m

D_M is the diameter of main and branch channel, m

X is the Martinelli parameter

U_m is the mixed velocity, m/s

U_{so} is the superficial velocity of oil, m/s

U_{sw} is the superficial velocity of water, m/s

H_o is the hold up

P is the Pressure, Pa

L is the Length, m

P is the total pressure, Pa

F_s is the surface tension force, N

V_o is the oil velocity, m/s

V_w is the water velocity, m/s

Re_m is the Reynolds mixture number

Q_o is the volumetric flow rate of oil, m^3

Q_w is the volumetric flow rate of water, m^3

A is the cross sectional area of the channel, m^2

Greek Symbols

μ is the viscosity, Pa.s

μ_m is the mixed viscosity, Pa.s

ρ is the density, Kg/m^3

ρ_m is the Mixed density, Kg/m^3

σ is the Interfacial tension, N/m

ϕ is the two phase multiplier

Π is the dimensionless group

θ is the Contact angle (°)

α_o is the volume fraction of mineral-oil

γ is the area distribution ratio

ρ_o is the oil density, Kg/m^3

ρ_w is the water density, Kg/m^3

α_w is the volume fraction of water

μ_o is the oil viscosity, Pa.s

μ_w is the water viscosity, Pa.s

ω is the vorticity, 1/s

θ_{wl} is the contact angle, ° (Degree)

β_o is the input phase fraction

Lowercase Letters

f is the friction factor

f_m is the friction factor of the mixture

e is the Roughness factor

l is the dimensionless droplet length

x is the mass fraction of oil

g is the gravity acceleration, m/s^2

u is the velocity, m/s

$\hat{n}$ is the surface normal

k is the local surface curvature

$\hat{n}_{wl}$ are the unit vectors normal to the wall

$\hat{t}_{wl}$ are the unit vectors tangential to the wall

p is the dynamic pressure, Pa

Abbreviations

CFD is the Computational fluid dynamics

VOF is the Volume of fluid

LIST OF FIGURES

LIST OF TABLES

CHAPTER 1

INTRODUCTION

1.1 OVERVIEW

Droplet based microfluidics has attracted the attention of lot of researchers due to its easy applicability in the field of food industry [1], diagnostic tests [2], cosmetics [3], supra-magnetic nanoparticle synthesis [4], single-cell RNA/DNA sequencing [5], droplet digital PCR [6], nanoparticle synthesis [7], drug delivery [8], and drug discovery [9], etc. Droplet miniaturization is critical in micro channels because plug, slug, and separated flow dominate the morphology of multiphase flow. Heat, mass, and other interfacial transit can be improved in gas-liquid, liquid-liquid, and gas-liquid-solid flows by producing micro or miniaturized droplets. A small droplet serves as a reagent vessel and a sample cage inside a continuous liquid phase [10]. Droplet flow provides several advantages over continuous flow, including the ability to scale down the reagent quantity to micro/Nano liters, shorten reaction time, and improve reaction efficiency [11]. This facilitates simpler management of operational parameters, such as cost reduction if expensive chemicals are used. There are two ways to make micro droplets: I) Active method II) Passive method [12]. The droplet is created utilizing external forces such as electrical, magnetic, or thermal energy in the active method. In passive method, droplet is created under the effect of the shape of the channel and the flow hydrodynamics. Micro droplets can be formed in a variety of ways, including T-junction, co-flow, flow-focusing, and some variants [13]. Shear force is pragmatic in these geometries to break down droplets. Various flow regimes, such as squeezing, dripping, jetting, and continuous regimes, may be seen. Also, there are several methods for lowering the size of a droplet in a microchannel. This include modifying the fluid characteristics [14], introducing constriction into the channel [15], producing a pattern on the inner wall of the channel [16], diverting the flow through T and Y channel or through channel network [17], etc. Researchers used multiphase numerical simulation to estimate different flow regimes based on

flow hydrodynamics. In the multiphase numerical simulation, momentum and continuity are employed as governing equations to compute the interface. A variety of methodologies may be used to simulate multiphase flow, including the volume of fluid (VOF) model, the level set method (LS), the phase-field method, and the lattice Boltzmann method (LBM) [18]. The VOF method [19] is a Eulerian-Eulerian variant in which the secondary phase is not dispersed inside the main phase but rather exists as an interface between the phases, which must be tracked while also calculating a momentum equation for each phase. Even on coarse meshes, the VOF maintains mass conservation, while the level set offers a defined contour for the interface and a smoothly differentiable field. The level set method [20] is a technique for describing moving fronts implicitly. The fundamental principle is that the front position is specified as the zero level set of an auxiliary field defined across the domain of interest. In the phase field technique, the state of the whole microstructure is represented continuously by a single variable known as the order parameter w [21]. For instance, $\phi = 1$, $\phi = 0$, and $0 < \phi < 1$ denote the precipitate, matrix, and interface, respectively. The latter is thus found by the area where w shifts from its precipitate value to its matrix value. The width of the interface is the range across which it changes. The phase field is the collection of values of the order parameter throughout the entire volume. The LBM is a numerical approach for studying fluid flows at the microscopic level that is analogous to the kinetic theory of gases [22]. Instead of solving the Navier–Stokes equations directly, streaming and collision (relaxation) processes are used to simulate a fluid density on a lattice. The approach is adaptable because the model fluid may be easily modified to imitate common fluid behavior such as vapor/liquid coexistence, allowing fluid systems such as liquid droplets to be mimicked. Furthermore, fluids in complicated settings, such as porous media, can be easily

simulated, whereas other CFD methods might be difficult to deal with when the boundaries are complex.

Table 1.1. Comparison between level set method and VOF method [23]

Characteristics & features	**Level set method**	**VOF method**
Governing equation	$\frac{\partial \phi}{\partial t} + u_i \frac{\partial \phi}{\partial x_i} = 0$	
Physical interpretation	Application of (Kinematic) free surface boundary condition ($D\varphi/Dt = 0$)	Transport equation of mass fraction (or concentration)
Location of interface	$\Phi = 0$ (usually)	$\Phi = 0.5$ (usually)
Re-processing of interface	Reinitialization (Redistancing) – PDE or Geometric approach	Reconstruction of free surface (SLIC, PLIC etc.)
Surface tension modelling	Easy to incorporate	Not straightforward
3D extension	Relatively straightforward	Not easy
Development	Osher and Sethian [24]	Hirt and Nichols [19]
Applications	Research in CFD, special effects in movies, etc.	Commercial codes in CFD (FLOW 3D, FLUENT, ANSYS, etc.), CADMAS-SURF, etc.

Table 1.2. Applications, advantages and disadvantages of VOF, LS and LBM Method [25]

	VOF & Level set method	LBM method
Applications	• Cardiovascular system • Arterial flow and pathologies • Respiratory flows • Medical devices	• Arterial flow and pathologies • Respiratory flows • Cell dynamics and interactions • Microfluidics/ lab-on-a-chip
Advantages	• Suited to larger space/time scale • Mature, well understood and robust • Handles macroscopic quantities	• Retains particle-based physics • Restricted to adjacent points • Simple basic boundary conditions • Incorporates physics naturally
Disadvantages	• Limited by continuum assumption • Time consuming mesh generation • Complex non-linear, non-local equations	• Stability limitations with basic model • Generally limited to square lattices • Relatively new method as compared with LS & VOF

1.2 DROPLET SPLITTING THROUGH T-JUNCTION OF A MICROCHANNEL

Droplet splitting through T-junction of a microchannel is a passive method. Mainly two types of breakup phenomena take place at T-junction of a microchannel: i) Breakup with tunnel ii) Breakup with obstruction. And one non-breakup phenomena: i) Alternate movement of droplets. These three types of flow are schematically shown in Figure 1.1.

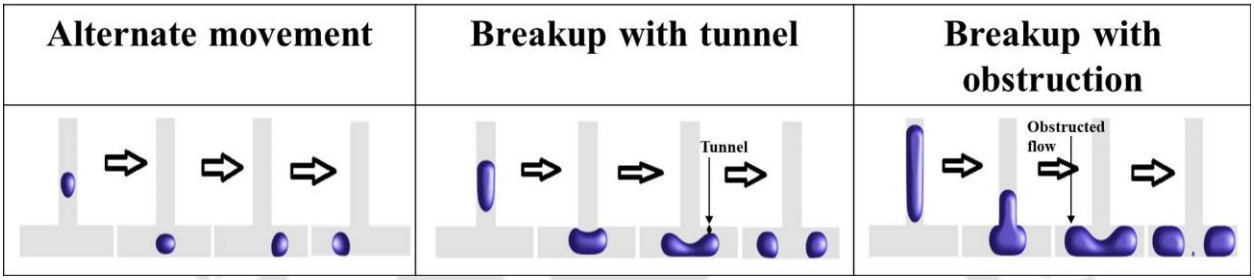

Figure 1.1. Type of breakup in a T-junction of a microchannel adopted from [26]

In case of breakup with tunnel, the breakup process is divided into three parts: i) Extension ii) Squeeze iii) Post-breakup [27]. The interface is warped from a circular shape to a spherical cap during the extension stage, and it eventually converts to a slug with a continuously flattening back interface. When the back interface simply leaves the main channel, it is completely flat. Following that, the upstream liquid squeezes the central section of the slug, indicating that the droplet breakup process has entered the squeeze stage. The liquid flows downstream via the "tunnel" wedged between the droplet and the branch wall (i.e. the lubricating liquid flow) during the squeeze stage, and the droplet is lengthened and pushed downstream in the branch. When the droplet becomes the shape of a dumbbell, it reduces the width of the neck between two branches. The lubricating liquid flow velocity is substantially larger than the droplet velocity. When the shear force of the lubricant liquid layer acting on the droplet exceeds the interfacial tension, a local vortex flow forms at the droplet's front edge, pushing the dumbbell-

shaped bubble towards the channel outlet. This vortex flow and the accumulated upstream pressure in the main channel aid in narrowing the neck in the center of the droplet, eventually causing the pinch-off of the neck and splitting of the droplet with tunnel. In case of breakup with obstruction, the breakup process is divided into three parts: i) Extension ii) Squeeze iii) Post-breakup [27]. In contrast to the "tunnel" breakup regime, the upstream liquid is unable to flow around the droplet to the downstream during the whole droplet breakup process in the obstructed breakup regime. During the extension stage, the droplet is twisted from a slug shape to a "T" shape before reverting to a slug shape in the branch. As, no upstream liquid can bypass the droplet, so surface tension force is the dominating force here. In the middle of the bifurcation, an arc-shaped depression emerges, and the droplet flow enters the squeeze stage. As time passes, the neck narrows until the droplet pinches off into two daughter droplets that still obstruct the branch. And alternate movement of droplets is due to pressure swing phenomena. The periodic difference in pressure in the left and right arm of the microchannel causes the alternate movement of the droplets. There is no squeezing and pinch-off stage of the droplets observed during an alternating flow of droplets. It happens for small droplets with low dispersed and moderate continuous phase velocity onsets. Only extension and pushing stages exist [27]. During the extension stage, the droplet makes contact with the opposing wall and deforms. As a result, the front interface flattens out gradually. The degree of deformation is inadequate to split the droplet since the shear force exerted on it is relatively little in comparison to the surface tension force. Following the extension stage, the droplet enters the pushing stage. The continuous phase runs across the space between the droplet's surface and the channel wall's corner. This results in the formation of a high-pressure zone on the left side of the T-junction. This increased pressure forces the droplet into the right side of the T-junction. When the second droplet arrives at the T-

junction, a high-pressure zone forms on the right side of the T-junction, pushing the droplet into the left side of the T-junction. As long as the velocity of the phases remains constant, this time-periodic change of pressure and alternating droplet motion will continue. Thus, the alternative motion of the water droplet is caused by the periodic swing of the high-pressure zone in the left and right sides of the T-junction microchannel.

1.3 DROPLET FORMATION IN A FLOW-FOCUSING GEOMETRY

Flow focusing on fluid dynamics is a technique whose goal is to produce droplets or bubbles using simple hydrodynamic procedures. The result is dispersed liquid or gas. Flow focusing has potential applications in the food, medical, pharmaceutical, cosmetic, photography, and environmental industries, etc. Droplet formation takes place in a flow-focusing geometry due to the balance in inertia, surface, viscous and pressure forces. According to the varied confinements, common microfluidic flow-focusing devices may be classified into three kinds: i) Axisymmetric capillary co-flowing device ii) The flow-focusing junction iii) Cross-junction geometry. Jetting and dripping are the two main flow regimes seen in a flow-focusing geometry. Other flow regimes which can be seen are: tubing, viscous displacement, dripping-plug, dripping-monodispersed, jetting-monodispersed, jetting-plug [28]. All these flow regimes are schematically shown in Figure 1.2.

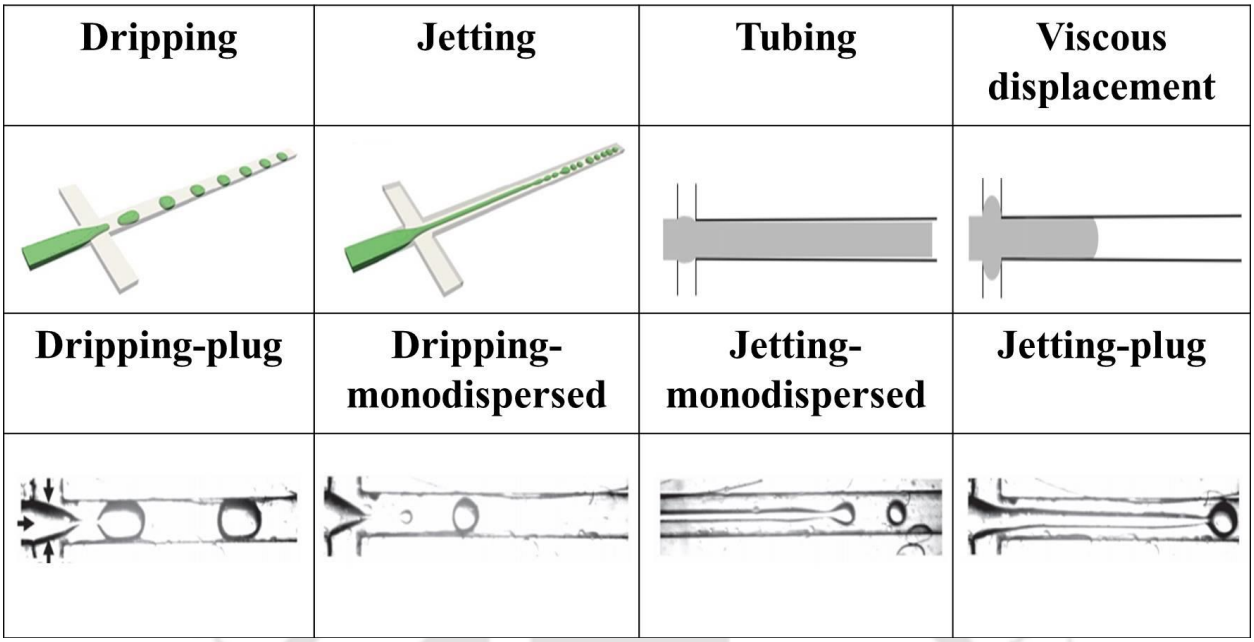

Figure 1.2. Different regimes in a flow focusing geometry adopted from [28] and [29]

The dripping–jetting transition may be calculated by comparing the capillary collapse time in Rayleigh–Plateau instability to the dispersed thread growth time [30], or by comparing the capillary time for interfacial disturbance growth and the fluid's convective flow time. The factors on which the size and frequency of the droplets depends are: i) surface tension ii) viscosity iii) contact angle. It can be seen that with increase in oil-water viscosity ratio, the droplet size decreases and frequency of droplet formation increases. This is because increasing the oil-water viscosity ratio means increasing the viscous force. This increases the shear force acting on the dispersed phase. Moreover, now, the shear force is greater than the interfacial tension. This leads to the breakup of the dispersed thread faster, generating tiny droplets. With the decrease in surface tension, the droplet size decreases and frequency of droplet formation increases.

The formation process of micro droplets in a flow-focusing is basically divided into three stages: i) Filling stage ii) Necking stage and iii) Detachment stage [31]. The two phases enter from three distinct inlets during the filling stage. The dispersed phase enters through the inlet which is symmetry with the X axis, and the continuous phase enters through the inlet which is symmetry with the Y axis, and the two fluids meet at the confluence of the micro channel. The two phases run downstream of the main channel due to the pressure in the second stage. Because of the combined influence of interfacial tension and viscous force, the dispersed phase's manifold is compressed by the continuous phase. Due to capillary instability and contact between the two phases, the continuous phase exerts a flow-focusing effect on the dispersed phase in the third stage. The symmetrical shear pressure of the continuous phase influences the dispersed phase on both sides, causing it to fail to remain stable and break into uniform droplets.

In case of dripping flow, the thickness of the neck of dispersed phase reaches critical and droplets are formed near the junction but in case of jetting flow, the thickness of the neck of dispersed phase doesn't reaches critical value, instead a lengthy jet is formed. Due to jet instability, it breaks into uniform droplets at a certain distance from the junction.

1.4 MULTI-FURCATION OF DROPLET THROUGH MULTI-FURCATING CHANNEL

The droplets multi-furcate due to the pressure drop and the shear stress of the flow field. The formation process of micro droplets in a multi-furcating channel is basically divided into three stages: i) Expansion ii) Squeezing and iii) Pinch-off [32]. During the expansion stage, the mother droplet spreads continuously until the moment that it firstly touches the sharp corners of the branches. During the squeezing stage, the mother droplet moves toward the junction under

the combined action of inertia force, shear force, surface tension and became into a thin threaded necklace-like structure due to the vortex formation in the sharp corners of the branches. After that it enters into the pinch-off stage where the mother droplet splits into five daughter droplets under the influence of local surface tension and pressure forces and pass through the five arms of the microchannel. The droplets passing through the five arms of the microchannel are not having the same size because of the difference in the pressure in the five arms of the microchannel.

Critical condition for multi-furcation of a single mother droplet into five daughter droplets can be found by tuning the dispersed and continuous phase velocities. Finding the oil fraction data, dimensionless droplet length in branch channel, area distribution ratio of droplet in branch channel and frequency of the droplets generated in each arm of the multi-furcating channel will help us in understanding the performance of the microfluidic device.

1.5 COMPARISON BETWEEN 2D AND 3D SIMULATIONS

Although 2D simulations take less computing time than 3D simulations, the 2D technique has numerous drawbacks over the 3D method. The 2D model is insufficient for estimating shear forces accurately. It can only provide an estimate. However, the general pattern of the shear force and the type of its influence will stay unchanged. Furthermore, 2D simulation does not adequately account for surface force and does not estimate viscous force with better precision. In comparison, the 3D technique considers surface and viscous force. As a result, the droplet's shape and size will vary, but the overall flow pattern (interfacial arrangement or volume fraction contours) will remain constant. Although 2D simulation is not ideal for accounting the absolute values of the various forces, it is useful for qualitative estimation of flow patterns. It is also

useful where there is influence of channel geometry. 2D simulation perfectly accounts the velocity field and fluid properties (except surface forces). Whereas 3D simulations are ideal for quantitative measurement (for measuring droplet length, neck thickness, film thickness, etc.).

1.6 OBJECTIVES AND SCOPE OF PRESENT RESEARCH WORK

Microfluidics has piqued the interest of many experts from industry and academia because microchannel-based devices allow us to scale down the reagent amount to micro/Nano liters, reduce reaction time, and improve reaction efficiency, and provide significant advantages in terms of environmental point of view. It also allows for the miniaturization of a wide range of existing scientific and industrial equipment. The literature review is discussed in the introduction section of the respective chapters. So, here in this thesis, we aim to explore:

I. A computational study on phase velocity mediated droplet splitting and its mechanism at T-junction microchannel

II. Influence of microchannel geometry on droplet breakup dynamics: a computational study

III. Numerical appraisal on liquid-liquid two-phase flow in a flow-focusing system

IIIa. 2D simulation of dripping and jetting flow in a flow-focusing geometry

IIIb. 3D simulation of dripping and jetting phenomena in a flow-focusing geometry

IV. Two-dimensional numerical simulation of droplet splitting in multi-furcating microchannel

1.7 ORGANIZATION OF THE THESIS

The present dissertation is organized into eight chapters:

1. The first chapter gives a brief introduction to about the droplet microfluidics, it's area of applicability, different methods to create droplet, different ways through which size of a droplet can be reduced, the different multiphase models.

2. CFD methodology in detail have been discussed in chapter two.

3. Chapter three reports the probable insights behind the droplet breakup and the mixed flow pattern in a microchannel T-junction. The velocities of the oil and water phases were altered to better understand the mechanics of the many forms of droplet breakup occurrences. The effects of the velocity field, pressure field, and vorticity magnitude on droplet breaking up have been investigated.

4. Chapter four reports the effect of width ratio and arm length ratio on droplet breakup dynamics in a microfluidic T-junction. Prediction of pressure drop using Lockhart and Martinelli approach and Dimensional analysis have been reported.

5. In chapter 5a, 2D simulations have been performed to investigate the effect of phase velocities on flow regime in a flow-focusing geometry. Regime transition criteria has been discussed. The effect of oil-water viscosity ratio and interfacial tension on droplet size is also investigated.

6. In chapter 5b, 3D simulations have been performed to investigate the effect of viscosity, surface tension, wettability and geometry on droplet size, frequency, droplet volume and droplet velocity in a flow-focusing geometry. Prediction of simulated non-dimensional droplet length has also been made using dimensional analysis.

7. Numerical simulation of droplet splitting in multi-furcating microchannel using 2D simulation has been reported in chapter 6. The mechanism for droplet multi-furcation has been explained in this chapter. Critical value of dispersed phase velocity at which multiple splitting takes place has been revealed. Study of three parameters (dimensionless droplet length, droplet frequency (counts per unit time), and area distribution ratio) have been done to understand the insight of the multi-furcation.

8. Finally, novel contributions from the preceding chapters are presented as conclusion and potential area for future scope are proposed in the chapter seven.

REFERENCES

1. Liu, Z.-M., Yang, Y., Du, Y., and Pang, Y., Advances in Droplet-Based Microfluidic Technology and Its Applications, *Chinese Journal of Analytical Chemistry*, 2017, vol. 45, no. 2, pp. 282-296.
2. Pollack, M.G., Pamula, V.K., Srinivasan, V., and Eckhardt, A.E., Applications of electrowetting-based digital microfluidics in clinical diagnostics, *Expert Review of Molecular Diagnostics*, 2011, vol. 11, no. 4, pp. 393-407.
3. Yukuyama, M.N., Ghisleni, D.D.M., Pinto, T.J.A., and Bou-Chacra, N.A., Nanoemulsion: process selection and application in cosmetics – a review, *International Journal of Cosmetic Science*, 2016, vol. 38, no. 1, pp. 13-24.
4. Zhang, Y., Fan, J., and Wang, L., Formation of Nanoliter Droplets in a Confined Microfluidic T-Shaped Junction: Formation Time and Droplet Volume, *Current Nanoscience*, 2009, vol. 5, no. 4, pp. 519-526.
5. Guo, S., Lin, W.N., Hu, Y., Sun, G., Phan, D.-T., and Chen, C.-H., Ultrahigh-throughput droplet microfluidic device for single-cell miRNA detection with isothermal amplification, *Lab on a Chip*, 2018, vol. 18, no. 13, pp. 1914-1920.
6. Perkins, G., Lu, H., Garlan, F., and Taly, V., *Chapter Three - Droplet-Based Digital PCR: Application in Cancer Research*, in *Advances in Clinical Chemistry*, G.S. Makowski, Editor. 2017, Elsevier. p. 43-91.
7. Wojnicki, M., Tokarski, T., Hessel, V., Fitzner, K., and Luty-Błocho, M., Continuous, monodisperse silver nanoparticles synthesis using microdroplets as a reactor, *Journal of Flow Chemistry*, 2019, vol. 9, no. 1, pp. 1-7.

8. Fontana, F., Ferreira, M.P.A., Correia, A., Hirvonen, J., and Santos, H.A., Microfluidics as a cutting-edge technique for drug delivery applications, *Journal of Drug Delivery Science and Technology*, 2016, vol. 34, no. pp. 76-87.

9. Dittrich, P.S. and Manz, A., Lab-on-a-chip: microfluidics in drug discovery, *Nature Reviews Drug Discovery*, 2006, vol. 5, no. 3, pp. 210-218.

10. Srinivasan, V., Pamula, V.K., and Fair, R.B., Droplet-based microfluidic lab-on-a-chip for glucose detection, *Analytica Chimica Acta*, 2004, vol. 507, no. 1, pp. 145-150.

11. Kobayashi, J., Mori, Y., and Kobayashi, S., Multiphase Organic Synthesis in Microchannel Reactors, *Chemistry – An Asian Journal*, 2006, vol. 1, no. 1-2, pp. 22-35.

12. Zhu, P. and Wang, L., Passive and active droplet generation with microfluidics: a review, *Lab on a Chip*, 2017, vol. 17, no. 1, pp. 34-75.

13. Christopher, G.F. and Anna, S.L., Microfluidic methods for generating continuous droplet streams, *Journal of Physics D: Applied Physics*, 2007, vol. 40, no. 19, pp. R319.

14. Timung, S., Tiwari, V., Singh, A.K., Mandal, T.K., and Bandyopadhyay, D., Capillary force mediated flow patterns and non-monotonic pressure drop characteristics of oil-water microflows, *The Canadian Journal of Chemical Engineering*, 2015, vol. 93, no. 10, pp. 1736-1743.

15. Dennis, S. and Smith, F.T., Steady flow through a channel with a symmetrical constriction in the form of a step, *Proceedings of the Royal Society of London. A. Mathematical and Physical Sciences*, 1980, vol. 372, no. 1750, pp. 393-414.

16. Yamasaki, Y., Goto, M., Kariyasaki, A., Morooka, S., Yamaguchi, Y., Miyazaki, M., and Maeda, H., Layered liquid-liquid flow in microchannels having selectively modified

hydrophilic and hydrophobic walls, *Korean journal of chemical engineering*, 2009, vol. 26, no. 6, pp. 1759-1765.

17. Salim, A., Fourar, M., Pironon, J., and Sausse, J., Oil–water two-phase flow in microchannels: Flow patterns and pressure drop measurements, *The Canadian Journal of Chemical Engineering*, 2008, vol. 86, no. 6, pp. 978-988.
18. Liu, J. and Trung Nguyen, N., Numerical simulation of droplet-based microfluidics-A review, *Micro and Nanosystems*, 2010, vol. 2, no. 3, pp. 193-201.
19. Hirt, C.W. and Nichols, B.D., Volume of fluid (VOF) method for the dynamics of free boundaries, *Journal of computational physics*, 1981, vol. 39, no. 1, pp. 201-225.
20. Sethian, J.A., *Level set methods and fast marching methods: evolving interfaces in computational geometry, fluid mechanics, computer vision, and materials science*. Vol. 3. 1999: Cambridge university press.
21. Qin, R. and Bhadeshia, H., Phase field method, *Materials science and technology*, 2010, vol. 26, no. 7, pp. 803-811.
22. lnamuro, T., Yoshino, M., and Suzuki, K., *An Introduction to the Lattice Boltzmann Method: A Numerical Method for Complex Boundary and Moving Boundary Flows*. 2022: World Scientific.
23. Lee, H., Water wave generation with source function in the level set finite element framework, *Journal of Mechanical Science and Technology*, 2015, vol. 29, no. 9, pp. 3699-3706.
24. Osher, S. and Sethian, J.A., Fronts propagating with curvature-dependent speed: Algorithms based on Hamilton-Jacobi formulations, *Journal of computational physics*, 1988, vol. 79, no. 1, pp. 12-49.

25. O'Connor, J., Day, P., Mandal, P., and Revell, A., Computational fluid dynamics in the microcirculation and microfluidics: what role can the lattice Boltzmann method play?, *Integrative Biology*, 2016, vol. 8, no. 5, pp. 589-602.

26. Chen, B., Li, G., Wang, W., and Wang, P., 3D numerical simulation of droplet passive breakup in a micro-channel T-junction using the Volume-Of-Fluid method, *Applied Thermal Engineering*, 2015, vol. 88, no. pp. 94-101.

27. Liu, X., Zhang, C., Yu, W., Deng, Z., and Chen, Y., Bubble breakup in a microfluidic T-junction, *Science Bulletin*, 2016, vol. 61, no. 10, pp. 811-824.

28. Fu, T., Wu, Y., Ma, Y., and Li, H.Z., Droplet formation and breakup dynamics in microfluidic flow-focusing devices: From dripping to jetting, *Chemical Engineering Science*, 2012, vol. 84, no. pp. 207-217.

29. Chen, Q., Li, J., Song, Y., Christopher, D.M., and Li, X., Modeling of Newtonian droplet formation in power-law non-Newtonian fluids in a flow-focusing device, *Heat and Mass Transfer*, 2020, vol. 56, no. 9, pp. 2711-2723.

30. Kovalchuk, N.M., Sagisaka, M., Steponavicius, K., Vigolo, D., and Simmons, M.J.H., Drop formation in microfluidic cross-junction: jetting to dripping to jetting transition, *Microfluidics and Nanofluidics*, 2019, vol. 23, no. 8, pp. 103.

31. Han, W., Chen, X., Wu, Z., and Zheng, Y., Three-dimensional numerical simulation of droplet formation in a microfluidic flow-focusing device, *Journal of the Brazilian Society of Mechanical Sciences and Engineering*, 2019, vol. 41, no. 6, pp. 1-10.

32. Du, M., Qi, T., Fan, W., and Chen, H., Numerical investigation of bubble breakup in a four-branched microchannel based on non-Newtonian pseudoplastic fluid, *Asia-Pacific Journal of Chemical Engineering*, 2020, vol. 15, no. 1, pp. e2393.

CHAPTER 2

CFD METHODOLOGY

2.1 CFD METHODOLOGY

Computational Fluid Dynamics (CFD) is the simulation of fluid engineering systems using modelling (mathematical physical problem formulation) and numerical methods (discretization methods, solvers, numerical parameters, and grid generation, among other things). Figure 2.1 depicts the procedure.

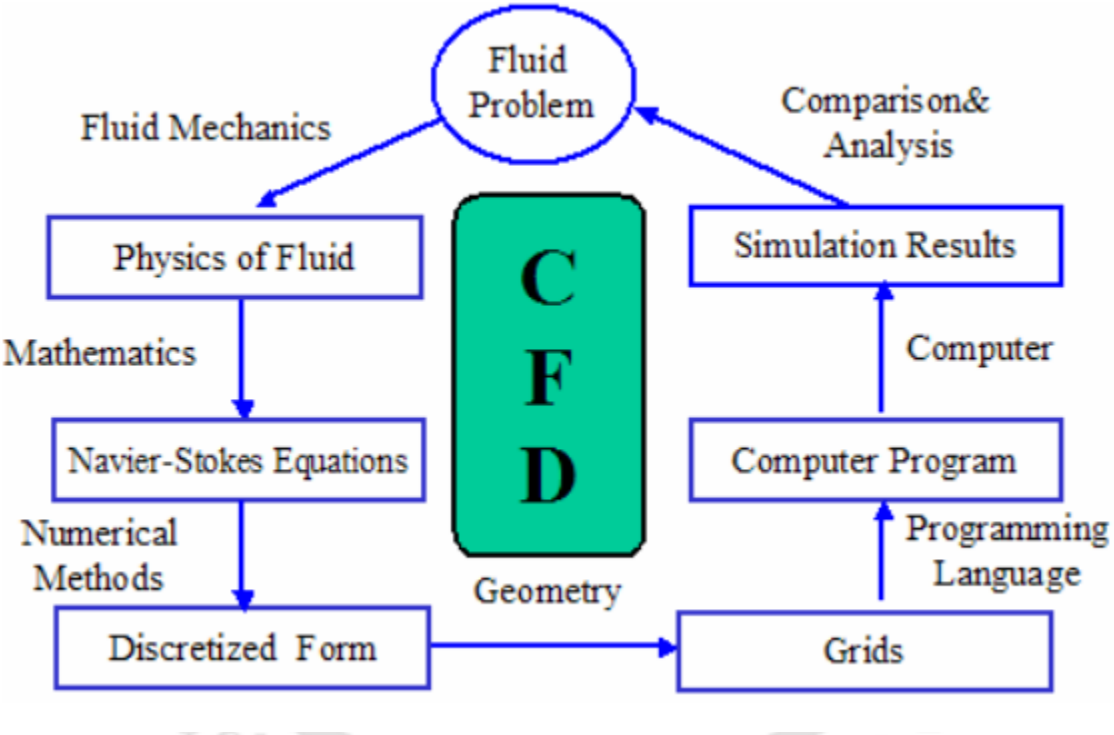

Figure 2.1. Process of Computational Fluid Dynamics [1]

To begin with, we have a fluid problem. To solve this problem, we must first grasp the physical properties of fluids through the use of Fluid Mechanics. Then we may use mathematical equations to reflect these physical properties. CFD's governing equation is the Navier-Stokes Equation. Because the Navier-Stokes Equation is analytical, it will be discretized by a computer. There are several numerical discretization methods, including Finite Difference, Finite Element,

and Finite Volume. As a result, because our discretization is dependent on them, we must also divide our entire problem area into multiple little parts. There are several apps available on the market to tackle CFD challenges, such as ANSYS FLUENT, COMSOL, and others. Workstations or supercomputers are frequently utilized to run the programs. Finally, the results of our simulation are visible. We may compare and contrast the results of the simulation with those of experiments and real-world challenges. If the results are inadequate to solve the issue, the technique must be repeated until a satisfying solution is identified. This is how the CFD technique works.

Another critical problem to solve when using CFD to describe multiphase flow is how to select a multiphase model to compute solutions. To guarantee that the computer can use the right continuity equations and apply them to the fluids in a fashion that most correctly simulates real-life fluid flow, an appropriate decision must be made for the multiphase model. There are several sorts of multiphase models, each with a varying amount of complexity [2]. The following are the multiphase model types, in order of increasing complexity and with brief descriptions:

1) **Lagrangian Model:** Individual particles from the secondary phase are monitored throughout the flow and are considered not to interact with one another, whereas continuity equations are solved for the primary phase as a whole entity. To close the system of flow equations, a modified van der Waals equation of state is applied. When the momentum conservation equation is combined with the van der Waals equation of state, the result is a particle equation of motion in which the total force acting on each particle is composed of many-body repulsive and viscous forces, two-body (particle–particle) attractive forces, and body forces such as gravitational forces.

2) Mixture Model: The primary and secondary phases are treated as one composite mixture, and the combined phases are solved with a single momentum equation. The mixture model is a straightforward multiphase model that may be used in a number of situations. It may be used to mimic multiphase flows in which the phases move at different speeds while remaining in local equilibrium over tiny spatial length scales. Finally, mixture models may be used to calculate non-Newtonian viscosity for homogeneous multiphase flows with strong coupling and phases moving at the same velocity.

3) Eulerian-Eulerian Model: Primary and secondary phases are handled as discrete continuous phases, with different momentum equations solved for each. The fluid-fluid and fluid-solid (granular) multiphase flows are not distinguished in the Eulerian-Eulerian multiphase model. A granular flow is simply one in which at least one phase has been classified as granular.

4) Volume of Fluid (VOF) Model: An Eulerian-Eulerian variant in which the secondary phase is not dispersed inside the main phase but rather exists as an interface between the phases, which must be tracked while also calculating a momentum equation for each phase. Prediction of jet breakup, motion of big bubbles in a liquid, mobility of liquid following a dam collapse, and steady or transient tracking of any liquid-gas interface are examples of typical applications.

An example has been demonstrated on 3D simulation of droplet formation in a flow-focusing geometry using VOF method. The dispersed phase is PDMS oil represented by green color and continuous phase is water represented by blue color in Figure 2.2. The viscosity ratio, $\left(\frac{\mu_o}{\mu_w}\right) = 25$, interfacial tension (σ) is 0.0118 N/m and contact angle (θ) = 140º.

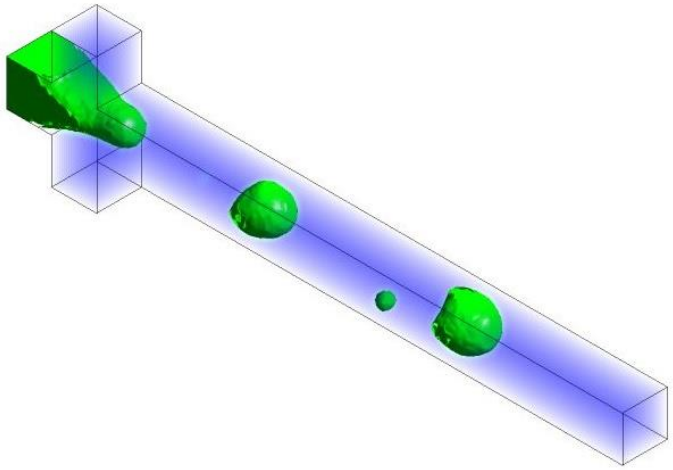

Figure 2.2. 3D representation of droplet formation in a flow-focusing geometry at $\left(\frac{\mu_o}{\mu_w}\right) = 25$, σ = 0.0118 N/m and θ = 140º.

5) Discrete Element Method: In this, momentum equations are applied to individual secondary phase particles as well as the primary phase as a whole. It is the most complicated multiphase model so far.

Advantages:

• Modeling Movement of Individual Particles

• Full stress and strain tensors can be measured

• Time Steps

• Progressive Failure

Disadvantages:

• Complex Particle Geometries and Arrangements

• Roughness, Texture

• Grain Crushing, Particle Breakage

• Non-Idealized Contacts

Applications:

• Civil Engineering (Geotechnical Engineering)

• Chemical Engineering

• Oil and gas production

• Geomechanics

• Mineral processing

• Biochemical Engineering

• Powder metallurgy

• Agricultural Industry

Depending on the typical flow regime present in a specific multiphase flow system, each multiphase flow model has applications to which it is best suited. The Mixture model and the Eulerian-Eulerian/VOF (Volume of fluid) models are the most often utilized multiphase models. Only the VOF (Volume of fluid) model [3] will work for separated flows since it anticipates the position of the interface and employs single phase models to forecast the flow in each phase.

There are variety of CFD packages available in the market like ANSYS FLUENT, COMSOL etc. We have used ANSYS FLUENT 2020 R2 Academic version to perform all our simulations.

The governing equations for the flow in gas-liquid or liquid-liquid Taylor flows are discussed in this chapter. The fluids in all of the numerical studies presented in the following

chapters are considered to be Newtonian fluids. The VOF (Volume of fluid) model [3], available in CFD solver ANSYS FLUENT, has been used for capturing the interface between the phases.

2.2 THE VOLUME OF FLUID (VOF) APPROACH

In the VOF method, continuity equation and momentum balance equations are solved, followed by a volume fraction equation. All the equations are taken from ANSYS FLUENT theory guide with minor modification of nomenclature and discussed below.

Continuity equation:

$$\frac{\partial \rho}{\partial t} + \nabla \cdot (\rho \mathbf{u}) = 0 \tag{2.2.1}$$

Momentum conservation equation:

$$\frac{\partial (\rho u)}{\partial t} + \nabla \cdot (\rho u \mathbf{u}) = \nabla \cdot (\mu \nabla u) - \nabla p + \rho g + F_s \tag{2.2.2}$$

In Eqs. (2.1) and (2.2), u is the velocity. α_w and α_o are the volume fraction of water and oil phase respectively and obey the relation ($\alpha_w + \alpha_o = 1$) and lie between 0 and 1 in each computational cell. The fluid properties of the mixed-phase are computed as follows

$$\rho = \alpha_w \rho_w + (1 - \alpha_w) \rho_o \tag{2.2.3}$$

$$\mu = \alpha_w \mu_w + (1 - \alpha_w) \mu_o \tag{2.2.4}$$

The volume fraction equation is given below

$$\frac{\partial \alpha_i}{\partial t} + u . \nabla \alpha_i = 0 \tag{2.2.5}$$

In Eq. (2.5), subscript *i* denotes the *i*th phase: water (w) or oil (o).

The surface tension force (F_s) by continuum surface force (CSF) used in Eq. (2.2.2) was calculated as

$$F_s = \sigma \left[\frac{\rho k \hat{n}}{\left(\frac{1}{2}\right)(\rho_w + \rho_o)} \right] \tag{2.2.6}$$

Where σ is the coefficient of surface tension, $\hat{n}$ the surface normal, and k the local surface curvature, which is calculated as

$$k = \nabla . \hat{n} \tag{2.2.7}$$

Where $\hat{n} = n / |n|$ and $n = \nabla . \alpha_i$.

The fluid presumed contact angle with the wall is utilized to alter the surface normal in cells near the wall. The curvature of the surface near the wall is adjusted as a result of this so-called dynamic boundary condition.

If θ_{wl} is the contact angle at the wall, then the surface normal at the live cell next to the wall is

$$\hat{n} = \hat{n}_{wl} \cos\theta_{wl} + \hat{t}_{wl} \sin\theta_{wl} \tag{2.2.8}$$

Where $\hat{n}_{wl}$ and $\hat{t}_{wl}$ are the unit vectors normal and tangential to the wall, respectively. The local curvature of the surface is determined by combining this contact angle with the typically calculated surface normal one cell away from the wall, and this curvature is utilized to change the body force term in the surface tension calculation.

In executing the VOF method, α_i and P are initially given in each computational cell center, and u is given at cell surfaces. ρ and μ at the interface can be determined by Eqs. (2.2.3) and (2.2.4) respectively. k and F_s are determined by Eqs. (2.2.7) and (2.2.6) respectively. Subsequently, the continuity (Eq. (2.2.1)) and momentum equation (Eq. (2.2.2)) are solved through a hydrodynamic scheme. The volume fraction equation is solved using a geo-reconstruction interpolation technique to achieve the highest accuracy. Importantly it is noted that the tracking of the interface between two phases is associated with this solution.

2.3 DISCRETIZATION METHOD

Eventually, using the commercial flow solver ANSYS FLUENT 2020 R2 Academic version, all of the equations were solved with the help of initial and boundary conditions. An unsteady state solution with explicit VOF had been employed. The PISO algorithm was utilized for velocity-pressure coupling. PRESTO was utilized to provide pressure. The spatial derivatives were discretized using the QUICK [4] method. Geo-reconstruction scheme has been used for clear interface.

2.4 THE EXPLICIT SCHEME

ANSYS FLUENT's conventional finite-difference interpolation algorithms are used to the volume fraction values derived at the preceding time step in the explicit approach.

$$\frac{\alpha_q^{n+1} p_q^{n+1} - \alpha_q^n p_q^n}{\Delta t} V + \sum_f \left(p_q U_f^n \alpha_q^n f \right) = \left[\sum_{p=1}^{n} (\dot{m}_{pq} - \dot{m}_{qp}) + S_{\alpha_q} \right] V$$

Where, n+1= index for new (current) time step

n = index for previous time step

$\alpha_{q,f}$ = face value of the qth volume fraction, computed from the first or second-order upwind, QUICK, modified HRIC, or CICSAM scheme

V = Volume of cell

U_f = volume flux through the face, based on normal velocity

2.5 INTERPOLATION NEAR THE INTERFACE

ANSYS FLUENT offers a specific interpolation technique to cells on the border between two phases in the geometric reconstruction and donor-acceptor schemes. Figures 2.3a, 2.3b and 2.3c depict an actual interface form as well as the interfaces assumed by these two approaches during calculation.

a)

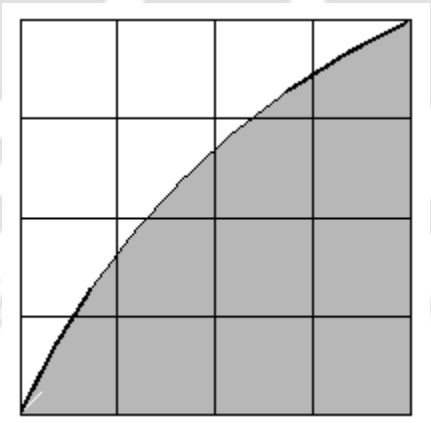

b)

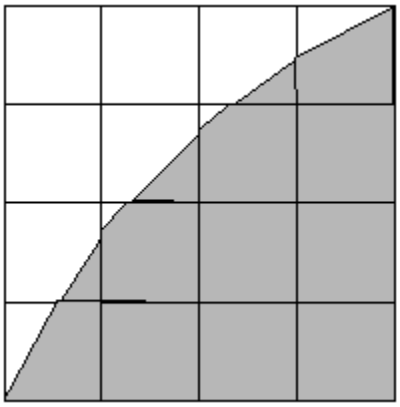

c)

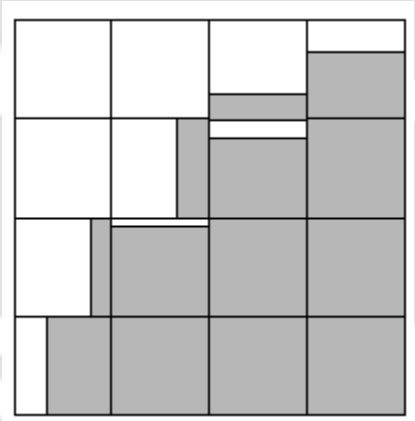

Figure 2.3. a) Actual interface shape **b)** Interface shape by Geo-reconstruction scheme **c)** Interface shape by donor-acceptor schemes (adopted from ANSYS Theory guide)

Rather of applying a specific treatment, the explicit and implicit schemes handle these cells with the same interpolation as cells that are totally filled with one phase or the other (i.e., using the conventional upwind, second-order, QUICK, modified HRIC, or CICSAM scheme).

2.5.1 The Geometric Reconstruction Scheme

When a cell is completely filled with one phase or another, the usual interpolation procedures used in ANSYS FLUENT are applied to get the face fluxes in the geometric reconstruction methodology. When the cell is at the interface of two phases, the geometric reconstruction technique is used.

Using a piecewise-linear method, the geometric reconstruction technique represents the interface between fluids. This is the most precise method in ANSYS FLUENT and is suitable for general unstructured meshes. It assumes that the interface between two fluids within each cell has a linear slope and uses this linear form to compute fluid advection across the cell faces.

Using information on the volume fraction and its derivatives in the cell, the initial stage of this reconstruction approach is to compute the position of the linear interface relative to the centre of each partially-filled cell. The second step is to calculate the amount of fluid advecting across each face using the computed linear interface representation and information on the face's normal and tangential velocity distributions. The third step is to compute the volume fraction in each cell using the flux balance determined in the previous step.

2.5.2 The Donor-Acceptor Scheme

In the donor-acceptor technique, the face fluxes are calculated using the standard interpolation algorithms in ANSYS FLUENT whenever a cell is completely filled with one phase or another. When the cell is at the interface between two phases, a "donor-acceptor" technique is used to calculate the amount of fluid advected across the face. To eliminate numerical diffusion at the interface, this approach identifies one cell as a donor of fluid from one phase and another (near) cell as an acceptor of the same amount of fluid. The amount of fluid

from one phase that may be convected across a cell border is restricted by the lesser of two values: the donor cell's filled volume or the acceptor cell's free volume.

The direction of the interface is also considered while computing the face fluxes. Depending on the direction of the volume fraction gradient of the q^{th} phase within the cell and that of the neighbor cell that shares the face in question, the interface orientation is either horizontal or vertical. Depending on the direction and velocity of the interface, flux values are estimated using pure up winding, pure down winding, or a mix of the two.

2.5.3 The Compressive Interface Capturing Scheme for Arbitrary Meshes (CICSAM)

Based on Ubbink's work [5], a high resolution differencing approach is the compressive interface capturing strategy for arbitrary meshes (CICSAM). The CICSAM scheme is especially well adapted to flows with high viscosity ratios between phases. CICSAM is implemented explicitly in ANSYS FLUENT and produces an interface that is nearly as sharp as the geometric reconstruction technique.

REFERENCES

1. Ashgriz, N. and Mostaghimi, J., An introduction to computational fluid dynamics, *Fluid flow handbook*, 2002, vol. 1, no., pp. 1-49.
2. Andersson, B., Andersson, R., Håkansson, L., Mortensen, M., Sudiyo, R., and Van Wachem, B., *Computational fluid dynamics for engineers*. 2011: Cambridge university press.
3. Hirt, C.W. and Nichols, B.D., Volume of fluid (VOF) method for the dynamics of free boundaries, *Journal of computational physics*, 1981, vol. 39, no., pp. 201-225.
4. Biswas, S., Gooh Pattader, P.S., and Mandal, T.K., A computational study on phase velocity mediated droplet splitting and its mechanism at T-junction microchannel, *J. Braz. Soc. Mech. Sci. Eng.*, 2021, vol. 43, no., pp. 391.
5. Ubbink, O., Numerical prediction of two fluid systems with sharp interfaces, 1997, vol. no., pp.

CHAPTER 3

A COMPUTATIONAL STUDY ON PHASE VELOCITY MEDIATED DROPLET SPLITTING AND ITS MECHANISM AT T – JUNCTION MICROCHANNEL

Chapter 3 A computational study on phase velocity mediated droplet splitting and its mechanism at t – junction microchannel

ABSTRACT

In this study, 2D numerical simulations were conducted to reveal the breakup and non-breakup mechanism of a droplet in a horizontal microfluidic T-junction using oil-water volume fraction contours, pressure profile, velocity profile, and vorticity profile. The numerical simulation is validated with experimental results taken from the literature. Two types of droplet breakup regimes, namely tunnel-breakup and obstructed breakup along with a non-breakup regime with the alternate movement of droplets were found. The tunnel breakup is mainly due to the formation of vortex flow in front of the droplets whereas the breakup at obstruction is induced by the formation of high upstream pressure in the main channel. Interestingly, a pressure swing phenomenon is identified, which drives the droplets in the horizontal microfluidic T-junction's alternating arms. Depending on the phase velocities, numerous mixed phenomena were also observed when the droplets flow through the horizontal T-junction microchannel. A flow pattern map is presented to guide the on-demand requirement of the flow behavior based on two dimensionless numbers namely capillary number and mixture Reynolds number. In pressure drop analysis, drift flux model provides the better prediction than the homogeneous model.

This chapter is published in **J. Braz. Soc. Mech. Sci. Eng**. (2021) 43:391

Chapter 3 A computational study on phase velocity mediated droplet splitting and its mechanism at t – junction microchannel

3.1. INTRODUCTION

The splitting up of a droplet into daughter droplets is a very important phenomenon in microfluidics as it increases the surface-to-volume ratio, which enhances mixing [1, 2], mass transfer [3, 4] and reaction kinetics [5] compared to bulk operations. A tiny droplet also can act as a reagent vessel and as an enclosure of a sample within a continuous liquid phase [6]. Droplet flow has various advantages over continuous flow, such as it scales down the reagent amount to micro/nanoliters, reduces reaction time, and enhances the efficiency of the reaction [5]. It is used in many fields like chemical engineering [7], biomedical engineering [8], life science [9], food industries [10], and cosmetic [11], etc.

The droplet fission is one of the methods to control the reagent amount in the dispersed phase. There are mainly two types of breaking process of a droplet: a) Active fission, b) Passive fission [12]. The passive fission has received much attention as it does not need any external forces, and droplets can be broken down at a predetermined location with controlled volume. One of the methods for passive fission is passing the fluids through a T-junction [13, 14]. Using volume of fluid (VOF) method [13], Chen et al. investigated the dynamics of droplet bifurcation in the T-junction of a microchannel and found four regimes, namely, break-up with a tunnel, break-up with discontinuous obstruction, break-up with permanent obstruction, and a regime without any break-up. Later, a correlation was proposed to predict the transition boundary between break up and non-break up regime [13]. Simulations were performed on the break-up phenomena of microdroplets in asymmetric T-junction microchannel. For asymmetric break-up,

it was observed that the two daughter droplets either travel in opposite directions through the two branches of the channel or both the droplets travel into the shorter outlet branch. A correlation was developed to predict the condition for droplet breakup in an asymmetric T-junction. The effect of viscosity on the break-up and non-break-up criteria were also reported in earlier literature [12]. Using the phase-field method [15] it was demonstrated that the viscosity ratio of the dispersed to continuous phase and the width ratio of the branch to main channels of a T-junction influence the droplet dynamics. In addition, it was also observed that the vortex flow formed within a droplet played an essential role in determining whether the droplet would break-up or not. In a 2D symmetric T-junction setting, it was shown that the critical droplet extension for the break-up depends on the capillary number in a narrow gap where interfacial force and viscous force were comparable [16]. An investigation has also been done on the droplet flow of water in a continuous oil phase and splitting of the droplets through the T-junction and 90º branch angle channel by the conservative level set method [7].

Link et al. [14] introduced the concept of an obstacle into the microchannel to induce breakup of a droplet. They also developed a correlation to distinguish the breaking and non-breaking regions based on the capillary number and maximum extension of the droplet. An investigation has been performed to demonstrate different droplet breakup modes in an injection nozzle and focussing orifice set up within a capillary microfluidic platform. The location of the droplet break up was found to depend on the distance between the nozzle tip and the orifice, as well as on the contraction region of the dispersed inner fluid at the entrance of the orifice. A capillary number was identified as a ratio of the local shear stress to capillary stress, that

determined the location of droplet breakup at the focussing orifice or the injection nozzle based on whether the capillary number exceeded a critical value or not. Three distinct types of tip-multi-breaking modes were also discussed in that report [17]. Splitting up of a single mother droplet into five daughter droplets using a multi-furcating channel has been investigated by Li et al. [18]. Further studies on the effect of flow resistance in the branch channel, particularly the length of branch channels on droplet splitting was carried out. It was found that bifurcation of the droplets through angle branches are useful in droplet manipulation and droplet sorting [18]. Investigation on the effect of initial droplet length and droplet velocity on droplet breakup in an asymmetric bifurcation with two angled branches has also been done [19].

Regulation of droplet traffic has a great application in the various field of medical and engineering. Cristobal et al. [20] fabricated a simple PDMS microfluidic channel to alternate the droplet traffic through two different branch channel having 90º bend by creating a bypass connector between the two bends. Also, it was found that the droplets either move alternatively through the outlets or collects through the shorter arm. Here, the T-junction acted as a hydrodynamic sieve or as a partial sorter depending upon the distance between the droplets. Beyond a threshold droplet dilution factor, the droplets were found to be driven towards the arm of the lowest hydrodynamic resistance [21].

Droplet size depends on the physical properties of the fluids like viscosity, interfacial tension, etc. and can be controlled by tuning the velocity of both the phases. For this reason, many researchers have explored the flow pattern maps in detail [22] . Salim et al. [23]

investigated the different flow patterns observed by injecting one fluid at a constant flow rate and second at a variable flow rate through two different microchannels. Flow patterns were investigated in the region before the T-junction of the microchannel. A numerical investigation has been done on the effect of flow rates of the continuous and dispersed phase, wall adhesion (contact angle), channel size, liquid-liquid distributers and liquid viscosity on flow regimes and slug length [24]. Moreover, focus on the formation of slug, plug and stratified flow in a microfluidic device through both simulation and experiment have been made. Transitions between the flow patterns were obtained by tuning the interfacial tension and viscosity of the dispersed phase [25].

Some of the authors have tried to establish the mechanism for droplet splitting. It was found that the breakup process of the droplet can be divided into four sequential stages: squeezing, transition, pinch-off, and thread rupture stages. The driving forces for the deformation of the droplet in each stage were analyzed. Also, the effect of viscosity was investigated on breakup processes [26]. The following two flow patterns - breakup with permanent obstruction and breakup with tunnels were also found along with two breakup stages - i) a quasi-steady deformation and ii) three-dimensional rapid pinching [27].

In the view of the above discussion, the flow phenomena in a microchannel T-junction and related physics are not explored meticulously to discover the myriad of mixed flow patterns. In the present work, we have focused on probable insights behind the droplet breakup and the

mixed flow pattern in a microchannel T-junction. 2D numerical simulation has been carried out using the Volume of Fluid (VOF) method. Velocities of both phases have been varied to understand the physics behind the different types of droplet breakup phenomena. The role of the velocity field, pressure field, and vorticity magnitude on breaking up of a droplet had been studied. The simulated results have revealed a time-dependent mixed flow regimes in which a time dependent characteristics of flow morphology has been observed at a constant phase flow rates. Apart from this, a breakup and a non-breakup flow regime have been identified in the present work. The results have also explored a pressure swing phenomenon near the T-junction as a main reason behind the alternative movement of the droplets via two arms of the microfluidic T-junction, which is not reported in the literature to date.

3.2. COMPUTATIONAL MODEL

In this study, the VOF method was used to simulate the dynamics of droplet breakup of water (dispersed phase, w) in mineral-oil (Marcol – 82) (continuous phase, o) at T-junction of a 2D microchannel under laminar flow conditions. The fluids were assumed to be incompressible and Newtonian.

3.2.1 Geometry, initial and boundary conditions

Geometry:

The solution domain consists of a horizontal 2D double T-junction microchannel. The details of the geometry of the computational domain are shown in Figure 3.1a. The geometry

consists of two inlets and two outlets and one main channel (length = 120 mm). The inlets, main channel and the outlets have an identical diameter (0.78 mm). The inlets (total length 4.78 mm) and outlets (total length 50 mm) are symmetrically attached to the main channel. The corresponding mesh of outlet T-junction is shown in Figure 3.1b.

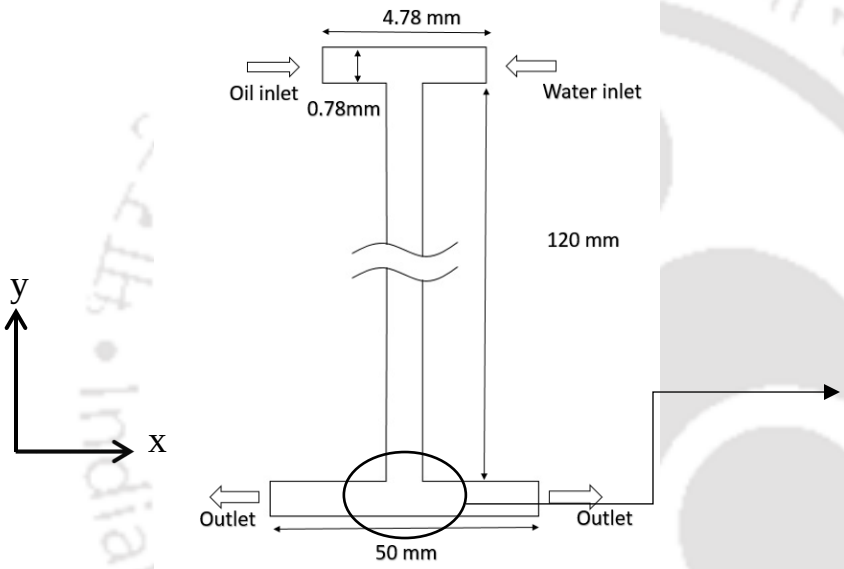

Figure 3.1. (a) Computational domain; and (b) Mesh

Mineral-Oil (Marcol – 82) and water have been selected as the two liquid phases for the study and their properties are listed below in Table 3.1.

Table 3.1. Fluid properties

Fluids Properties	**Water**	**Mineral-Oil (Marcol 82)**
Density	997 kg/m3	843 kg/m3
Viscosity	0.001 Pa.s	0.0306 Pa.s
Oil-water interfacial tension	0.0301 N/m	
Contact angle of oil on glass in water	51^0	

Initial and Boundary conditions:

- The channel was initially filled with oil (continuous phase), then water (dispersed phase) and oil were flowed through the inlets.
- The operating pressure was set as atmospheric pressure.
- Velocity at inlets:

  at oil inlet, $u_x = u_{oil}$ and $u_y = 0$

  at water inlet, $-u_x = u_{water}$ and $u_y = 0$
- No-slip and impermeable conditions imposed at the walls.
- Pressure outlet boundary condition (Gauge pressure = 0).
- Time steps were suitably chosen according to Courant no.

3.2.2 Convergence, grid independency and model validation

The convergence was decided based on the residual values of the continuity equations and the velocity components. The convergence limits were set of the order of ~ 10^{-3} for the continuity equation and ~ 10^{-5} for the velocity components.

The present numerical solver was validated by comparing our simulated results with the previous experimental result of Salim et al. [23]. To obtain optimum grid size, a grid independency study was carried out by considering three different mesh sizes (92300, 108438 and 118542 cells) as shown in Table 3.2a, b and c respectively. Here the parameter C_0, a constant term defined by Salim et al. [23] has been predicted in the Table 3.2. The parameter C_0 was defined as $C_0 = V_{meas} / (V_w + V_o)$, where V_{meas} represents the average drop/pattern velocity in the main channel, V_w and V_o are the superficial velocity of the water and the oil phases, respectively. However, the system with 118542 cells was giving better prediction (Table 3.2c) of the C_0 values. So, this grid (118542 cells) has been secleted as the optimum grid size and performed the all simulations presented in the manuscript. To strengthen the statement, we have predicted experimentaly obtained droplet or slug velocity (Salim et al. [23]) using optimised grid size (118542 cells) as shown in Figure 3.2. The deviations in prediction is within ±3.3% which is a highly acceptable value. Table 3.3. represents the variation of drop size with mesh elements in the main channel at V_w = 0.04 m/s and V_o = 0.18 m/s. The table shows that the existing grid also predicts the droplet size very well. Grid mesh (118542 cells) gives the percentage deviation of 1.3 which is lowest among the three. So grid mesh (118542 cells) is selected for all 2D computation performed in this work.

Table 3.2. Grid independence study on C_0 at different grid sizes,- (A) 92300 mesh elements, (B) 108438 mesh elements, and (C) 118542 mesh elements

(A)

For mesh elements 92300							
Sl. No.	**Velocity of water (m/s)**	**Velocity of oil (m/s)**	**Mixture velocity (m/s)**	**Flow pattern**	**Experimental C_0**	**Simulated C_0**	**Percentage Deviation**
1	0.04	0.14	0.18	Slug	1.28	1.32	3.0
2	0.01	0.18	0.19	Droplet	1.06	1.41	24.8
3	0.04	0.18	0.22	Slug	1.28	1.40	8.5
4	0.035	0.10	0.135	Slug	1.28	1.32	3.0
5	0.02	0.10	0.12	Droplet	1.06	1.29	17.8
6	0.01	0.10	0.11	Droplet	1.06	1.31	19.0

(B)

For mesh elements 108438							
Sl. No.	**Velocity of water (m/s)**	**Velocity of oil (m/s)**	**Mixture velocity (m/s)**	**Flow pattern**	**Experimental C_0**	**Simulated C_0**	**Percentage Deviation**
1	0.04	0.14	0.18	Slug	1.28	1.30	1.5

2	0.01	0.18	0.19	Droplet	1.06	1.39	23.7
3	0.04	0.18	0.22	Slug	1.28	1.38	7.2
4	0.035	0.10	0.135	Slug	1.28	1.30	1.5
5	0.02	0.10	0.12	Droplet	1.06	1.27	16.5
6	0.01	0.10	0.11	Droplet	1.06	1.29	17.8

(C)

For mesh elements 118542							
Sl. No.	**Velocity of water (m/s)**	**Velocity of oil (m/s)**	**Mixture velocity (m/s)**	**Flow pattern**	**Experimental C_0**	**Simulated C_0**	**Percentage Deviation**
1	0.04	0.14	0.18	Slug	1.28	1.28	0
2	0.01	0.18	0.19	Droplet	1.06	1.37	22.6
3	0.04	0.18	0.22	Slug	1.28	1.36	5.8
4	0.035	0.10	0.135	Slug	1.28	1.28	0
5	0.02	0.10	0.12	Droplet	1.06	1.25	15.2
6	0.01	0.10	0.11	Droplet	1.06	1.27	16.5

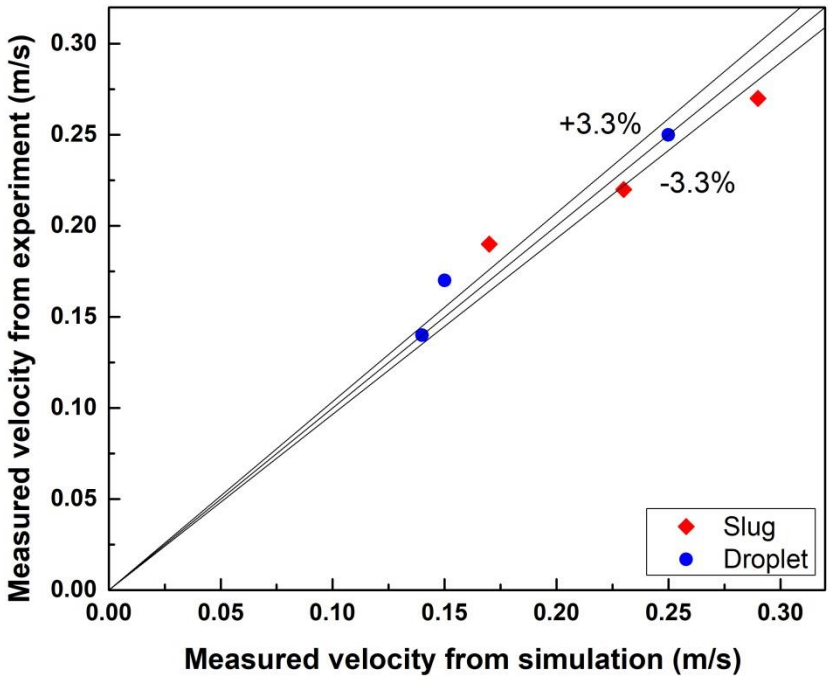

Figure 3.2. Grid independence study- Experimentally measured slug velocity (adopted from Salim et al. [23]), vs simulated slug velocity at 118542 cells.

Table 3.3 Variation of drop size with mesh elements in the main channel at V_w = 0.04 m/s and V_o = 0.18 m/s

Mesh elements	Drop size from Salim et al. [23] (mm)	Drop size from simulation (mm)	Percentage deviation
92300	0.78	0.71	9.0

108438	0.78	0.74	5.1
118542	0.78	0.77	1.3

3.3. Results and Discussions

Simulations produce two types of droplet breakup regimes, namely tunnel-breakup and obstructed breakup, along with a non-breakup regime. Various mixed flow regimes are also observed when the droplets flow through the horizontal T-junction microchannel. In order to reveal the breakup and non-breakup mechanisms, the current investigation provides a detailed analysis of the droplet breakup dynamics that includes the evolution of droplet, oil-water interface, pressure profile, velocity profile, and vorticity profile distribution. In the simulations, we have varied the superficial velocities of the water (dispersed phase) and oil (continuous phase) through the horizontal microchannel T-junction. A flow pattern map and the insight physics of the flow phenomena have also been described in the subsequent sections.

3.3.1 Breakup regimes

3.3.1.1 Bifurcation of single droplet with tunnel – For bifurcation with a tunnel, the mother droplet reaches the T-junction and elongates to bifurcate into two daughter droplets (Figure 3.3a). In this case, gaps exist between the upper tips (both right and left arm of the T-junction) of the elongated droplet and the upper inner wall of the arms of the T-junction, as shown in Figure

3.3a. The continuous oil phase is occupying the gap and is looking like a tunnel. With time, the elongated mother droplet is completely bifurcated into two daughter droplets as shown in Figure 3.3b.

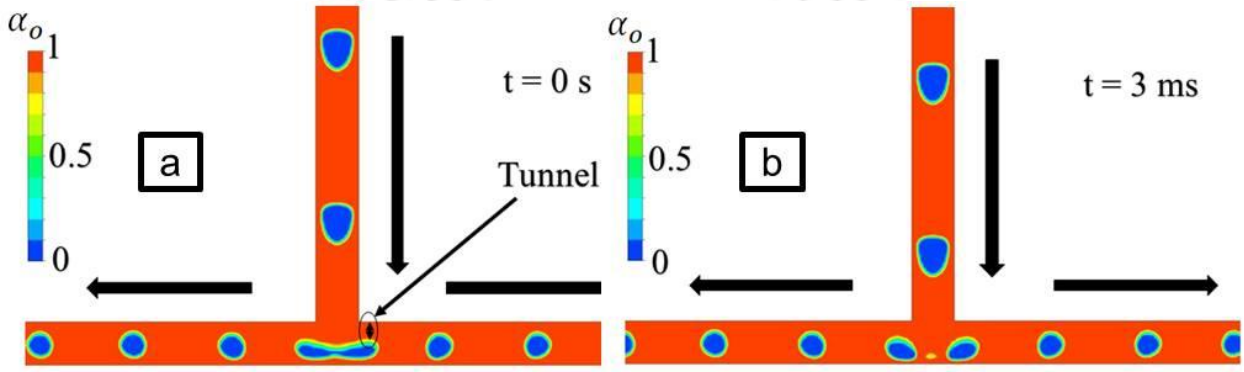

Figure 3.3. Volume fraction contour of mineral oil – water at V_w = 0.04 m/s and V_o = 0.18 m/s at different time interval: (a) elongated mother droplet; and (b) bifurcated droplets.

3.3.1.2 Bifurcation of a single droplet with obstruction – In case of bifurcation with obstruction, the mother droplet first obstructs the channel near T-junction almost completely, then elongates to symmetrically bifurcate into two daughter droplets. In both the arms, within the channel near T-junction, there is almost no gap (unlike tunnel) or negligible gaps between the upper tips of the droplet and the inner wall of the arms, as presented in Figure 3.4a. This observation also accords with the earlier literature [15, 27]. After a small time interval (within 2 ms), the mother droplet completely bifurcates into two daughter droplets, as shown in Figure 3.4b.

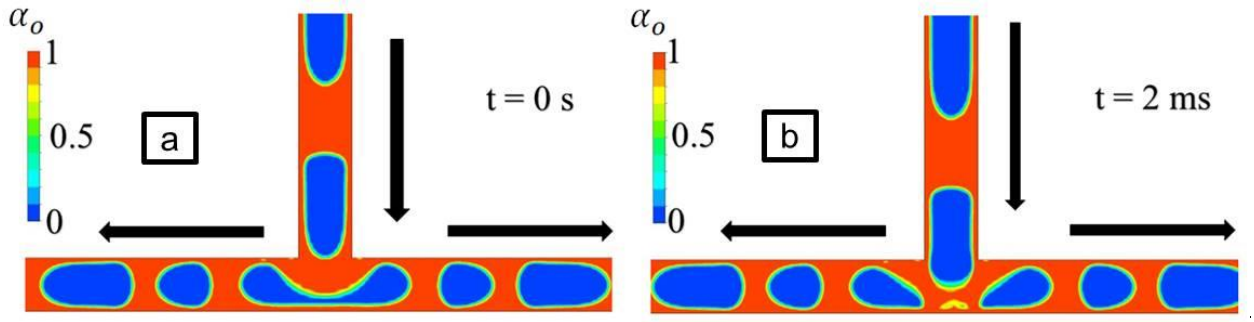

Figure 3.4. Volume fraction contour of mineral oil – water at V_w = 0.12 m/s and V_o = 0.18 m/s at different time values: (a) elongated mother droplet; and (b) bifurcated droplets.

3.3.2 Non - breakup regime

3.3.2.1 Alternate movement of droplets – In this case, mother droplets are not broken down into daughter droplets rather they move through the branch channels alternatively, as shown in the sequential images in Figure 3.5. The droplet marked as 1 in the main arm in Figure 3.5a moves into the left–hand arm of the T-junction (Figure 3.5b). On the other hand, the next droplet marked with 2 (Figure 3.5b) moves into the right–hand arm of the microchannel T-junction, as shown in Figure 3.5c. At a constant phase flow rates, this alternative movement is continuing with the progress of the flow. A representative relative time of occurrence has been mentioned in the respective figures (Figures 3.5a-3.5c). The velocity ranges of all the above described flow patterns have been summarized in Table 3.4.

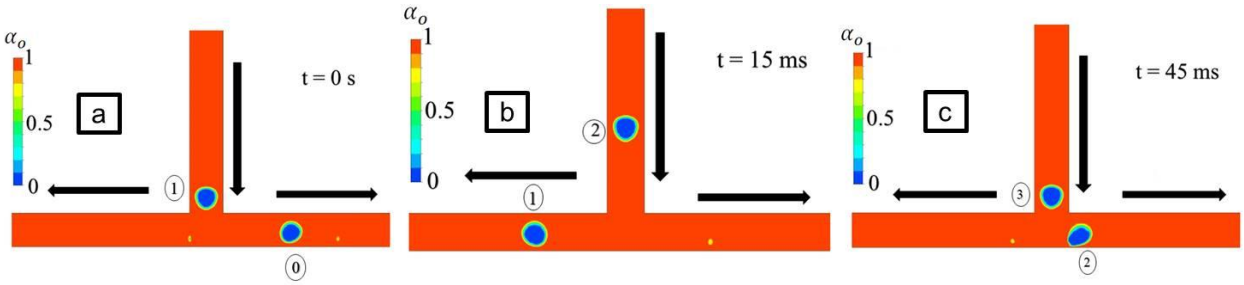

Figure 3.5. Volume fraction contour of mineral oil-water at V_w = 0.01 m/s and V_o = 0.18 m/s microchannel at different time values: (a) Droplet marked as 0 moves through the right arm of the T-junction; (b) Droplet marked as 1 moves through left arm of the T-junction; and (c) Droplet marked as 2 moves through right arm of the T-junction.

Table 3.4. Velocity ranges for breakup and non – breakup regimes

Sl. No.	Phenomena	Superficial Velocity (m/s)	
		Dispersed phase (V_w)	Continuous phase (V_o)
1	Alternate movement of droplets (AM)	0.01	0.18
		0.01	0.26
		0.02	0.26
2	Bifurcation of single droplet with tunnel (BT)	0.04	0.18
		0.035	0.10
3	Bifurcation of single droplet with obstruction (BO)	0.08	0.10

3.3.3 Mixed flow regimes

Mixed flow regimes consist of flow phenomena in which the droplets make some new trends in its movements rather than just break up and non-breakup when it reaches the T-junction. For example, the coalescence of two droplets and then bifurcates into two droplets or remains as a single droplet and steer to one direction, etc.

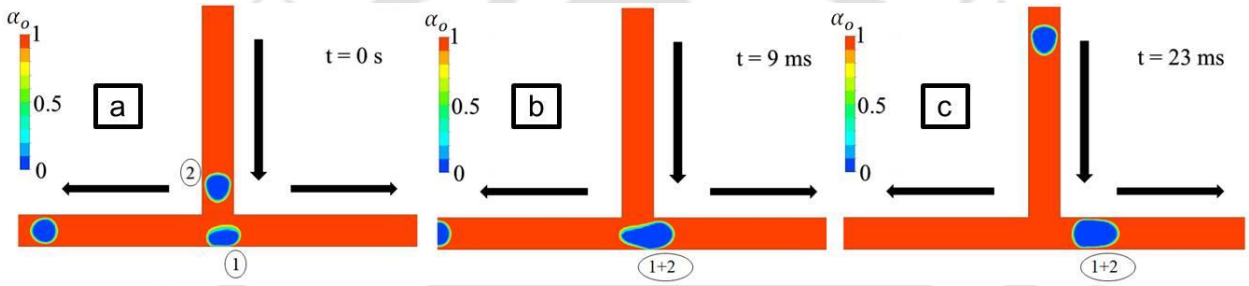

Figure 3.6. Coalescence of two droplets and moving in one direction at V_w = 0.01 m/s and V_o = 0.10 m/s: (a) Droplet marked as 1 arrived at the T-junction; (b) Two droplets marked as 1 and 2 get coalesced with each other; and (c) The coalesced droplet marked as (1+2) moves through the right arm of the T-junction.

3.3.3.1 Coalescence of two droplets and one directional movement- At certain superficial velocities of the dispersed and the continuous phases, two droplets merge at the T-junction of the microchannel and then moves through one of the arms of the microchannel as shown in Figure 3.6. Droplets marked with 1 and 2, merge together at the T-junction (Figure 3.6b) and then moves through the right–hand arm of the microchannel T-junction (Figure 3.6c). The relative time of occurrence has been mentioned in the respective figures (Figures 3.6a-3.6c).

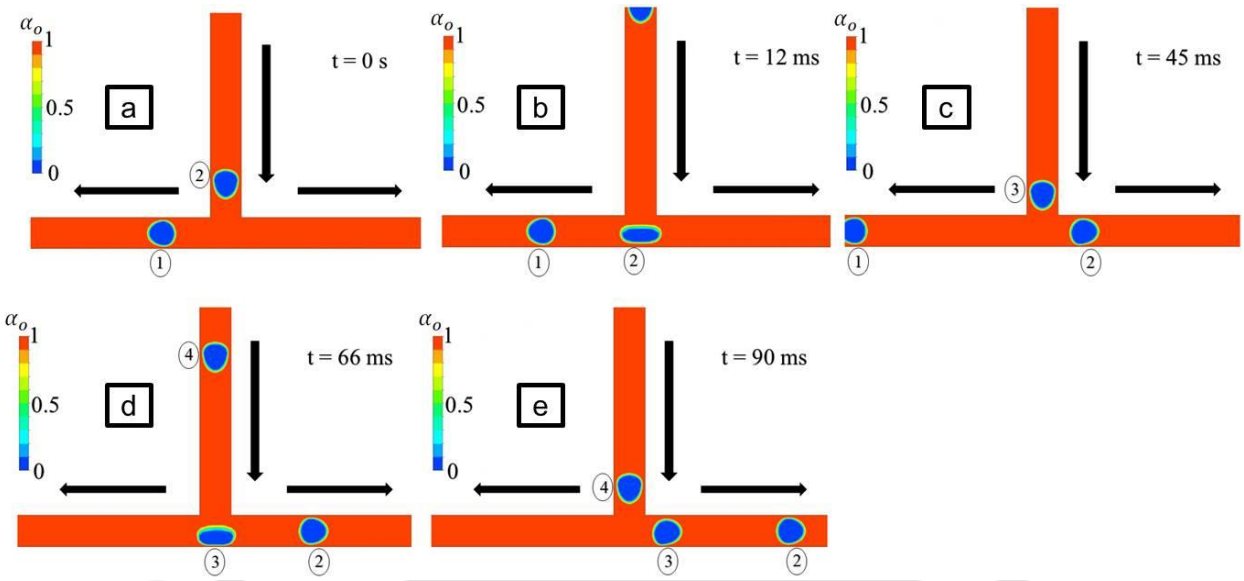

Figure 3.7. Random movement of droplets at V_w = 0.01 m/s and V_o = 0.10 m/s: (a) Droplet marked as 1 moves through left arm of the T-junction; (b) Droplet marked as 2 arrived at the T-junction; (c) Droplet marked as 2 moves through the right arm of the T-junction; (d) Droplet marked as 3 arrived at the T-junction; and (e) Droplet marked as 3 moves through the right arm of the T-junction.

3.3.3.2 Random movement of droplets- In case of the random movement of droplets as shown in Figure 3.7, droplets move through the arms of the microchannel randomly. Here the movement of the droplet is not following any particular sequence. Droplet marked with 1 move through left-hand arm (Figure 3.7a, b) whereas droplet marked with 2 and 3 moves into right-hand arm of the microchannel T-junction (Figure 3.7b, c, d, e). At a constant flow rate, this random movement is continuing with the progress of the flow. The time of occurrence has also been mentioned in the respective figures (Figures 3.7a-3.7e).

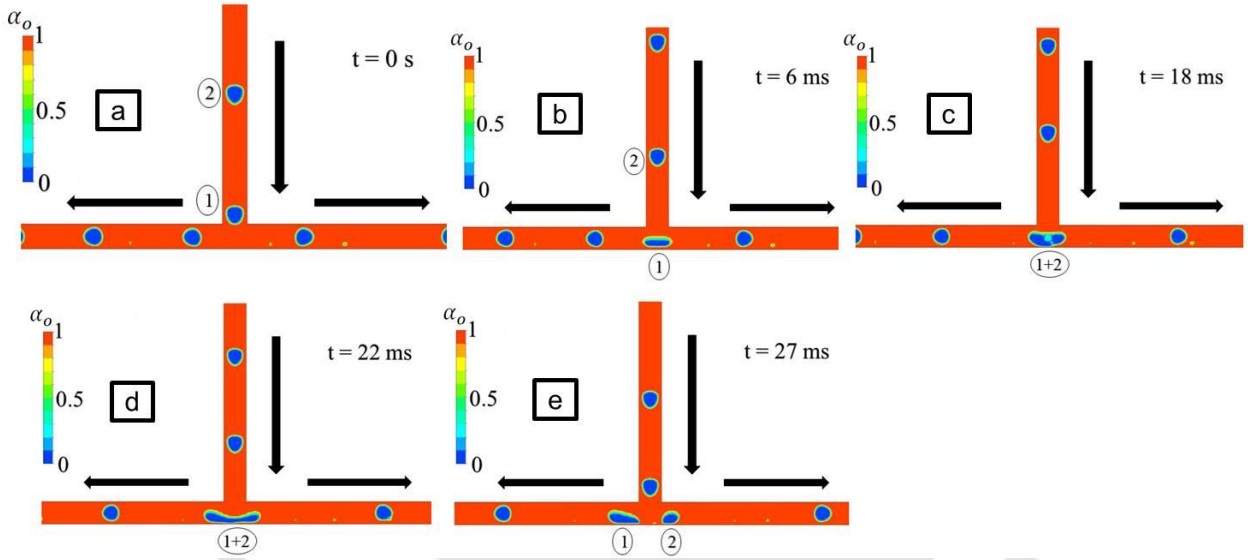

Figure 3.8. Two droplets are coalescing and bifurcated at V_w = 0.02 m/s and V_o = 0.18 m/s: (a) Droplet marked as 1 is arriving at the T-junction; (b) Droplet marked as 1 arrives at the T-junction; (c) The droplet marked as (1+2) is the coalesced droplet; (d) The coalesced droplet marked as (1+2) is elongated and preparing to bifurcate; and (e) The coalesced elongated droplet is bifurcated.

3.3.3.3 Coalescence of two droplets and bifurcation - In case of coalescence of two droplets and bifurcation as shown in Figure 3.8, droplet marked with 1 and 2 merge together when they arrive at the T-junction (Figure 3.8c,d) and then bifurcates into two halves and move through the two arms of the microchannel (Figure 3.8e). Droplet marked as 1 moves through the left-hand arm whereas droplet marked as 2 moves through the right-hand arm of the microchannel T-

junction. A representative time of occurrence has been mentioned in the respective figures (Figures 3.8a-3.8e).

Table 3.5. Mixed flow regimes and their velocity combination

Sl. No.	Phenomena	Superficial Velocity (m/s)	
		Dispersed phase (V_w)	Continuous phase (V_o)
1	Random movement of droplets (RM) + Two droplets coalesce and move in one direction (CM)	0.01	0.10
2	Alternate movement of droplets (AM) + Two droplets coalesce and move in one direction (CM) + Two droplets coalesce and bifurcation (CB)	0.02	0.18
3	Alternate movement of droplets (AM) + Two droplets coalesce and bifurcation (CB) + Bifurcation with tunnel (BT)	0.035	0.18
4	Alternate movement of droplets (AM) + Two droplets coalesce and bifurcation (CB)	0.035	0.26
5	Bifurcation with tunnel (BT) + Bifurcation	0.08	0.18

	with obstruction (BO)		
6	Bifurcation with tunnel (BT) + Bifurcation with obstruction (BO)	0.12	0.26
7	Bifurcation with tunnel (BT) + Bifurcation with obstruction (BO)	0.12	0.18
8	Random movement of droplets (RM) + Two droplets coalesce and move in one direction (CM)	0.02	0.10

The mixed flow regimes at different velocities are summarized in Table 3.5. A flow pattern map is also developed considering all types of flow behaviour (Figure 3.9). To make a generalize flow pattern map and to dig out the fundamental aspects, two dimensionless number namely Capillary number, $Ca = \frac{\mu_c U}{\sigma}$ and Mixer Reynolds number, $\mathrm{Re}_m = \frac{DV_{mix}\rho_{mix}}{\mu_{mix}}$ have been plotted on X-axis and Y-axis respectively. μ_c is the viscosity of continuous phase, U is the mixer velocity, and σ is the interfacial tension, D = Diameter of the channel, V_{mix} = mixture velocity, ρ_{mix} = mixture density, μ_{mix} = mixture viscosity. The flow pattern map (Figure 3.9) shows the following three distinct regions,-

a) Region- I: Not a Ca number induced region, where flow patterns are not changing with capillary number at a constant mixer Renolds number. Here, alternate movement of droplets flow pattern is decidedly dominated.

b) Region- II: A highly capillary number induced region, where flow patterns are drastically changing with capillary number at a constant mixer Renolds number. In this region, truly mixed flow patterns have been observed. Flow patterns mentioned by the selrial number 1, 3, 4, 5, and 8 in the Table 4 are the dominating flow patterns. It indicates that the stabilizing capillary force and the destabilizing viscous force are not appropriately balanced in this flow condition range. That is why, instead of a single flow morphology, multiple morphologies are appearing in these range of flow conditions.

c) Region- III: May not be a capillary number induced region, where flow patterns may change with capillary number at a constant mixer Renolds number. Here, a combined flow pattern, namely bifurcation with tunnel (BT) and bifurcation with obstruction (BO) has been found.

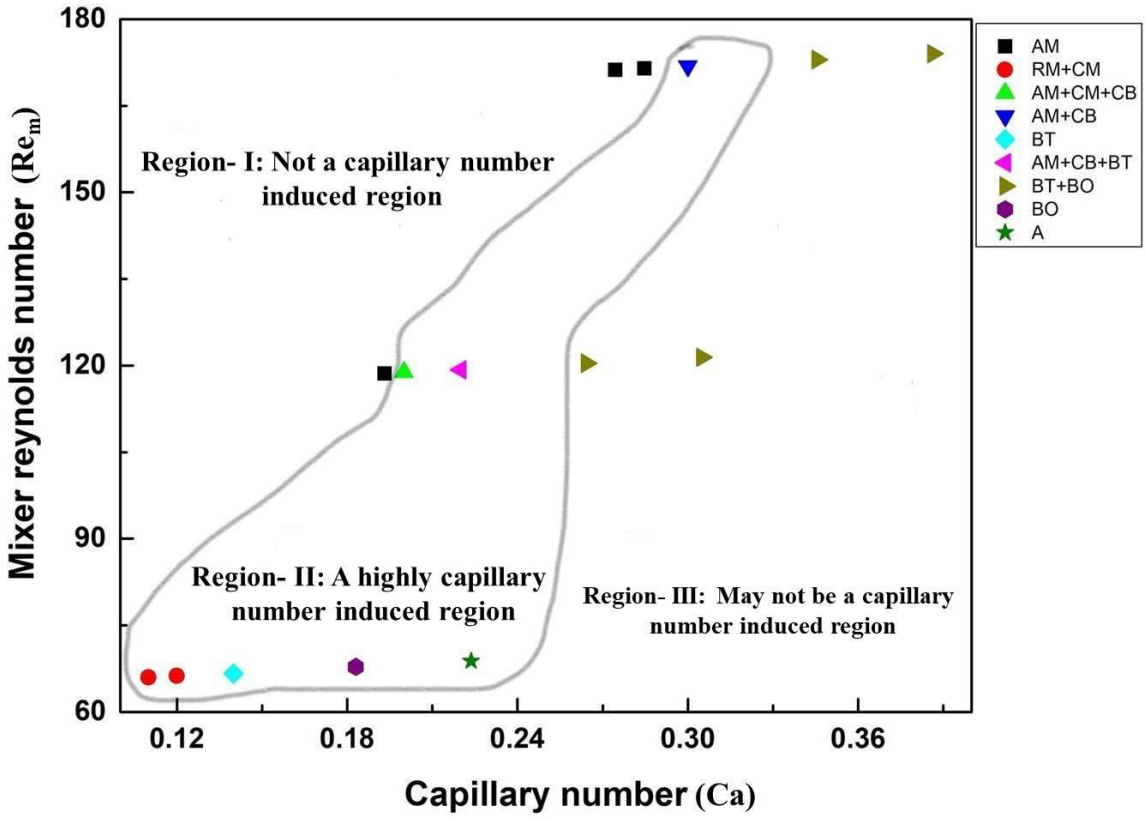

Figure 3.9. Flow pattern map,- Capillary number (Ca) vs Mixer Reynolds number (Re_m): AM - Alternate movement of droplets, RM - Random movement of droplets, CM - Two droplets coalesce and move in one direction, CB - Two droplets coalesce and bifurcate, BT - Bifurcation with tunnel, BO - Bifurcation with obstruction, A - Annular flow.

Bifurcation with tunnel and bifurcation with obstruction (BT+BO) occurs at higher Mixer Reynolds number and capillary number. They occupy a wider area of the map. Alternate

movement of droplets (AM) occurs at higher Mixer Reynolds number and lower to moderate capillary number, and they occupy a moderate area of the map. A truly mixed flow pattern region comprising of (a) random movement of droplets and coalescence of two droplets and movement in one direction (RM+CM), (b) Alternate movement of droplets-Two droplets coalesce and moving in one direction-Two droplets coalesce and bifurcation (AM+CM+CB), (c) Alternate movement of droplets-Two droplets coalesce and bifurcation (AM+CB), (d) Alternate movement of droplets-Two droplets coalesce and bifurcation-Bifurcation with tunnel (AM+CB+BT) (e) and (g) Annular flow (A) occur at lower to moderate Ca values covering lower to higher Re_m.

3.3.4 The insight physics behind non- breakup and breakup of the droplets

This section provides a plausible explanation for the non-breakup and breakup phenomena observed in the T-junction microchannel. For this purpose, the subsequent sections have reported oil-water volume fraction profile, pressure profile, velocity profile, and vorticity profile distribution. The scale for the magnitude of the different parameters has shown on the respective figures' left–hand side. Here, the units used for dynamic pressure, vorticity, and velocity vector are Pa, 1/s, and m/s, respectively.

3.3.4.1 Pressure swing mediated alternate movement of droplets

Figure 3.10 depicts the flow behavior of droplets moving alternatively in the two arms of the T-junction microchannel. A relative time sequence of 0 s, 13 ms, and 20 ms for the flow volume fraction along with the corresponding dynamic pressure, velocity vector, and vorticity

are presented (Figure 3.10). During an alternate movement of droplets, there is no squeezing and pinch-off stage of the droplets are observed (Figure 3.10a). It occurs for small droplets and onsets at low water superficial velocity (0.01 m/s) and moderate oil superficial velocity (0.18 m/s). There exist only extension and pushing stages [28]. In the extension stage, the droplet touches the opposite wall and gets deform. As a result, the front interface gets gradually flatten. As the shear force acting on the droplet is very less as compared to the surface tension force, the degree of deformation is insufficient to split the droplet. After the extension stage, the droplet enters into the pushing stage.

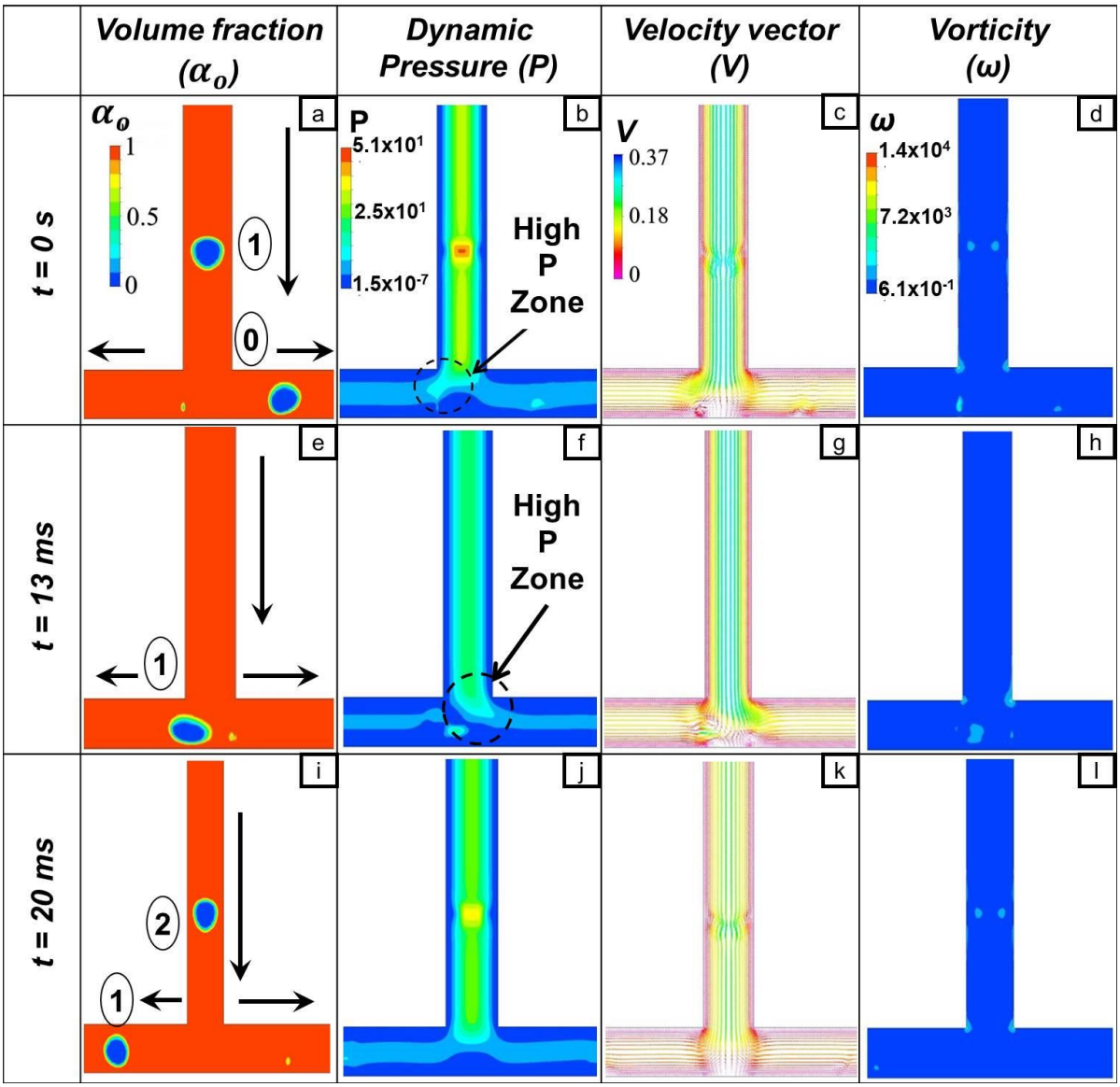

Figure 3.10. Volume fraction contour of mineral oil-water, Dynamic pressure field contour, Velocity vectors and Vorticity data during alternate movement of droplets at T-junction of the microchannel.

The oil phase flows through the gap existing between the surface of the water droplet and the corner of the channel wall. This creates a high-pressure zone on the left-hand side of the T-junction, which is clearly visible in Figure 3.10b. This higher pressure pushes the droplet into the right-hand side of the T-junction as observed in Figure 3.10a. The existence of higher pressure on the left-hand side is well supported by the velocity (Figure 3.10c) and vorticity profile (Figure 3.10d). Similarly, when the second droplet comes at the T-junction, a high-pressure zone is created on the right-hand side of the T-junction (Figure 3.10f), which pushes the droplet into the left-hand side of the T-junction (Figure 3.10i). This time-periodic variation of the pressure and the alternate droplet motion continues as long as the velocity of the phases is kept constant. Thus the periodic swing of the high-pressure zone in the left and right-hand sides of the T-junction microchannel leads to the alternate motion of the water droplet.

3.3.4.2 Pressure and vortex mediated droplet breakup with tunnel

Figure 3.11 represents the droplet split up in the two arms of the T-junction microchannel. A relative time sequence of 0 s, 6 ms, and 8 ms for the flow volume fraction along with the corresponding dynamic pressure, velocity vector, and vorticity are shown (Figure 3.11). The only bifurcation with tunnel (no mixed flow pattern) was observed at low water (0.04 m/s) and oil (0.18 m/s) superficial velocity. In this case, the water droplets were sandwiched between the channel walls when they moved through the two outlet branches of the T-junction away from the T-junction. The space between the droplet and channel wall near the T-junction was occupied by the lubricating oil film. The bullet-shaped droplet flowing through the main channel approaches towards the T-junction (Figure 3.11a). The corresponding pressure profile (Figure

3.11b) indicates that the droplets are bearing high pressure (red to yellow color band in the figure), which is supported by a strong velocity field, as observed in Figure 3.11c. The droplet with high pressure hits the front wall of the T-junction and gets deformed and squeezed (Figure 3.11e). Two vortices are formed (Figure 3.11h) at the front end of the droplets when the shear force of the lubricating film acting on the deformed droplet is comparable to the interfacial tension. On the other hand, a relatively low-pressure zone exists at the junction and in the two arms of the T-junction (Figure 3.11b), which strengthens the vortices near/below the deformed droplets (Figure 3.11h). This vortex flow and the accumulated upstream pressure help to narrow the neck in the middle of the droplet (Figure 3.11e) and finally induce the pinch-off the neck (Figure 3.11i) and split the droplet.

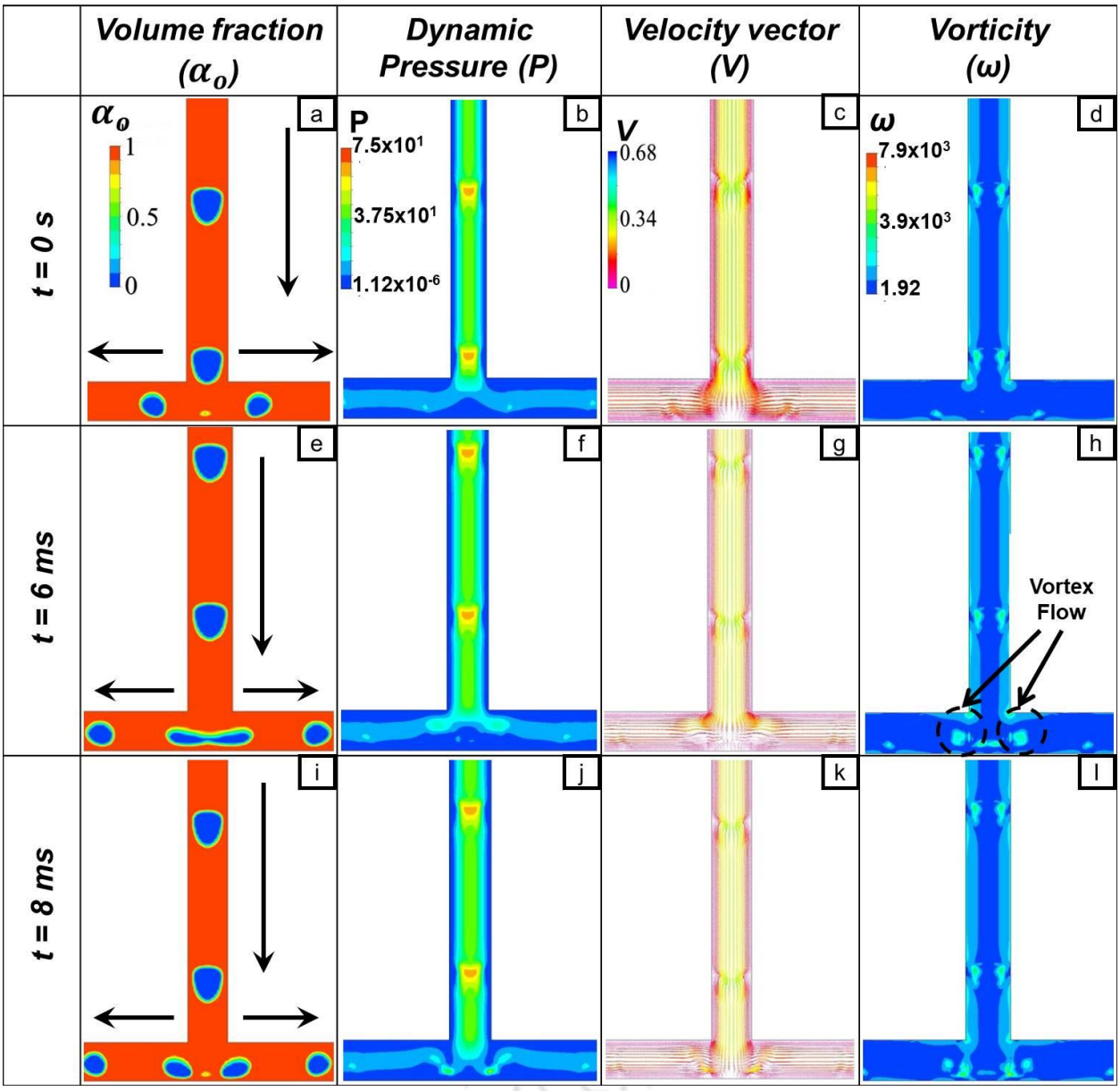

Figure 3.11. Volume fraction contour of mineral oil-water, Dynamic pressure field contour, Velocity vectors and Vorticity data during breakup with tunnel of droplets at T-junction of the microchannel.

We have represented the circulation pattern within daughter droplets below:

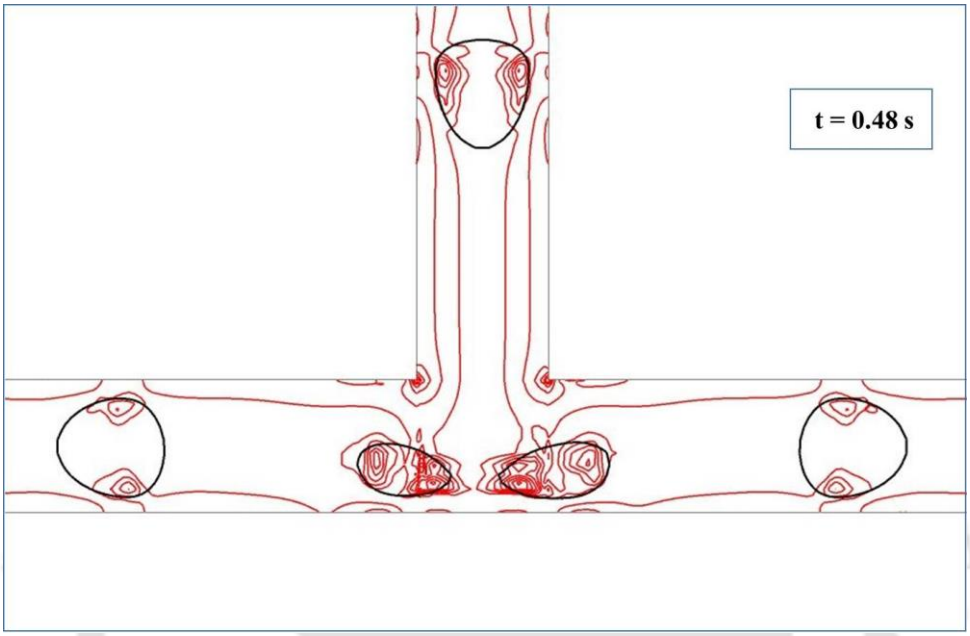

Figure 3.12. Recirculation pattern within daughter droplets at V_w = 0.04 m/s and V_o = 0.18 m/s.

A mother droplet bifurcates into two daughter droplets. There are two major vortices created at the T-junction on the mother droplets which enhance the bifurcation of mother droplet. Two more additional vortices are also created around the corner of the T-junction. All these circulatory motions try to sweep away the nearly splitting or completely splitted water masses of the mother droplet. The daughter droplets are also associated with small vortices even at faraway position from the T-junction.

3.3.4.3 Reason for droplet breakup with obstruction

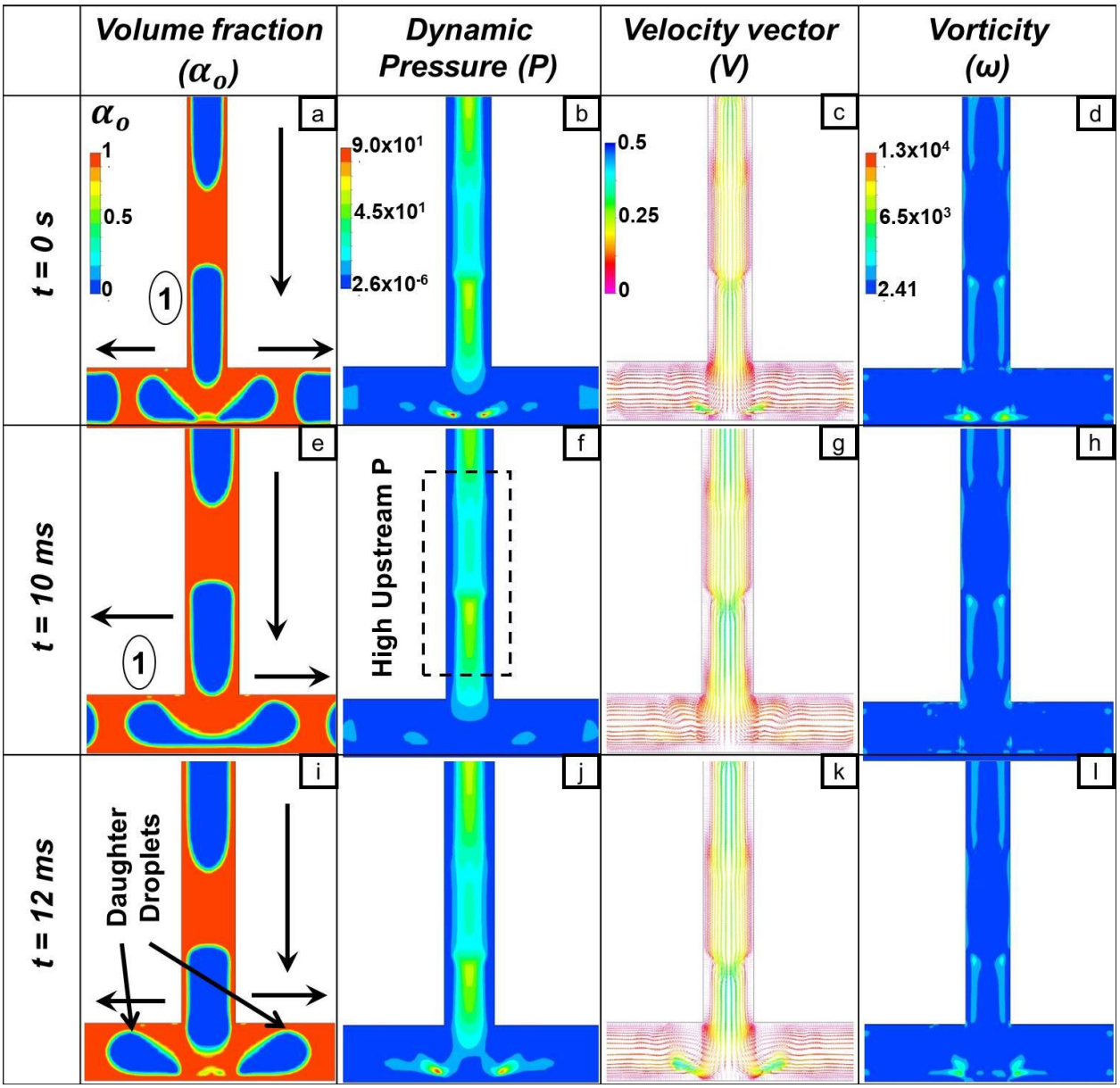

Figure 3.13. Volume fraction contour of mineral oil-water, Dynamic pressure field contour, Velocity vectors and Vorticity data during breakup with obstruction of droplets at T-junction of the microchannel.

Perfect flow of bifurcation with obstruction (no mixed flow) was observed at low water (0.08 m/s) and oil superficial velocity (0.10 m/s). This flow regime has three distinct stages, namely, i) Extension ii) Squeeze and iii) Pinch-off. These three stages are also present in bifurcation with tunnel flow, but it can clearly be visualized here because of larger water droplets due to relatively higher water superficial velocity compared to the bifurcation with tunnel flow. In the extension stage, the bullet-shaped water droplet passing through the main channel approaches towards the T-junction and gets elongated due to shear forces acting on the droplet marked as 1 (Figure 3.13a). Also the vorticity is higher around the interface of the droplet marked as 1 (Figure 3.13d). The existence of shear force is well supported by intense pressure (Figure 3.13b), velocity (Figure 3.13c) and vorticity (Figure 3.13d) profile. The vortex shown in Figure 3.13d pulls the elongated droplet towards the junction area away from the main channel. After reaching the junction, the droplet-1 is squeezed due to the upstream pressure and vortex field. Now the droplet-1 is so deformed that it takes double tumbled shape (Figure 3.13e) and occupies the maximum area of the channel. So the flow of the continuous phase (oil) is obstructed, and pressure is accumulated in the junction area (Figure 3.13f). As a result, the shear force cannot overcome the surface force, but the accumulated pressure field forces the deformed droplet in a complete pinch-off (Figure 3.13i). So the combined effect of larger droplet size, pressure accumulation, and occurrence of vortices at the T-junction causes the bifurcation with obstruction.

It is very important to note that 2D simulations must provide the clear ideas about the influence of various two-phase flow parameters, like volume fraction contours (shape of the

droplets), pressure and velocity field, vorticity, geometrical parameters of the channel, etc. on the hydrodynamics. However, it is well known that flow through micro channels/devices is surface and viscous forces dominated flow. 2D simulation is not accounting the surface force accurately, and also, it is not estimating viscous force with higher precision. However, from this study, the readers can get a clear idea about the types of geometry of micro channels/devices which are suitable for droplet splitting and miniaturizations. They can also understand the importance of the various forces which are responsible behind such hydrodynamics. So, 2D simulation is not very appropriate in sense of accounting the absolute values of the various forces, but it is significant in terms of qualitative estimation of flow patterns, influence of channel geometry, velocity field, fluid properties (except surface forces), types of daughter branches of the channel, etc.

3.3.5 Force balance model for droplet splitting at T-junction of the microchannel

This section proposes droplet splitting criteria by balancing the fundamental forces acting on the deformed droplet. The analysis has been adopted from Na et al. 2019 [29]. For this, let us consider the deformation of a droplet progressing through the T-junction, as shown below in Figure 3.14. Figure 3.15. depicts the film and gutter region in the main channel. A 3D T-junction microchannel has been considered with depth *h* and width *w*. The depth is not shown in the figure. The width of the main and branch channels are taken the same i.e. *w*. The figure also shows the distribution and position of various forces and pressure drop acting on the deformed droplet. According to the figure, the pressure drop on the droplet in the main channel is balanced

by the net pressure drop working on the droplet's neck, body, and nose. So, the pressure drop equation is given as:

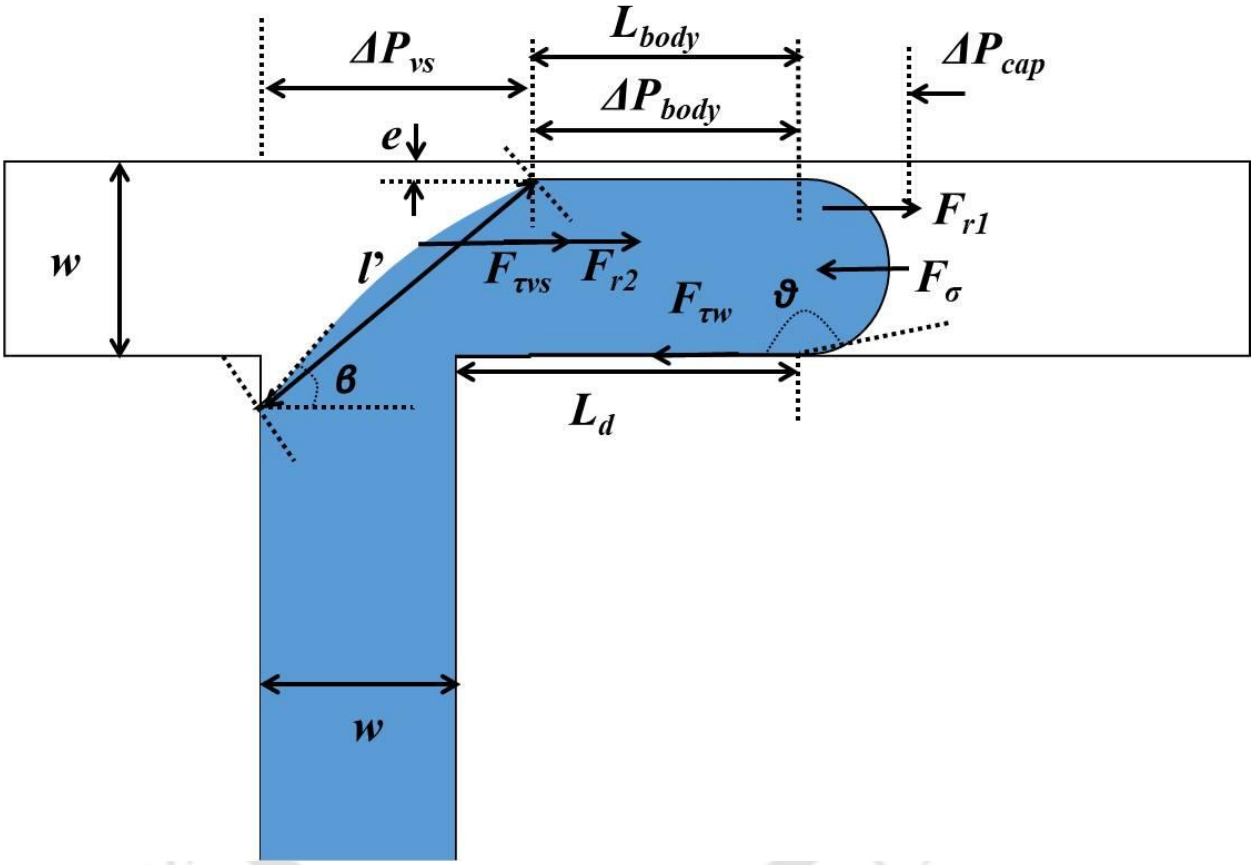

Figure 3.14. Forces acting on the droplet progressing towards T-junction

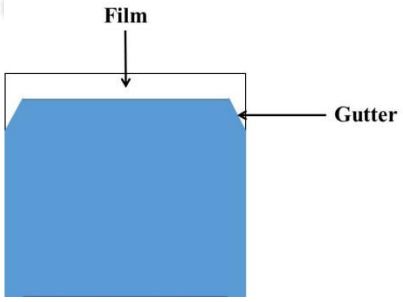

Figure 3.15. Diagram depicting the film and gutter region

$$\Delta P = \Delta P_{vs} + \Delta P_{body} + \Delta P_{cap} \quad (3.3.5.1)$$

Where:

ΔP_{vs} is the pressure drop at the neck of the droplet.

ΔP_{body} is the pressure drop caused by the thin film.

ΔP_{cap} is the capillary pressure term due to the interface curvatures.

ΔP_{vs} may be calculated applying Bernoulli equation in the film and gutter region, which gives,

$$\Delta P_{vs} = \frac{\rho_c \left(v_c^{\,2} - v_e^{\,2}\right)\cos\beta}{2} \quad (3.3.5.2)$$

Where,

ρ_c = density of continuous phase

v_c = velocity of continuous phase

v_e = average flow velocity of the liquid film in the gutters

β = angle between dispersed phase and wall of microchannel

Pressure drop caused by the thin film (ΔP_{body}) is approximately calculated considering the Poiseuille flow of the continuous phase. The pressure drop is obtained as,

$$\Delta P_{body} = \frac{a\mu_c L_{body} Q_e}{h^4} \quad (3.3.5.3)$$

Where,

a = dimensionless parameter that depends on the aspect ratio μ_c,

L_{body} = main length of the droplet

μ_c = viscosity of continuous phase

Q_e = flow rate of the liquid film

h = depth of the microchannel

On the other hand, following capillary pressure near the nose of the droplet is calculated considering the Young-Laplace equation and dimensions of the microchannel,

$$\Delta P_{cap} = 2\sigma\cos\theta\left(\frac{1}{w}+\frac{1}{h}\right) \quad (3.3.5.4)$$

Where,

σ = Interfacial tension

θ = contact angle between dispersed phase and wall of microchannel

w = width of the microchannel

h = depth of the microchannel

The different components of the forces acting on the deformed droplet are also shown in Figure 3.14. Here, the shear force and pressure drop on both sides destabilize the droplet, and interfacial tension stabilizes the droplet. The force balance on the droplet, while it passes through the T-junction, is given by,

$$F = F_{\sigma} + F_{\tau vs} + F_{\tau w} + F_{r1} + F_{r2} \tag{3.3.5.5}$$

Where,

F_{σ} = the interfacial tension force

$F_{\tau vs}$ = the viscous shear force acting on the neck

$F_{\tau w}$ = the viscous force of the solid wall acting on the droplet

F_{r1} = the viscous drag of the thin film acting on the droplet tip

F_{r2} = the viscous drag of the continuous phase acting on the neck

The interfacial tension force is calculated as the product of capillary pressure drop and the cross-sectional area of the channel.

$$F_{\sigma} = \Delta P_{cap} hw = 2\sigma \cos\theta \left(\frac{1}{w} + \frac{1}{h}\right) hw \tag{3.3.5.6}$$

The viscous shear force acts on the neck structure of the dispersed phase and points downstream of the channel and is given by:

$$F_{\tau vs} = \frac{h\mu_c (v_c - v_d) l' \cos\beta}{\varepsilon} \tag{3.3.5.7}$$

Where,

v_d = velocity of dispersed phase

l' = neck length

ε = thickness of the two-phase interface

According to the Berthier [30] the viscous force of the lower solid wall acting on the droplet is given by,

$$F_{\tau w} = \frac{-hL_d 6\mu_d v_d}{w} \tag{3.3.5.8}$$

Where,

L_d = drag length

μ_d = viscosity of dispersed phase

ΔP_{body} and ΔP_{vs} cause the flow resistance on the tip and body of the droplet, respectively. The corresponding force can be obtained by multiplying the pressure difference with the cross-sectional area as follows,

$$F_r = F_{r1} + F_{r2} = \Delta P_{body} he + \Delta P_{vs} hl' = \left(\frac{a\mu_c L_{body} Q_e}{h^4}\right) he + \left(\frac{\rho_c (v_c^{\,2} - v_e^{\,2}) \cos\beta}{2}\right) hl' \tag{3.3.5.9}$$

Where,

e = the gap width of the liquid film

Therefore the net force acting on the deformed droplet is given by:

$$F = F_{\sigma} + F_{\tau vs} + F_{\tau w} + F_{r1} + F_{r2} = 2\sigma\cos\theta\left(\frac{1}{w}+\frac{1}{h}\right)hw + \frac{h\mu_c(v_c - v_d)l'\cos\beta}{\varepsilon} + \frac{-hL_d 6\mu_d v_d}{w} + \left(\frac{a\mu_c L_{body} Q_e}{h^4}\right)he + \left(\frac{\rho_c({v_c}^2 - {v_e}^2)\cos\beta}{2}\right)hl' \quad (3.3.5.10)$$

Also, the forces acting on droplet splitting depend upon the forces acting upon the droplet formation. So, Eq. 10 supports the droplet splitting phenomena. The direction of all the forces is shown in Figure 3.14. Based on it, the droplet splitting condition can be written as,

Also, the droplet will split at the T-junction of the microchannel if

$$F_{\tau vs} + F_{r1} + F_{r2} > (F_{\tau w} + F_{\sigma}) \quad (3.3.5.11)$$

Or,

$$\frac{h\mu_c(v_c - v_d)l'\cos\beta}{\varepsilon} + \left(\frac{a\mu_c L_{body} Q_e}{h^4}\right)he + \left(\frac{\rho_c({v_c}^2 - {v_e}^2)\cos\beta}{2}\right)hl' > \left(\frac{-hL_d 6\mu_d v_d}{w}\right) + \left(2\sigma\cos\theta\left(\frac{1}{w}+\frac{1}{h}\right)hw\right) \quad (3.3.5.12)$$

The droplet will coalesce at the T-junction of the microchannel if

$$F_{\tau vs} + F_{r1} + F_{r2} < (F_{\tau w} + F_{\sigma}) \quad (3.3.5.13)$$

Or,

$$\frac{h\mu_c(v_c - v_d)l'\cos\beta}{\varepsilon} + \left(\frac{a\mu_c L_{body} Q_e}{h^4}\right)he + \left(\frac{\rho_c({v_c}^2 - {v_e}^2)\cos\beta}{2}\right)hl' < \left(\frac{-hL_d 6\mu_d v_d}{w}\right) + \left(2\sigma\cos\theta\left(\frac{1}{w}+\frac{1}{h}\right)hw\right) \quad (3.3.5.14)$$

At V_w = 0.04 m/s V_o = 0.18 m/s, the droplet bifurcation takes place at the T-junction in our simulation.

Here the whole model is based on 3D geometry. But our simulation is based on 2D geometry. For this we have considered unit depth of the microchannel and perform the validation of the model. This is the overall approximation.

Putting all the values which corresponds to the velocity set, V_w = 0.04 m/s and V_o = 0.18 m/s from our simulation into the model, we get the following:

$$F_\sigma = \Delta P_{cap} hw = 2\sigma \cos\theta \left(\frac{1}{w} + \frac{1}{h}\right) hw \quad (3.3.5.15)$$

Or, F_σ = 0.00003 N

$$F_{\tau vs} = \frac{h\mu_c (v_c - v_d) l' \cos\beta}{\varepsilon} \quad (3.3.5.16)$$

Or, $F_{\tau vs}$ = 0.000003 N

$$F_{\tau w} = \frac{-hL_d 6\mu_d v_d}{w} \quad (3.3.5.17)$$

Or, $F_{\tau w}$ = -0.00000001 N

$$F_r = F_{r1} + F_{r2} = \Delta P_{body} he + \Delta P_{vs} hl' = \left(\frac{a\mu_c L_{body} Q_e}{h^4} \right) he + \left(\frac{\rho_c (v_c^{\,2} - v_e^{\,2}) \cos\beta}{2} \right) hl' \quad (3.3.5.18)$$

Or, F_r = 19.95 N

So, $F_{\tau vs} + F_r$ = 0.000003 + 19.95 = 19.96 N which is greater than $F_{\tau w} + F_\sigma$= 0.00003 N

This confirms that the force balance model is satisfying our simulation result.

3.3.6 Prediction of pressure drop using existing models

In this section an attempt has been made to predict the present simulated pressure drop date using homogeneous model and drift flux models. A brief about the models have been discussed below.

In homogeneous flow model, two-phase flow is consider as a pseudo single phase flow, in which two phases are uniformly mixed. The physical properties of the mixture are intended based on mass fraction and hold-up values. According to homogeneous model, the two-phase pressure gradient is calculated based on the following equation [31],

$$\frac{dp}{dz} = \frac{2 f_m \rho_m U_m^2}{D} \quad (3.3.6.1)$$

Where the mixture velocity $U_m = U_{so} + U_{sw}$ (3.3.6.2)

Mixture density $\rho_m = H_o\rho_o + (1-H_o)\rho_w$ (3.3.6.3)

The friction factor can be obtained as

$$f_m = \frac{16}{\mathrm{Re}_m} \quad \text{for } \mathrm{Re}_m < 2100 \tag{3.3.6.4a}$$

$$= \frac{0.079}{\mathrm{Re}_m^{0.25}} \quad \text{for } 2100 < \mathrm{Re}_m < 2\text{x}10^4 \tag{3.3.6.4b}$$

Where $\mathrm{Re}_m = \frac{\rho_m U_m D}{\mu_m}$ (3.3.6.5)

The mixture viscosity μ_m is calculated from McAdams formula given by,

$$\frac{1}{\mu_m} = \frac{x}{\mu_w} + \frac{1-x}{\mu_o} \tag{3.3.6.6}$$

Where x is the mass fraction of dispersed phase (water here).

Prediction shown in Figure 3.16 has a large deviation from the simulated results (average error around ±54.8%). To improve the accuracy in prediction, we have reformed the drift flux model. In support of incorporation of drift flux model, a β_o vs H_o plot has been presented below (Figure 3.17). It shows that there is a significant difference between β_o vs H_o , which is an indication of presence of drift velocity similar to a slip between two phases. Drift flux model is commonly used in such cases to predict the pressure drop or pressure gradient.

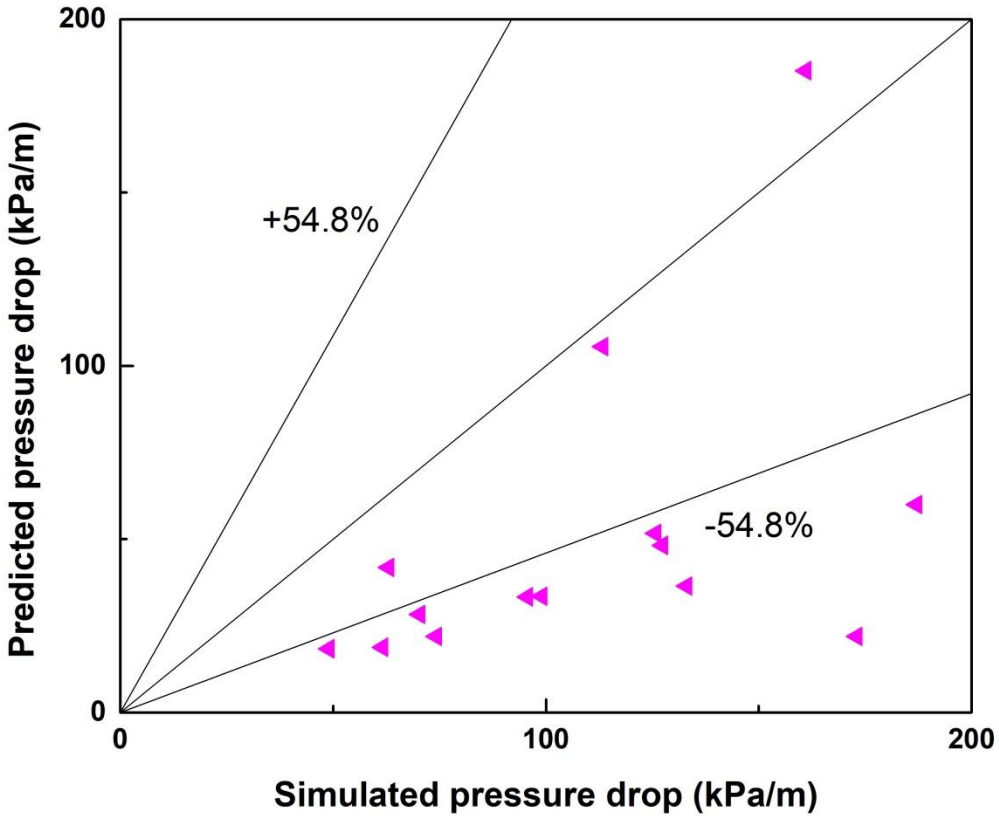

Figure 3.16. A comparison between present simulated results and data obtained from homogeneous model

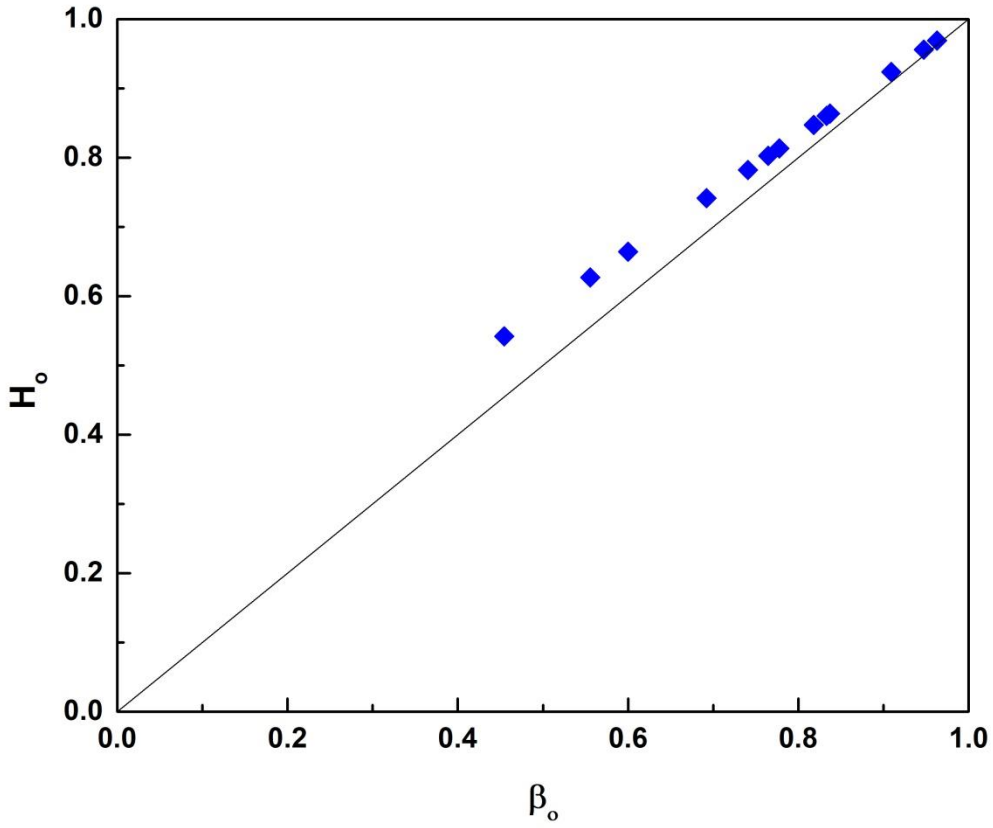

Figure 3.17. In case of simulated result, β_o vs H_o plot showing a significant deviation between them

The drift flux model is developed based on the concept of drift velocity of dispersed phase [29] and a brief about the model has been elaborated in the next paragraph.

The drift flux model has been adopted to modify the in-situ velocity of the water phase (velocity of dispersed phase, u_w) as-

$$u_w = C_1 j + C_2 u_\infty \quad (3.3.6.7)$$

Where u_∞ is the rise or falling velocity due to buoyancy or gravity and j is the volumetric flux of the two-phase mixture, viz

$$j = j_w + j_o \quad (3.3.6.8)$$

The individual volume fluxes j_o and j_w are expressed as

$$j_o = \frac{Q_o}{A} \quad and \quad j_w = \frac{Q_w}{A} \quad (3.3.6.9)$$

In a horizontal tube buoyancy or gravity effects are absent and $u_\infty = 0$

$$\therefore u_w = C_1 j \quad (3.3.6.10)$$

where C_1 is the measure of the water velocity relative to the weighted mean velocity of the mixture (j). From literature the value of C_1 is assumed as an asymptotic value of 0.84. Substituting this value in the expression of H_o and using Eq. (3.3.6.9 & 3.3.6.10), we get

$$H_o = 0.84 \frac{Q_o}{Q_o + Q_w} \quad (3.3.6.11)$$

Considering drift velocity, mixture density can easily be calculated putting Eq. (3.3.6.11) into Eq. (3.3.6.3) and finally pressure gradient can be obtained from Eq. (3.3.6.1). The output of this analysis gives a significant improvement as presented in Figure 3.18. The average deviation has been reduced to about ± 43.2%.

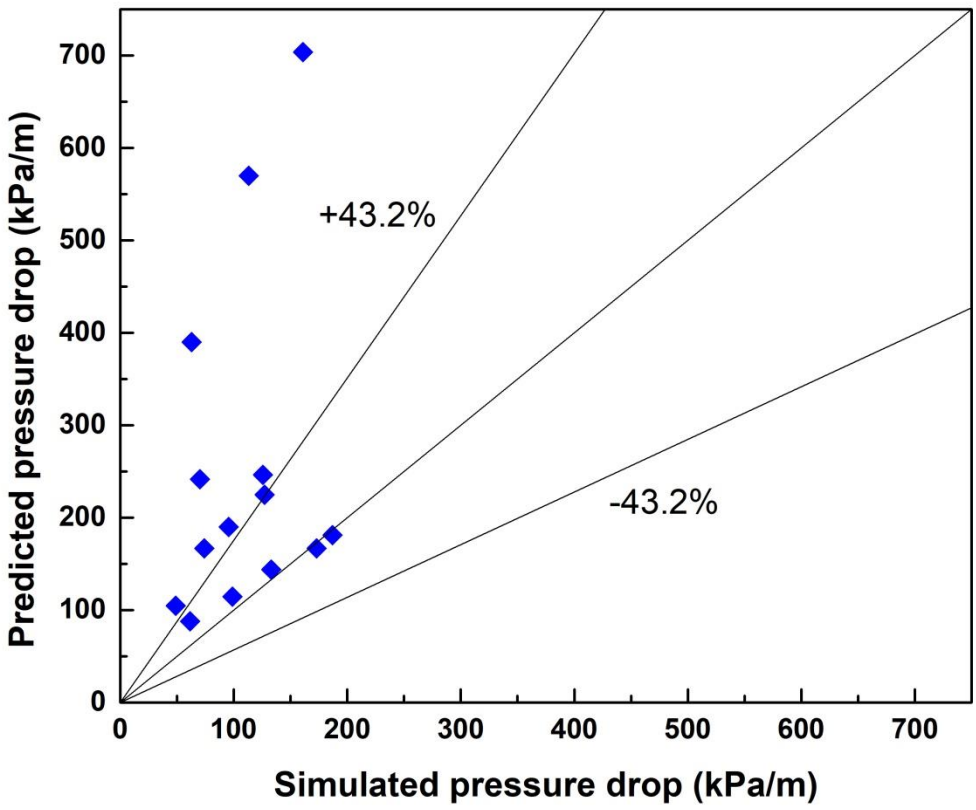

Figure 3.18. A comparison between present simulated results and data obtained from drift flux model

The present simulated pressure drop data has also been predicted using two more pressure drop models specific to Taylor flow. First one is stagnant film model adopted from Jovanovic et al. 2011 [32] and second one is taken from Kashid and Agar, 2007 [33].

In stagnant film model, the total pressure drop is calculated using the following equation:

$$\Delta P_T = \frac{8\mu_c U(1-\varepsilon)L}{R^2} + \frac{8\mu_D U_D \varepsilon L}{(R-h)^2} + \frac{L}{L_U} 7.16(3Ca)^{\frac{2}{3}} \frac{\sigma}{D} \qquad (3.3.6.12)$$

In the model taken from Kashid and Agar, the total pressure drop is calculated using the following equation:

$$\Delta P_T = \frac{L}{L_U}\left(\frac{8\mu_c U(1-\varepsilon)L}{R^2} + \frac{8\mu_D U\varepsilon L}{R^2}\right) + \frac{2L - L_U}{L_U}\left(\frac{2\sigma}{D} Cos\theta\right) \qquad (3.3.6.13)$$

Where L, L_U, U, μ_c, μ_D, R, ε, U_D, and h refer to the capillary length, slug unit length, mixed velocity, continous phase viscosity, dispersed pjase viscosity, capillary radius, dispersed phase fraction length, dispersed phase velocity, and film thickness, respectively. The pressure drop is calculated using these two model and have been tabulated in Table 3.6.

Table 3.6. Summary of the differences between the simulated liquid–liquid data and data estimated using the most referenced liquid–liquid models

Liquid - liquid combination	Jovanovic et al., 2011 Eq. 3.3.6.12	Kashid and Agar, 2007 Eq. 3.3.6.13	Drift flux model
Water/Mineral - oil	89 %	99.6 %	43.2 %

Table 3.6 represents the comparision among the three models. The percentage deviations of these two model are higher than the Drift flux model.

3.4. SUMMARY

In this study, the 2D-CFD simulation has been carried out to investigate the influence of phase velocity on droplet splitting in a T-junction microchannel. The simulated results have explored various fundamental aspects of different types of droplet splitting phenomena. The model has been validated with the previous experimental data present in the literature (Salim et al. [23]). We have successfully simulated droplet non-breakup and droplet breakup flow regimes, changing the phase velocities of two phases. Two types of droplet breakup regimes, namely tunnel-breakup and obstructed breakup has been observed. New flow morphology, namely mixed flow pattern, transient in nature, has also been observed in a wide range of phase velocities. This transient behavior has been characterized by the alteration of the flow patterns at constant flow rates. Different flow patterns have been presented in the form of a flow pattern map. It has been found that pressure swing phenomena at the T-junction have instigated the movement of the droplets in alternate directions. The formation of vortex flow at the front ends

of the droplets is one of the critical reasons for droplet breakup with tunnel. On the other hand, the resultant effect of larger droplet volume, upstream pressure buildup, and vortex flow are found to be responsible for droplet bifurcation with obstruction. Present simulated pressure drop data have been predicted using homogeneous, drift flux model and stagnant film model [32] and another model taken from Kashid and Agar, 2007 [33]. The results show that drift flux model gives the higher accuracy in prediction. These findings will help in better understanding of droplet splitting and will have direct application in microfluidic platform based device.

REFERENCES

1. Leman, M., Abouakil, F., Griffiths, A.D., and Tabeling, P., Droplet-based microfluidics at the femtolitre scale, *Lab Chip*, 2015, vol. 15, no. 3, pp. 753-65.
2. Bezagu, M., Arseniyadis, S., Cossy, J., Couture, O., Tanter, M., Monti, F., and Tabeling, P., A fast and switchable microfluidic mixer based on ultrasound-induced vaporization of perfluorocarbon, *Lab Chip*, 2015, vol. 15, no. 9, pp. 2025-9.
3. Kashid, M.N., Renken, A., and Kiwi-Minsker, L., Gas–liquid and liquid–liquid mass transfer in microstructured reactors, *Chemical Engineering Science*, 2011, vol. 66, no. 17, pp. 3876-3897.
4. Mitra, S., Singh, S.K., Shevchenko, E., Sachan, M., Ghosh, A., Basak, M., and Gooh Pattader, P.S., Efficient microextraction process exploiting spontaneous interfacial convection driven by Marangoni and electric field induced instability: A computational fluid dynamics study, *Physics of Fluids*, 2020, vol. 32, no. pp. 014102.
5. Kobayashi, J., Mori, Y., and Kobayashi, S., Multiphase Organic Synthesis in Microchannel Reactors, *Chemistry – An Asian Journal*, 2006, vol. 1, no. 1-2, pp. 22-35.
6. Srinivasan, V., Pamula, V.K., and Fair, R.B., Droplet-based microfluidic lab-on-a-chip for glucose detection, *Analytica Chimica Acta*, 2004, vol. 507, no. 1, pp. 145-150.
7. Jangir, P. and Jana, A.K., CFD simulation of droplet splitting at microfluidic T-junctions in oil–water two-phase flow using conservative level set method, *Journal of the Brazilian Society of Mechanical Sciences and Engineering*, 2019, vol. 41, no. 2, pp. 75.

8. Li, Z. and Li, L., Multiple splitting of droplets using multi-furcating microfluidic channels, 2019, vol. 13, no. 2, pp. 024112.

9. Berry, S.B., Lee, J.J., Berthier, J., Berthier, E., and Theberge, A.B., Droplet incubation and splitting in open microfluidic channels, *Analytical Methods*, 2019, vol. 11, no. 35, pp. 4528-4536.

10. Chen, J., Vestergaard, M., Shen, J., Solem, C., Dufva, M., and Jensen, P.R., Droplet-based microfluidics as a future tool for strain improvement in lactic acid bacteria, *FEMS Microbiology Letters*, 2018, vol. 365, no. 23, pp.

11. Schreiber, J. and Diec, K.H., (2010). vol. no. pp.

12. Cheng, W.L., Sadr, R., Dai, J., and Han, A., Prediction of Microdroplet Breakup Regime in Asymmetric T-Junction Microchannels, *Biomedical Microdevices*, 2018, vol. 20, no. 3, pp. 72.

13. Chen, B., Li, G., Wang, W., and Wang, P., 3D numerical simulation of droplet passive breakup in a micro-channel T-junction using the Volume-Of-Fluid method, *Applied Thermal Engineering*, 2015, vol. 88, no. pp. 94-101.

14. Link, D.R., Anna, S.L., Weitz, D.A., and Stone, H.A., Geometrically Mediated Breakup of Drops in Microfluidic Devices, *Physical Review Letters*, 2004, vol. 92, no. 5, pp. 054503.

15. Chen, Y. and Deng, Z., Hydrodynamics of a droplet passing through a microfluidic T-junction, *Journal of Fluid Mechanics*, 2017, vol. 819, no. pp. 401-434.

16. Leshansky, A.M. and Pismen, L.M., Breakup of drops in a microfluidic T junction, *Physics of Fluids*, 2009, vol. 21, no. 2, pp. 023303.

17. Zhu, P., Kong, T., Lei, L., Tian, X., Kang, Z., and Wang, L., Droplet Breakup in Expansion-contraction Microchannels, *Scientific Reports*, 2016, vol. 6, no. 1, pp. 21527.

18. Li, Z., Li, L., Lioa, M., He, L., and Wu, P., Multiple splitting of droplets using multi-furcating microfluidic channels, *Biomicrofluidics*, 2019, vol. no. pp.

19. Wang, X., Liu, Z., and Pang, Y., Droplet breakup in an asymmetric bifurcation with two angled branches, *Chemical Engineering Science*, 2018, vol. 188, no. pp. 11-17.

20. Cristobal, G., Benoit, J.-P., Joanicot, M., and Ajdari, A., Microfluidic bypass for efficient passive regulation of droplet traffic at a junction, *Applied Physics Letters*, 2006, vol. 89, no. 3, pp. 034104.

21. Engl, W., Roche, M., Colin, A., Panizza, P., and Ajdari, A., Droplet Traffic at a Simple Junction at Low Capillary Numbers, *Physical Review Letters*, 2005, vol. 95, no. 20, pp. 208304.

22. Darekar, M., Singh, K.K., Mukhopadhyay, S., and Shenoy, K.T., Liquid–Liquid Two-Phase Flow Patterns in Y-Junction Microchannels, *Industrial & Engineering Chemistry Research*, 2017, vol. 56, no. 42, pp. 12215-12226.

23. Salim, A., Fourar, M., Pironon, J., and Sausse, J., Oil–water two-phase flow in microchannels: Flow patterns and pressure drop measurements, *The Canadian Journal of Chemical Engineering*, 2008, vol. 86, no. 6, pp. 978-988.

24. Raj, R., Mathur, N., and Buwa, V.V., Numerical Simulations of Liquid−Liquid Flows in Microchannels, *Industrial & Engineering Chemistry Research*, 2010, vol. 49, no. 21, pp. 10606-10614.

25. Timung, S., Tiwari, V., Singh, A.K., Mandal, T.K., and Bandyopadhyay, D., Capillary force mediated flow patterns and non-monotonic pressure drop characteristics of oil-water microflows, *The Canadian Journal of Chemical Engineering*, 2015, vol. 93, no. 10, pp. 1736-1743.

26. Sun, X., Zhu, C., Fu, T., Ma, Y., and Li, H.Z., Dynamics of droplet breakup and formation of satellite droplets in a microfluidic T-junction, *Chemical Engineering Science*, 2018, vol. 188, no. pp. 158-169.

27. Hoang, D.A., Portela, L.M., Kleijn, C.R., Kreutzer, M.T., and van Steijn, V., Dynamics of droplet breakup in a T-junction, *Journal of Fluid Mechanics*, 2013, vol. 717, no. pp. R4.

28. Liu, X., Zhang, C., Yu, W., Deng, Z., and Chen, Y., Bubble breakup in a microfluidic T-junction, *Science Bulletin*, 2016, vol. 61, no. 10, pp. 811-824.

29. Na, Z., Wei, L., and Yongqing, H., Dynamic behavior and driving force model of droplet formation in a T-junction microchannel, *Journal of Micromechanics and Microengineering*, 2019, vol. 29, no. 11, pp. 115002.

30. Berthier, J., *Chapter 14 - Introduction to Droplet Microfluidics and Multiphase Microflows*, in *Micro-Drops and Digital Microfluidics (Second Edition)*, J. Berthier, Editor. 2013, William Andrew Publishing. p. 493-532.

31. Isbin, H.S., *One-dimensional two-phase flow, Graham B. Wallis, McGraw-Huill, New York (1969)*. 1970, Wiley Online Library.

32. Jovanović, J., Zhou, W., Rebrov, E.V., Nijhuis, T., Hessel, V., and Schouten, J.C., Liquid–liquid slug flow: hydrodynamics and pressure drop, *Chemical Engineering Science*, 2011, vol. 66, no. 1, pp. 42-54.

33. Kashid, M.N. and Agar, D.W., Hydrodynamics of liquid–liquid slug flow capillary microreactor: flow regimes, slug size and pressure drop, *Chemical Engineering Journal*, 2007, vol. 131, no. 1-3, pp. 1-13.

CHAPTER 4

INFLUENCE OF ARM LENGTH AND WIDTH RATIO ON DROPLET SPLITTING: A COMPUTATIONAL STUDY

Chapter 4 Influence of arm length and width ratio on droplet splitting: a computational study

ABSTRACT

In this study, the effect of width ratio (branch channel width/main channel width) on droplet breakup dynamics in a horizontal microfluidic T-junction using oil-water volume fraction contours, pressure profile, and velocity profile has been investigated using 2D simulation. Simulations have been also conducted to reveal the effect of branch arm length ratio (right arm length/left arm length) on droplet breakup dynamics. The numerical simulation is validated with experimental results taken from the literature. Two types of breakup regimes, along with a non-breakup regime, have been found. The breakup regimes are tunnel breakup, and obstructed breakup, and the non-breakup regime is the alternate movement of droplets. The tunnel breakup and the obstructed breakup are mainly due to the pressure difference in the branch channel and the direction of the velocity vectors which are towards the branch's exit and the pressure swing phenomenon is the reason behind the alternate movement of the droplets. Breakup with tunnel is found in WR = 0.75, 0.5, breakup with obstruction is found in WR = 0.25 and alternate movement is found in WR = 1 for Vw = 0.01 m/s, Vo = 0.18 m/s. It has been found that breakup tendency increases as we decrease the width ratio (1, 0.75, 0.5, and 0.25) and increase the arm length ratio (0.4, 0.6, and 0.9). Droplet breakup conditions have been studied. Mixed flow patterns have been displayed with the help of a flow pattern map for the width ratio = 1, 0.75, 0.5, and 0.25. Prediction of simulated pressure gradient have also been done with the help of the Lockhart and Martinelli approach and Dimensional analysis for width ratio = 1.

4.1. INTRODUCTION

Droplet splitting has always been an attraction for researchers due to its wide range of applications in the field of micro and Nano fluidics [1]. Droplet splitting can be done through T and Y – junction [2, 3], creating constriction in the microchannel [4], creating patterns on the inner segment of the microchannel, changing fluid properties [5], and through the channel network [6]. Mainly the droplet breakup in a confined geometry is controlled by dominated surface tension forces over viscous, inertial or gravitational forces [7]. Also, droplet splitting is of great importance because of the availability of a higher surface-to-volume ratio, smaller throughput, and higher heat, mass, and other interfacial transportation phenomena within the droplet. This helps in the easier control of the operating parameters, like reduction in operating cost where costly chemicals are in use. Also, droplet-based system reacts in a very short interval of time. It shows great potential for application in the field of biopharmaceuticals [8], emulsification [9], chemical engineering [10], life science [11] etc.

Experimentally, tunnel breakup, breakup with obstruction, and alternate movement were identified. These are mainly bounded to confined geometry, where surface tension force is the dominating force over the viscous, inertial, or gravitational forces [12]. The tunnel break up and break up with obstruction mainly contains three stages: i) Entering ii) Squeezing iii) Post-breakup and the alternate movement contains four stages: i) Entering ii) Squeezing iii) Stabilizing iv) Non-breakup [13].

Various researchers had varied the width ratio and came to some important conclusions. Investigations have been done on uniform width ratio and non – uniform width ratio. In case of

uniform width ratio, left arm, and right arm widths, both are equally increased or decreased. Whereas, in non – uniform width ratio, both the widths are not equally increased or decreased. Actually, the width ratio, the ratio of the main channel to branch channel, directly affects the deformation of droplets during its extension and squeeze stage at low capillary number. When the width ratio increases, the tendency of the breakup of the droplets also increases [14] . Bedram and Moosavi [15] suggested micro droplet breakdown at an asymmetric T - junction with branches of similar lengths and varying widths (non - uniform width ratio). They statistically and analytically studied the case and compared their suggested technique to that of Link et al. [6]. When the lengths are identical and the widths are uneven, the breakup time and pressure drop are less than in the uniform size T - junction with varied length outlets of the channels. The VOF approach was used to investigate droplet breakdown in T - junction geometries. To create equal and different size droplets, symmetric and asymmetric T - junctions were utilized, respectively. The effects of the channel width ratio (left arm width/right arm width) and the capillary number on the size and length of the formed droplets, as well as the production time, have been investigated and debated [2]. An investigation has been done on the breakup of micro-droplets through asymmetric T - junctions with branches of identical lengths and different widths (non – uniform width ratio). An equation of the critical capillary number for the onset of droplet breakup at asymmetric T - junctions are developed [16]. It was statistically examined using the VOF technique for gas-liquid two-phase flow via a microchannel T - junction and discovered four breakup regimes: "tunnel" breakdown, obstructed breakup, mixed breakup, and non-breakup. The velocity and pressure distributions in the inflow field are investigated. The influence of the width ratio between the main channel and the branch on bubble shape is also

investigated (uniform width ratio). Increasing the width ratio of the main channel to the branch channel results in the alteration of the bubble breakup regime, which moves through the non-breakup, "tunnel" breakup, and obstructed breakup regimes consecutively [12]. A 2D simulation has been done on gas-liquid two-phase flow in a microfluidic device with a T – junction where the bubbles enter from the main channel. Numerical simulation on uniform width ratio (Main channel width/ branch channel width) has shown that a higher width ratio is favorable for both symmetrical and asymmetrical break – up of the bubbles. At least a width ratio of 2 is required to break the spherical bubble with the initial extension of $\varepsilon_0 = 1/\pi$ [14]. Experiments have been performed at various angles to reveal the breaking process of the droplets. A critical length has been found, and it depends on the geometry that controls the breakup process. A theory has been proposed assuming a small capillary number, and it describes well the conditions of the breakup process [17].

Researches have also been carried out on branching and asymmetric T – junction. Asymmetric droplet formation is the main phenomenon for asymmetric T – junction. Unequal reagent volume through the two arms of the T – junction have a great application in biomedical and life sciences. An investigation has been done on the breakup of the droplet in asymmetric T – junction microchannel with branches of unequal length and same cross-sections and found four modes of droplet breakup, namely primary, transition, bubble, and non-breakups. Droplets of asymmetric sizes are generated in the case in of asymmetric T – junction. To predict the breakup and non - breakup of the droplet-based on the parent droplet size and the capillary number, an empirical correlation is also established [18]. A study of the dissociation and dispersal of droplets at a branching T-junction has also been conducted. The effects of two-phase flow rates,

two-phase Reynolds number, and dispersed phase capillary number on droplet volume distribution have been investigated. Correlations for estimating the volume distribution ratio have also been created [19].

Some of the authors have investigated the droplet breakup process in constricted geometry. Gai et al. [4] investigated experimentally and describes the entire dimensionless group required to visualize the droplet breakup process through a constricted geometry in a concentrated emulsion. Rosenfeld et al. [20] describes the many approaches for recognizing droplet splitting, tracking droplet locations, and characterizing droplet deformations in a concentrated emulsion with a large number of drops (N > 4000). They also discovered that crucial flow rates and droplet deformations exist below which no break-up occurs. Bick et al. [21] evaluated the influence of volume fraction on droplet breakdown in an emulsion flowing through a constriction in a tapered microchannel in an experimental setting. They observed that when the droplet volume fraction goes below 0.50 with constant flow velocity, the breakdown fraction decreases dramatically. The droplet dynamic snap-off mechanism under a brief, sudden constriction has been studied. Two breakup phenomena were observed: I total breakup, ii) partial breakup, and one non-breakup phenomenon. It was also discovered that the droplet's initial size, velocity, and viscosity all have an effect on the breaking process [22]. To further understand the flow characteristics, an experimental study of pressure drop analysis of droplet break-up flow passing through a constriction in a microchannel was carried out. Using pressure drop analysis, the effect of important factors such as surfactant content, fluid flow velocity, and fluid viscosity on droplet break-up was investigated [23].

The aforementioned discussions show that studies on width ratio (branch channel width/main channel width) and branch arm length ratio (right arm length/left arm length) are not explored well. In the present study, a computational investigation has been targeted to reveal the influence of width ratio and arm length ratio on droplet splitting in a microfluidic T -junction. The simulations have been continued by varying width ratio and arm ratio from 1 to 0.25 (1, 0.75, 0.5, 0.25) and 0.4 to 0.9 (0.4, 0.6, 0.9) respectively. The insight physics behind breaking and non – breaking phenomena have been explained with the help of pressure field and velocity field magnitude. The VOF method has been adopted in the simulation. A study on droplet breakup conditions has been done. Mixed flow patterns have been displayed with the help of flow pattern map for the width ratio = 1, 0.75, 0.5, and 0.25. Prediction of simulated pressure gradient has also been made with the help of the Lockhart and Martinelli approach and Dimensional analysis for width ratio = 1.

4.2. COMPUTATIONAL MODEL

A 2D geometry of the microchannel T-junction is considered in simulation. Figure 4.1(a) shows detailed dimensions of the microchannel geometry having an internal diameter of 0.78 mm and length of 120 mm, considered in the present computational work. Oil and water (viscosity ratio: 30.6 and density ratio: 0.84) being introduced into the microchannel through the two shorter arms of a T- junction and are flowing coaxially through the exits having long arms of the T – junction. For the computation purpose, an unsteady state solver has been employed. Figure 4.1 (b) represents meshed geometry of a section as shown in the figure.

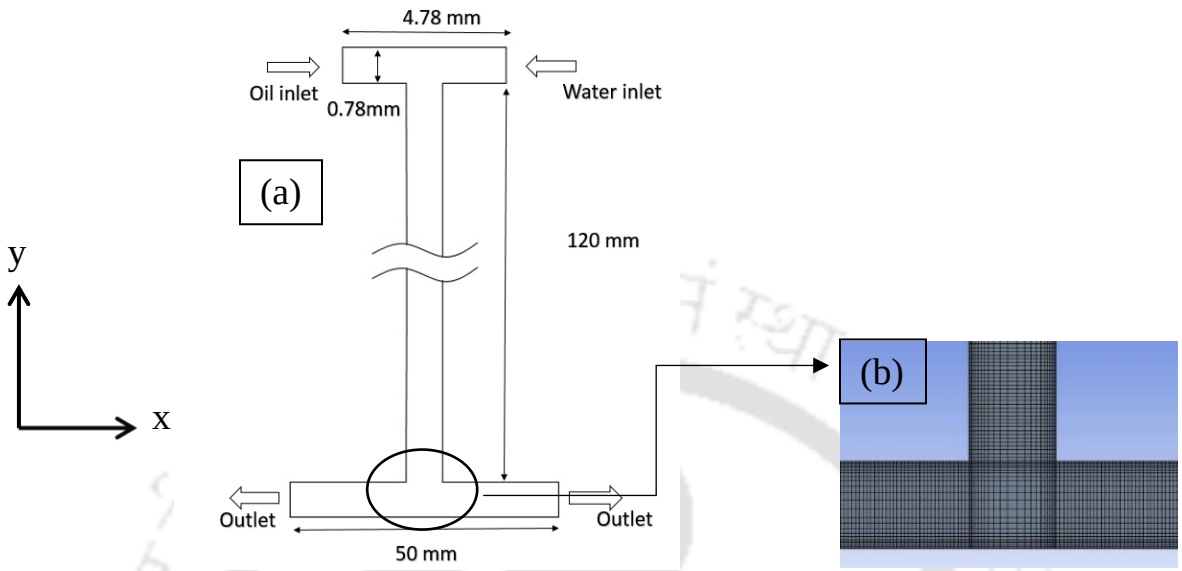

Figure 4.1. (a) Computational domain; and (b) Mesh

Oil and water have been selected as fluid pair for the study and their properties are listed below in the Table 4.1.

Table 4.1. Fluid properties

Fluids Properties	**Water**	**Mineral-Oil (MARCOL 82)**
Density (kg/m^3)	997	843
Viscosity (Pa.s)	0.001	0.0306
Oil – water interfacial tension (N/m)	0.0301	
Contact angle of oil – water on glass (^{0})	51	

4.2.1 Initial and boundary conditions

The channel was first filled with oil, and then water and oil were pumped via the inlets. The operating pressure was set to be equal to the ambient pressure. At the walls, no-slip and impermeable conditions were established. The outflow boundary condition was the pressure outlet (Gauge pressure = 0). The time step was determined by fulfilling the Courant no. The Velocity inlets were as follows:

At x = 22.61 and y = 120.78, $U_x = U_{oil}$ and $U_y = 0$

At x = 27.39 and y = 120.78, $-U_x = U_{water}$ and $U_y = 0$

4.2.2 Convergence, grid independency and model validation

The effect of arm length ratio and width ratio on flow pattern is the main concern of this chapter whereas influence of phase velocity on flow pattern is the main concern of chapter 3. The basic geometry, fluid pair and flow conditions are same in both the cases. So, the grid independence study of this chapter is not done separately. It is considered same as mentioned in chapter 3.

4.3. RESULTS AND DISCUSSIONS

When mineral oil and water flow through the horizontal T-junction microchannel, it turns into droplets flows. Three different types of flow regime i.e. non-breakup, tunnel-breakup, obstructed breakup, have been observed in the present simulation. In order to understand the mechanisms of droplet breakup and non-breakup, the current investigation provides a detailed analysis of the droplet dynamics through the horizontal T-junction microchannel. It includes the

evolution of an interface between dispersed and continuous (water and oil) phases and distribution of pressure, velocity profile. The width ratio (branch channel width/main channel width) has been varied (1, 0.75, 0.5, and 0.25), and its effect on droplet breakup has been examined. The effect of arm length ratio (right arm length/left arm length) on droplet dynamics has also been studied based on varied values (0.4, 0.6, and 0.9) and its effect on droplet breakup is observed. Variation of water (V_w = 0.01, 0.04 m/s) and oil (V_o = 0.18 m/s) velocities, has also been deliberate in both the cases. A study on droplet breakup conditions has been done. Mixed flow patterns have been shown with the help of flow pattern map for the width ratio = 1, 0.75, 0.5, and 0.25. Prediction of simulated pressure gradient has also been done with the help of the Lockhart and Martinelli approach and Dimensional analysis for width ratio = 1. The outcomes of the simulation have been systematically illustrated in the subsequent sections.

4.3.1 Influences of width ratio on droplet breakup dynamics

The effects of width ratio have been inferred based on following set of velocities, i.e. $V_w = 0.01$ *m/s,* $V_o = 0.18$ *m/s.* Width ratios have been changed; keeping the velocities constant**.**

4.3.1.1 Droplet dynamics at different width ratios and velocities set of Vw = 0.01 m/s, Vo = 0.18 m/s

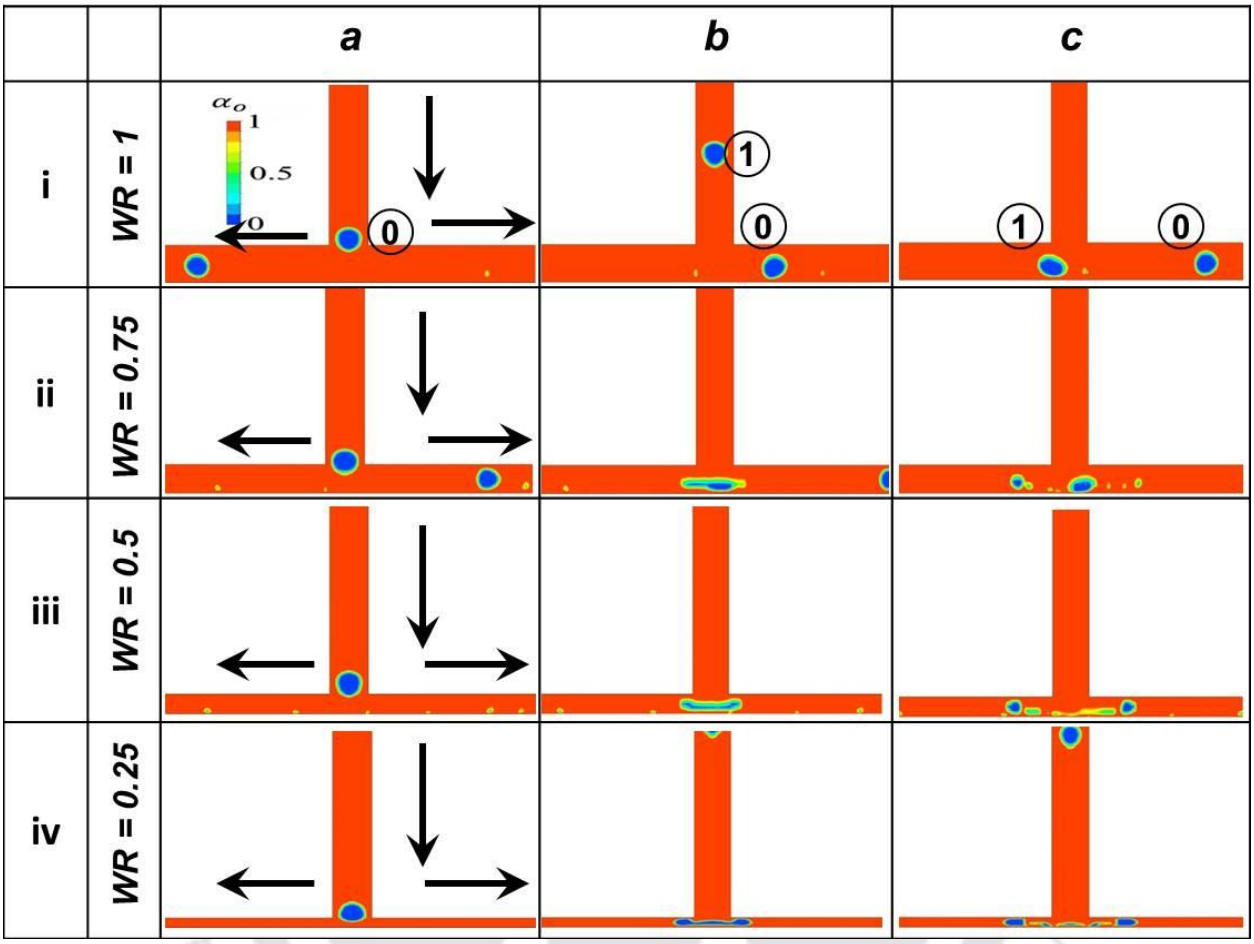

Figure 4.2. Width ratio alters the two-phase flow morphology. Red and blue color represents the volume fraction contour of oil and water respectively. Three columns refer three different locations of the droplets in microchannel along with time of progression at constant phase flow rate (V_w = 0.01 m/s, V_o = 0.18 m/s).

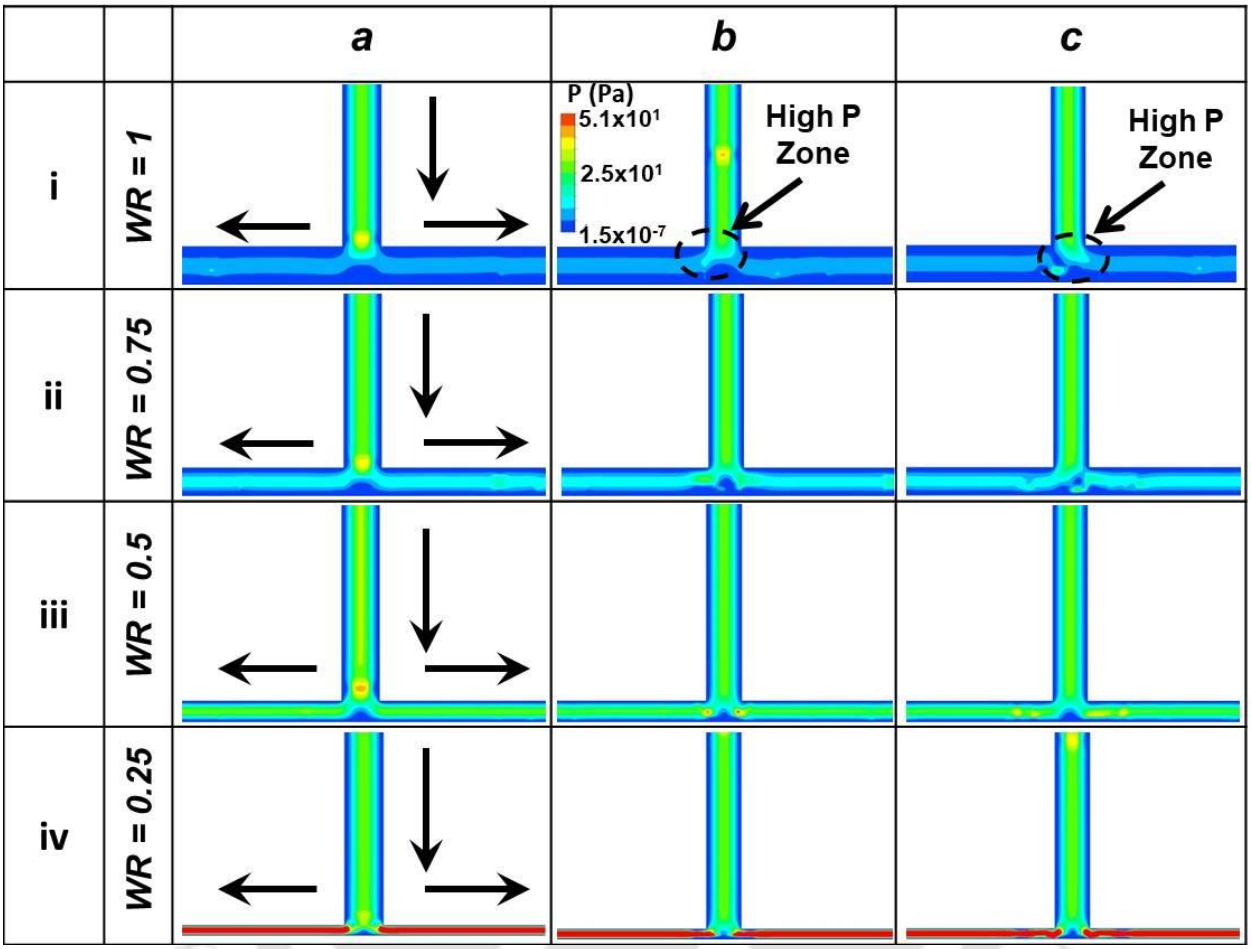

Figure 4.3. Width ratio alters the two-phase flow morphology. Dynamic pressure profile corresponds to Figure 4.2. Three columns refer three different locations of the droplets in microchannel along with time of progression at constant phase flow rate (V_w = 0.01 m/s, V_o = 0.18 m/s).

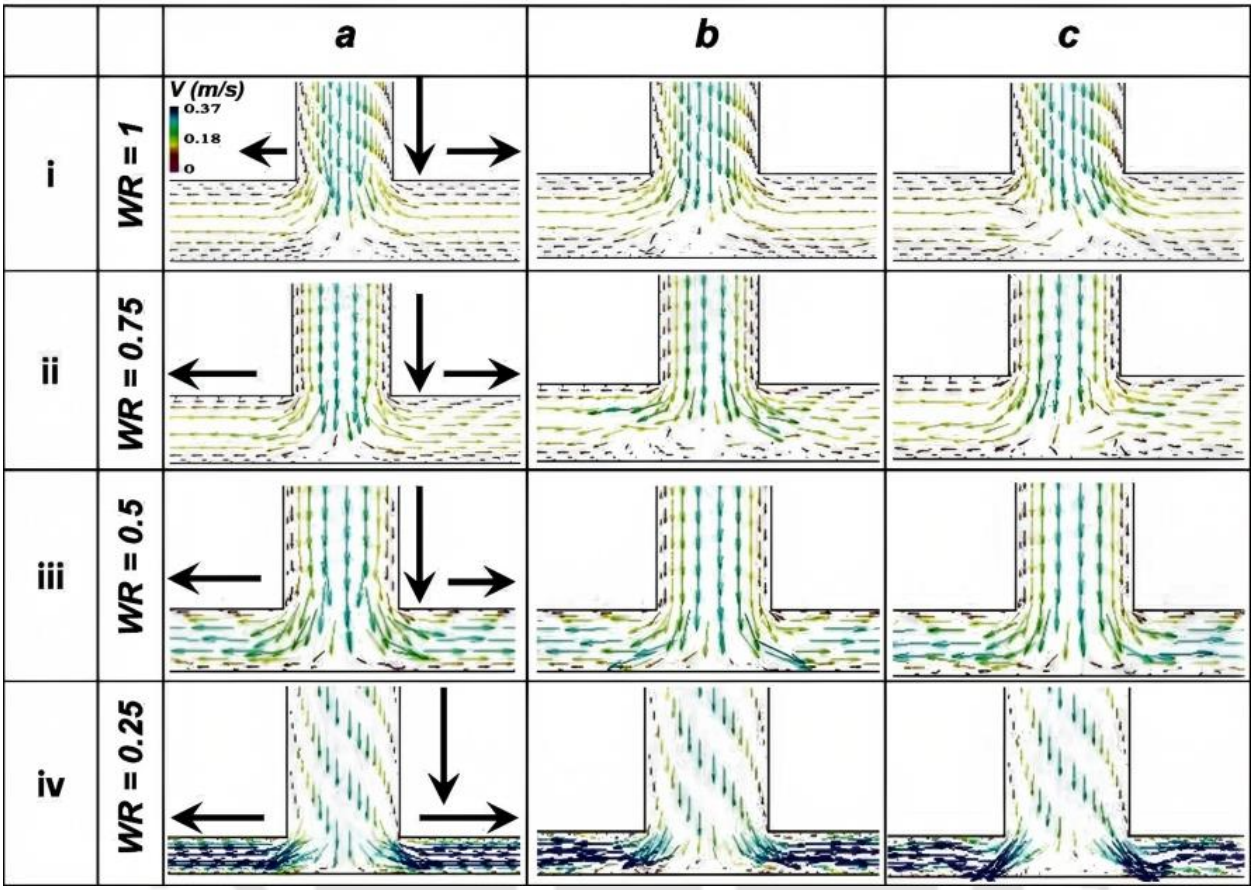

Figure 4.4. Width ratio alters the two-phase flow morphology. Velocity vector profile corresponds to Figure 4.2. Three columns refer three different locations of the droplets in microchannel along with time of progression at constant phase flow rate (V_w = 0.01 m/s, V_o = 0.18 m/s).

In case of width ratio = 1, it has been observed that there is alternate movement of droplets in which the droplets are not splitting into the fragments or daughter droplets (Figure 4.2ia, 4.2ib, 4.2ic). When the droplet 0 is at a position just above the T-junction (Figure 4.2ia), there is high incoming upstream pressure coming towards the droplet (Figure 4.3ia). After reaching at the junction, it steers to the right hand side due to high pressure zone development in

the left hand side (Figure 4.3ib). The continuous phase velocity helps in the movement of the droplet 0 into the right hand side supported by the velocity vectors (Figure 4.4ib). When droplet 1 reaches the junction, it steers to the left hand side due to high pressure zone development in the right hand side (Figure 4.3ic). The continuous phase velocity helps in the movement of the droplet 1 into the left hand side supported by the velocity vectors (Figure 4.4ic).

In case of width ratio = 0.75, bifurcation with tunnel is observed in which the droplets get bifurcated into two daughter droplets with gap exist between upper tip of the elongated droplet and the upper inner walls of the arms of the T-junction. The droplet is pushed towards the T-junction due to high incoming upstream pressure (Figure 4.3iia). The green color in the channel indicates that there exists high pressure zone (Figure 4.3iia). When the droplet hit the opposite wall of the T – junction with that pressure, it becomes dumbbell shape from bullet shape. When the shear force of the lubricating film acting on the droplet is comparable to the interfacial tension, then a vortex flow is formed (Figure 4.4iib) at the base of the droplet. This vortex flow helps the dumbbell shape droplet to come to the outlets. The vortices are formed in a zone of high pressure. Also, The accumulated upstream pressure helps to get narrow the neck and finally induces the pinch – off the neck (Figure 4.2iic).

In case of width ratio = 0.5, bifurcation with tunnel is observed in which the droplets get bifurcated into two daughter droplets with gap exist between upper tip of the elongated droplet and the upper inner walls of the arms of the T-junction. When the droplet is at a position just above the T-junction (Figure 4.2iiia), there is high incoming upstream pressure coming towards the droplet (Figure 4.3iiia) due to which it reaches the T-junction. The green color in the channel indicates that there exists high pressure zone (Figure 4.3iiia). When the droplet hit the opposite

wall of the T – junction with that pressure, it becomes dumbbell shape from bullet shape. When the shear force of the lubricating film acting on the droplet is comparable to the interfacial tension, then a vortex flow is formed (Figure 4.4iiib) at the base of the droplet. This vortex flow helps the dumbbell shape droplet to come to the outlets. The vortices are formed in a zone of high pressure. Also, The accumulated upstream pressure helps to get narrow the neck and finally induces the pinch – off the neck (Figure 4.2iiic).

When the width ratio is equal to 0.25, bifurcation with obstruction is observed in which the droplets are bifurcated into two daughter droplets with a negligible gap between the upper tip of the elongated droplet and the upper inner walls of the T-junction arms. This flow regime has three distinct stages, namely, i) Extension ii) Squeeze and iii) Pinch-off. These three stages are also present in bifurcation with tunnel flow. In the extension stage, the bullet-shaped water droplet passing through the main channel approaches towards the T-junction and gets elongated due to shear forces acting in the annular space between the channel wall and surface of the droplet (Figure 4.2iva). The existence of shear force is well supported by intense pressure (Figure 4.3iva) and velocity profile (Figure 4.4iva). The vortex shown in Figure 4.4ivb pulls the elongated droplet towards the junction area away from the main channel. After reaching the junction, the droplet is squeezed due to the upstream pressure and vortex field. Now the droplet is so deformed that it takes double tumbled shape (Figure 4.2ivb) and occupies the maximum area of the channel. So the flow of the continuous phase (oil) is obstructed, and pressure is accumulated in the junction area (Figure 4.3ivb). As a result, the shear force cannot overcome the surface force, but the accumulated pressure field forces the deformed droplet in a complete

pinch-off (Figure 4.2ivc). So the combined effect of larger droplet size, pressure accumulation, and occurrence of vortices at the T-junction causes the bifurcation with obstruction.

It has been observed that, with the decrease of the width ratio, the breakup tendency increases.

4.3.2 Influence of arm length ratio (right arm length/left arm length) on droplet breakup dynamics at constant width ratio (WR = 1) and velocities set (*Vw = 0.04 m/s, Vo = 0.18 m/s*)

The effects of arm length ratio have been inferred based on one set of velocities, i.e. V_w = *0.04 m/s,* V_o = *0.18 m/s.* Initially, arm length ratios have been changed; keeping the velocities constant.

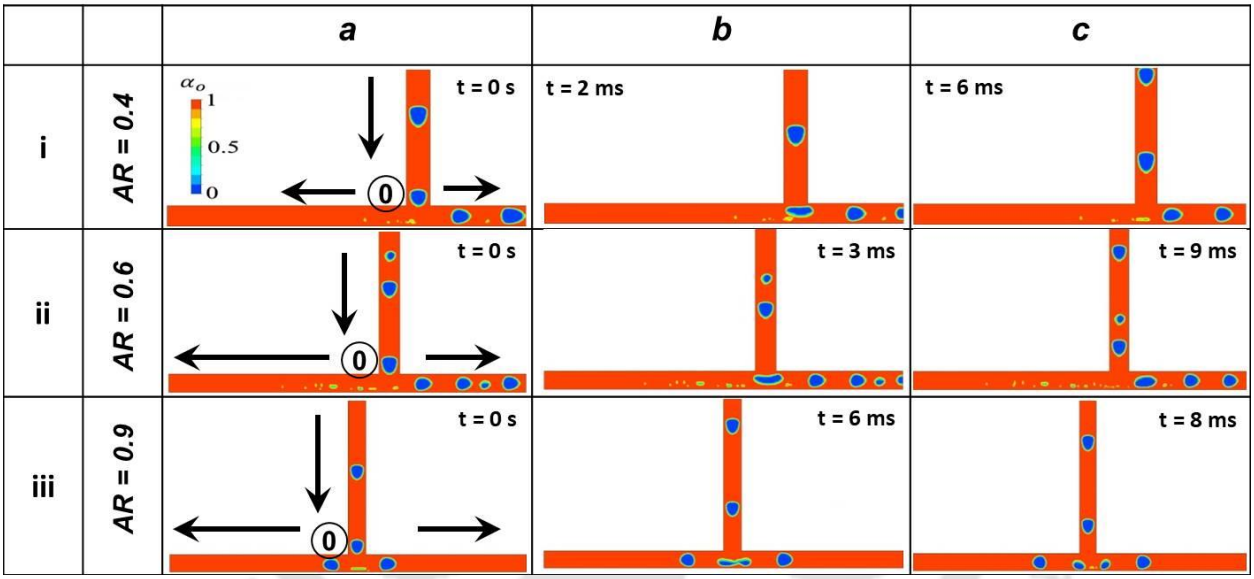

Figure 4.5. Arm length ratio alters the two-phase flow morphology. Red and blue color represents the volume fraction contour of oil and water respectively. Three columns refer three different locations of the droplets in microchannel along with time of progression at constant phase flow rate (V_w = 0.04 m/s, V_o = 0.18 m/s).

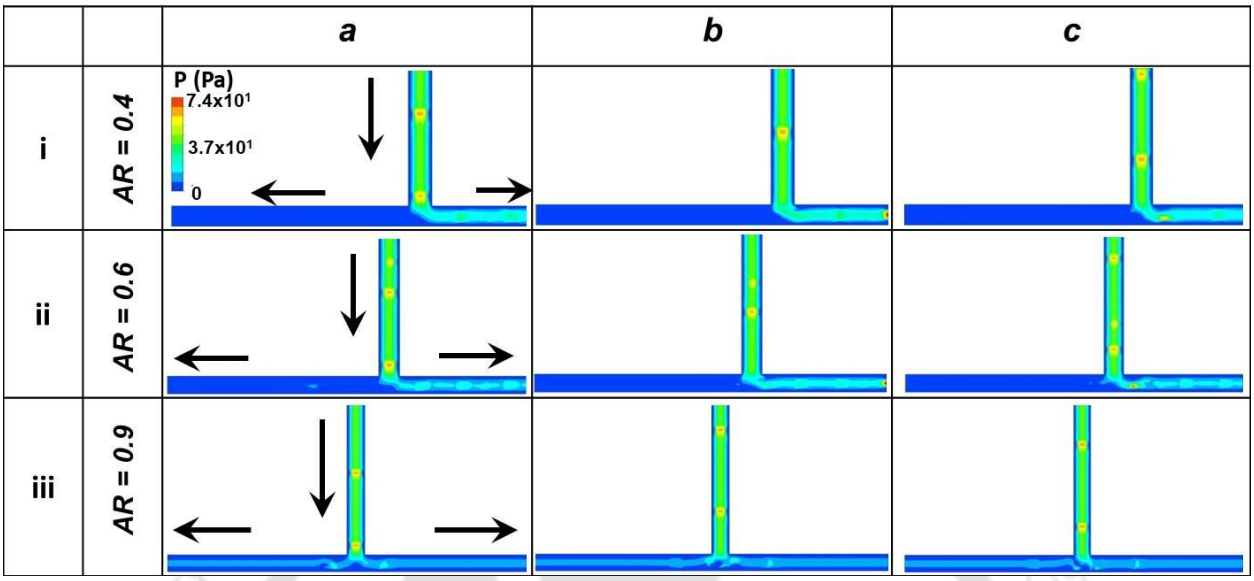

Figure 4.6. Arm length ratio alters the two-phase flow morphology. Dynamic pressure profile corresponds to Figure 4.5. Three columns refer three different locations of the droplets in microchannel along with time of progression at constant phase flow rate (V_w = 0.04 m/s, V_o = 0.18 m/s).

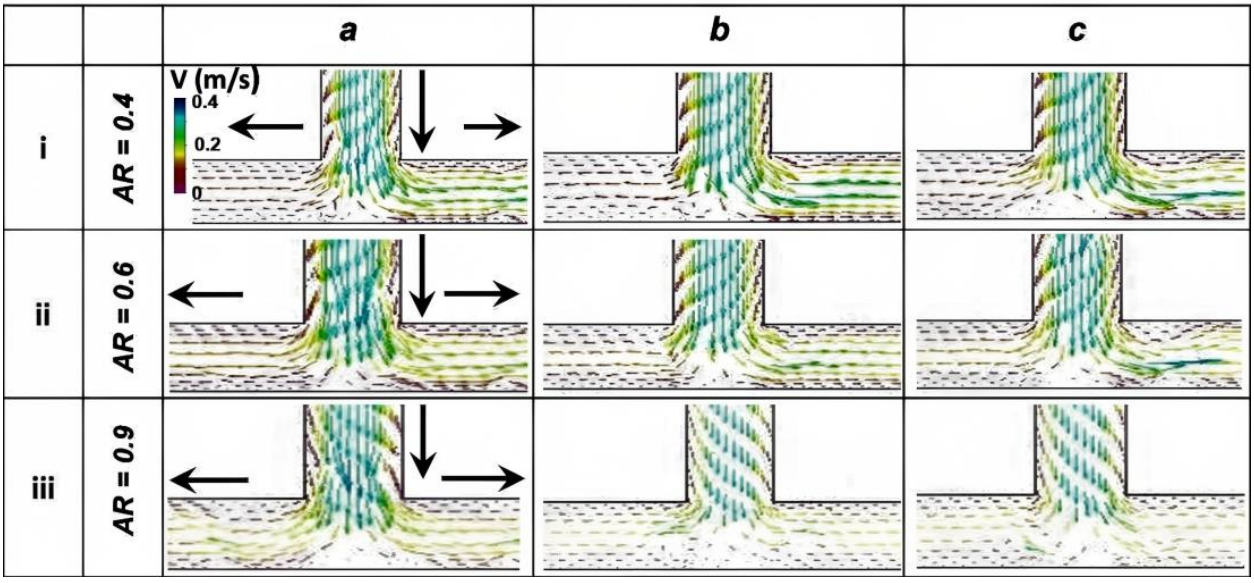

Figure 4.7. Arm length ratio alters the two-phase flow morphology. Velocity vector profile corresponds to Figure 4.5. Three columns refer three different locations of the droplets in microchannel along with time of progression at constant phase flow rate (V_w = 0.04 m/s, V_o = 0.18 m/s).

In case of arm length ratio = 0.4 and 0.6, the droplets do not bifurcate and pass through the right hand arm of the microchannel. From dynamic pressure contour we get that, there is relative high pressure zone on the right arm of the microchannel. We can say that there is pressure difference between left and right arm of the microchannel. The velocity of the continuous phase is also high on the right arm of the microchannel.

In case of arm length ratio = 0.9, the droplets bifurcate and the daughter droplets pass through both the arms of the microchannel. From Figure 4.6iiia, 4.6iiib and 4.6iiic, we can say that there is no pressure difference between the left and right arm of the microchannel. The velocity of the continuous phase is moderate on both the arms of the microchannel.

With the increase of the arm length ratio, it has been observed that the tendency of the bifurcation increases.

4.3.3 Droplet breakup condition

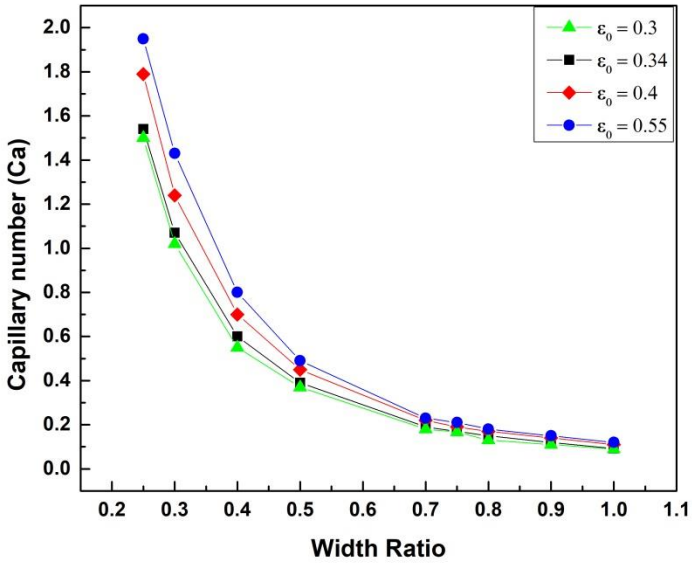

Figure 4.8. Capillary number vs. width ratio for $\varepsilon_0 = 0.3$, $\varepsilon_0 = 0.34$, $\varepsilon_0 = 0.4$ and $\varepsilon_0 = 0.55$

Figure 4.8 represents a graph between width ratio and capillary number, $Ca = \frac{\mu_c U}{\sigma}$, μ_c is the viscosity of continuous phase, U is the mixer velocity, and σ is the interfacial tension, which has been plotted to draw the details of the droplet breakup condition based on initial extension (ε_0). The initial extension can be defined as $\left(\frac{l_0}{\pi w_0}\right)$, where l_0 is the length of the droplet before reaching the T-junction and w_0 is the width of the droplet before reaching the T-junction. The black line corresponds to initial extension (ε_0) = 0.34 for the velocity (V_w = 0.01 m/s, V_o = 0.18 m/s), the red line corresponds to initial extension (ε_0) = 0.4 for the velocity (V_w = 0.04 m/s, V_o =

0.18 m/s), the green line corresponds to initial extension (ε_0) = 0.3 for the velocity (V_w = 0.005 m/s, V_o = 0.18 m/s) and the blue line corresponds to initial extension (ε_0) = 0.55 for the velocity (V_w = 0.06 m/s, V_o = 0.18 m/s). The capillary number is calculated for width ratios of (0.25, 0.3, 0.4, 0.5, 0.7, 0.75, 0.8, 0.9, and 1.0). Link et al.[6] concluded in his work that for initial extension $\varepsilon_0 > 1$, the droplets always break. But in the present work it is observed that the droplets also bifurcate for initial extension value, ε_0 = 0.3, 0.34, 0.4 and 0.55. This plot gives the idea of a critical width ratio at which droplet starts to break at a particular ε_0. At constant initial flow rate, viscous forces becoming stronger at a particular width ratio. It tells which width ratio is required to split a droplet. Also, it tells that with increase in the initial extension the critical breakup width ratio also increases and the corresponding capillary number decreases. For initial extension of 0.3, 0.34, 0.4 and 0.55, breakup starts from width ratio of 0.5 (Ca = 0.37), 0.7 (Ca = 0.19), 0.8 (Ca = 0.17), and 0.9 (Ca = 0.15) respectively.

4.3.4 Mixed flow regimes and flow pattern map

Mixed flow regimes are flow phenomena in which the droplets exhibit new patterns in their motions rather than only breakdown and non-breakup when they approach the T-junction. For example, the coalescence of two droplets then bifurcates into two droplets or remains as a single droplet and steers to one direction, etc. Various mixed flow regimes were found for width ratio = 1, 0.75, 0.5 and 0.25. Flow pattern maps have been developed through which the mixed flow regimes are displayed for all the width ratios. Two dimensionless quantities, namely capillary number (Ca) and mixer Reynolds number (Re_m), have been displayed on the X- and Y-

axes, respectively, to create a generalized flow pattern map and extract the essential characteristics. Figure 4.9, Figure 4.10, Figure 4.11, and Figure 4.12 represents the flow pattern maps for width ratio 1, 0.75, 0.5 and 0.25 respectively.

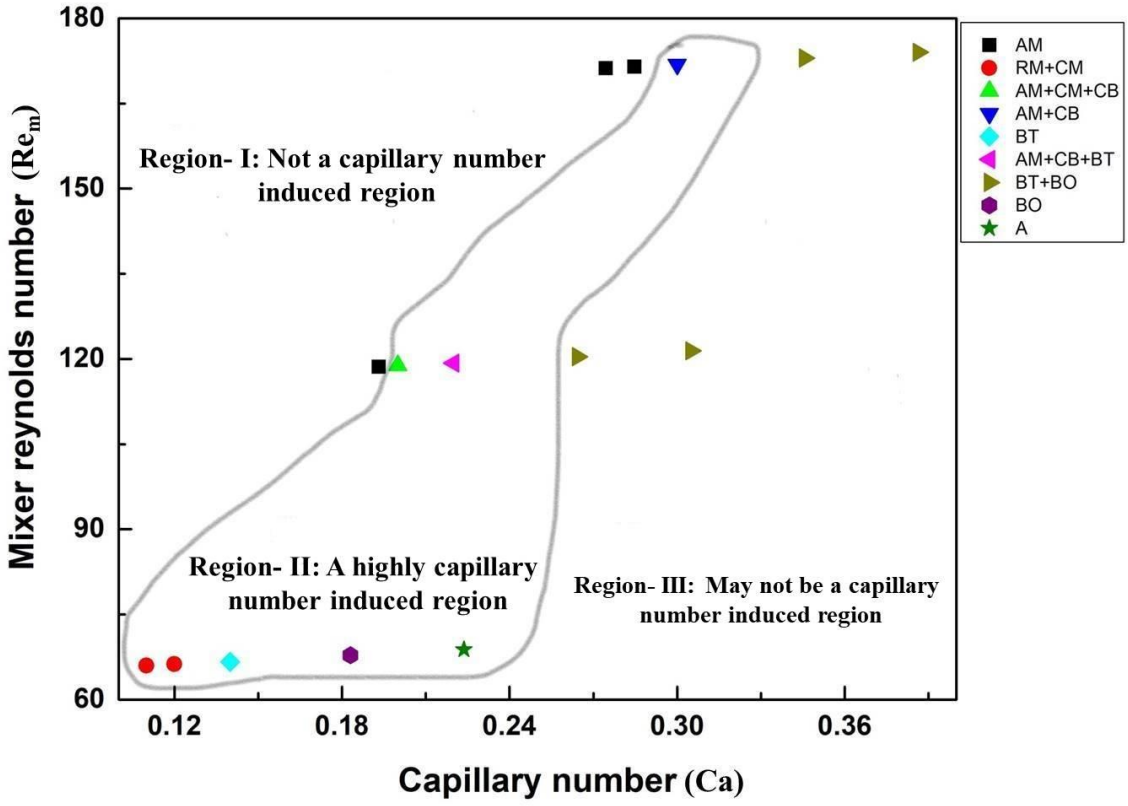

Figure 4.9. Flow pattern map for width ratio = 1—Capillary number (Ca) vs mixer Reynolds number (Re_m): AM alternate movement of droplets, RM random movement of droplets, CM two droplets coalesce and move in one direction, CB two droplets coalesce and bifurcate, BT bifurcation with the tunnel, BO bifurcation with obstruction, A annular flow

This flow pattern map shows the three distinct regions:

a) Region- I: There is no capillary number induced area. At constant mixer Reynolds number, the flow patterns exhibit little change with capillary number. The alternating movement of droplets (AM) is prevalent in this case.

b) Region- II: A highly capillary number induced region. A strongly capillary number induced area in which flow patterns show variation with the capillary number at constant mixer Reynolds number. In this region, mixed flow patterns have been observed. Alternate movement of droplets + two droplets coalesce and bifurcate (AM+CB), alternate movement of droplets + two droplets coalesce and move in one direction + two droplets coalesce and bifurcate (AM+CM+CB), Alternate movement of droplets + two droplets coalesce and bifurcate + bifurcation with the tunnel (AM+CB+BT), random movement of droplets + two droplets coalesce and move in one direction (RM+CM) , bifurcation with the tunnel (BT), bifurcation with obstruction (BO), annular flow (A) are the dominating flow patterns.

c) Region- III: It's possible that this isn't a capillary number-induced area. At constant mixer Reynolds number, the flow pattern may shift with capillary number. A combined flow is discovered, namely Bifurcation with tunnel + Bifurcation with obstruction (BT+BO).

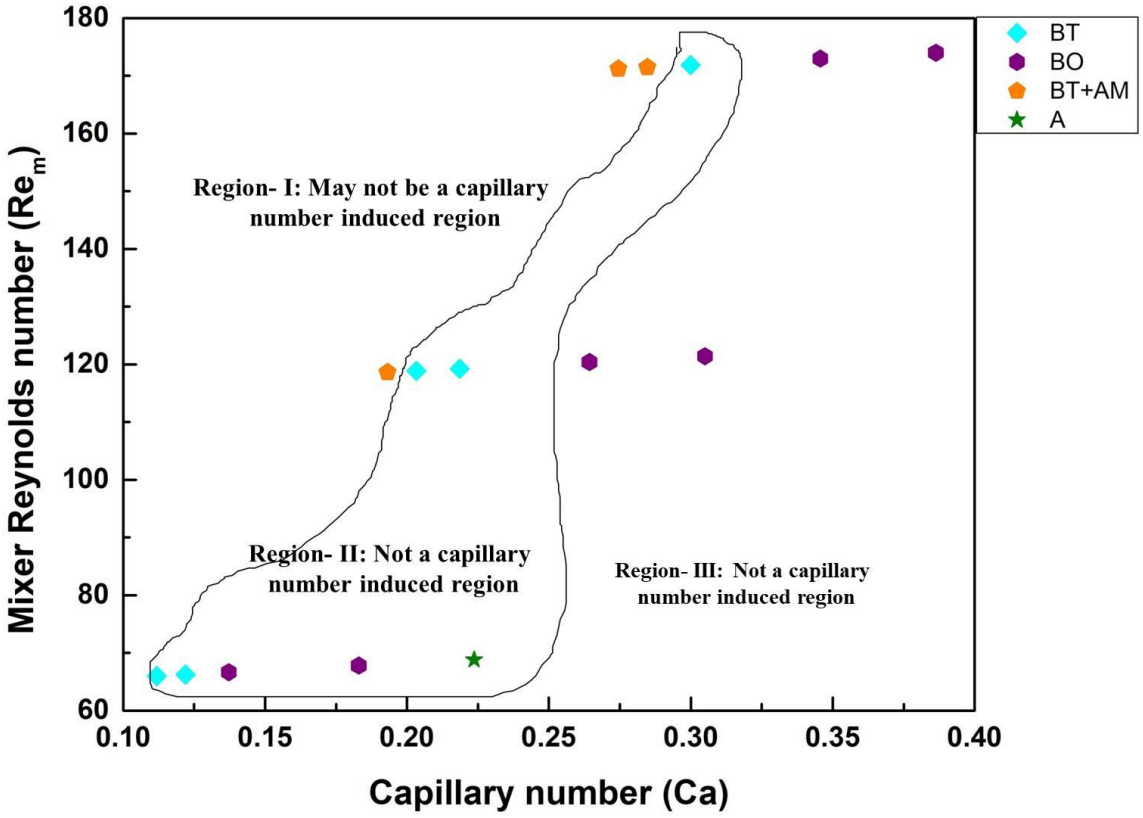

Figure 4.10. Flow pattern map for width ratio = 0.75 - Capillary number (Ca) vs mixer Reynolds number (Re_m): AM alternate movement of droplets, BT bifurcation with the tunnel, BO bifurcation with obstruction, A annular flow

This flow pattern map shows the three distinct regions:

a) Region- I: It's possible that this isn't a capillary number-induced area. At a fixed mixer Reynolds number, the flow pattern may alter with the capillary number. A combined flow is discovered, namely Bifurcation with the tunnel + Alternate movement (BT+AM).

b) Region- II: There is no capillary number induced area. At constant mixer Reynolds number, the flow patterns exhibit little change with capillary number. The dominant flow patterns here are bifurcation with tunnel (BT), bifurcation with obstruction (BO), and annular flow (A).

c) Region- III: There is no capillary number induced area. At constant mixer Reynolds number, the flow patterns exhibit little change with capillary number. Here, only one regime - bifurcation with obstruction (BO) is found.

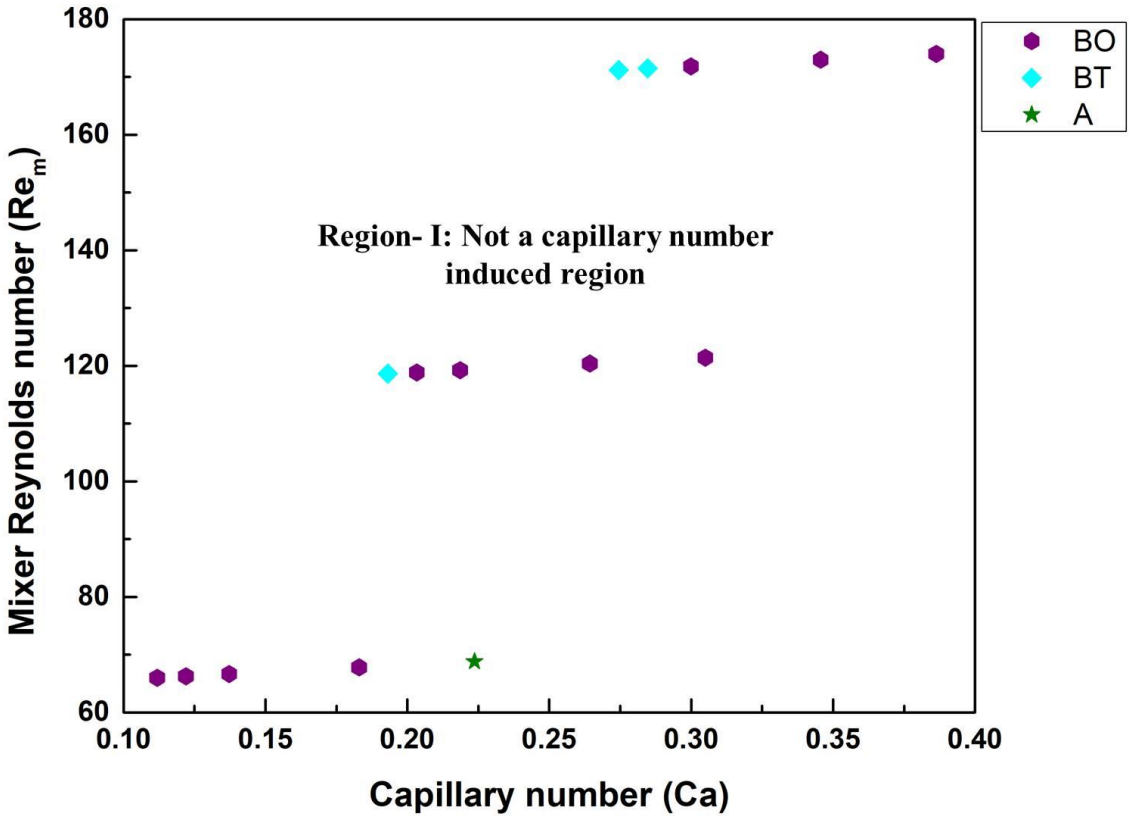

Figure 4.11. Flow pattern map for width ratio = 0.5 - Capillary number (Ca) vs mixer Reynolds number (Re_m): BT bifurcation with the tunnel, BO bifurcation with obstruction, A annular flow

In this flow pattern map, the whole region is Not a capillary number induced region. Bifurcation with obstruction (BO), bifurcation with tunnel (BT) and annular flow (A) are found here.

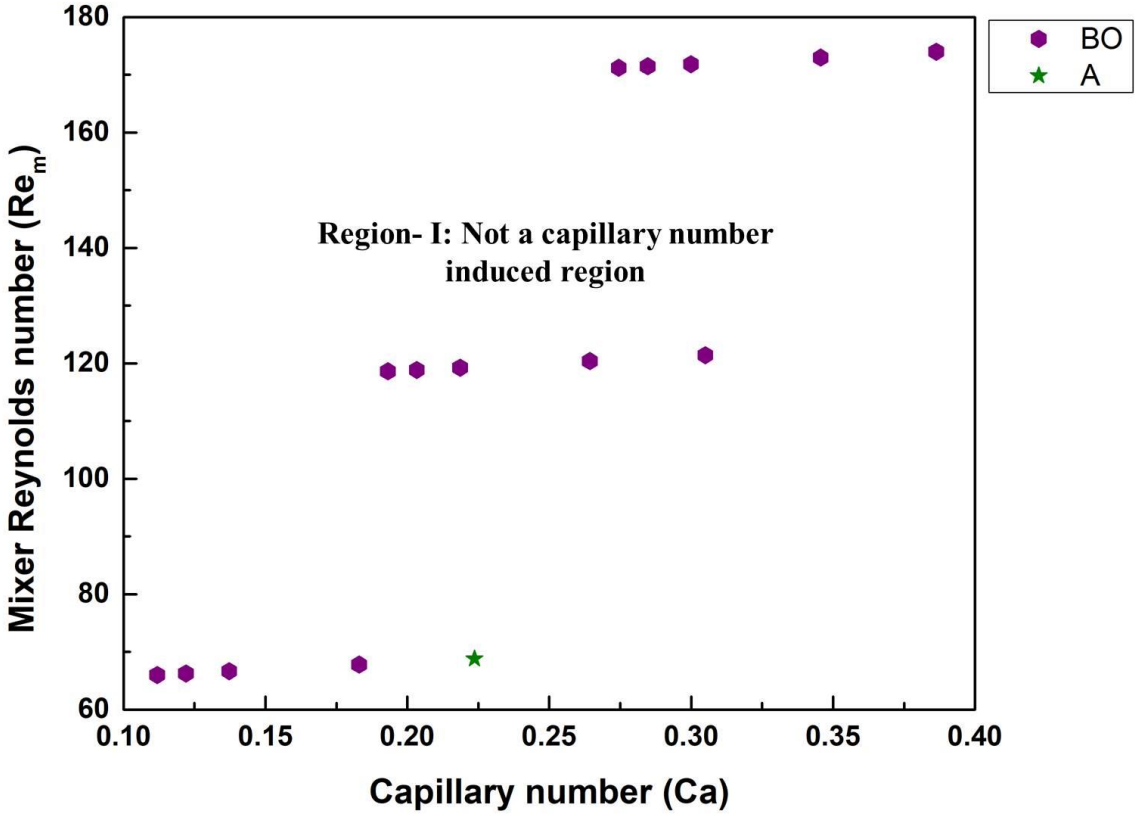

Figure 4.12. Flow pattern map for width ratio = 0.25 - Capillary number (Ca) vs mixer Reynolds number (Re_m): BO bifurcation with obstruction, A annular flow

In this flow pattern map, the whole region is Not a capillary number induced region. Bifurcation with obstruction (BO) and annular flow (A) are dominating flow patterns here.

In Figure 4.9, bifurcation with tunnel + bifurcation with obstruction (BT+BO) occur at high mixer Reynolds number and capillary number and occupy a broader map area. Alternate movement of droplets (AM) occurs at high mixer Reynolds number and low to moderate capillary number and occupies a moderate map area. The mixed flow regime comprises of a) Alternate movement of droplets + two droplets coalesce and bifurcate (AM+CB), b) alternate movement of droplets + two droplets coalesce and move in one direction + two droplets coalesce and bifurcate (AM+CM+CB), c) Alternate movement of droplets + two droplets coalesce and bifurcate + bifurcation with the tunnel (AM+CB+BT), d) random movement of droplets + two droplets coalesce and move in one direction (RM+CM) , e) bifurcation with the tunnel (BT), f) bifurcation with obstruction (BO), g) Annular flow (A). Annular flow (A) occurs at low mixer Reynolds number and moderate capillary number.

In Figure 4.10, bifurcation with obstruction (BO) occurs at high mixer Reynolds number and capillary number and fills a larger map area. Bifurcation with tunnel + alternating droplet movement (BT+AM) occurs at high mixer Reynolds number and low to moderate capillary number, and occupies a moderate map area. Bifurcation with tunnel (BT) occurs at low to high mixer Reynolds numbers and low to moderate capillary numbers and takes up a modest plot area. Annular flow (A) occurs when the mixer Reynolds number is low and the capillary number is modest.

In Figure 4.11, bifurcation with obstruction (BO) happens when the mixer Reynolds number and capillary number are low to high, and it fills a larger map area. Bifurcation with tunnel (BT) happens when the mixer Reynolds number is high and the capillary number is low to moderate, and it fills a modest map area. Annular flow (A) occurs when the mixer Reynolds number is low and the capillary number is modest.

In Figure 4.12, at low to high mixer Reynolds number and capillary number, bifurcation with obstruction (BO) occurs and occupies the whole map. Annular flow (A) occurs when the mixer Reynolds number is low and the capillary number is modest.

4.4. LOCKHART AND MARTINELLI APPROACH

Martinelli parameter (X) has been evaluated from the single-phase pressure drop calculation, which is as follows:

$$X^2 = \frac{\phi_g^2}{\phi_l^2} = \frac{\left(\frac{dp}{dx}\right)_l}{\left(\frac{dp}{dx}\right)_g} \tag{4.4.1}$$

Where

$$\phi_l^2 = \frac{\left(\frac{dp}{dx}\right)_{tp}}{\left(\frac{dp}{dx}\right)_l} \tag{4.4.2}$$

And

$$\phi_g^2 = \frac{\left(\frac{dp}{dx}\right)_{tp}}{\left(\frac{dp}{dx}\right)_g} \tag{4.4.3}$$

Where g and l denote the gas and liquid phase, respectively

Single-phase pressure gradient is calculated using the standard formula of pressure gradient as

$$\left(\frac{dp}{dx}\right) = \left(\frac{2f\rho u^2}{D}\right)$$
$$f = \frac{16}{\mathrm{Re}} \quad for \quad \mathrm{Re} < 2100 \tag{4.4.4}$$
$$f = \frac{0.079}{\mathrm{Re}^{0.25}} \quad for \quad \mathrm{Re} > 2100$$
$$\mathrm{Re} = \frac{Dv\rho}{\mu}$$

Where f, ρ, μ, D, and v are friction factor, density, viscosity, diameter, and velocity of fluids.

A graph has been plotted between ϕ^2_w and 1/X as shown in Figure 4.13. Then the predicted pressure gradient for the T-junction having width ratio = 1 and internal diameter of 0.78 mm is obtained from the equation of the curve (ϕ^2_w = 24.117*(1/X)^2+20.03*(1/X)-5.68), where $\phi^2_w = [(dp/dx)_{tp}/(dp/dx)_w]$. Percentage deviation between predicted and simulated pressure gradient is calculated. The average absolute error is coming out to be 52%, given in Figure 4.14.

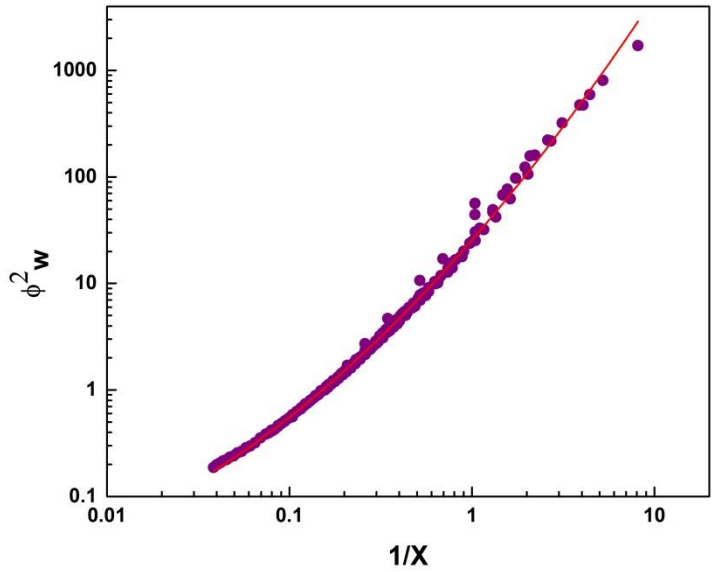

Figure 4.13. Plot between ϕ^2_w and 1/X

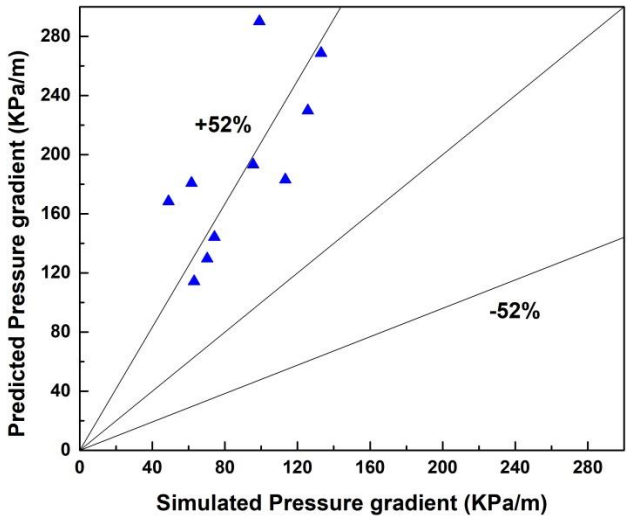

Figure 4.14. Comparison between predicted and simulated pressure gradient using Lockhart and Martinelli approach

4.5. DIMENSIONAL ANALYSIS

4.5.1 Set up

Dimensional analysis has been set up for general two-phase flow (both the liquid are immiscible to each other) through a T-junction having a width ratio = 1 and internal diameter of 0.78mm. The first step in dimension analysis is to list all the parameters and then state their dimensions with respect of mass 'm', length 'l', and time 't'. Schematic of T-junction is shown in Figure 4.15.

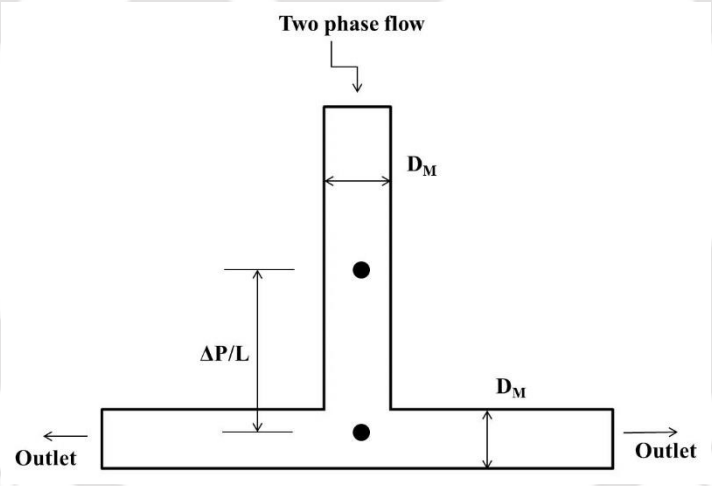

Figure 4.15. Schematics of the T-junction

The list that will be analyzed is:

ΔP/L (i.e. the pressure gradient from upstream to downstream)	(m/l^2t^2)
U_m (Mixed velocity)	(l/t)
ρ_m (Mixed density)	(m/l^3)

μ_m (Mixed viscosity) (m/lt)

σ (i.e. interfacial tension) (m/t^2)

D_M (i.e. internal diameter of the main channel and branch channel) (l)

e (Roughness factor) (l)

Here, $U_m = V_o + V_w$ (V_o = oil velocity and V_w = water velocity)

ρ_m = (Hold up of water phase * Density of water) + (Hold up of oil phase * Density of oil)

μ_m = (Viscosity of oil + Viscosity of water)/ ((Viscosity of water * Mass fraction of water) + (Viscosity of oil * Mass fraction of oil))

4.5.2 Procedure

There are seven parameters listed i.e. "n" = 7. There are three primary parameters i.e. length (l), mass (m) and time (t) i.e. “m” = 3.

So, number of independent groups = 7-3 = 4

So, $f(\Pi_1, \Pi_2, \Pi_3, \Pi_4) = 0$

Where, f is some function, or in an alternate expression:

$\Pi_1 = f_1(\Pi_2, \Pi_3, \Pi_4)$

where f_1 is some function different to function f .

Taking an arbitrary choice of three parameters: ρm, U_m, D_M

Group 1: $\Pi_1 = \{(\rho_m)^a, (U_m)^b, (D_M)^c\} (\Delta P/L)$

$$\{(m/l^3)^a, (l/t)^b, (l)^c\}\ (m/l^2t^2) = m^0l^0t^0$$

m: a+1 = 0 ; l: -3a+b+c-2 = 0 ; t: -b-2 = 0

or, a = -1 or, c = 1 or, b = -2

a = -1, b = -2, c = 1

therefore, $\Pi_1 = \{(\rho_m)^{-1}, (U_m)^{-2}, (D_M)^1\}\ (\Delta P/L)$

$= (D_M/ \rho_m U^2_m)(\Delta P/L)$

By similar procedures the rest of the groups can be derived:

Group 2: $\Pi_2 = \{(\rho_m)^{-1}, (U_m)^{-1}, (D_M)^{-1}\}\ (\mu_m) = \mu_m / \rho_m D_M U_m$

Group 3: $\Pi_3 = \{(\rho_m)^{-1}, (U_m)^{-2}, (D_M)^{-1}\}\ (\sigma) = \sigma / \rho_m D_M U^2_m$

Group 4: $\Pi_6 = \{(\rho_m)^0, (U_m)^0, (D_M)^{-1}\}\ (e) = e/D_M$

Therefore, we have

$$\frac{\Delta P}{L}\left(\frac{D_M}{\rho_m U_m^2}\right) = \lambda\left(\frac{\mu_m}{\rho_m U_m D_M}\right)^a\left(\frac{\sigma}{\rho_m U_m^2 D_M}\right)^b\left(\frac{e}{D_M}\right)^c \qquad (4.5.2.1)$$

This is the pressure gradient in terms of the dimensionless group.

Where λ, a, b and c are constants. These constants are evaluated from multiple regression analysis in Microsoft Excel using our own simulated data. From this analysis we have estimated λ = 0.008, a = 0.4, b = 0.34, c = 0. Therefore, Eq. (4.5.2.1) becomes

$$\frac{\Delta P}{L} = 0.008\left(\frac{\mu_m}{\rho_m U_m D_M}\right)^{0.4}\left(\frac{\sigma}{\rho_m U_m^2 D_M}\right)^{0.34}\left(\frac{\rho_m U_m^2}{D_M}\right) \quad (4.5.2.2)$$

The regression coefficient and standard error of Eq. (4.5.2.2) are found to be 0.9 and 0.2 respectively. The dimensional analysis has predicted the simulated pressure gradient data for width ratio = 1 with an average error of 4.3 %, as shown in Figure 4.16. It is better than the prediction estimated by Lockhart and Martinelli approach. The present correlation is applicable within the range of Mixer Reynolds number of 15-130 and capillary number in the range of 0.04-0.71.

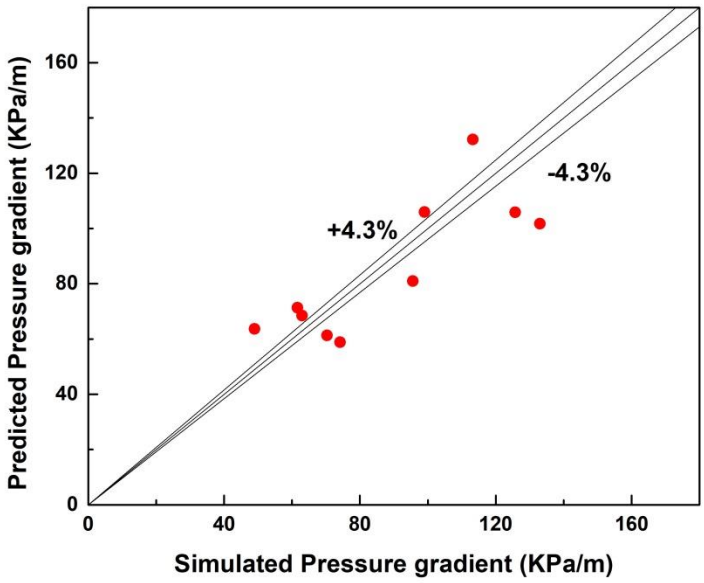

Figure 4.16. Comparison between simulated and predicted pressure gradient using Eq. (4.5.2.2)

4.6. SUMMARY

In this study, the 2D-CFD simulation has been carried out to investigate the influence of width ratio and arm length ratio on droplet splitting. The model has been validated with the previous experimental data present in the literature [24]. The tunnel breakup and the obstructed breakup are mainly due to the pressure difference in the branch channel and the direction of the velocity vectors which are towards the branch's exit and the pressure swing phenomenon is the reason behind the alternate movement of the droplets. Breakup with tunnel is found in WR = 0.75, 0.5, breakup with obstruction is found in WR = 0.25 and alternate movement is found in WR = 1 for Vw = 0.01 m/s, Vo = 0.18 m/s. It has been found that breakup tendency increases as

we decrease the width ratio (1, 0.75, 0.5, and 0.25) and increase the arm length ratio (0.4, 0.6, and 0.9). Droplet breakup condition has been revealed based on initial extension. Flow pattern maps have been developed through which the mixed flow regimes and other flow regimes are displayed for all the width ratios (1, 0.75, 0.5, and 0.25). Mainly three distinct regions are found: i) Not a Ca induced region ii) Highly Ca induced region iii) May be Ca induced region. Prediction of simulated pressure gradient for width ratio = 1 has been made through Lockhart and Martinelli approach, and a percentage deviation of 52% has been found. Dimensional analysis has also been done for width ratio = 1 and 4.3 % of average error is found between predicted and simulated pressure gradient, which is better than Lockhart and Martinelli approach.

REFERENCES

1. Ding, Y., Howes, P.D., and deMello, A.J., Recent advances in droplet microfluidics, *Analytical chemistry*, 2019, vol. 92, no. 1, pp. 132-149.
2. Bedram, A. and Moosavi, A., Numerical Investigation of Droplets Breakup in a Microfluidic T-Junction, *Applied Mechanics and Materials*, 2012, vol. 110-116, no. pp. 3269-3277.
3. Fei, Y., Zhu, C., Fu, T., Gao, X., and Ma, Y., The breakup dynamics of bubbles stabilized by nanoparticles in a microfluidic Y-junction, *Chemical Engineering Science*, 2021, vol. 245, no. pp. 116867.
4. Gai, Y., Khor, J.W., and Tang, S.K.Y., Confinement and viscosity ratio effect on droplet break-up in a concentrated emulsion flowing through a narrow constriction, *Lab on a Chip*, 2016, vol. 16, no. 16, pp. 3058-3064.
5. Deka, D.K., Boruah, M.P., Pati, S., Randive, P.R., and Mukherjee, P.P., Tuning the Splitting Behavior of Droplet in a Bifurcating Channel through Wettability–Capillarity Interaction, *Langmuir*, 2020, vol. 36, no. 35, pp. 10471-10489.
6. Link, D.R., Anna, S.L., Weitz, D.A., and Stone, H.A., Geometrically Mediated Breakup of Drops in Microfluidic Devices, *Physical Review Letters*, 2004, vol. 92, no. 5, pp. 054503.
7. Qian, J.-y., Li, X.-j., Wu, Z., Jin, Z.-j., and Sunden, B., A comprehensive review on liquid–liquid two-phase flow in microchannel: Flow pattern and mass transfer, *Microfluidics and Nanofluidics*, 2019, vol. 23, no. 10, pp. 1-30.

8. Ozdalgic, B., Ustun, M., Dabbagh, S.R., Haznedaroglu, B.Z., Kiraz, A., and Tasoglu, S., Microfluidics for microalgal biotechnology, *Biotechnology and Bioengineering*, 2021, vol. 118, no. 4, pp. 1716-1734.

9. Madadelahi, M., Madou, M.J., Nokoorani, Y.D., Shamloo, A., and Martinez-Chapa, S.O., Fluidic barriers in droplet-based centrifugal microfluidics: Generation of multiple emulsions and microspheres, *Sensors and Actuators B: Chemical*, 2020, vol. 311, no. pp. 127833.

10. Dressler, O.J., Casadevall i Solvas, X., and DeMello, A.J., Chemical and biological dynamics using droplet-based microfluidics, *Annual Review of Analytical Chemistry*, 2017, vol. 10, no. pp. 1-24.

11. Lu, H., Caen, O., Vrignon, J., Zonta, E., El Harrak, Z., Nizard, P., Baret, J.-C., and Taly, V., High throughput single cell counting in droplet-based microfluidics, *Scientific reports*, 2017, vol. 7, no. 1, pp. 1-9.

12. Liu, X., Zhang, C., Yu, W., Deng, Z., and Chen, Y., Bubble breakup in a microfluidic T-junction, *Science Bulletin*, 2016, vol. 61, no. 10, pp. 811-824.

13. Chen, Y. and Deng, Z., Hydrodynamics of a droplet passing through a microfluidic T-junction, *Journal of Fluid Mechanics*, 2017, vol. 819, no. pp. 401-434.

14. Wu, L.-Y., Liu, L.-B., Han, X.-T., Li, Q.-W., and Yang, W.-B., Numerical simulation on dynamic behaviors of bubbles flowing through bifurcate T-junction in microfluidic device, *Chin. Phys. B*, 2019, vol. 28, no. 10, pp. 104702.

15. Bedram, A. and Moosavi, A., Droplet breakup in an asymmetric microfluidic T junction, *The European Physical Journal E*, 2011, vol. 34, no. 8, pp. 78.

16. Samie, M., Salari, A., and Shafii, M.B., Breakup of microdroplets in asymmetric T junctions, *Physical Review E*, 2013, vol. 87, no. 5, pp. 053003.

17. Ménétrier-Deremble, L. and Tabeling, P., Droplet breakup in microfluidic junctions of arbitrary angles, *Physical Review E*, 2006, vol. 74, no. 3, pp. 035303.

18. Cheng, W.L., Sadr, R., Dai, J., and Han, A., Prediction of Microdroplet Breakup Regime in Asymmetric T-Junction Microchannels, *Biomedical Microdevices*, 2018, vol. 20, no. 3, pp. 72.

19. Ma, P., Fu, T., Zhu, C., and Ma, Y., Asymmetrical breakup and size distribution of droplets in a branching microfluidic T-junction, *Korean Journal of Chemical Engineering*, 2019, vol. 36, no. 1, pp. 21-29.

20. Rosenfeld, L., Fan, L., Chen, Y., Swoboda, R., and Tang, S.K.Y., Break-up of droplets in a concentrated emulsion flowing through a narrow constriction, *Soft Matter*, 2014, vol. 10, no. 3, pp. 421-430.

21. Bick, A.D. and Tang, S.K.Y., Effect of volume fraction on droplet break-up in an emulsion flowing through a microfluidic constriction, *Applied Physics Letters*, 2019, vol. 115, no. 9, pp. 093702.

22. Li, Z., Gu, Z., Li, R., Wang, C., Chen, C., Yu, C., Zhang, Y., Shu, Q., and Su, J., Investigation on droplet dynamic snap-off process in a short, abrupt constriction, *Chemical Engineering Science*, 2021, vol. 235, no. pp. 116496.

23. Liang, X., Wang, X., Lu, S., Wang, K., and Luo, G., Pressure drop analysis for the droplet break-up flow in a locally constrictive microchannel, *Chemical Engineering Science*, 2021, vol. 230, no. pp. 116190.

24. Salim, A., Fourar, M., Pironon, J., and Sausse, J., Oil–water two-phase flow in microchannels: Flow patterns and pressure drop measurements, *The Canadian Journal of Chemical Engineering*, 2008, vol. 86, no. 6, pp. 978-988.

CHAPTER 5

NUMERICAL APPRAISAL ON LIQUID-LIQUID TWO-PHASE FLOW IN A FLOW-FOCUSING SYSTEM

Chapter 5a

TWO-DIMENSIONAL SIMULATION OF DRIPPING AND JETTING FLOW IN A FLOW-FOCUSING GEOMETRY

ABSTRACT

2D simulations have been performed to investigate flow regimes in a flow-focusing geometry by changing the dispersed phase and continuous phase velocities. The dispersed phase is the Polydimethylsiloxane (PDMS), and the continuous phase is the water. Simulations have been performed in a range of oil-water viscosity ratio $\left(\frac{\mu_o}{\mu_w}\right)$ from 3-50, interfacial tension ranges from 0.0118-0.002 N/m. The walls of the microchannel are considered to be PMMA surfaces. The contact angle (θ) of an oil droplet in the presence of water wetting the PMMA surface is 140°. Two types of flow regimes, namely dripping and jetting, were observed in our study by changing the dispersed phase and continuous phase velocities. The sequential time steps of void fraction contour have been presented to explore the mechanism of droplet formation. The droplet pinch-off ~~time~~ and jet growth time have been calculated for dripping and jetting regime respectively. The outcomes are summarized in the form of flow pattern map at a viscosity ratio of 12 and interfacial tension of 0.0118 N/m, which shows the transition boundary between dripping and jetting phenomena. The simulated transition boundary gives good agreement with the analytical solution available in the literature. The effect of oil-water viscosity ratio and interfacial tension on droplet size is also investigated. These findings will help to understand different flow regimes and its transition in a flow focusing geometry and will have direct application in the microfluidic platform-based devices. The idea of the manuscript matches with the scope of the journal as it is based on multiphase flow using 2D simulations.

5a.1. INTRODUCTION

Droplet-based microfluidics in immiscible fluids is one of the emerging fields in recent years due to its wide application in medicine [1], food [2], tissue engineering [3], cell therapy [4]. With this approach, one may regulate cell size and monodispersity while eliminating the need to immunize medicines during cell culture. They can quickly isolate cells from the external environment. Microdroplets can be created using two methods: I) Active technique II) Passive technique [5]. In active technique, the droplet is generated using external forces like electrical, magnetic forces, or thermal energies. The passive techniques include the geometry of the channel and the flow hydrodynamics. There are several configurations through which microdroplets can be created, such as T-junction, co-flow, flow-focusing, and some variations [6]. Shear force is used in these geometries in order for droplets to be broken down. A variety of flow regimes may be seen, such as squeezing, dripping, jetting, and continuous regimes. In order to forecast the different flow regimes based on the flow parameters, researchers have employed multiphase numerical simulation. Momentum and continuity are used as governing equations to determine the interface in the multiphase numerical simulation. Multiphase flow may be modeled using a variety of approaches, including the volume of fluid (VOF) model, the level set method (LS), the phase-field method, and the lattice Boltzmann method [7]. Some of the authors have investigated both experimentally and numerically the various factors which influence the droplet formation in a flow-focusing geometry.

Yobas et al. [8] investigated the droplets generation in a flow-focusing geometry. For water-in-oil droplets, they generated over 10^4 droplets per second, and for oil-in-water droplets, they generated over 10^3 droplets per second. Increase in droplet diameter and formation

frequency are attributed to an increasing flow rate of the continuous phase. Both experiments and numerical simulations of droplet generation in flow-focusing geometry have been done here. Effects of three-dimensional circular orifices and two-dimensional rectangular constrictions within the flow-focusing device were compared. 2D rectangular geometry produces bigger droplets with a lower frequency than 3D circular geometry as, discovered by Ong et al. [9]. Lu et al.[10] investigated the breakup dynamics of the gas-liquid interface for Taylor bubble formed in a microfluidic flow-focusing geometry. Studies have shown a power-law relationship between the minimum diameter of a gaseous thread and the liquid viscosity, along with the time less than the ultimate pinch-off. There are radial and axial variations to the surface and azimuthal curvature. During bubble formation, interfacial force is responsible for the growth of the gas-liquid surface. These values are determined by liquid viscosity. Numerical investigation on droplet generation in a microfluidic flow-focusing device has been done using the level set method. The size of the droplets increases as the flow rate increases, while the frequency of the droplets decreases. Droplet size is reduced, and frequency rises as phase viscosity increases. Interfacial tension increases droplet size, and frequency decreases with increasing interfacial tension.[11] Droplet size in a CFF (Co-axial Flow Focusing) device has been numerically investigated in terms of flow rates, viscosities, interfacial tension, and nozzle and orifice sizes. Using a wide variety of non-dimensional variables, a correlation is established that accurately predicts the droplet size with less than 15% error. Smaller droplets result from lower interfacial tension and higher viscosity of the continuous phase fluid. On the other hand, higher fluid viscosity of the dispersed phase and greater nozzle diameter may cause larger droplets. Droplet diameter also increases with a higher dispersed phase flow rate. In case of droplet size, orifice

length is less important than orifice radius when the orifice length is the same [12]. Experiments were done on the breakup dynamics of semi-dilute polymer solutions in a flow-focusing microchannel. PEO (Poly (ethylene oxide)) solutions that have been semi-diluted produce similar breakdown morphology to those that have been diluted. The transition time between two regimes may be estimated by analyzing the temporal variability of extensional strain rates. An increase in extensional viscosity is caused by strain hardening and results in delayed breaking [13]. A numerical investigation on double emulsion formation in a hierarchical flow-focusing channel was done using a free-energy ternary lattice Boltzmann model. To do this, they calculated the capillary counts of fluids in the inner (Ca_i), mid-phase (Ca_m) and outer-phase (Ca_o) phases. Ca_i and Ca_m can be altered in different ways in the two-step formation region to produce distinct morphologies. The researchers also observed that the ratio of interfacial tension might have a substantial influence on the form of the droplets in emulsions. Channel geometry has a considerable impact on changes in formation regimes and double emulsion sizes [14]. Iqbal et al. [15] used numerical simulation to investigate the influence of intersection angle and wettability on droplet formation in a microfluidic flow-focusing device. It was observed that the size of the droplets increases as the flow rate ratios rise. A high flow rate ratio and increased contact angles create large diameter droplets. The biggest droplets are produced by the form with perpendicular intersection angles. Soroor et al. [16] investigated the droplet generation process by developing numerical and experimental methods. A flow-focusing droplet generator was built using numerical simulation. Using the 2D phase-field method, a newly designed microfluidic device's manufacturing process was predicted before it was manufactured. There were less than five percent of simulations that were different from the experiments. An extensive range of flow rate

ratios was used to model and build the device. A possible application of this study's findings is the determination of the best flow regime for minimizing shear stress on cells while increasing droplet frequency and monodispersity. Chekifi et al. [17] investigated the breakup of air bubbles in the flow-focusing configuration using CLSVOF. There is an inverse relationship between dispersed phase viscosity and bubble size. Moreover, the bubble's volume varies inversely with orifice size.

In view of the above discussions, learning of the fundamental aspects of liquid-liquid two-phase flow in flow focusing geometry is limited. So, the present work aims on a numerical study to explore the effect of phase velocities and fluid properties on flow regime in a 2D flow-focusing geometry. The dispersed phase is the PDMS oil (polydimethylsiloxane), and the continuous phase is the water. Simulations were performed in a wide range of oil-water viscosity ratio $\left(\frac{\mu_o}{\mu_w} = 3-50\right)$ and interfacial tension (0.0118-0.002 N/m). The walls of the microchannel are considered to be PMMA surfaces. In presence of water, the contact angle (θ) of an oil droplet with PMMA surface is 140°. The simulated results revealed two flow regimes – I) Dripping and II) Jetting. Dripping and jetting phenomena with sequential time steps are presented to explore the insight of the droplet formation. The droplet pinch-off time and jet growth time has been calculated for dripping and jetting regime respectively. The outcomes are summarized in the form of flow pattern map to indicate the transition boundary between dripping and jetting phenomena. The simulated transition boundary is in well agreement with the analytical solution available in the literature. The effect of oil-water viscosity ratio and interfacial tension on droplet size is also investigated.

5a.2. COMPUTATIONAL MODEL

5a.2.1. Geometry, initial and boundary conditions

The solution domain consists of a horizontal 2D flow-focusing microchannel. Figure 5a.1a shows the dimensions of the computational domain's geometry. Three inlets (each of 0.6 mm in length) and a main channel make up the complete geometry. Figure 5a.1b depicts the optimum mesh size of the flow-focusing geometry in its corresponding dimensional space. The optimum mesh was achieved through grid independency study as discussed in the next section.

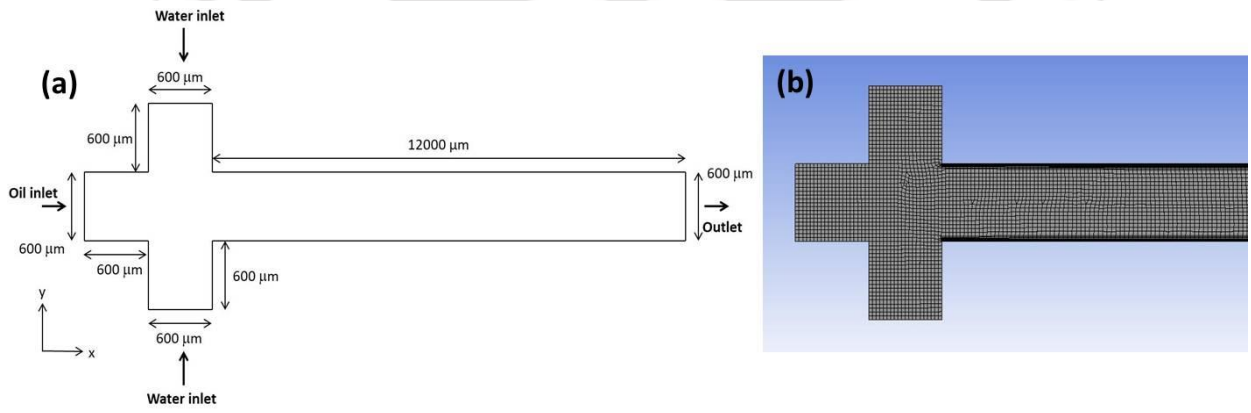

Figure 5a.1. a) Computational domain b) Mesh

Water (continuous phase) occupied the channel at first, and subsequently, oil (dispersed phase) and water passed through the inlets. Atmospheric pressure was selected as ~~the~~ operating pressure. $u_x = u_{oil}$ and $u_y = 0$, $-u_y = 0$ at the oil inlet, and $u_y = u_{water}$, $-u_y = u_{water}$, and $u_x = 0$ at the water inlet. Impermeable and non-slip characteristics were imposed on the walls. The gauge pressure at the outflow was 0 Pa. Time intervals were set based on Courant's number in computational process.

The properties of two phases namely Polydimethylsiloxane (PDMS) and water have been enlisted below in Table 5a.1.

Table 5a.1. Fluid properties

Fluids Properties	**Water**	**Polydimethylsiloxane (PDMS)**
Density (kg/m3)	997	920
Viscosity (mPa.s)	0.92	11
PDMS-water interfacial tension (N/m)	0.0118	
Contact angle of PDMS on PMMA in water (^{o})	140	

5a.2.2. Grid independence, code verification, and validation

Using three different quadrilateral mesh (4742, 9628, and 14371 cells), a grid independence study was conducted to determine the optimal grid size (Figure 5a.2). Optimum grid size was confirmed based on the minimum % deviation of dimensionless droplet length (L/W_c) with respect to literature data reported by Fu et al. [18]. The computational results were converged across (10^{-5}) time steps. There was a residual of 10^{-3} for both the continuity and velocity function. Figure 5a.2 represents comparison of the simulated data with the experimental data of Fu et al. [18]. X and Y axis represent continuous phase velocity and dimensionless

droplet length (L/Wc) respectively at oil flow rate (Q_o) of 100 µL/min. The plot indicates that the values obtained from the 14371 cells are closer to the experimental data. For detailed analysis, values were extracted and compared in in Table 5a.2. Mesh with 14371 cells confirms a deviation of 2.7 %, which is the lowest among three. The deviation of grid with 9628 and 4742 cells are 5.4 % and 8.1 % respectively. So, in this respect, we have chosen grid with 14371 cells.

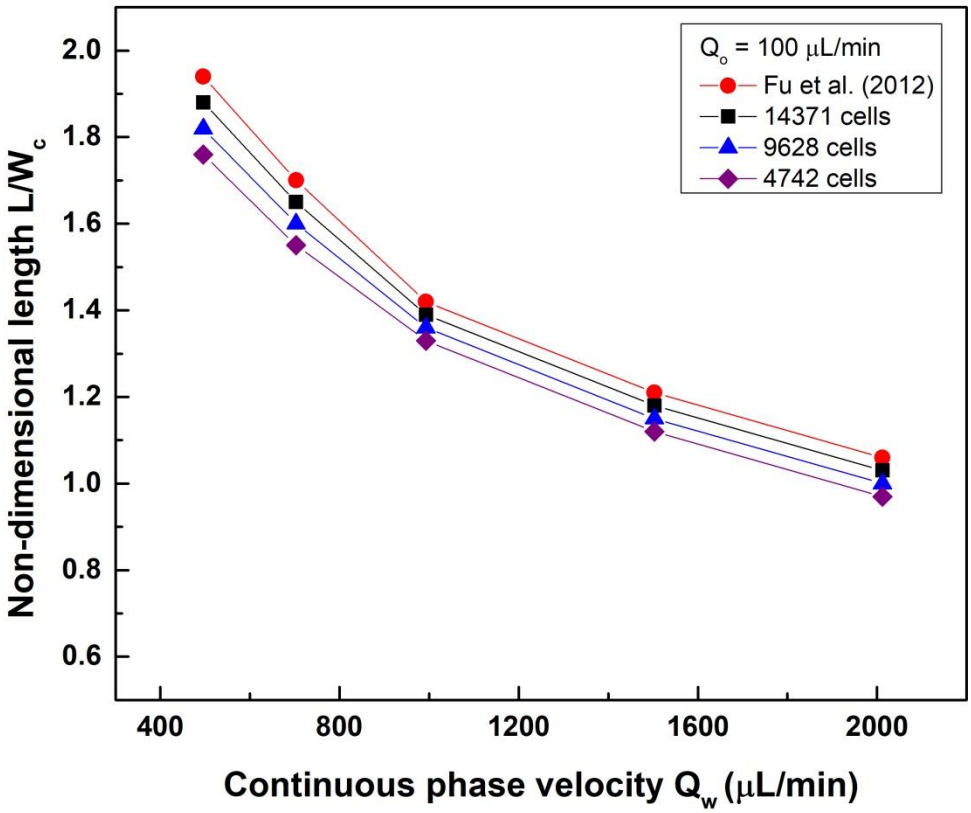

Figure 5a.2. Plot for grid independency study with mesh of 4742, 9628 and 14371 cells. Red symbols represents experimental data taken from Fu et al. [18]. Purple, blue and black symbols indicate results obtained from mesh having cells of 4742, 9628 and 14371 cells respectively

Table 5a.2. Comparisons of experimental dimensionless droplet length with simulated results obtained from the different grid's sizes

Grid	**No. of cells**	**Experimental L/W_c**	**Simulated L/W_c**	**Percentage deviation** $\left(\frac{Exp-Sim}{Exp}\right)\times 100$
Grid-1	4742	1.94	1.76	9.3
		1.7	1.55	8.8
		1.42	1.33	6.3
		1.21	1.12	7.4
		1.06	0.97	8.5
			Average error	***8.1***
Grid-2	9628	1.94	1.82	6.2
		1.7	1.6	5.9
		1.42	1.36	4.2
		1.21	1.15	5.0
		1.06	1	5.7
			Average error	***5.4***

Grid-3	14371	1.94	1.88	3.1
		1.7	1.65	2.9
		1.42	1.39	2.1
		1.21	1.18	2.5
		1.06	1.03	2.8
			Average error	***2.7***

The solver code has been verified against the analytical equation for flow between parallel plates when both the plates are fixed which is presented below:

$$U = \frac{1}{2\mu}\left(\frac{-\partial P}{\partial X}\right)\left(By - y^2\right)$$

Where,

B = Distance between the plates

y = Distance of point from one of the plate

μ = Dynamic viscosity of continuous fluid

$$U_{\max}\left(at\ y = \frac{B}{2}\right) = \frac{1}{8\mu}\left(\frac{-\partial P}{\partial X}\right)B^2$$

So, $$\frac{U}{U_{\max}} = 4\left(\frac{y}{B}\right)\left(1 - \frac{y}{B}\right) \qquad (5a.2.2.1)$$

A comparison is shown in Figures 5a.3. Figure 5a.3 depicts a velocity profile at the section A-A as marked in the Figure 5a.3a, which is placed a little far from the nose of the droplet. The graphic depicts a parabolic velocity profile, which is particularly evident in the event of a fully developed flow, as well as a velocity profile computed using a benchmark problem (equation 5a.2.2.1). We have plotted normalized velocity and radial distance from the center along the X and Y axis respectively (Figure 5a.3b). The figure gives a good agreement between two.

Figure 5a.4a and 5a.4b depicts us streamline function contour for continuous phase and dispersed phase respectively. They both notify us about formation of curl at the junction of flow-focusing geometry at t = 0.25 s. This formation of curl accords with the results of Fu et al. [19].

This confirms the verification of the code with a higher accuracy.

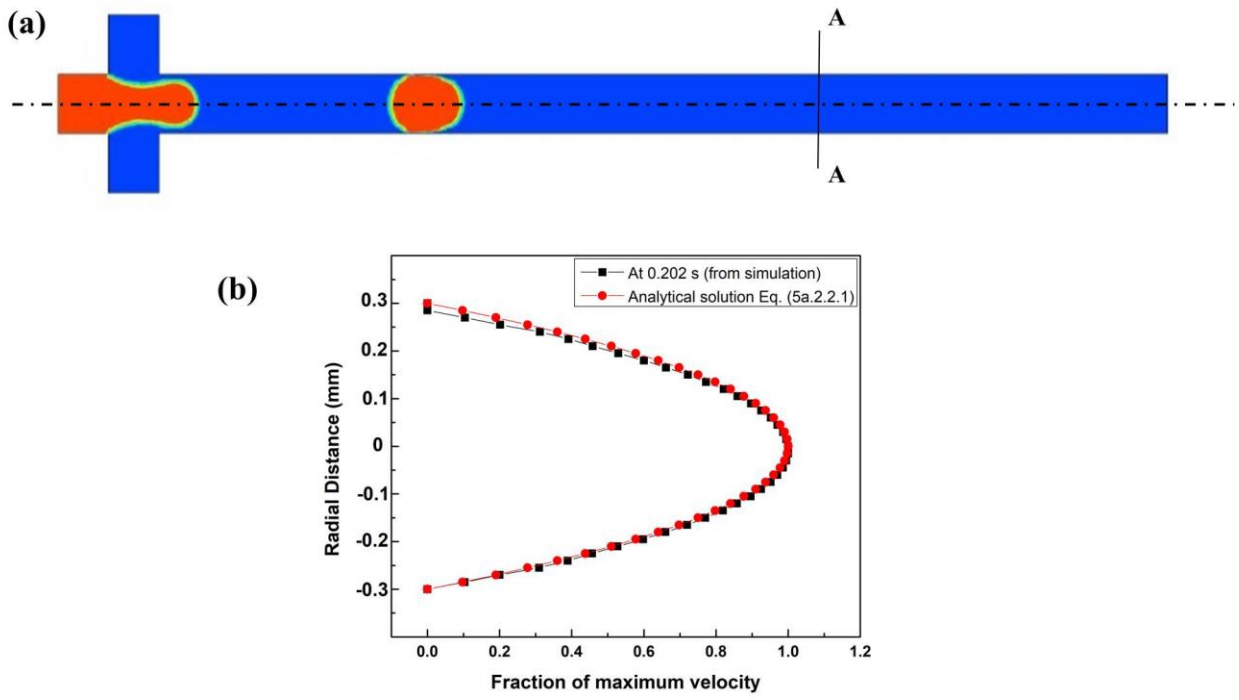

Figure 5a.3. Velocity profile at the section A-A confirms the code verification. The profile has been captured at a time step of 0.202 s: a, Sectional plane (A-A) along with volume fraction contour; and b, Black color represents the parabolic velocity profile captured from simulation and red color represents the parabolic velocity profile obtained from analytical equation for flow between parallel plates when both the plates are fixed (5a.2.2.1)

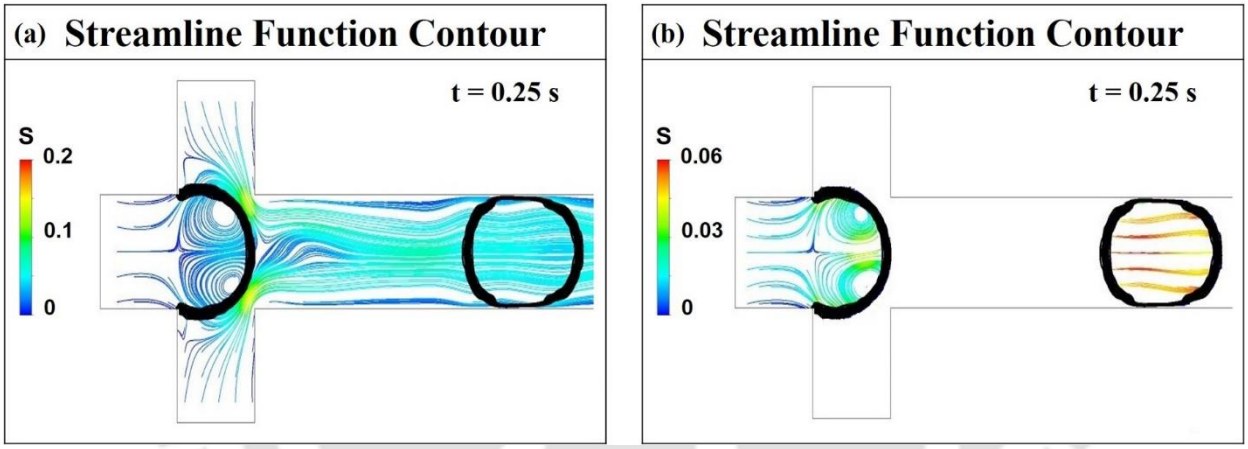

Figure 5a.4. Streamline function contour depicting curl at the junction of flow-focusing geometry: a, For continuous phase; and b, For dispersed phase

5a.3. RESULTS AND DISCUSSIONS

The present work investigates the portrayal of velocity, fluid properties of the dispersed and continuous phase on transition between dripping and jetting flow. It will help us to unfold the inside physics of dripping and jetting flow by understanding the role of inertia, viscous and

surface force behind these two marvels. The velocity of the dispersed and continuous phases was varied in the range of (0.01 – 0.08) m/s and (0.025 – 0.15) m/s respectively. The mechanism of dripping and jetting flow were explored by analyzing the sequential time steps of the development of volume fraction, and velocity field. The droplet pinch-off time and jet growth time has been calculated for dripping and jetting regime respectively. The outcomes are summarized in the form of flow pattern map which shows the transition boundary between dripping and jetting phenomena. The X and Y axis of the flow pattern map is presented as Capillary (Ca_{water}) and Weber (We_{oil}) number respectively. The simulated transition boundary also accords with the analytical solution available in the literature. The effect of oil-water viscosity ratio and interfacial tension on droplet size is also investigated. The detailed analysis of the simulated results has been discussed in the subsequent sections.

5a.3.1 Effect of inertia on dripping and jetting flow

Phase velocity is one of the important parameters, which governs the transition of dripping and jetting flow. A typical illustration of a dripping flow observed at V_o = 0.01 m/s and V_w = 0.02 m/s has been shown in Figure 5a.5. The figure shows the sequential time steps (TS) of volume fraction contour, which explains the development of a dripping flow. In the dripping flow, droplet pinch-off occurs near the junction of two phases. This leads to the generation of small spherical droplets close to the junction, whose diameters are approximately equal to the width of the channel. In this flow-focusing geometry, the oil phase enters along the X-axis and meets the water streams coming from the positive and negative direction of Y-axis at the junction (Figure 5a.5a). The water jets hit the oil stream and deformed it as shown in Figure 5a.5b. A neck of the oil stream is spawned due to the continuously increasing pressure on the oil

stream exerted by the two water jets (Figure 5a.5c). The thickness of the neck decreases gradually with the passage of time (Figures 5a.5b-e). As a result, a bulged oil stream is observed in front of the oil stream as in Figure 5a.5d. Once the pressure drop between upstream and downstream of the bulged oil stream reaches its maximum, the thickness of the neck became critical, which leads to the breakage of the bulged oil stream (Figure 5a.5e) and generate a pendant shaped droplet. This pendant shaped oil droplet so formed is pushed downstream by the phase velocity, which is transformed into a prolate shaped oil droplet by balancing the interfacial, viscous and pressure forces (Figure 5a.5f). These numerical results highly accord with the experimental investigation on dripping phenomena reported by Fu et al. [18].

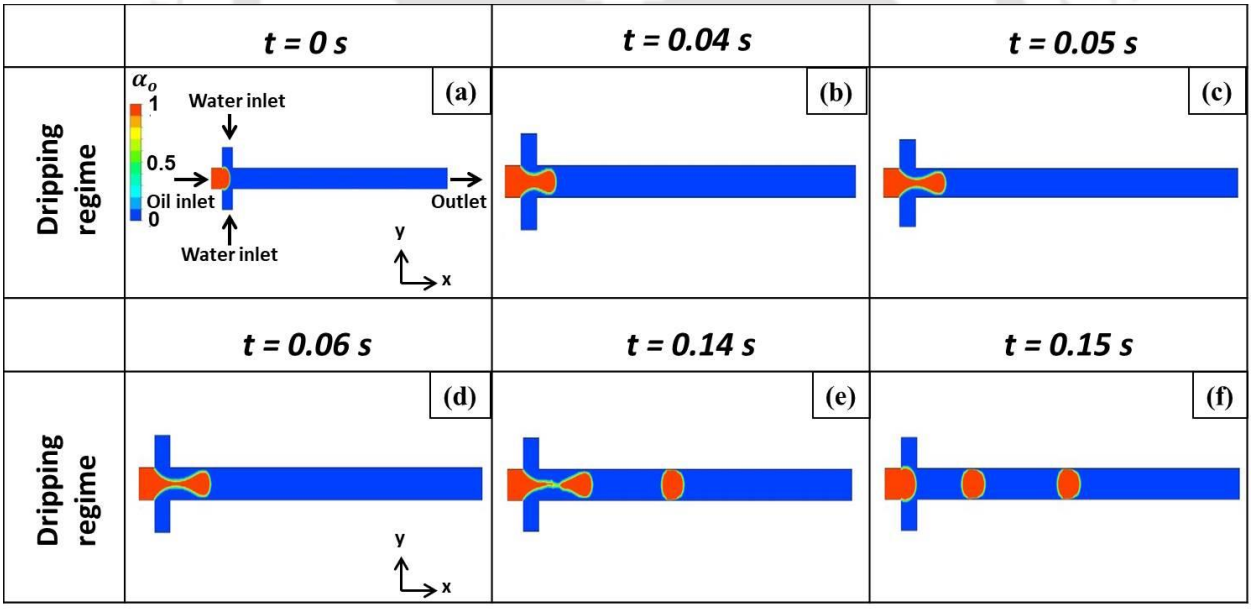

Figure 5a.5. The various time steps indicating the formation mechanism of dripping flow at $\frac{\mu_o}{\mu_w}$ = 12, σ = 0.0118 N/m, and θ = 140°

To understand the insights of the dripping phenomena, the sequential of time steps (TS) of continuous phase's velocity vectors have also been extracted from the simulated results and presented in Figure 5a.6. It is revealing how the continuous phase helps in the pinch-off of the oil stream and generates a spherical oil droplet. At TS = 0 s, the dispersed phase doesn't cross the junction, so the velocity vectors of both the streams (along positive and negative Y-axis) of the continuous phase collide each other just in front of the oil stream at the junction (Figure 5a.6a). Oil phase is moving forward with time, and interacting with the velocity field of continuous phase, which leads to a necking of the dispersed phase at TS = 0.04 s (Figure 5a.6b). Further, intensity of the velocity vector of the continuous phase escalates on the surface of the oil stream due its bulged shaped morphology, which enforces to elongate the neck and neck is becoming thinner and thinner with progress of time (Figure 5a.6c-d). The Figure 5a.6e (TS = 0.14 s) shows a very interesting phenomena where inertial force due velocity field of the continuous phase is so strong that it is overwhelming the stabilizing viscous and surface forces of the dispersed phase and the thickness of the neck becomes critical. This critical neck thickness breaks down easily and generates a lumpy mass from the bulged oil stream, similar to a pendant shaped droplet, which is transformed into distinct oblate droplet (TS = 0.15 s, Figure 5a.6f).

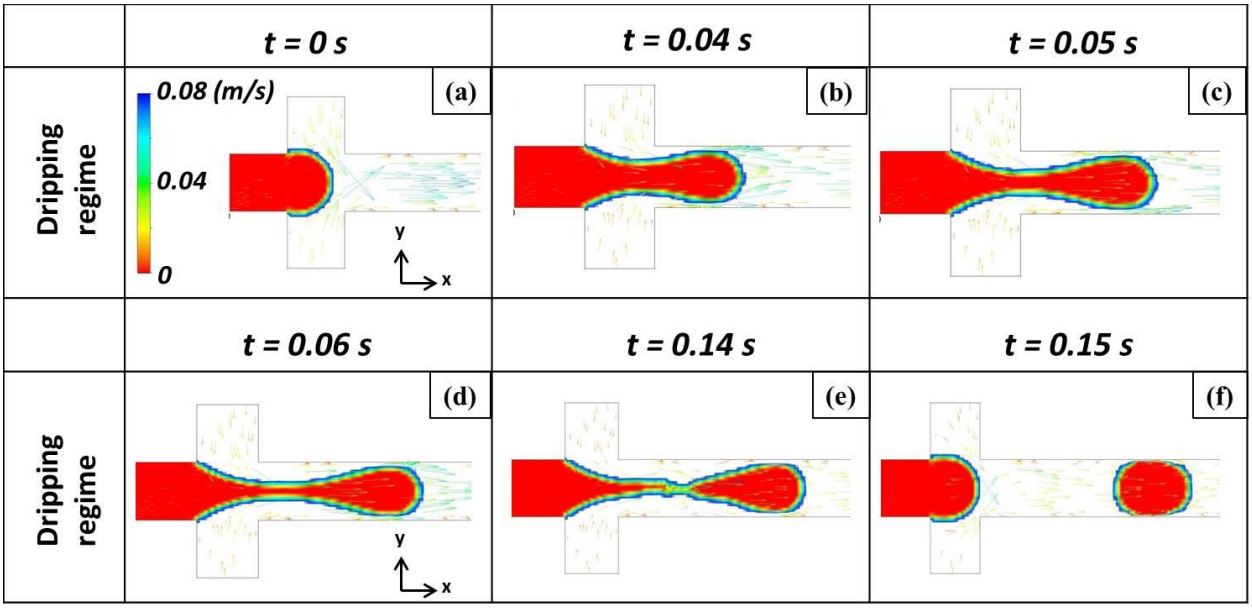

Figure 5a.6. Velocity vectors at different time steps explaining the inside physics of dripping flow at $\frac{\mu_o}{\mu_w}$ = 12, σ = 0.0118 N/m, and θ = 140°

Jetting is another important flow pattern in flow-focusing geometry which leads the formation of small droplets of the dispersed phase at distant point from the junction. A representative result of the sequential time steps of volume fraction contour of such flow is shown in Figure 5a.7 at oil and water velocity of 0.02 m/s (V_o) and 0.02 m/s (V_w) respectively. In this case (Figure 5a.7), flow directions are also same as mentioned before in the section of the dripping flow regime. The oil stream is deformed due to the normal stresses exerted by two water jets coming from the opposite directions, as explained for the dripping flow, which leads to a necking on the oil stream as shown in Figure 5a.7b (TS = 0.02 s). The thickness of the neck progressively decreases over time (Figures 5a.7c-e) but it doesn't reach the critical value due to insufficient viscous stresses and inertial force of the continuous phase, rather a thin oil stream is

formed along the positive X-axis. Here viscous force of the dispersed phase along with interfacial force is the dominating force over the viscous drag of the continuous phase and causes the continuous length elongation of the oil stream [20]. As a result of which a long jet with a pendant oil mass at the front of the oil stream is observed (Figure 5a.7e). With time, oil thread grows longer and longer and reaches to a critical condition, where the viscous drag of continuous phase becomes so stronger that can overcome the interfacial force of the viscous oil thread. This leads to the generation of the prolate shaped droplet which is converted to the prolate shaped droplet with time (Figure 5a.7f).

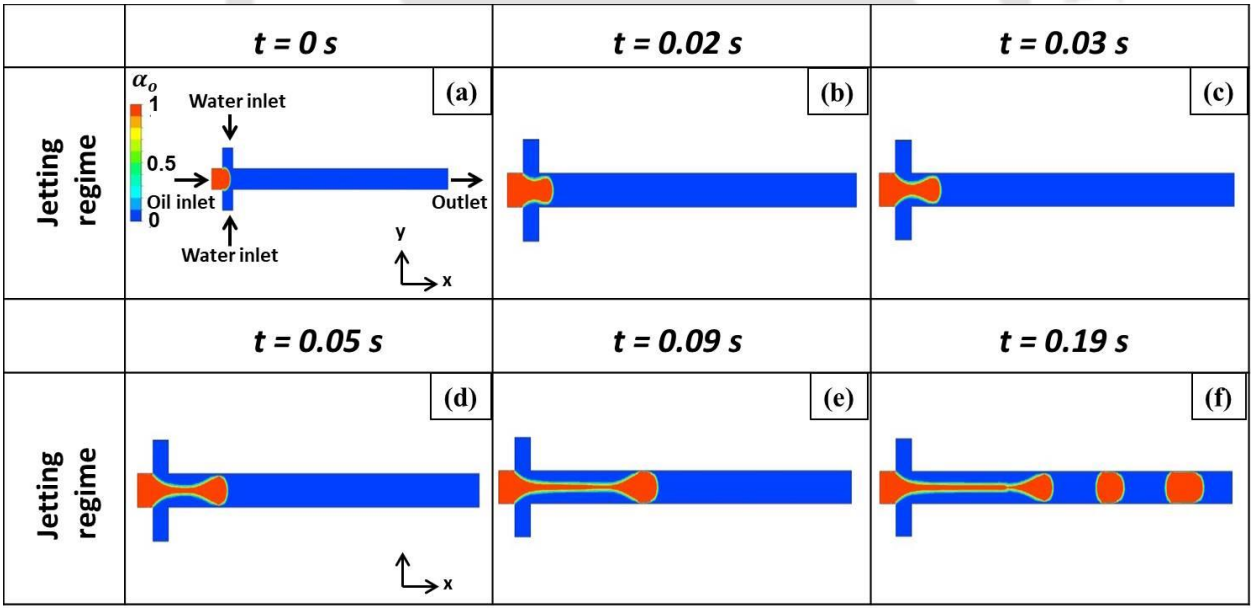

Figure 5a.7. The various time steps illustrating the formation of jetting phenomena at $\frac{\mu_o}{\mu_w}$ = 12, σ = 0.0118 N/m, and θ = 140°

In order to expose the perception of the jetting flow, the velocity vectors estimated from the simulations, which reveals how the inertia of continuous and dispersed phase help in the generation of a spherical oil droplet. Figure 5a.8 shows the sequential time step images of the velocity vectors of a typical jetting flow. Initially i.e. at TS = 0 s, the dispersed phase does not pass the junction therefore the velocity vectors of both streams of the continuous phase (along the positive and negative Y-axis) meet immediately in front of the oil stream at the junction (Figure 5a.8a). The oil phase advances with time and interacts with the velocity field of the continuous phase, resulting in a necking of the dispersed phase at TS = 0.02 s (Figure 5a.8b). Furthermore, the intensity of the velocity vector of the continuous phase increases on the surface of the oil stream owing to its bulged shaped morphology, which drives the neck to elongate, and the neck becomes thinner and thinner with time but it does not reach to the critical value due to low viscous stresses of the continuous phase; instead, a thin oil stream forms along the positive X-axis (Figure 5a.8b-e). Because of this, the magnitude of the velocity vector inside the dispersed phase increases gradually. This higher velocity vector of the dispersed phase leads to elongation of the oil stream further, creating a lengthy jet (Figure 5a.8e). Due to the jet's instability, driven by the interfacial tension, droplet formation takes place near the end of the lengthy jet (Figure 5a.8f). After the formation of the droplet, the magnitude of the velocity vector within the dispersed phase decreases (Figure 5a.8f). The present data accords with Fu et al. [18].

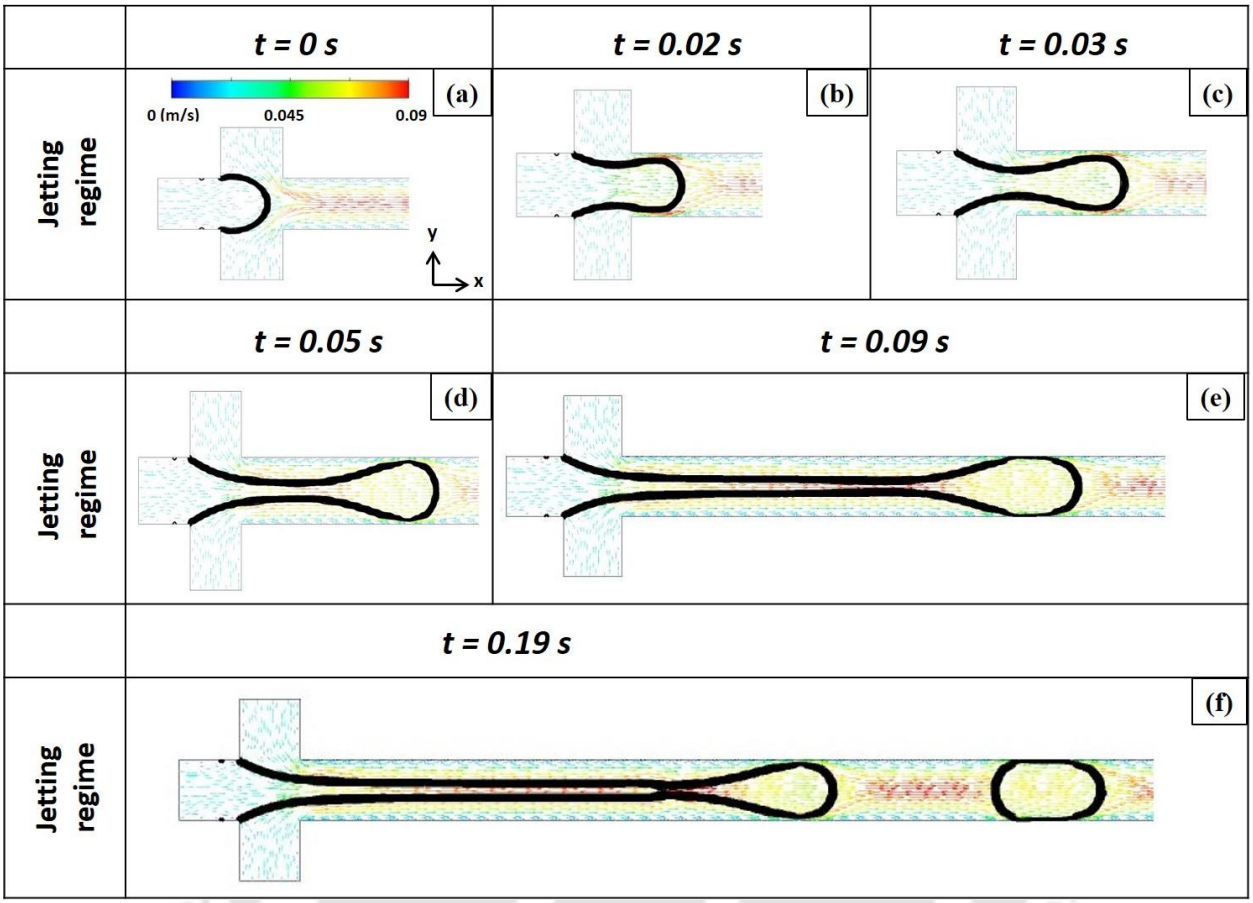

Figure 5a.8. Velocity vectors at different time steps to explain the inside physics of jetting flow at $\frac{\mu_o}{\mu_w} = 12$, $\sigma = 0.0118$ N/m, $\theta = 140°$

5a.3.2 Flow pattern map

The observations of the dripping and jetting flow in a wide range of oil and water superficial velocity as discussed above have further been summarized in the form of flow pattern map. Two dimensionless numbers, namely the capillary number (Ca_w) and the weber number (We_o), have been plotted on the X and Y-axis, respectively, to create a generalized flow pattern

map as shown in Figure 5a.9. This figure will help to visualize the essential characteristics of the dripping and jetting flow in a single window. Mainly, two types of flow patterns were observed: I) Dripping flow, and II) Jetting flow. Dripping is restricted to low (0.0046) to moderate (0.17) weber numbers of the dispersed phase and low (0.002) to high (0.0127) capillary numbers of the continuous phase. On the other hand, the jetting regime is limited to low (0.01) to high (0.0127) capillary numbers of continuous phases and moderate (0.064) to high (0.29) weber number of dispersed phase. The dripping regime occupies a more significant portion and the lower part of the map. The jetting regime occupies comparatively a smaller portion and the upper part of the map. The present flow pattern map has been compared with the experimental data available in the literature (Fu et al. [18]). The transition boundary between the dripping and jetting regime obtained from the present work gives a good agreement with Fu et al. as shown in Figure 5a.9.

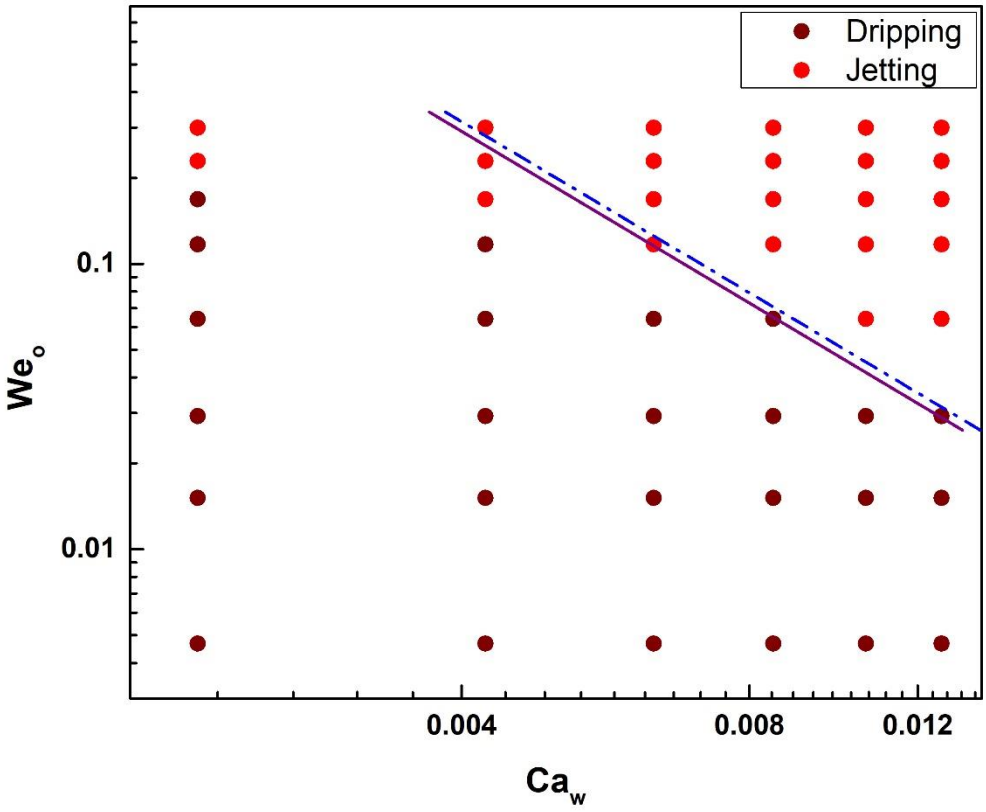

Figure 5a.9. Flow pattern map of dripping and jetting regimes obtained from 2D simulation; capillary number (Ca_w) of continuous phase vs. Weber number (We_o) of dispersed phase; solid line represents simulated transition boundary; dash dot line indicates transition boundary taken from Fu et al. [18]

5a.3.3 Influence of viscous force on dripping and jetting flow

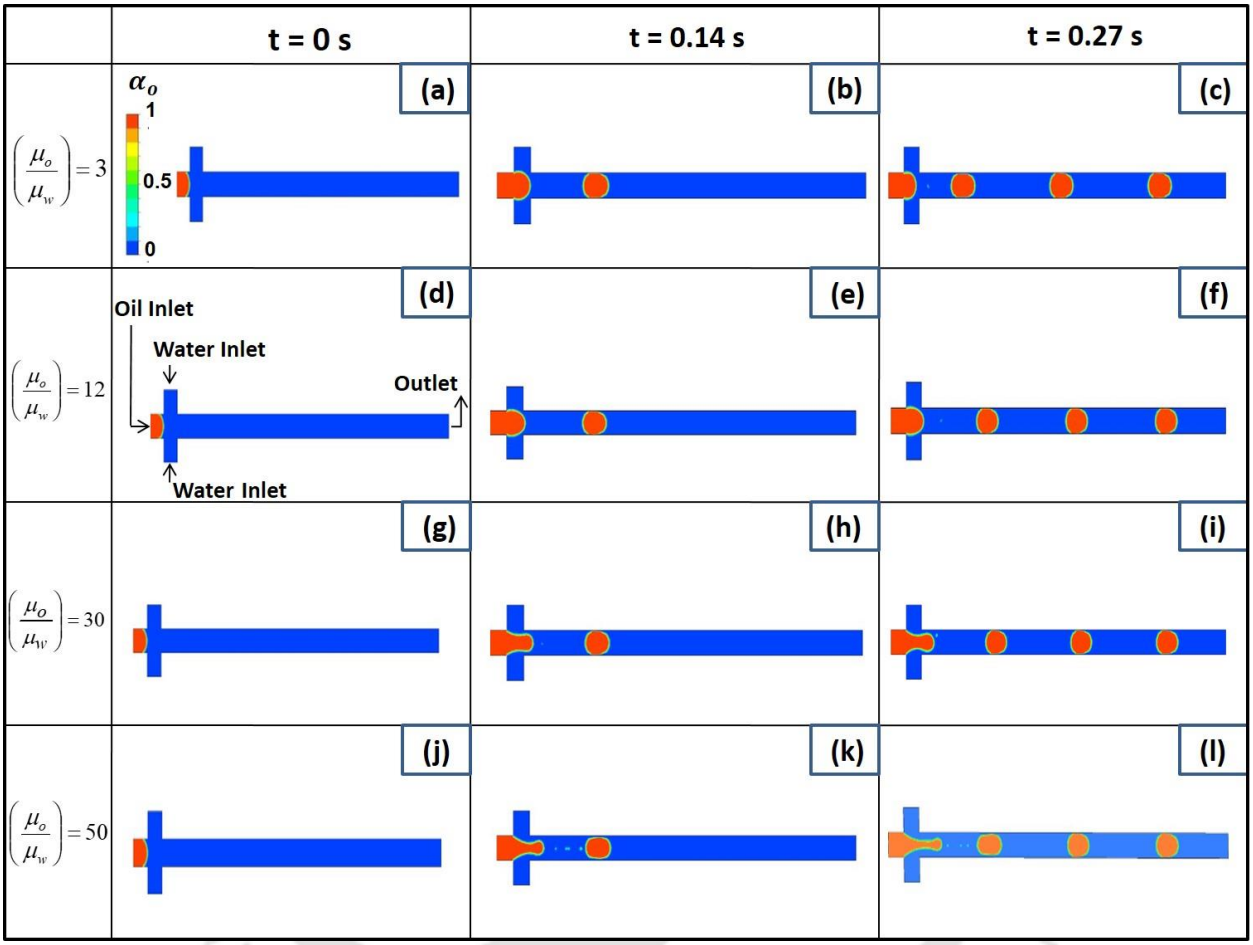

Figure 5a.10. Time variation of volume fraction contour of dripping regime at different oil-water viscosity ratio

This section represents the effect of oil-water viscosity ratio on the dripping flow. Figure 5a.10a-c, 5a.10d-f, 5a.10g-i, and 5a.10j-l represents the sequential time steps of volume fraction contour for oil-water viscosity ratio = 3, 12, 30, and 50 respectively. We can observe that with increase in oil-water viscosity ratio, the droplet size decreases gradually (Figure 5a.11). Here, viscous force increases with increasing the oil-water viscosity ratio, which intensifies the shear

force acting on the dispersed phase. This leads to the breakup of the dispersed thread early and smaller droplets at higher viscosity ratio.

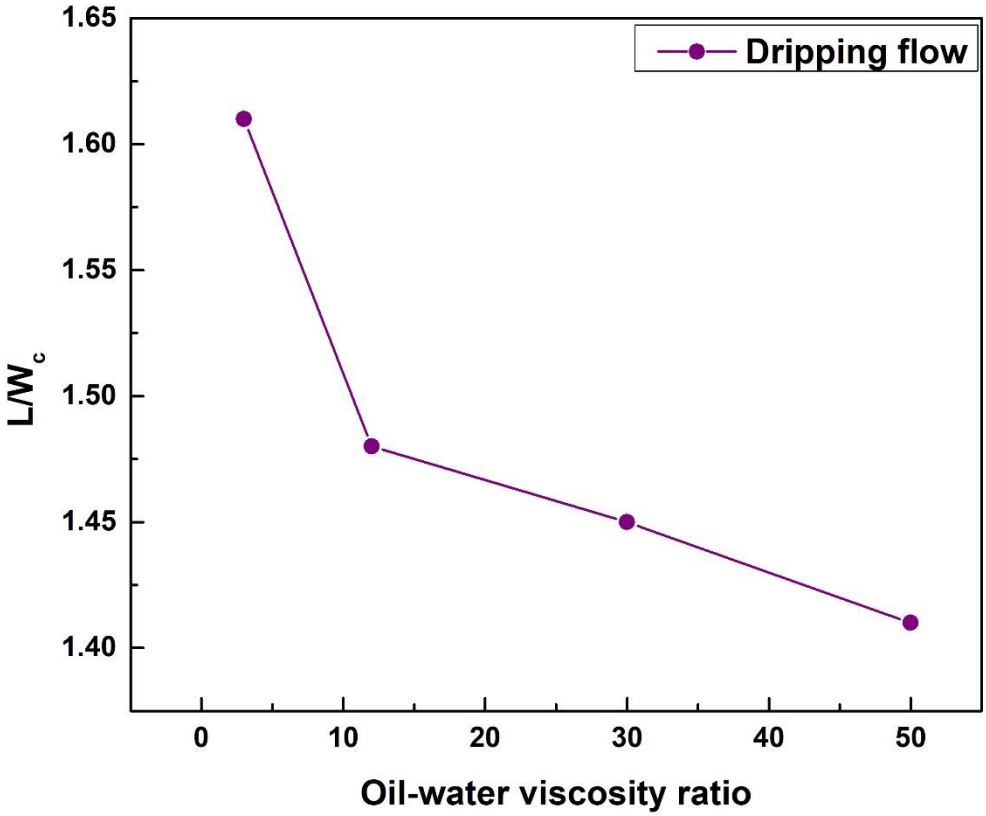

Figure 5a.11. Effect of oil-water viscosity ratio on non-dimensional droplet length

Figure 5a.12 represents the effect of viscosity on jetting regime. Figure 5a.12a-c, 5a.12d-f, 5a.12g-i, and 5a.12j-l represents the sequential time steps of volume fraction contour for oil-

water viscosity ratio = 3, 12, 30, and 50 respectively. It is observed that jet length increases with increase in the oil-water viscosity ratio. It means that higher oil viscosity is lingering the pinch off process, which is delaying in the formation of droplets. Subsequently, the time scale of jet growth increases with increase in the oil-water viscosity ratio, which is supported by the volume fraction contour of the Figure 5a.12. The figure depicted that droplets are formed at low oil-water viscosity ratio (3 and 12). On contrary, not a single droplet is formed at higher viscosity ratio 30 (Figure 5a.12 g-i) and 50(Figure 5a.12 j-l), because, viscous force of the dispersed phase enhances the stability of the oil thread. High viscous fluids usually give flat velocity profile, which brings the stability of the phases. As a result, no droplet is generated in case of oil-water viscosity ratio 30 and 50 in the length scale of the present simulation. Droplets may be formed in higher dimension of axial length of geometry.

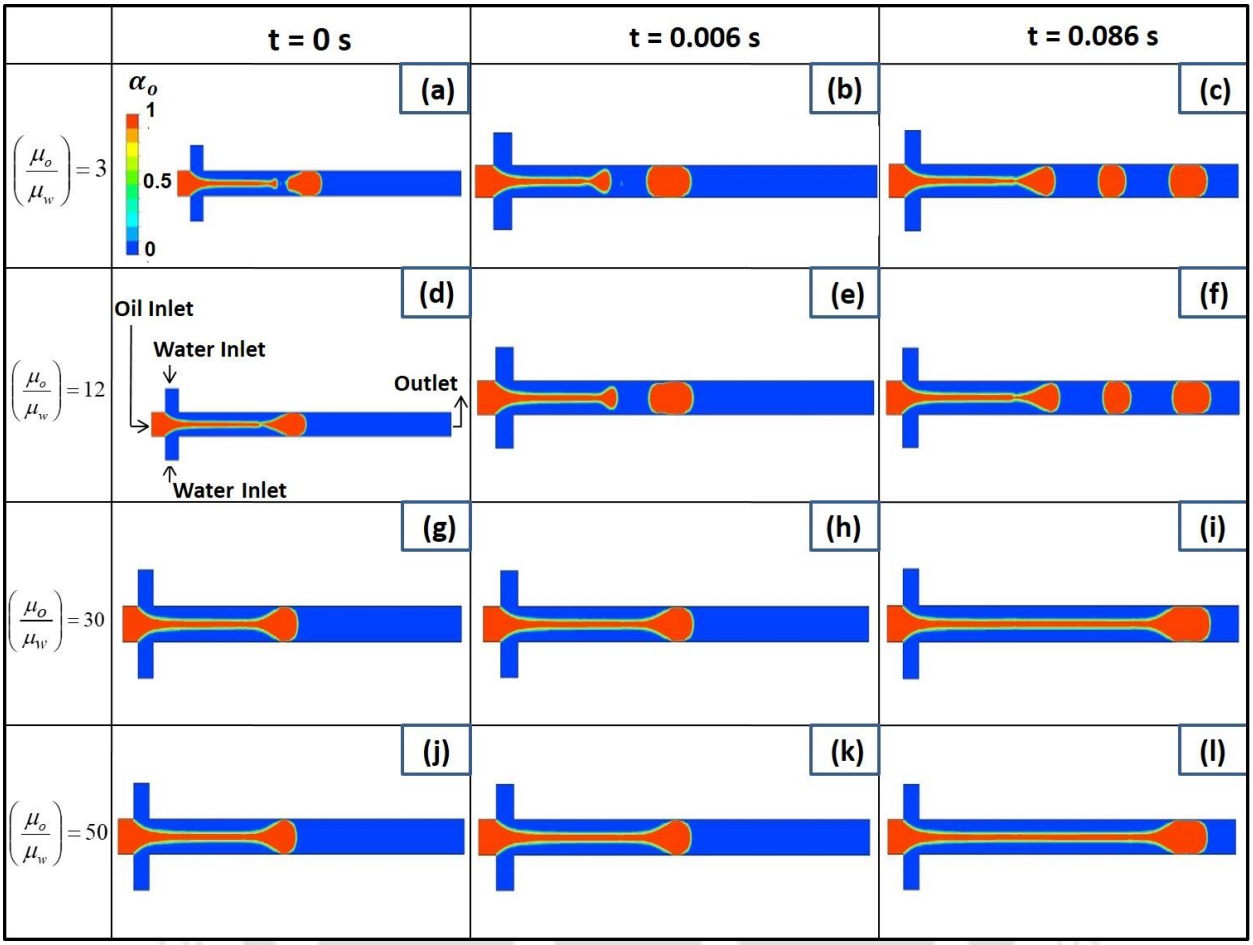

Figure 5a.12. Time variation of volume fraction contour of jetting regime at different oil-water viscosity ratio

5a.3.4 Portrayal of surface force on dripping and jetting flow

Surface force always plays a vital role in the dripping and jetting flow. Figure 5a.13 represents the effect of surface tension on dripping regime. Figure 5a.13a-c, 5a.13d-f, 5a.13g-i, and 5a.13j-l represents the sequential time steps of volume fraction contour for surface tension = 0.0118 N/m, 0.008 N/m, 0.005 N/m, and 0.002 N/m respectively. It is observed that the droplet size decreases gradually with decrease in interfacial tension. Herein, the interfacial tension reduces, so the shear force becomes dominating now. Here, low interfacial tension (0.002 N/m) leads to the elongation of the oil thread as observed in Figure 5a.13k, which is nothing but initiation of a jetting flow. Finally, the thin oil thread breaks up into tiny droplets. From energy conservation point of view, it is important to note that total energy reduces by lowering the interfacial tension and now more surface area is generated by taking birth of new droplets, which helps to keep total surface energy same.

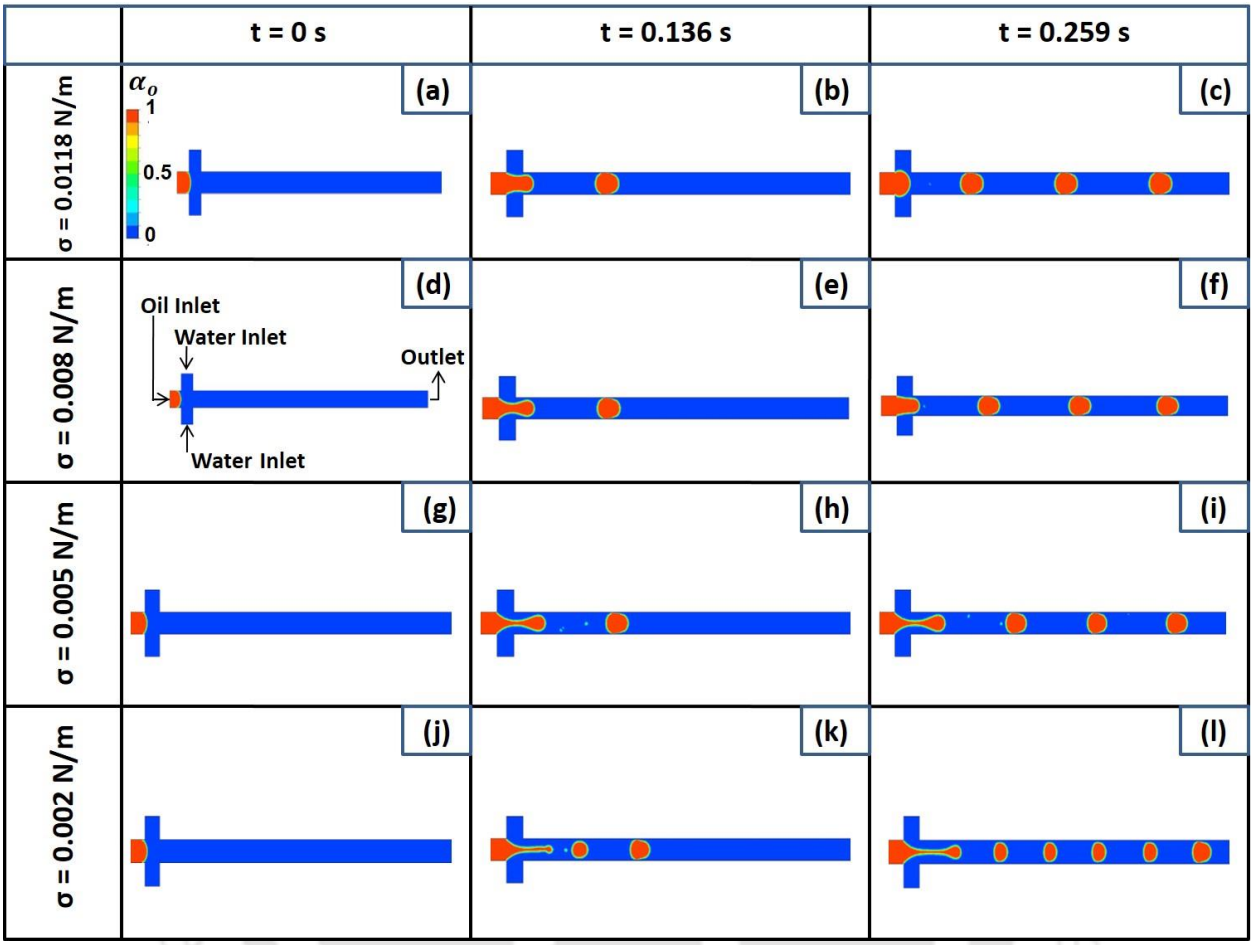

Figure 5a.13. Time variation of volume fraction contour of dripping regime at different interfacial tension

Figure 5a.14 represents the effect of surface tension on jetting regime. Figure 5a.14a-c, 5a.14d-f, 5a.14g-i, and 5a.14j-l represents the sequential time steps of volume fraction contour at surface tension 0.0118 N/m, 0.008 N/m, 0.005 N/m, and 0.002 N/m respectively. With the decrease in surface tension values, the jet length increases. Here, the time scale of jet growth increases with the decrease in surface tension values. In the present simulated conditions, the droplets are formed at σ = 0.0118 N/m (Figure 5a.14a-c), whereas a long oil thread (Figure

5a.14d-l) is observed for rest of the interfacial values (σ = 0.008, 0.005, and 0.002 N/m). Droplets may be formed in higher dimension of axial length of geometry. Viscous effect of continuous phase is gradually becoming dominating because of continuous lowering the interfacial forces of the dispersed phase.

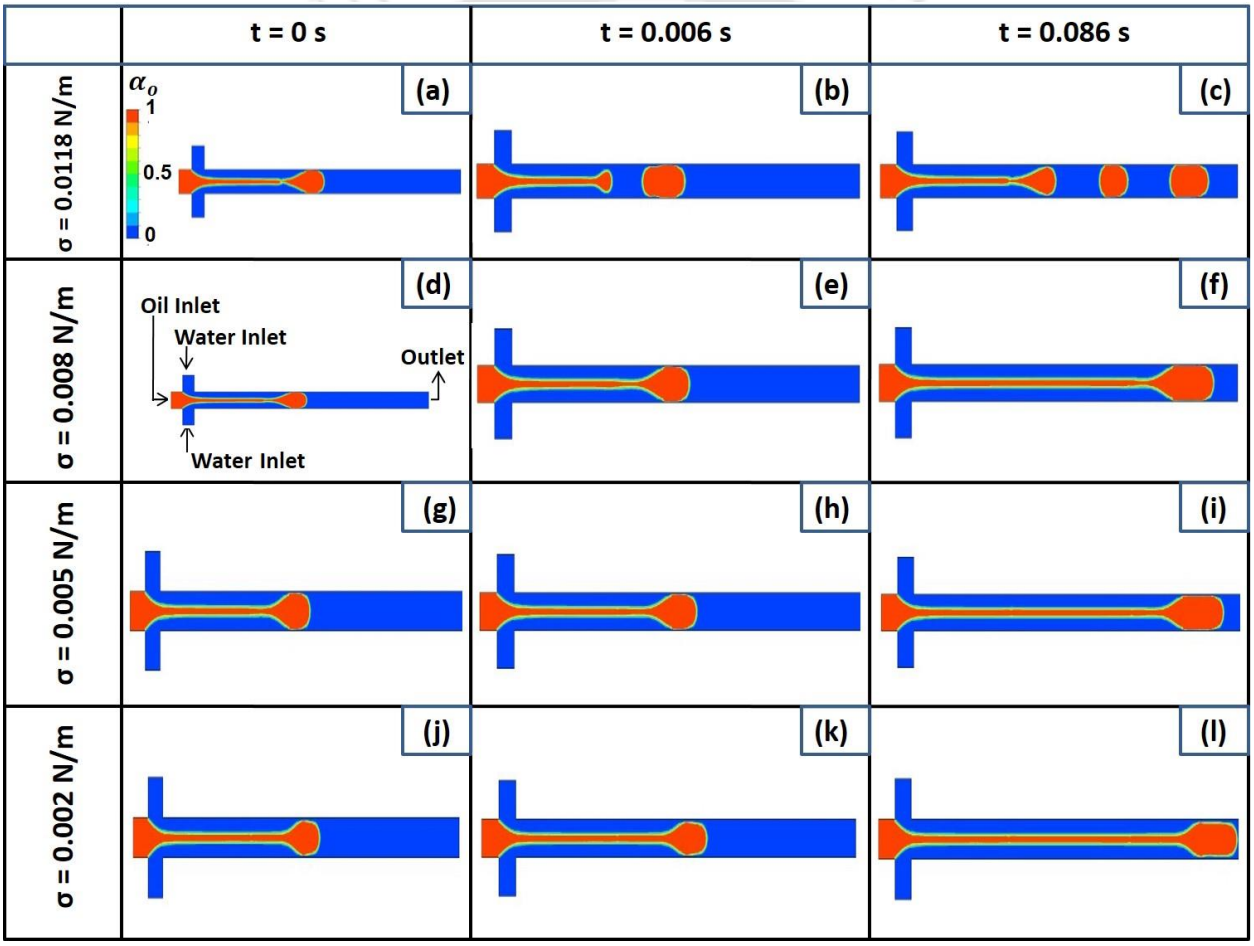

Figure 5a.14. Time variation of volume fraction contour of jetting regime at different interfacial tension values

5a.3.5 Transition criteria of dripping to jetting flow

According to Utada et al. [21], the time scale of drop pinch-off and the time scale of jet development can be analyzed to determine transition criteria from dripping to jetting. The Rayleigh-Plateau instability can be applied to explain the physics behind this transition as the process is comparable with the classic process for drop generation from a cylindrical fluid thread. Because of interfacial tension, the system tries to minimize its surface area and that is why the fluid thread leaves some fluid volume in the form droplets, which is nothing but the splitting of the fluid thread. That is why instability is associated with the fluid cylinders/jets. It is important to consider two radii associated with the fluid thread, - a) radius of the thread, and b) radius of the curvature of the wave accompanying with fluid thread. The radius of wave's curvatures is opposite in nature at peak and trough; - it is positive (+ve) at peak and negative (-ve) at trough. According to Young–Laplace, pressure decreases at trough and increase at peak. Now, the decay of the fluid thread will take place over time if radius of curvature of the wave dominates over the radius of the thread.

Anyway, assume the fluids are Newtonian and the jet is composed of a single fluid, Udata et al. [21] proposed the following equation to calculate the time scale of droplet pinch-off.

$$t_p = \frac{CR_{jet}\mu_c}{\sigma} \qquad (5a.3.5.1)$$

Here C = constant (100) when μ_d/μ_c = 11 [according to Powers et al. [22]], R_{jet} = Unperturbed jet radius and μ_c = viscosity of continuous phase.

R_{jet} can be found from the following equation [23]

$$\frac{R_{jet}^2}{R_c^2} = \frac{1+\frac{Q_d}{Q_c} - \sqrt{1+\frac{Q_d}{Q_c}\frac{\mu_c}{\mu_d}}}{2+\frac{Q_d}{Q_c}-\frac{\mu_c}{\mu_d}} \qquad (5a.3.5.2)$$

Where, R_c = Radius of cylindrical capillary

Now, using the values for dripping regime, we got R_{jet} = 0.00026 m. So, the theoretical value of t_p for dripping regime is 0.0022 s.

The t_p has also been estimated from the present simulated data. The t_p estimation methodology can be understood from the sample calculation described in the figure below. The figure describes that the oil jet is growing for TS = 0 to 0.004 s. After this, pinch off is taking place at TS = 0.006 s (Figure 5a.15), which is accepted as simulated value of t_p.

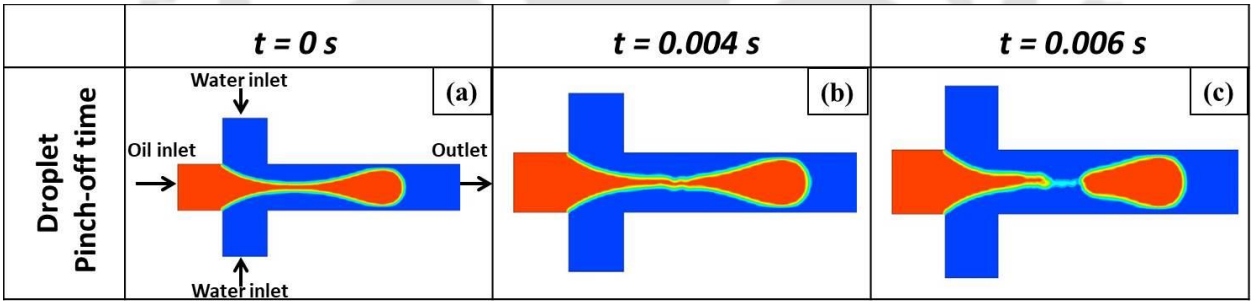

Figure 5a.15. Estimation of t_p from simulated data

The time scale of jet growth can be calculated as [21]

$$t_g = \frac{R_{jet}^3}{Q_{sum}} \qquad (5a.3.5.3)$$

Where, t_g is the time scale required for jet to fully grow. After this time period, jet prepares itself for pinch off. It is noticed that the t_g is proportional to cube of the unperturbed jet radius and inversely proportional to the sum of the flow rate of dispersed and the continuous phase (Eq. 5a.3.5.3). Here, calculated value of R_{jet} is 0.00026 m. So, the theoretical value of t_g for jetting regime is 0.001 s. On the other hand, simulated value of t_g for jetting regime is 0.004 s, as represented in Figure 5a.16.

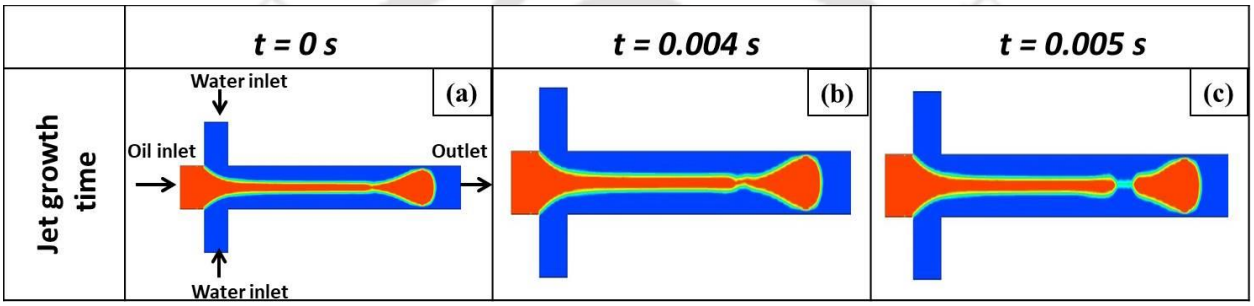

Figure 5a.16. Estimation of t_g from simulated data

Here, t_g (theoretical and simulated) < t_p (theoretical and simulated), which full fills the transition criteria mentioned by Udata et al. [22]. So, the jet will grow continuously, resulting the jetting flow and droplets may develop at far downstream. At this condition, effective capillary number of the interface is given by the following expression [21].

$$Ca = \frac{t_{pinch}}{t_g} = \frac{\mu_c v}{\sigma} \qquad (5a.3.5.4)$$

Where, v is the downstream velocity of the inner fluid.

The Eq. 5a.3.5.4 yields Ca = 2.2 ~ 1, so transition between dripping and jetting takes place at v = 0.02 m/s.

5a.4. SUMMARY

In this study, 2D-CFD simulations have been carried out to study the effect of flow velocity on flow regime using the VOF method. The model has been authenticated with earlier experimental data present in the literature (Fu et al. [18]). We have effectively simulated the different flow regimes based on dispersed and continuous phase velocity. A mechanism on dripping and jetting phenomena also has been discussed. A flow pattern map has been presented identifying the dripping and jetting regimes. It has been observed that the dripping is restricted to low to moderate weber numbers of the dispersed phase and low to high capillary numbers of the continuous phase. At the same time, the jetting regime is limited to low to high capillary numbers of continuous phases and moderate to high weber number of dispersed phase. Theoretical and simulated droplet pinch-off time and jet growth time has also been calculated and compared. The confirmation of the transition between dripping and jetting has been done through the calculation of the effective capillary number of the interface. The droplet size decreases with increase in oil-water viscosity ratio and with decrease in interfacial tension. The time scale of jet growth increases with increase in oil-water viscosity ratio and with decrease in interfacial tension.

REFERENCES

1. Shembekar, N., Chaipan, C., Utharala, R., and Merten, C.A., Droplet-based microfluidics in drug discovery, transcriptomics and high-throughput molecular genetics, *Lab on a Chip*, 2016, vol. 16, no., pp. 1314-1331.
2. Sanguansri, P. and Augustin, M.A., Nanoscale materials development – a food industry perspective, *Trends in Food Science & Technology*, 2006, vol. 17, no., pp. 547-556.
3. Agarwal, P., Choi, J.K., Huang, H., Zhao, S., Dumbleton, J., Li, J., and He, X., A Biomimetic Core-Shell Platform for Miniaturized 3D Cell and Tissue Engineering, *Particle & particle systems characterization : measurement and description of particle properties and behavior in powders and other disperse systems*, 2015, vol. 32, no., pp. 809-816.
4. Wen, N., Zhao, Z., Fan, B., Chen, D., Men, D., Wang, J., and Chen, J., Development of Droplet Microfluidics Enabling High-Throughput Single-Cell Analysis, *Molecules*, 2016, vol. 21, no., pp. 881.
5. Zhu, P. and Wang, L., Passive and active droplet generation with microfluidics: a review, *Lab Chip*, 2017, vol. 17, no., pp. 34-75.
6. Christopher, G.F. and Anna, S.L., Microfluidic methods for generating continuous droplet streams, *Journal of Physics D: Applied Physics*, 2007, vol. 40, no., pp. R319-R336.
7. Jing, L. and Nam-Trung, N., Numerical Simulation of Droplet-Based Microfluidics - A Review, *Micro and Nanosystems*, 2010, vol. 2, no., pp. 193-201.

8. Yobas, L., Martens, S., Ong, W.-L., and Ranganathan, N., High-performance flow-focusing geometry for spontaneous generation of monodispersed droplets, *Lab on a Chip*, 2006, vol. 6, no., pp. 1073-1079.

9. Ong, W.-L., Hua, J., Zhang, B., Teo, T.-Y., Zhuo, J., Nguyen, N.-T., Ranganathan, N., and Yobas, L., Experimental and computational analysis of droplet formation in a high-performance flow-focusing geometry, *Sensors and Actuators A: Physical*, 2007, vol. 138, no., pp. 203-212.

10. Lu, Y., Fu, T., Zhu, C., Ma, Y., and Li, H.Z., Experimental investigation on the breakup dynamics for bubble formation in viscous liquids in a flow-focusing device, *Chemical Engineering Science*, 2016, vol. 152, no., pp. 516-527.

11. Han, W., Chen, X., Wu, Z., and Zheng, Y., Three-dimensional numerical simulation of droplet formation in a microfluidic flow-focusing device, *Journal of the Brazilian Society of Mechanical Sciences and Engineering*, 2019, vol. 41, no., pp. 265.

12. Rahimi, M., Yazdanparast, S., and Rezai, P., Parametric study of droplet size in an axisymmetric flow-focusing capillary device, *Chinese Journal of Chemical Engineering*, 2020, vol. 28, no., pp. 1016-1022.

13. Xue, C.-D., Chen, X.-D., Li, Y.-J., Hu, G.-Q., Cao, T., and Qin, K.-R., Breakup Dynamics of Semi-dilute Polymer Solutions in a Microfluidic Flow-focusing Device, *Micromachines*, 2020, vol. 11, no., pp. 406.

14. Wang, N., Semprebon, C., Liu, H., Zhang, C., and Kusumaatmaja, H., Modelling double emulsion formation in planar flow-focusing microchannels, *Journal of Fluid Mechanics*, 2020, vol. 895, no. A22, pp. A22.

15. Iqbal, S., Bashir, S., Ahsan, M., Bashir, M., and Shoukat, S., Effect of Intersection Angle and Wettability on Droplet Generation in Microfluidic Flow-Focusing Device, *Journal of Fluids Engineering*, 2020, vol. 142, no., pp.

16. Soroor, M., Zabetian Targhi, M., and Tabatabaei, S.A., Numerical and experimental investigation of a flow focusing droplet-based microfluidic device, *European Journal of Mechanics - B/Fluids*, 2021, vol. 89, no., pp. 289-300.

17. Chekifi, T., Boukraa, M., and Aissani, M., DNS using CLSVOF method of single micro-bubble breakup and dynamics in flow focusing, *Journal of Visualization*, 2021, vol. 24, no., pp. 519-530.

18. Fu, T., Wu, Y., Ma, Y., and Li, H.Z., Droplet formation and breakup dynamics in microfluidic flow-focusing devices: From dripping to jetting, *Chem. Eng. Sci.*, 2012, vol. 84, no., pp. 207-217.

19. Fu, Y., Bai, L., Zhao, S., Zhang, X., Jin, Y., and Cheng, Y., Simulation of reactive mixing behaviors inside micro-droplets by a lattice Boltzmann method, *Chemical Engineering Science*, 2018, vol. 181, no., pp. 79-89.

20. Utada, A.S., Fernandez-Nieves, A., Stone, H.A., and Weitz, D.A., Dripping to jetting transitions in coflowing liquid streams, *Phys. Rev. Lett.*, 2007, vol. 99, no., pp. 094502.

21. Utada, A.S., Lorenceau, E., Link, D.R., Kaplan, P.D., Stone, H.A., and Weitz, D.A., Monodisperse Double Emulsions Generated from a Microcapillary Device, *Science (New York, N.Y.)*, 2005, vol. 308, no., pp. 537-541.

22. Powers, T.R., Zhang, D., Goldstein, R.E., and Stone, H.A., Propagation of a topological transition: the Rayleigh instability, *Physics of Fluids*, 1998, vol. 10, no., pp. 1052-1057.

23. Kovalchuk, N.M., Sagisaka, M., Steponavicius, K., Vigolo, D., and Simmons, M.J.H., Drop formation in microfluidic cross-junction: jetting to dripping to jetting transition, *Microfluid. Nanofluidics*, 2019, vol. 23, no., pp. 103.

CHAPTER 5b

THREE-DIMENSIONAL SIMULATION OF DRIPPING AND JETTING PHENOMENON IN A FLOW-FOCUSING GEOMETRY

ABSTRACT

3D simulations have been performed on a flow-focusing geometry using the VOF method to study the effect of viscosity, surface tension, wettability and geometry on droplet generation for the dripping regime. Here the dispersed phase is the PDMS oil (polydimethylsiloxane), and the continuous phase is the water. Simulations were performed at different oil-to-water viscosity ratios $\left(\frac{\mu_o}{\mu_w}\right)$ of 3, 12, 27, and 50. The interfacial tension between PDMS oil and water is 0.0118 N/m. It has been reduced to 0.008 N/m, 0.005 N/m, and 0.002 N/m, and simulations were performed. The walls of the microchannel are considered to be PMMA surfaces. The contact angle of an oil droplet on the PMMA surface in the presence of water is 140°. The effect of wettability was shown at various contact angles (angle created by water droplet on the PMMA surface in the presence of oil) of 0°, 40°, 90°, 135° and 180°. Frequency of droplet (1/s), non-dimensional droplet length (L/W_c), droplet volume (nL), and droplet velocity (m/s) have been calculated for each of the cases. A flow pattern map has been developed identifying the dripping and jetting regimes. A comparison between normal geometry and two constricted geometries (having different orifice lengths) based on the frequency of droplet, non-dimensional droplet length, droplet volume and droplet velocity has been made for both dripping and jetting regimes. Prediction of simulated non-dimensional droplet length has also been made using dimensional analysis.

5b.1. INTRODUCTION

Microfluidics technology has attracted researchers for several years for its wide applications, such as controllable size and monodispersity [1, 2] of droplets. They also give improved flow control, rapid mixing, and no dispersion. The droplets formed to act as a microreactor with a volume of reactants in the range of nanolitre to picolitre. This reduces the experimental costs, which are dependent on expensive solutions. There are several configurations through which microdroplets can be created, such as T-junction, co-flow, flow-focusing, and some variations [2]. Droplet-based microfluidics is widely used in drug delivery [3], chemical reaction and mixing [4], and emulsification [5].

The droplet formation process is affected by several parameters such as viscosity, dispersed and continuous phase velocity, surface tension, contact angle, the geometry of the device. Several researchers have done both experimental as well as simulation work on the flow-focusing device [1, 6, 7]. Several breakup regimes can be found by tuning the parameters as mentioned above, such as dripping, jetting, and continuous regimes. The breakup process is not fully understood due to its dependence on several independent parameters such as viscosity, dispersed and continuous phase velocity, surface tension, contact angle, and the geometry of the device. To understand the breakup process numerically, there are several multiphase modelling approaches such as the Volume of Fluid (VOF) technique, level set method (LS), phase-field method, and lattice Boltzmann method [8]. Some of the authors have investigated both experimentally and numerically the various factors which influence the droplet formation in a flow-focusing geometry.

Yobas et al.[9] investigated the monodispersed droplets generation on a flow-focusing geometry. They achieved droplet generation rates of over 10^4 per second for water-in-oil

droplets and over 10^3 per second for oil-in-water droplets. The droplet diameter and generation frequency increases greatly with flow rate of continuous phase. Experiments and numerical simulations of droplet generation in flow-focusing geometry have been done. Comparison has been made for 3D circular orifice and 2D rectangular constrictions placed inside the flow-focusing device. It was found that the 2D rectangular geometry generates droplets of larger size and lower frequency than the 3D circular geometry [10]. The influence of interfacial tension on droplet production in a flow-focusing microfluidic device was investigated experimentally. Increased interfacial tension causes droplet diameter to grow while generation frequency decreases [11]. Roberts et al. [12] investigated the formation of monodisperse droplets in a flow-focusing device employing hydrophilic and hydrophobic surfaces. Using the expression, $Ca_i W_{or}/L_{or} \propto Ca_o$, where W_{or} = width of the orifice, L_{or} = length of the orifice, a connection between inner and outer capillary numbers has been discovered to explain the border between stable jetting and droplet generation. When the inner fluid wetted the channel that was significantly thinner than the channel height, jets were produced. When it did not moisten the channel, it produced droplets in the order of the orifice height. In [13] a modified level set approach was used to analyse droplet generation in microchannels. They discovered that the modified level set approach is more feasible since it raised the mass transfer ratio in the droplet formation process by 50%. To describe the droplet production process in a flow-focusing generator that operates in the squeezing regime, where droplet size is generally bigger than channel width, a 3D physical model based on conservation of mass and a semi-analytical model have been built. By anticipating the pressure drop along the 3D corner gutter between the droplet curvature and channel walls, it properly calculates droplet size, spacing, and creation frequency. With a 10% error rate, the

model properly predicts the experimental data [14]. COMSOL was used to conduct a numerical investigation of the droplet formation process in a microfluidic flow-focusing system. It was discovered that the droplet size is more dependent on capillary number than the flow ratio [15]. Experiments have been done to produce droplets using negative pressure in flow-focusing geometry. The droplet volume is found to be related to the pressure ratio by a power law of 1.3 [16]. The impact of viscosity difference between two miscible fluids collected from a dispersed fluid on droplet generation in a flow-focusing geometry have been studied. The condition with 80 percent glycerol bound by 10 percent glycerol gives a superior particle encapsulation mechanism [17]. Flow regime mapping of aqueous two-phase system droplets in flow-focusing geometries was investigated experimentally. In the case of a 30° arrangement, bigger droplets are created in the jetting flow regime, whereas larger droplets are obtained in the dripping flow regime. When P (continuous phase) is raised, droplet formation increases; when P (dispersed phase) is increased, droplet generation decreases [18]. Numerical investigation on droplet generation in a microfluidic flow-focusing device has been done using the level set method. It was discovered that as the flow rate ratio increases, the frequency lowers, and the droplet size grows. With a rise in continuous phase viscosity, the frequency rises, and the size of the droplets shrinks. The size of the droplets grows larger, and the frequency lowers as the interfacial tension increases [19]. Rahimi et al. [20] investigated the effect of device geometry on droplet size in co-axial flow-focusing microfluidic droplet generation devices. They observed that the continuous phase flow rate influenced droplet formation significantly. Droplet diameter was only 4% greater at the highest nozzle-to-orifice distance than at the minimum nozzle-to-orifice distance. Their model accurately predicts droplet size in a co-axial flow-focusing geometry by 3-6%. Aqueous droplet production in a

high inertial airflow inside a flow-focusing geometry was numerically simulated. The continuous and scattered phases are air and water, respectively. Among the flow regimes identified were dripping, unstable dripping, clogging, stratified flow, multi-satellite droplet generation, and unstable jetting [21]. The largest droplet was made in the plugging regime at Re = 0.5, Ca = 0.01, whereas the smallest one was created in the unstable dripping regime at Re = 50, Ca = 0.0005. In the unstable dripping regime, at Re = 50, Ca = 0.01, the greatest output rate (1900 Hz) may be attained [21]. An experimental study on droplet formation in a flow-focusing microchannel in the presence of surfactants has been done. The inclusion of surfactants reduced the areas in the flow pattern map occupied by the squeezing and dripping regimes, whereas the threading and jetting regimes occupied its extended portions. Furthermore, between the expansion and necking drop formation stages, drag forces surpass the surface tension force [22]. By adjusting the power-law index and the consistency coefficient of the continuous phase, the VOF approach was used to investigate droplet size, spacing between droplets, formation frequency, and droplet velocity. With an increase in n or K, the non-dimensional length and spacing both decrease. The formation frequency and droplet velocity increase as n or K is increased [6]. Experiments have been done within hydrophobic and hydrophilic surfaces, and different stages of droplet generation were reported with two immiscible liquids inside a flow-focusing device. An inverse emulsion occurs in the hydrophilic condition. The formation of single and double T-junctions in the hydrophilic channel results in the formation of droplets. When compared to hydrophilic channels, uncoated hydrophobic channels yield monodisperse droplets at a larger capillary number [23]. CLSVOF was used in 3D numerical simulation to investigate the effects of several physicochemical factors (interfacial tension, dispersed phase viscosity, flow rate) on

droplet dynamics and flow regime changeover. The dispersed phase is termed oil, while the continuous phase is water/glycerol solutions. Droplet length and volume decrease as viscosity and flow rate ratios rise, yet droplet velocity and liquid layer thickness rise. Droplet length is determined using scaling formulae based on Ca. The droplet deformation index shows that near-spherical droplets are formed in all jetting regime conditions [24]. 3D numerical simulation has been done on bubble formation in viscous fluids by a microfluidic flow-focusing junction using VOF method. In the case of high viscosity ratios, the Geo-Reconstruction approach was determined to be more suited than the CICSAM. As the viscosity rises, the length of the bubbles decreases. At the same flow rate, there is a recirculation flow around the Taylor bubble with low viscosity and a bypass flow with high viscosity [25]. Iqbal et al. [26] studied the effect of intersection angle and wettability on droplet generation in a microfluidic flow-focusing device using numerical simulation. It was discovered that as the flow rate ratios increase, the size of the droplets grows. Large diameter droplets are produced via a high flow rate ratio and greater contact angles. The shape with perpendicular intersection angles produces the largest droplets. Experiment and numerical simulation have been done to study the droplet size in an axisymmetric flow-focusing capillary device. Higher continuous phase fluid viscosity and lower interfacial tension result in smaller droplets, whereas a higher dispersed phase flow rate produces larger droplets, according to the findings. The size of the flow-focusing orifice had a significant impact on the size of the produced droplets. Over a wide range of dimensionless parameters, the droplet size is predicted with a maximum error of 15%.[27] Chekifi et al. [28] investigated the breakup of air bubble in flow-focusing configuration using CLSVOF. They discovered that the bubble size is inversely related to the dispersed phase's viscosity and directly proportional to

interfacial tension. In addition, the size of the bubble is inversely proportional to the orifice width. Fatehifar et al. [29] looked at the effects of non-Newtonian power-law droplets in Newtonian liquid on droplet size and detachment time in three different regimes: squeezing, dripping, and jetting. For all three regimes, they discovered that droplet size reduces as dispersed phase viscosity increases. With a rise in dispersion phase viscosity, droplet pinch-off is also delayed. Numerical and experimental investigation of a flow-focusing droplet-based microfluidic device has been done for drug delivery and cell transport. Simulation was used to help with the fabrication of microfluidic devices. The numerical results were found to be in good agreement with the experimental results obtained in the microfluidic device that was developed. Up to 280 particles or cells inside droplets can be transported per second using this approach [30].

In view of the above discussion, a detailed study of the effect of viscosity, surface tension, wettability and channel geometry on droplet generation is limited. In the present work, 3D simulations have been performed to investigate the effect of viscosity, surface tension, wettability and geometry on droplet generation in a flow-focusing geometry. The dispersed phase is the PDMS oil (polydimethylsiloxane), and the continuous phase is the water. The dripping regime has been studied by varying the viscosity of the dispersed phase, interfacial tension, wettability and introducing two different types of constriction configuration into the geometry. The different oil-to-water viscosity ratios $\left(\frac{\mu_o}{\mu_w}\right)$ which are taken for the study are 3, 12, 27, and 50. The interfacial tension between PDMS oil and water is 0.0118 N/m. It has been reduced to 0.008 N/m, 0.005 N/m, and 0.002 N/m, and simulations were performed. The walls of the microchannel are considered to be PMMA surfaces. The

contact angle of an oil droplet on the PMMA surface in the presence of water is 140°. The effect of wettability was shown at various contact angles (angle created by water droplet on the PMMA surface in the presence of oil) of 0°, 40°, 90°, 135° and 180°. The frequency of droplet (1/s), non-dimensional droplet length (L/W_c), droplet volume (nL), and droplet velocity (m/s) has been calculated in each of the cases. A flow pattern map has been developed identifying the dripping and jetting regimes. A comparison between normal geometry and two different constricted geometries (having different orifice lengths) based on the frequency of droplet, non-dimensional droplet length, droplet volume and droplet velocity has been made for both dripping and jetting regimes. Prediction of simulated non-dimensional droplet length has also been made using dimensional analysis.

5b.2. COMPUTATIONAL MODEL

5b.2.1. Geometry, initial and boundary conditions

The solution domain consists of a horizontal 3D flow-focusing microchannel. The details of the geometry of the computational domain are shown in Figure 5b.1a. The geometry consists of three inlets (length = 0.6 mm) and one main channel. The inlets and main channel have an identical width (0.6 mm). The corresponding mesh of the flow-focusing geometry is shown in Figure 5b.1b.

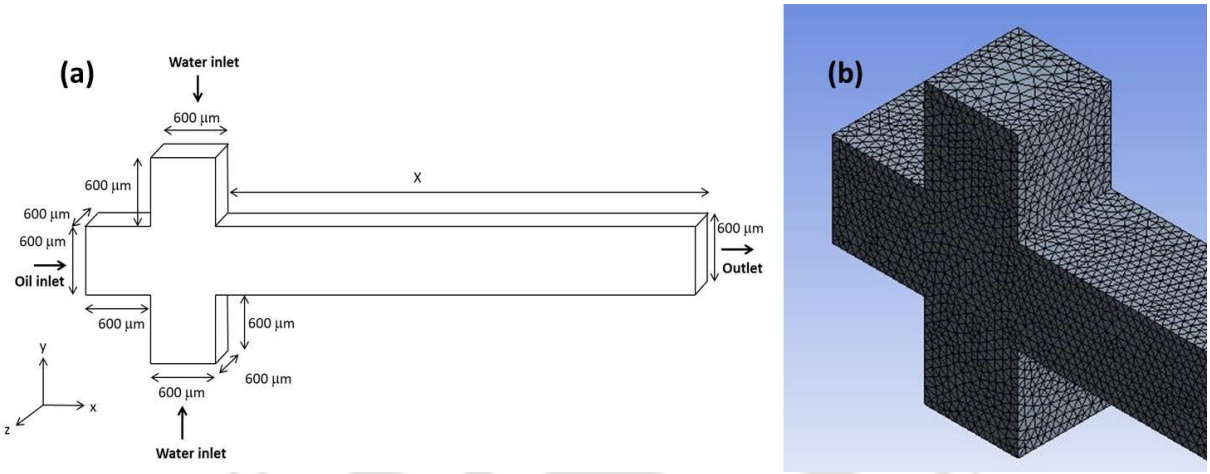

Figure 5b.1. (a) Computational domain; and (b) Mesh

Table 5b.1. Length of the channel

Variables	**Dimensions (in µm)**
X	7000 (dimension taken for simulating the dripping regime) 14000 (dimension taken for simulating the jetting regime)

Water (continuous phase) occupied the channel at first, and subsequently, oil (dispersed phase) and water passed through the inlets. Atmospheric pressure was chosen as the operational pressure. At x = 0 and y = 0, $u_x = u_{oil}$ and $u_y = 0$; at x = 0.6 mm and y = 1.2 mm, $u_y = u_{water}$ and $u_x = 0$; and at x = 0.6 mm and y = -0.6 mm, $-u_y = u_{water}$ and and $u_x = 0$. Impermeable and non-slip characteristics were imposed on the walls. At the outflow, a gauge

pressure of 0 Pa was employed. According to the Courant number, appropriate time steps were chosen.

PDMS (polydimethylsiloxane) and water have been selected as the two liquid phases for the study, and their properties are listed below in Table 5b.2.

Table 5b.2. Fluid properties [1]

Fluids Properties	**Water**	**PDMS (polydimethylsiloxane)**
Density	997 kg/m3	920 kg/m3
Viscosity	0.001 Pa.s	0.011 Pa.s
Oil-water interfacial tension	0.0118 N/m	
Contact angle of oil on PMMA in water	140º	

5b.2.2. Grid independence, code verification, and validation

Using three different tetrahedral mesh (47585, 95171 and 144199 cells), a grid independence study was conducted to determine the optimal grid size (Figure 5b.2). Optimum grid size was confirmed based on the minimum % deviation of dimensionless droplet length (L/W_c) with respect to literature data reported by Fu et al. [1]. The computational results were converged across (10^{-5}) time steps. There was a residual of 10^{-3} for both the continuity and velocity function [31]. Figure 5b.2 represents comparison of the simulated data with the

experimental data of Fu et al. [1]. X and Y axis represent continuous phase velocity and dimensionless droplet length (L/W_c) respectively at oil flow rate (Q_o) of 100 µL/min. The plot indicates that the values obtained from the 144199 cells are closer to the experimental data. For detailed analysis, values were extracted and compared in Table 5b.3. Mesh with 144199 cells confirms a deviation of 5.7 %, which is the lowest among three. The deviation of grid with 95171 and 47585 cells are 9.1 % and 12.1 % respectively. So, in this respect, we have chosen grid with 144199 cells.

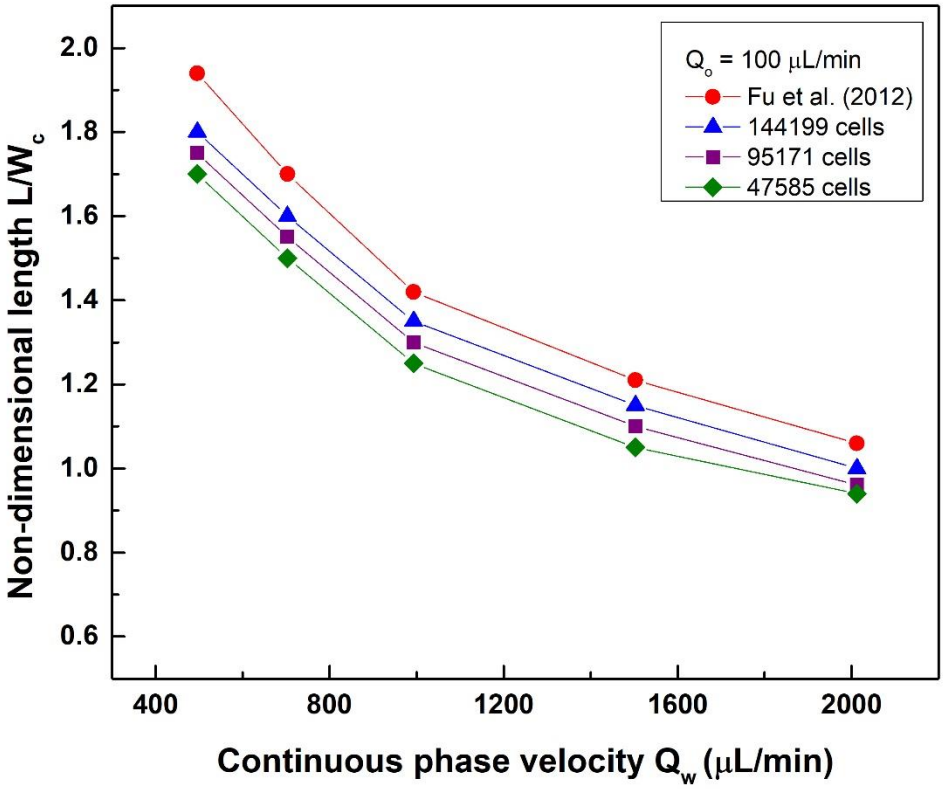

Figure 5b.2. Plot for grid independency study with mesh of 47585, 95171 and 144199 cells. Red symbols represents experimental data taken from Fu et al. [1]. Green, violet and blue symbols indicate results obtained from mesh having cells of 47585, 95171 and 144199 respectively

Table 5b.3. Comparisons of experimental dimensionless droplet length with simulated results obtained from the different grid's sizes

Grid	**No. of cells**	**Experimental L/W_c**	**Simulated L/W_c**	**Percentage deviation** $\left(\frac{Exp-Sim}{Exp}\right)x100$
Grid-1	47585	1.94	1.7	12.3
		1.7	1.5	11.8
		1.42	1.25	11.9
		1.21	1.05	13.2
		1.06	0.94	11.3
		Average error		***12.1***
Grid-2	95171	1.94	1.75	9.7
		1.7	1.55	8.8
		1.42	1.3	8.4

		1.21	1.1	9
		1.06	0.96	9.4
		Average error		***9.1***
Grid-3	144199	1.94	1.8	7.2
		1.7	1.6	5.8
		1.42	1.35	4.9
		1.21	1.15	4.9
		1.06	1	5.6
		Average error		***5.7***

We have verified the code employed in the solver against the standard velocity profile equation adopted from McCabe, Smith, and Harriott as given below,

$$\frac{u}{u_{\max}} = 1 - \left(\frac{r}{r_w}\right)^2 \qquad (5b.2.2.1)$$

A comparison is shown in Figures 5b.3. Figure 5b.3 depicts a velocity profile at the section A-A as marked in the Figure 5b.3a, which is placed a little far from the nose of the droplet. The graphic depicts a parabolic velocity profile, which is particularly evident in the event of a fully developed flow, as well as a velocity profile computed using a benchmark problem (Eq. 5b.2.2.1). We have plotted normalized velocity and radial distance from the

center along the X and Y axis respectively (Figure 5b.3b). The figure gives a good agreement between two.

Figure 5b.4a and 5b.4b depicts us streamline function contour for continuous phase and dispersed phase respectively. They both notify us about formation of curl at the junction of flow-focusing geometry at t = 0.094 s. This formation of curl accords with the results of Fu et al. [1].

This confirms the verification of the code with a higher accuracy.

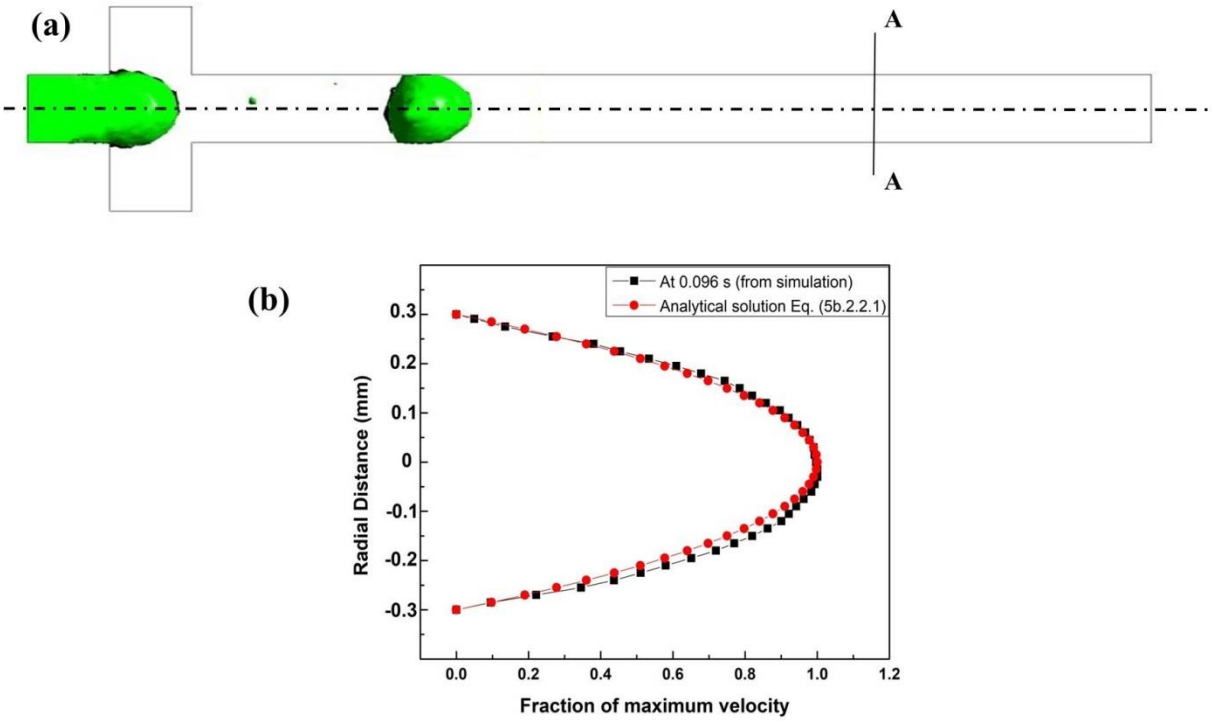

Figure 5b.3. Velocity profile at the section A-A confirms the code verification. The profile has been captured at a time step of 0.096 s: (a) Sectional plane (A-A) along with Iso-surface visualization; and (b) Black color represents the parabolic velocity profile captured from

simulation and red color represents the parabolic velocity profile obtained from standard velocity profile equation (5b.2.2.1)

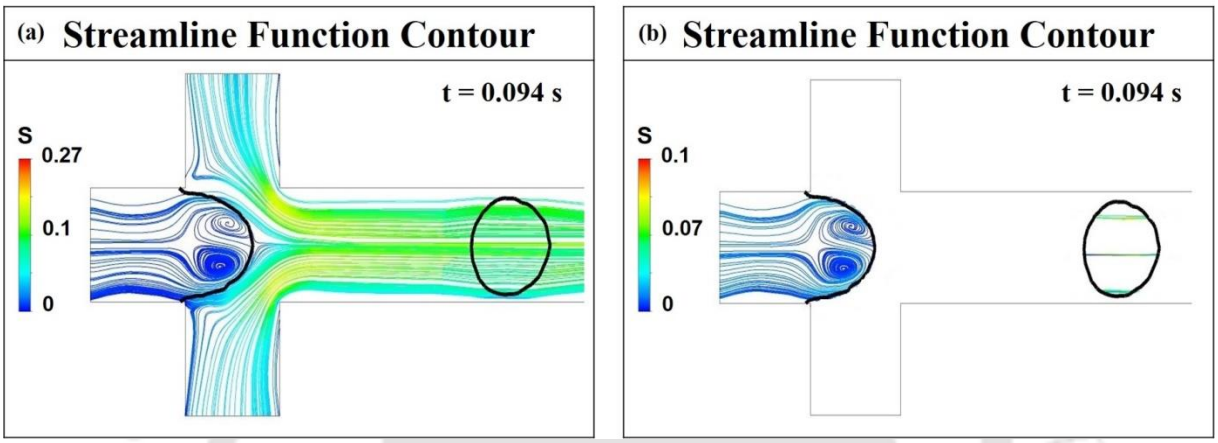

Figure 5b.4. Streamline function contour depicting curl at the junction of flow-focusing geometry: (a) For continuous phase; and (b) For dispersed phase

5b.3. RESULTS AND DISCUSSIONS

The present work investigates the effect of the viscosity ratio, surface tension and wettability on droplet generation using 3D simulation. The frequency of droplet, non-dimensional droplet length, droplet volume, and droplet velocity has been calculated in each of the cases. A flow pattern map has been developed identifying the dripping and jetting regimes. A comparison between normal geometry and two different constricted geometries (having different orifice lengths) based on the frequency of droplet, non-dimensional droplet length, droplet volume and droplet velocity has been made for both dripping and jetting

regimes. Prediction of simulated non-dimensional droplet length has also been made using dimensional analysis.

5b.3.1 Effect of physicochemical parameters (dispersed phase viscosity, interfacial tension, and wettability) on the dripping regime

The effect of various physicochemical parameters such as viscosity ratio, interfacial tension, and wettability on the dripping regime has been observed. Simulations were performed at dispersed phase velocity, V_o = 0.014 m/s and continuous phase velocity, V_w = 0.05 m/s.

5b.3.1.1 Effect of viscous force on dripping flow

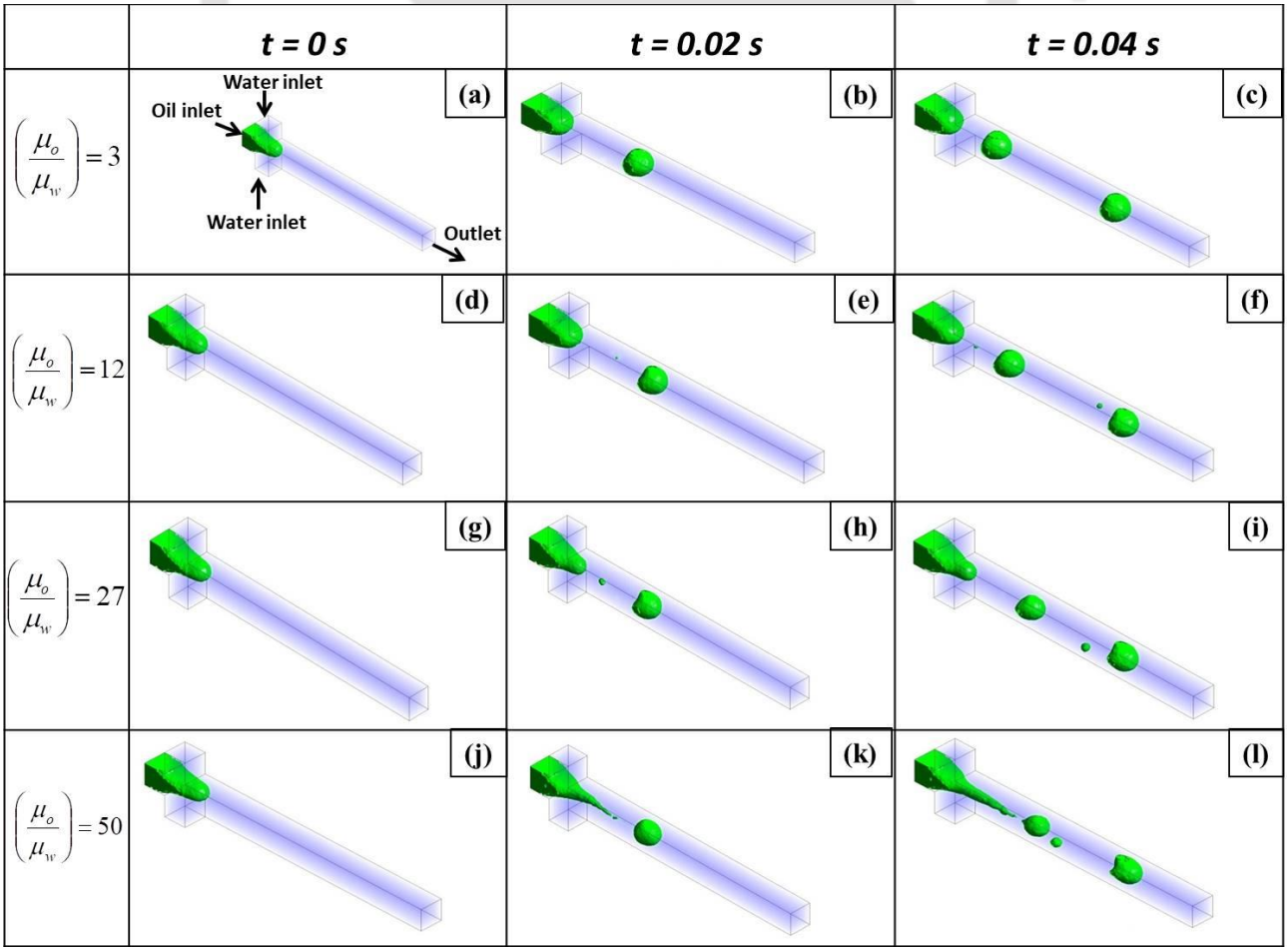

Figure 5b.5. Time variation of Iso-surface visualization of dripping regime at different oil-water viscosity ratio

From Figure 5b.5, it was observed that PDMS droplets were formed in a continuous water medium. The dispersed phase and continuous phase is represented by green and light blue colour in the figure. The same colour terminology has been maintained throughout the manuscript. The droplets became smaller in size, and the generation per unit time increases with increase in the oil-water viscosity ratio. This is because increasing the oil-water viscosity ratio means increasing the viscous force. This increases the shear force acting on the dispersed phase. Moreover, now, the shear force is greater than the interfacial tension. This leads to the breakup of the dispersed thread faster, generating tiny droplets with more no. of counts per unit time, represented in Figures 5b.6a and 5b.6b.

As the non-dimensional droplet length decreases with increased oil-water viscosity, the droplet volume also decreases, presented in Figure 5b.6c. Figure 5b.6d represents the droplet velocity in the channel. The droplet velocity increases with increase in oil-water viscosity ratio. As the viscous force increases, the breakup of the dispersed thread become faster leads to generation of more droplets per count with high velocity.

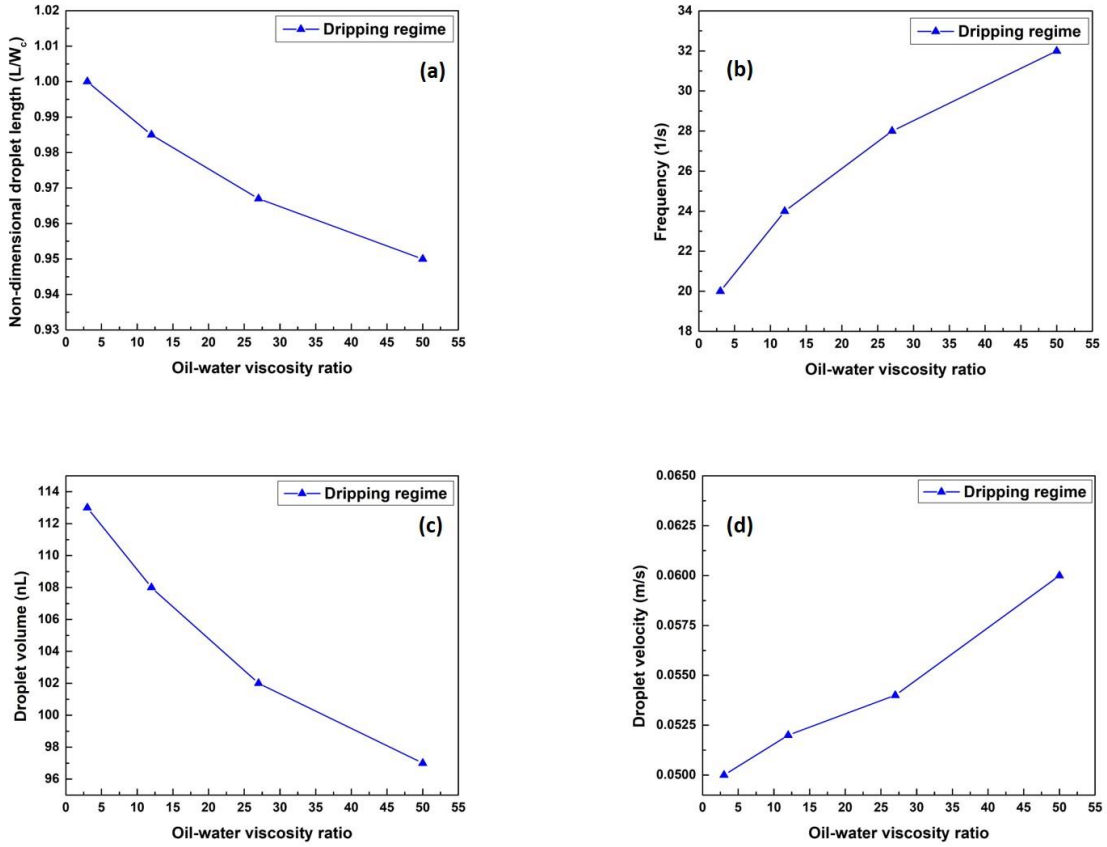

Figure 5b.6. (a) Non-dimensional droplet length vs oil-water viscosity ratio for dripping regime; (b) Frequency of droplet formation vs oil-water viscosity ratio for dripping regime; (c) Droplet volume vs oil-water viscosity ratio for dripping regime; and (d) Droplet velocity vs oil-water viscosity ratio for dripping regime

5b.3.1.2 Effect of surface force on dripping flow

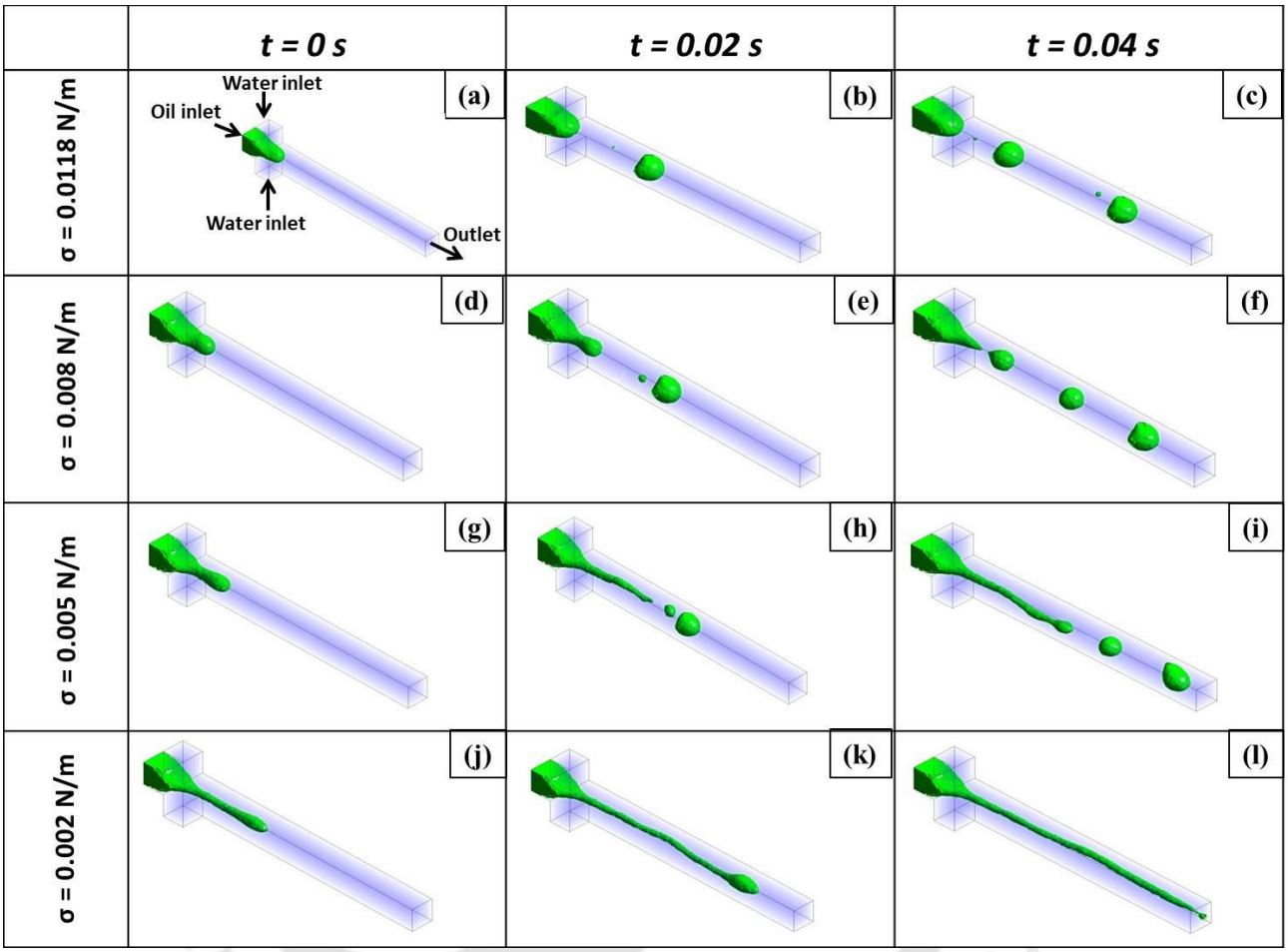

Figure 5b.7. Time variation of Iso-surface visualization of dripping regime at different surface tension values

From Figure 5b.7, it can be observed that droplets of PDMS were formed in a continuous water medium. Initially, the interfacial tension of the system is 0.0118 N/m. Then it has been decreased to 0.008 N/m, 0.005 N/m, and 0.002 N/m. Droplet size decreases with a decrease in the interfacial tension. At 0.008 N/m, small droplets were generated compared to the droplets' size at 0.0118 N/m. At 0.005 N/m, smaller droplets appear compared to the

droplets' size at 0.008 N/m. At 0.002 N/m, a long continuous thread of oil is formed in a water medium instead of oil droplets.

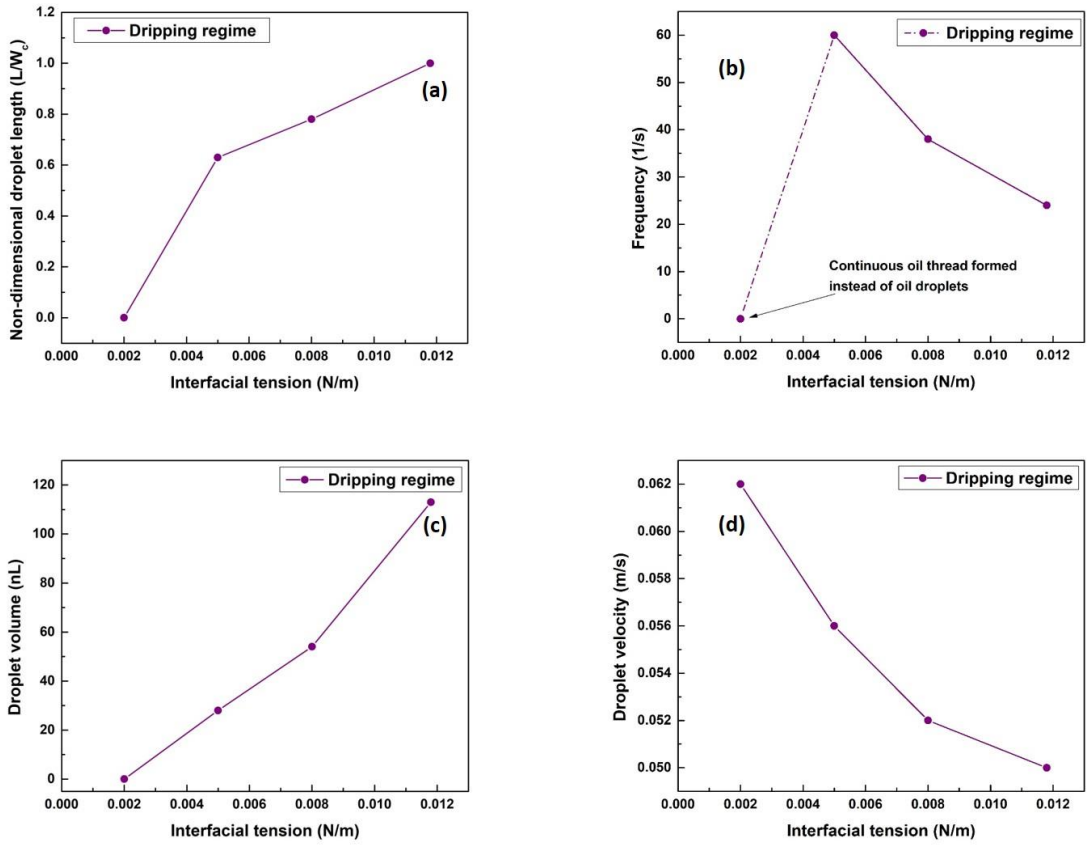

Figure 5b.8. (a) Non-dimensional droplet length vs interfacial tension for dripping regime; (b) Frequency of droplet formation vs interfacial tension for dripping regime; (c) Droplet volume vs interfacial tension for dripping regime; and (d) Droplet velocity vs interfacial tension for dripping regime

Figure 5b.8b tells us that frequency is 0 Hz for 0.002 N/m as continuous oil thread is formed instead of oil droplets. Droplets onset at the interfacial tension of 0.005 N/m and frequency at this condition is 60 Hz. Then, it decreases continuously with an increase in the interfacial tension. For 0.005 N/m, the viscous force is comparable to surface tension force, so

the dispersed thread breaks up faster, generating smaller droplets with high frequency. For 0.008 N/m, the surface tension force increased slightly, so comparatively bigger droplets were generated with lower frequency. Moreover, for 0.0118 N/m, the surface tension force has increased further, generating the biggest droplet with the lowest frequency. So, non-dimensional droplet length increases with interfacial tension and frequency decreases with increase in surface tension, as presented in Figure 5b.8a and 5b.8b [32]. As the non-dimensional droplet length increases with interfacial tension, the droplet volume also increases, as shown in Figure 5b.8c. Figure 5b.8d represents the variation of droplet velocity with interfacial tension. It decreases with an increase in interfacial tension. With the increase in interfacial tension, the dispersed thread breaks slowly, generating bigger droplets with low velocity.

5b.3.1.3 Effect of wettability on dripping flow

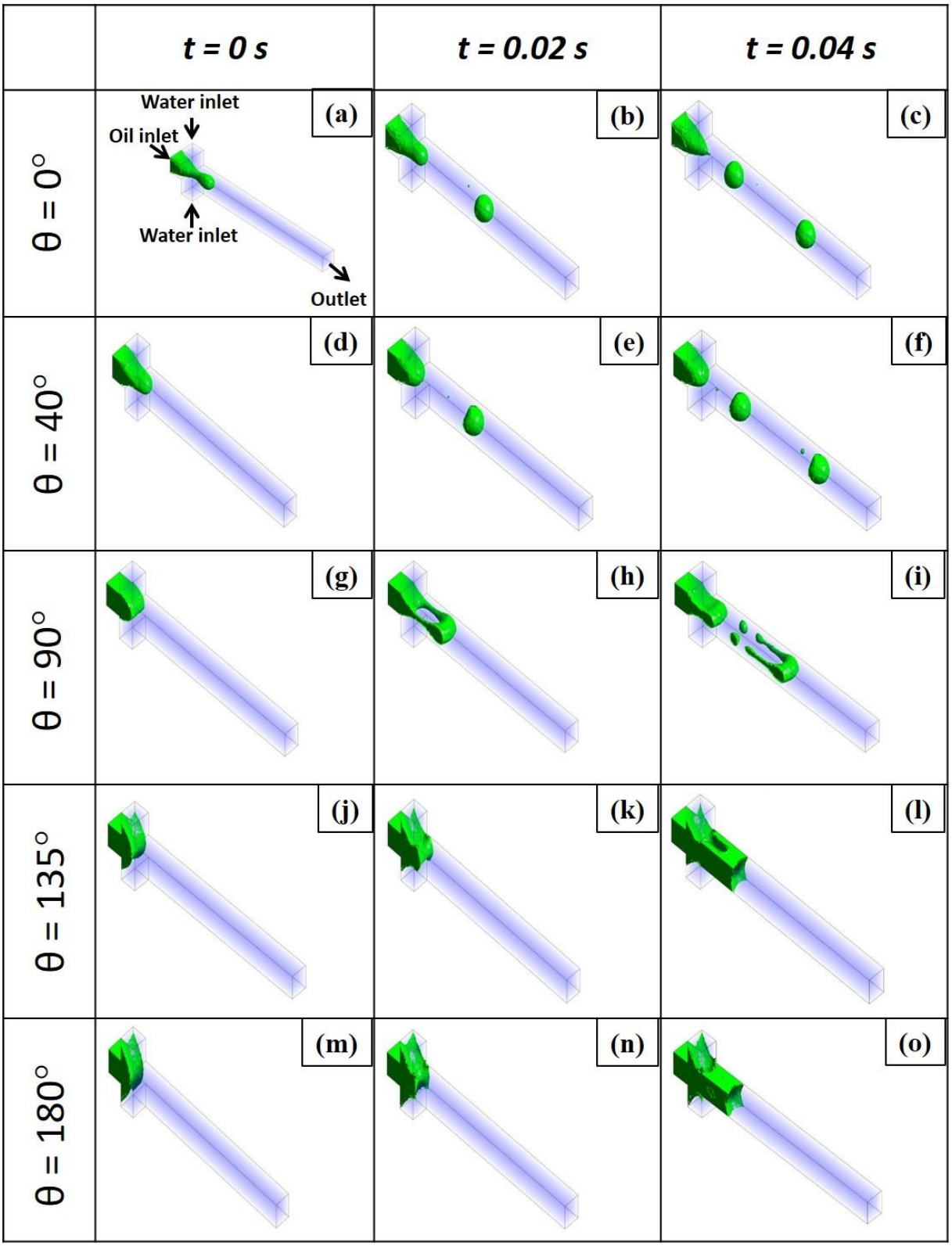

Figure 5b.9. Time variation of Iso-surface visualization of dripping regime at different contact angles

Figure 5b.9 depicts the effect of contact angle on droplet generation. Here θ is the angle created by the water droplet on the PMMA surface in the presence of oil. When both fluids enter into the channel, it was seen that at θ < = 90º, the channel is entirely hydrophilic. So, the water acts as the continuous phase, and droplets of PDMS formed in it. As we gradually increase the θ above 90°, the channel becomes hydrophobic. In that case, the water became the dispersed phase in the continuous oil medium. At θ = 180º, the channel becomes superhydrophobic. So, a continuous thread of water was formed in the continuous oil medium.

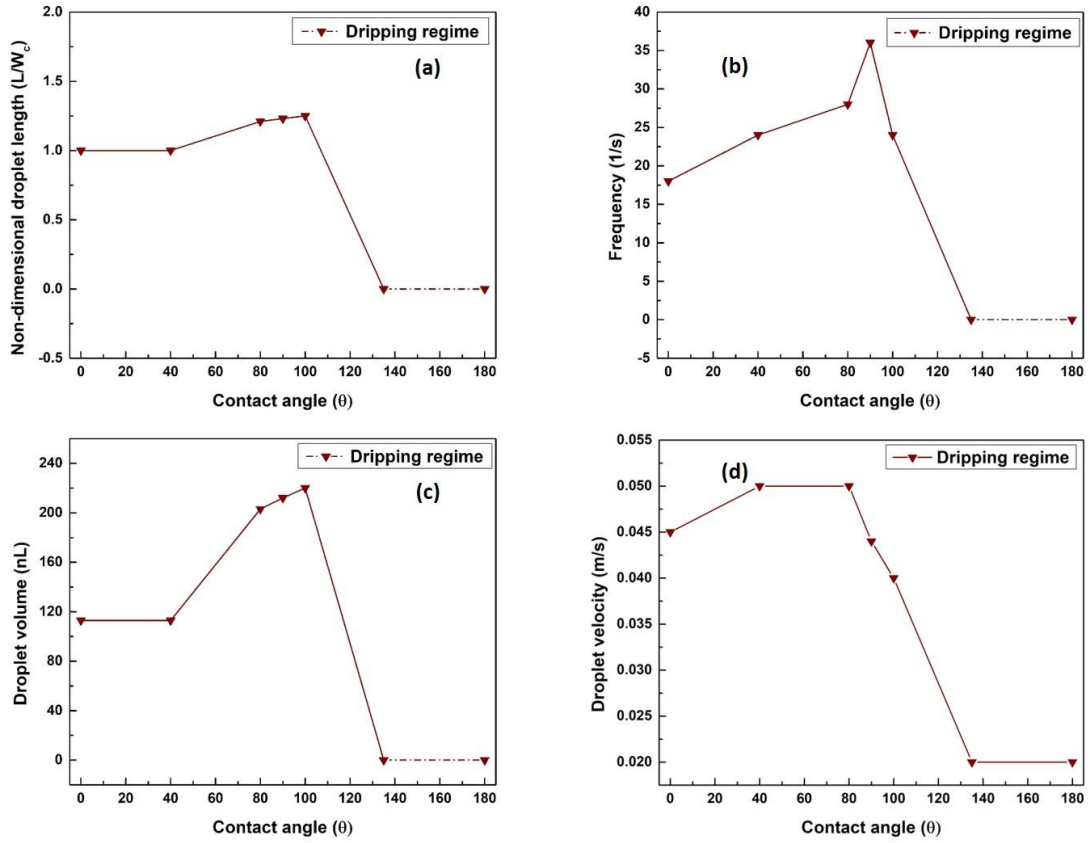

Figure 5b.10. (a) Non-dimensional droplet length vs contact angle for dripping regime; (b) Frequency of droplet formation vs contact angle for dripping regime; (c) Droplet volume vs contact angle for dripping regime; and (d) Droplet velocity vs contact angle for dripping regime

Figure 5b.10a represents the variation of non-dimensional droplet length with contact angle. The non-dimensional droplet length is linear for $\theta = 0°$ to $\theta = 90°$. As θ below 90°, the channel is hydrophilic in nature. So, surface tension force dominates over the elasticity due to which smaller droplets formed. As we increase θ above 90°, the hydrophobicity increases. This increases the droplet length as elasticity dominates over surface tension force. At $\theta = 100°$ (hydrophobic), we got the highest value of non-dimensional droplet length of 1.25. At $\theta = 135°$ (hydrophobic) and $\theta = 180°$ (superhydrophobic), a long continuous thread of water is forming in the oil medium. The corresponding droplet volume data is shown in Figure 5b.9c.

For $0° < \theta < 90°$, the adhesive force of water on the channel wall, i.e., a wall resistance to the flow is increasing for $\theta = 0°$ to 90°. At $\theta = 40°$ (hydrophilic), the continuous phase (water), unable to cut the dispersed phase (PDMS) thread faster, leads to the generation of fewer droplet counts per unit time with low droplet velocity. At $\theta = 0°$ (super hydrophilic), the least droplet count is generated per unit time with the lowest droplet velocity than $\theta = 40°$. For $90° < \theta < 180°$, the adhesive force of water on the channel wall, i.e., a wall resistance to the flow is decreasing for $\theta = 90°$ to 180°. At $\theta = 100°$, the dispersed phase (PDMS) restricts the continuous phase (water) to enter the channel, resulting in pressure built-up cause's intermediate slug formation with fewer counts per unit time with less droplet velocity. At $\theta = 135°$, a long thread of water is forming in a continuous oil medium with lesser velocity than θ

= 100°. Similarly, at θ = 180°, a long thread of water is forming in a continuous oil medium with the same velocity as for θ = 135°. In this way, we can say that the frequency increases for θ = 0° to θ = 90° and then decreases for θ = 90° to θ = 180°, as shown in Figure 5b.10b. The value of frequency is highest for θ = 90°. Also, the droplet velocity increases for θ = 0° to θ = 80°, then it decreases for θ = 80° to θ = 180°, as shown in Figure 5b.10d.

5b.3.2 Jetting regime

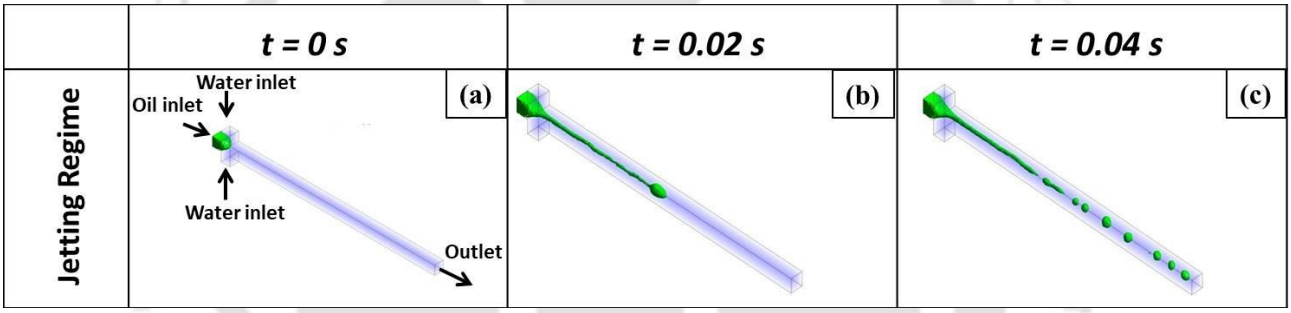

Figure 5b.11. Time variation of Iso-surface visualization of jetting regime

In case of jetting flow, dispersed phase droplet were formed at distant point from the junction. A representative result of the sequential time steps of such flow is shown in Figure 5b.11 at oil and water velocity of 0.037 m/s (V_o) and 0.15 m/s (V_w) respectively. In jetting mode, raising the continuous phase velocity increases the capillary pressure created at the end of the thread, causing the thread to take a long-form; the instability of this long jet causes the head to detach and form droplets [28].

Table 5b.4. Values of frequency (1/s), non-dimensional droplet length (L/W_c), droplet volume (nL), droplet velocity (m/s) in jetting regime for $\frac{\mu_o}{\mu_w}$ = 12, σ = 0.0118 N/m and θ = 40° (water wetting the PMMA surface in the presence of PDMS) at V_o = 0.037 m/s and V_w = 0.15 m/s

	Frequency (1/s)	**Non-dimensional droplet length (L/W_c)**	**Droplet volume (nL)**	**Droplet velocity (m/s)**
Values	120	0.67	33.4	0.24

Table 5b.4 represents the values of frequency (1/s), non-dimensional droplet length (L/W_c), droplet volume (nL), droplet velocity (m/s) for jetting regime for oil-water viscosity ratio = 12, σ = 0.0118 N/m and θ = 40° (water wetting the PMMA surface in the presence of PDMS) at V_o = 0.037 m/s and V_w = 0.15 m/s.

5b.3.3 Flow pattern map

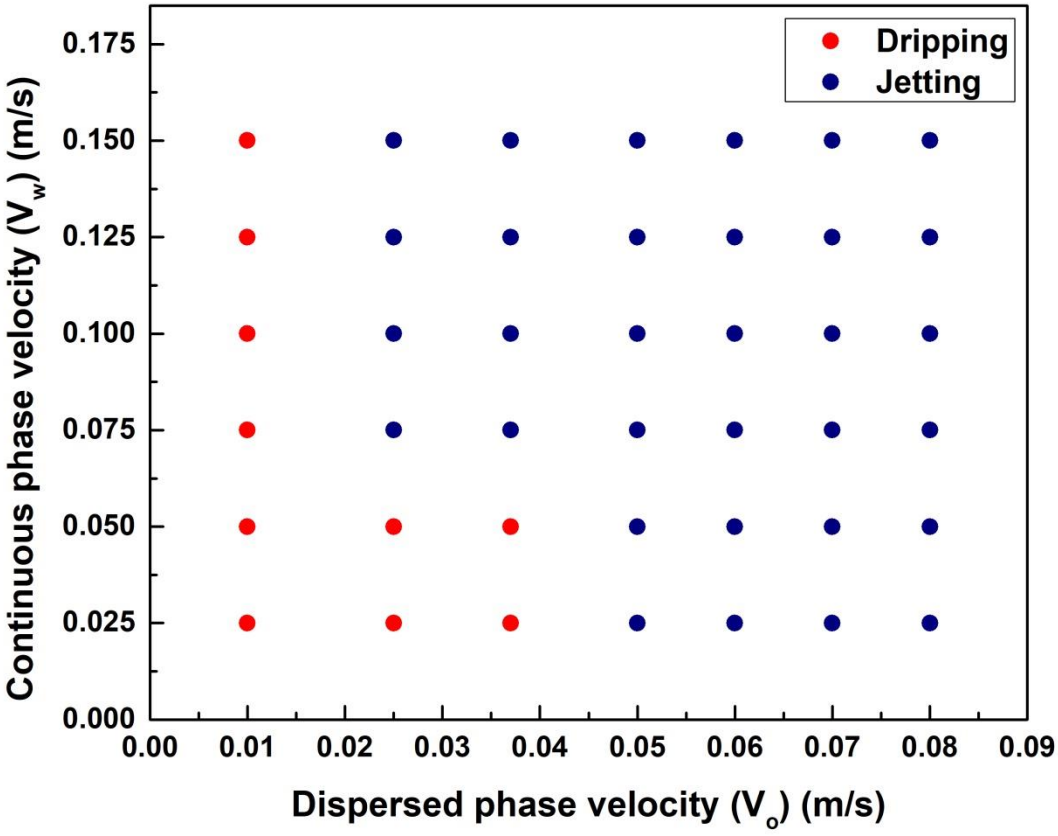

Figure 5b.12. Flow pattern map indicating the dripping and jetting regime for $\frac{\mu_o}{\mu_w}$ = 12, σ = 0.0118 N/m and θ = 40° (water wetting the PMMA surface in the presence of PDMS)

The dripping and jetting regime for oil-water viscosity ratio = 12, σ = 0.0118 N/m, and θ = 40° (water wetting the PMMA surface in the presence of PDMS) is shown in Figure 5b.12. The flow mode is determined by the flow velocities of both phases. Dripping and jetting were the most common flow regimes observed. Droplets form around the nozzle area in the case of dripping regimes. The dispersed phase's velocity is fast enough; the continuous

phase's shear stress is strong enough and comparable to the surface tension force; and high capillary pressure is created at the dispersed thread's end, causing it to break up into droplets. At low dispersed phase velocity, the dripping regime emerges. The jetting regime was noticed as the dispersed phase velocity was increased. Due to the large inertia force, a long jet is produced. The jet's instability caused it to break up and create droplets at the end [28].

A flow pattern map has been developed indicating the dripping and jetting regime, as shown in Figure 5b.12. The jetting regime occupies the most portion of the map. It stays on the central and right parts of the map. At the same time, the dripping regime occupies a small portion and stays in the left part of the map.

5b.3.4 Effect of constriction

The effect of constriction has been investigated for both dripping and jetting regimes. Two flow-focusing geometries with constriction having different orifice lengths have been developed, and simulations were performed. Frequency (1/s), non-dimensional droplet length (L/W_c), droplet volume (nL) and droplet velocity (m/s) has been calculated for the constricted geometries and compared with the normal geometry for dripping and jetting regimes. A schematic diagram of the constricted geometry is given in Figure 5b.13. The lengths of the orifice in case of the contricted geometries is given in Table 5b.5.

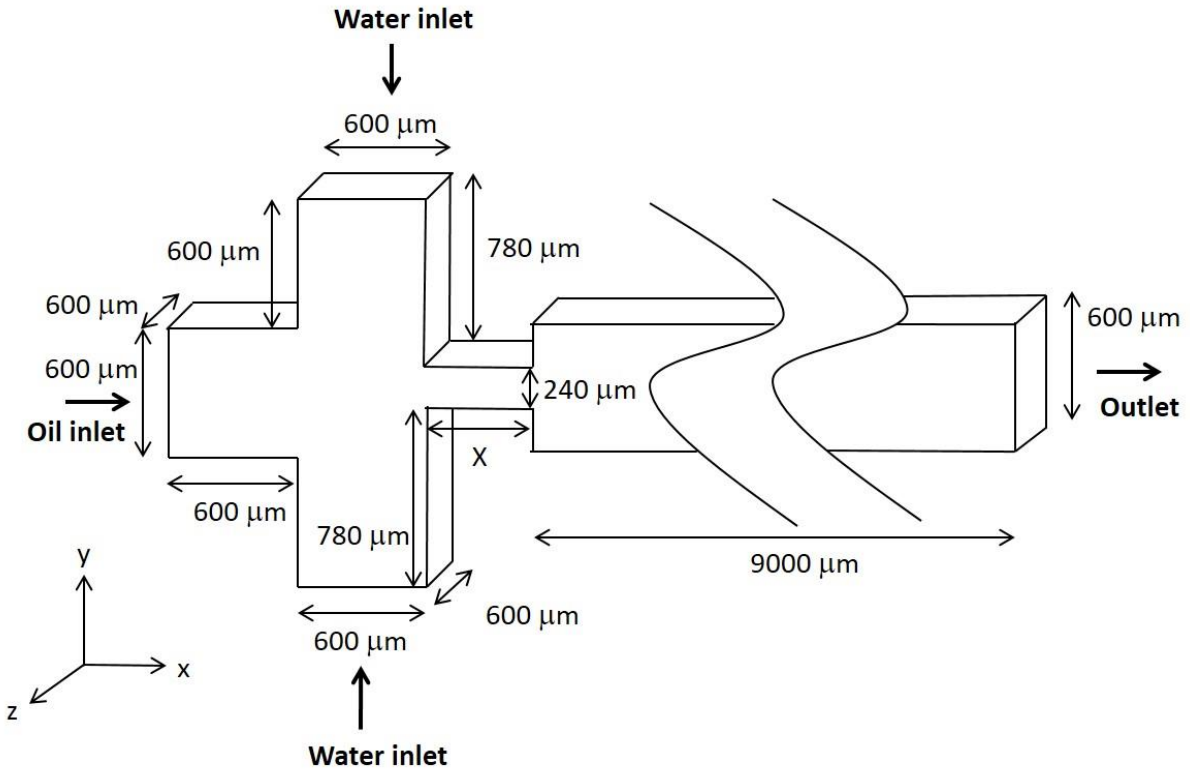

Figure 5b.13. Constricted geometry

Table 5b.5. Length of the orifice in constricted geometry 1 and 2

Constricted geometry	**Value of X (in µm) (Length of the orifice)**
Constricted geometry 1	180
Constricted geometry 2	600

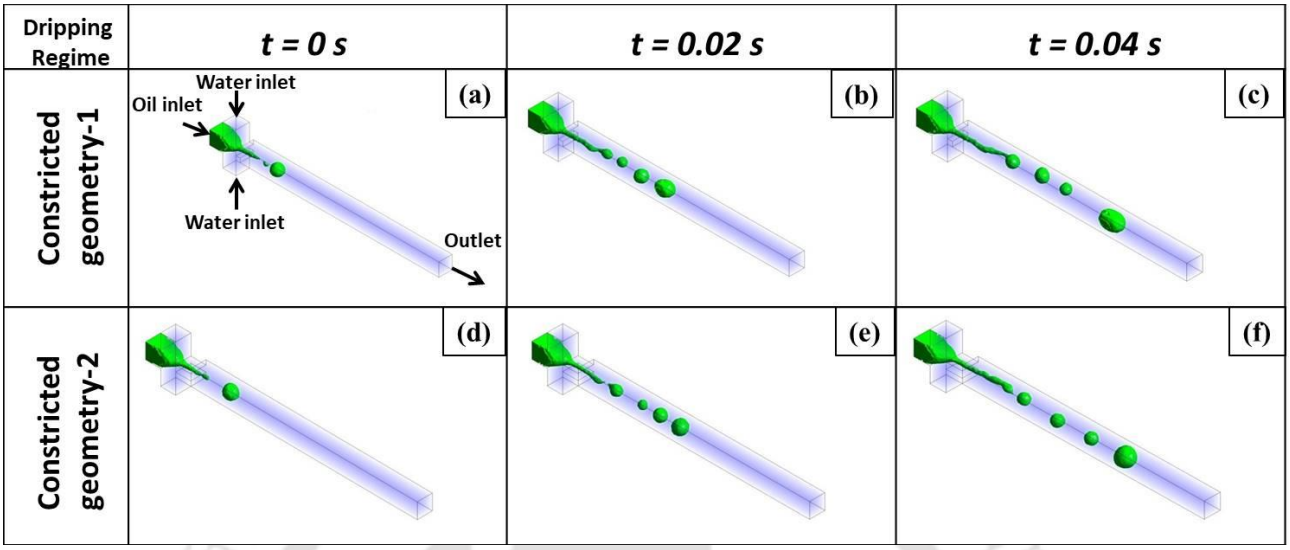

Figure 5b.14. Time variation of Iso-surface visualization of dripping regime at constricted geometry 1 and constricted geometry 2

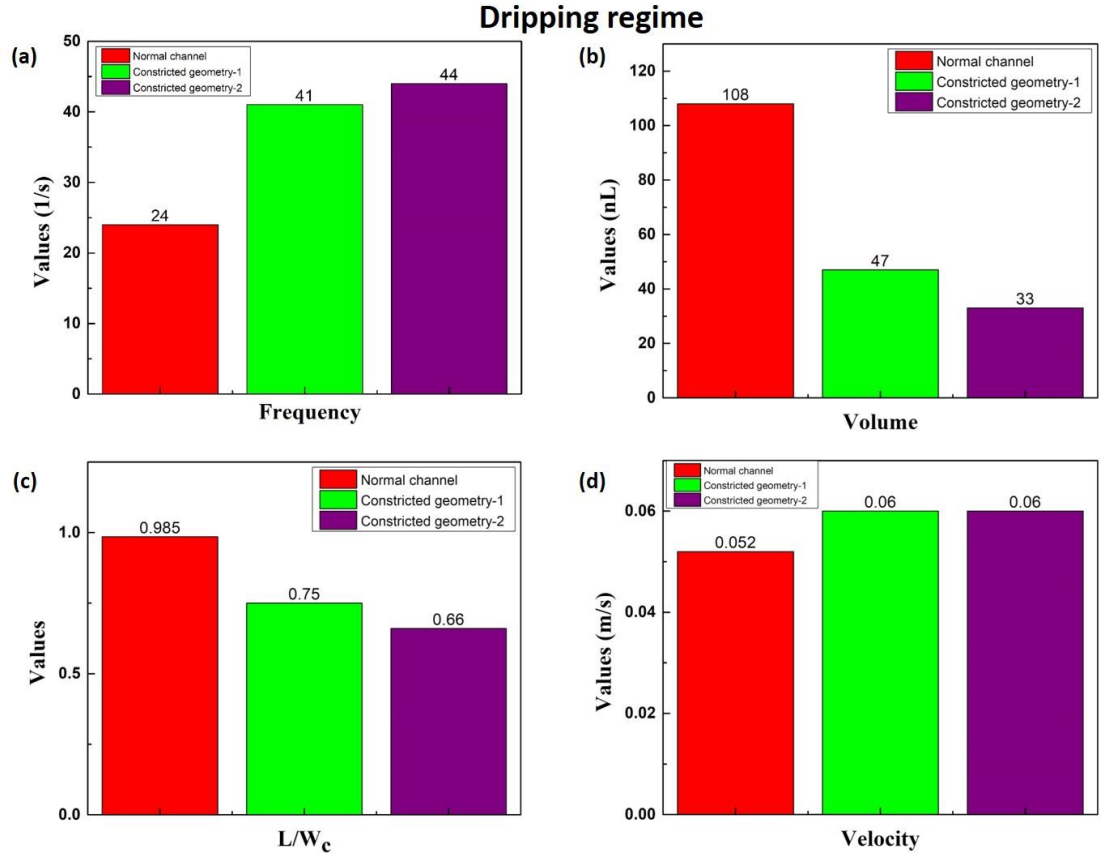

Figure 5b.15. Comparison between normal geometry, constricted geometry 1 and constricted geometry 2 in dripping regime for $\frac{\mu_o}{\mu_w}$ = 12, σ = 0.0118 N/m and θ = 40° (water wetting the PMMA surface in the presence of PDMS) at V_o = 0.014 m/s and V_w = 0.05 m/s

Figure 5b.14 represents droplet generation in dripping regime for oil-water viscosity ratio = 12, σ = 0.0118 N/m and θ = 40° (water wetting the PMMA surface in the presence of PDMS) at V_o = 0.014 m/s, V_w = 0.05 m/s in flow-focusing constricted geometry 1 and constricted geometry 2 with respect of time. Figure 5b.15 represents a comparison between normal geometry, constricted geometry 1 and constricted geometry 2 for the dripping regime. In the case of constricted geometry 1, introducing a constriction (having orifice length = 180

μm) near the inlet leads to narrowing of the passage near the channel inlet. This increases the pressure at the constricted zone, increasing the shear force applied by the continuous phase, which allows cutting the dispersed phase thread head faster, producing many droplets in a short time with small sizes. Increasing the orifice length further (600 μm) leads to further increases in the pressure at the constricted zone. This allows cutting the dispersed phase thread head even faster, producing many more droplets in a much shorter time with much smaller sizes. So, the value of frequency is higher in constricted geometry 2; the non-dimensional droplet length is smallest in the case of constricted geometry 2, droplet volume is lowest in the case of constricted geometry 2. The value of droplet velocity is near about the same in all three geometries.

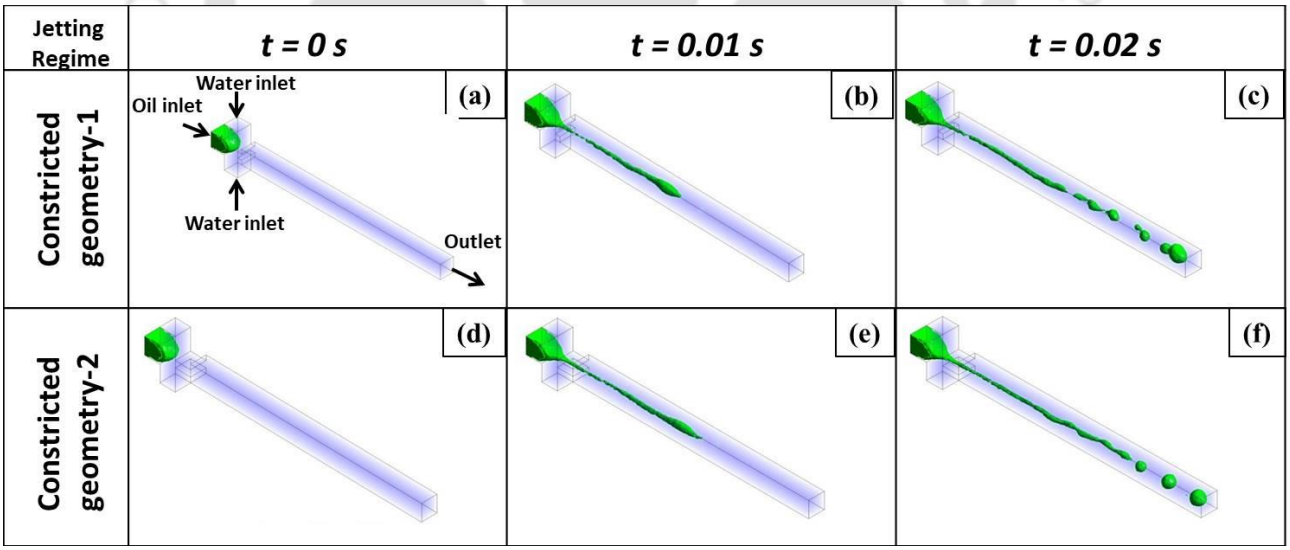

Figure 5b.16. Time variation of Iso-surface visualization of jetting regime at constricted geometry 1 and constricted geometry 2

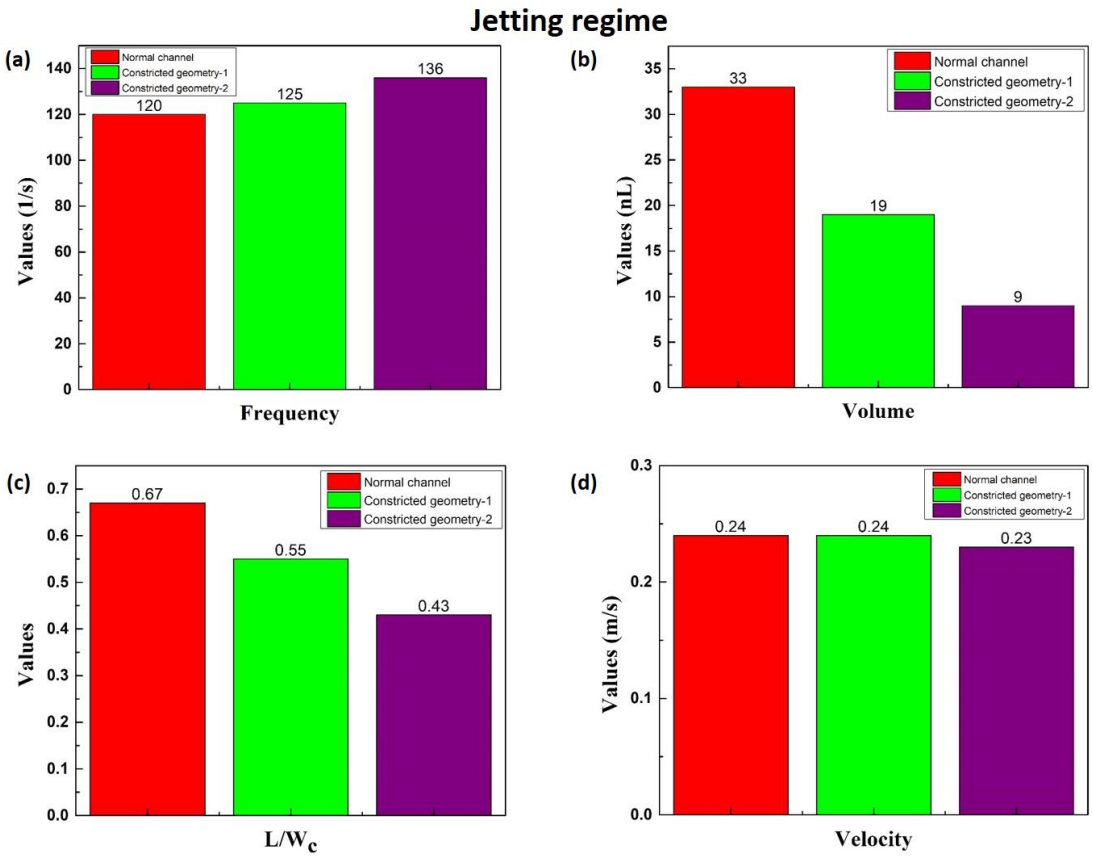

Figure 5b.17. Comparison between normal geometry, constricted geometry 1 and constricted geometry 2 in jetting regime for $\frac{\mu_o}{\mu_w}$ = 12, σ = 0.0118 N/m and θ = 40° (water wetting the PMMA surface in the presence of PDMS) at V_o = 0.037 m/s and V_w = 0.15 m/s

Figure 5b.16 represents droplet generation in jetting regime for oil-water viscosity ratio = 12, σ = 0.0118 N/m and θ = 40° (water wetting the PMMA surface in the presence of PDMS) at V_o = 0.037 m/s, V_w = 0.15 m/s in flow-focusing constricted geometry 1 and constricted geometry 2 with respect of time. Figure 5b.17 represents a comparison between normal geometry, constricted geometry 1 and constricted geometry 2 for the jetting regime. In the case of constricted geometry 1, introducing a constriction (having orifice length = 180

μm) near the inlet leads to narrowing of the passage near the channel inlet. This increases the pressure at the constricted zone, increasing the shear force applied by the continuous phase, which allows cutting the dispersed phase thread head faster, producing many droplets in a concise time with small sizes. Increasing the orifice length further (600 μm) leads to further increases in the pressure at the constricted zone. This allows cutting the dispersed phase thread head even faster, producing many more droplets in a much shorter time with much smaller sizes. So, the value of frequency is higher in constricted geometry 2; the non-dimensional droplet length is smallest in the case of constricted geometry 2, droplet volume is lowest in the case of constricted geometry 2. The value of droplet velocity is near about the same in all three geometries.

5b.4. DIMENSIONAL ANALYSIS

5b.4.1 Set up

We have followed the methodology of Buckingham's Pi-Theorem to derive the dimensionless groups for the present system using the mixer properties of the working fluids. Dimensional analysis has been set up for general two-phase flow (both the liquid are immiscible to each other) for the present system. The first step in dimension analysis is to list all the parameters and then state their dimensions concerning mass 'm', length 'l', and time 't'.

The list that will be analyzed is:

L (length of the droplet) (l)

U_m (Mixed velocity) (l/t)

ρ_m (Mixed density) (m/l^3)

μ_m (Mixed viscosity) (m/lt)

σ (i.e. interfacial tension) (m/t^2)

W_c (width of the channel) (l)

Here, $U_m = V_o + V_w$ (V_o = oil velocity and V_w = water velocity)

ρ_m = (Hold up of water phase * Density of water) + (Hold up of oil phase * Density of oil)

μ_m = (Viscosity of oil + Viscosity of water)/ ((Viscosity of water * Mass fraction of water) + (Viscosity of oil * Mass fraction of oil))

5b.4.2 Procedure

There are six parameters listed i.e. "n" = 6. There are three primary parameters i.e. length (l), mass (m) and time (t) i.e. “m” = 3.

So, number of independent groups = 6-3 = 3

So, $f(\Pi_1, \Pi_2, \Pi_3) = 0$

Where, f is some function, or in an alternate expression:

$\Pi_1 = f_1(\Pi_2, \Pi_3)$

where f_1 is some function different to function f .

Taking an arbitrary choice of three parameters: ρ_m, U_m, W_c

Group 1: $\Pi_1 = \{(\rho_m)^0, (U_m)^0, (W_c)^{-1}\} (L) = L/ W_c$

Group 2: $\Pi_2 = \{(\rho_m)^{-1}, (U_m)^{-1}, (W_c)^{-1}\} (\mu_m) = \mu_m / \rho_m W_c U_m$

Group 3: $\Pi_3 = \{(\rho_m)^{-1}, (U_m)^{-2}, (W_c)^{-1}\}\ (\sigma) = \sigma / \rho_m W_c U^2_m$

Therefore, we have

$$\frac{L}{W_c} = \lambda\left(\frac{\mu_m}{\rho_m U_m W_c}\right)^a \left(\frac{\sigma}{\rho_m U_m^2 W_c}\right)^b \quad (5b.4.2.1)$$

Where λ, a and b are constants. These constants are evaluated using multiple regression analysis in Microsoft Excel using the non-dimensional droplet length data acquired from our simulation. From the analysis, we have estimated λ as 4.75, a as 0.38 and b as 0.007 and equation (5b.4.2.1) becomes

$$\frac{L}{W_c} = 4.75\left(\frac{\mu_m}{\rho_m U_m W_c}\right)^{0.38} \left(\frac{\sigma}{\rho_m U_m^2 W_c}\right)^{0.007} \quad (5b.4.2.2)$$

The regression coefficient and standard error of equation (5b.4.2.2) are 0.99 and 0.01, respectively. The proposed correlation using dimensionless analysis gave a prediction of simulated non-dimensional droplet length with an average absolute error of 1.8%, given in Figure 5b.18. The present correlation has a range of Mixer Reynolds number of 2.92 - 91.94 and capillary number in the range of 0.0002 - 0.008.

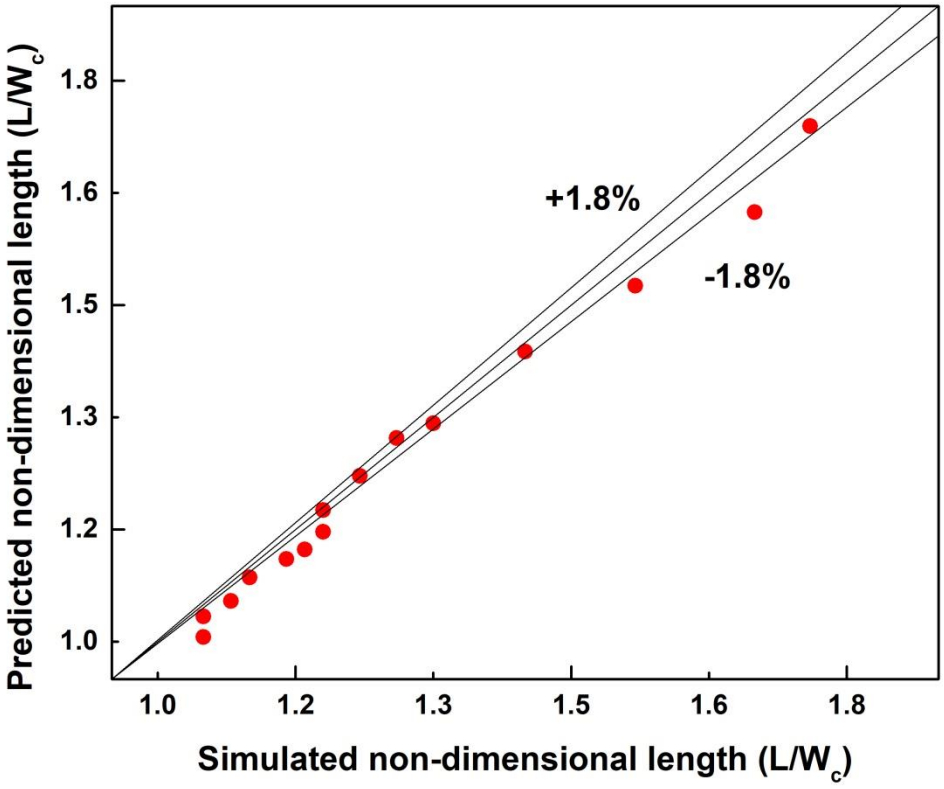

Figure 5b.18. Comparison between predicted and simulated non-dimensional droplet length using Eq. (5b.4.2.2)

5b.5. COMPARISION BETWEEN 2D AND 3D SIMULATION

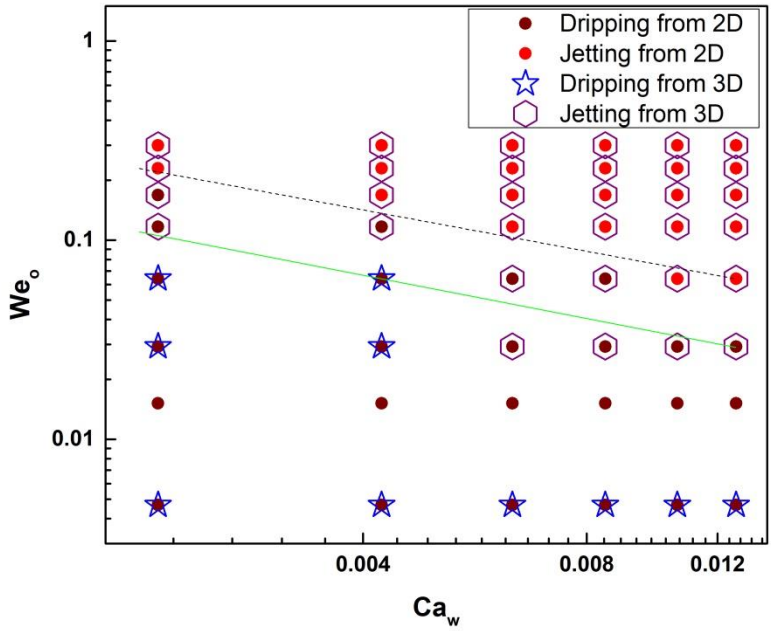

Figure 5b.19. Flow pattern map having 2D and 3D simulation data: black dash line indicates 2D transition line; green solid line indicates 3D transition line

The flow pattern maps obtained from both the 2D and 3D simulations have been overlapped to compare the 2D and 3D simulation results as shown in Figure 5b.19. Figure 5b.19 tells that the overall flow pattern map is similar but there is a deviation in transition boundaries from dripping to jetting. The transition line of 2D simulation has been shifted upwards with respect to the transition line of 3D simulation in the flow pattern map. Due to this, the dripping area is larger in case of 2D as compared to 3D. However, 2D transition boundary closely matches with Fu et al. [1] as discussed in Figure 5a.9. It may be due to using

of not very fine grid in case of 3D simulation. Due to the lack of computational facility, the simulation was not run at very fine grid.

Moreover, 2D and 3D simulations shows some difference in droplet size also but the overall flow pattern map remains almost same. The percentage deviation of the droplet size in 2D and 3D has been calculated. Droplet sizes for four set of velocities has been estimated in 2D and 3D simulation separately. The percentage deviation has been found with respect of 2D results and is shown in Table 5b.6. The average percentage deviation is coming out to be 4.5%.

Table 5b.6. Difference in droplet size in case of 2D and 3D simulation result

Velocity set	Droplet size in 2D (mm)	Droplet size in 3D	Percentage deviation
V_o = 0.01 m/s, V_w = 0.025 m/s	0.95	0.908	4.4
V_o = 0.01 m/s, V_w = 0.05 m/s	0.9	0.86	4.2
V_o = 0.01 m/s, V_w = 0.075 m/s	0.86	0.82	4.6
V_o = 0.01 m/s, V_w = 0.1 m/s	0.81	0.77	4.9
Average percentage deviation			4.5

If someone uses 2D simulation instead of 3D simulation, then non-axisymmetric nature should be implemented in the 2D simulation to improve the results. 3D simulation can capture more accurate flow situation; - It may be axisymmetric or non-axisymmetric.

5b.6. SUMMARY

In this study, 3D-CFD simulations have been carried out to investigate the effect of viscosity, surface tension and wettability on droplet generation using the VOF method. The model has been authenticated with earlier experimental data present in the literature (Fu et al. [1]). We have effectively simulated droplet formation based on viscosity, surface tension and wettability. It has been observed that the droplet became smaller in size with an increase in the oil-water viscosity ratio. The frequency increases with an increase in the oil-water viscosity ratio. On the other hand, droplets became larger with the increase in the interfacial tension. The droplet is not generated at 0.002 N/m (i.e., 0 Hz frequency) as a continuous oil thread is observed. In the present simulation, droplets onset at the interfacial tension of 0.005 N/m and frequency at this condition is 60 Hz. Then, it decreases continuously with an increase in the interfacial tension. Droplet velocity decreases with an increase in the interfacial tension. The effect of wettability was studied by changing wettability angles (θ) (angle created by water droplet on the PMMA surface in the presence of oil) from 0º-180º. For $\theta <= 90º$, water is the continuous phase in which droplets of PDMS were formed. For $\theta > 90$, the water became the dispersed phase in the continuous oil medium. At $\theta = 135°$ and 180º, the channel becomes super hydrophobic, which gives an annular flow configuration in the channel. Here, the oil phase warps the channel surface, and the water phase turns into a continuous thread flowing

through the center of the channel. Wettability also influences the non-dimensional droplet length (L/W_c). The highest value of L/W_c and droplet volumes are 1.25 and 220 nL, respectively, at $\theta = 100°$. The frequency increases from 18-36 Hz for a change of θ from 0°-90° respectively, and then it decreases due to a change of θ from 90°-180°. It is important to note that a water thread is formed beyond $\theta = 135°$. That is why droplet frequency is considered 0 Hz. The droplet velocity increases from 0.045-0.050 m/s for change in θ from 0°-80° and then it decreases from 0.050-0.020 for the θ ranging from 80°-180°. Two flow regimes were identified and have been presented in the form of a phase diagram for oil-water viscosity ratio = 12, $\sigma = 0.0118$ N/m and $\theta = 40°$ (water wetting the PMMA surface in the presence of oil). Comparison between normal geometry and two different constricted geometry (having different orifice lengths) based on non-dimensional droplet length, frequency, droplet volume, droplet velocity has been made for both dripping and jetting regimes at oil-water viscosity ratio = 12, $\sigma = 0.0118$ N/m and $\theta = 40°$ (water wetting the PMMA surface in the presence of oil). It has been found that the value of non-dimensional droplet length and droplet volume is lowest in the case of constricted geometry 2 for both regimes. The frequency value is highest in the case of constricted geometry 2 for both regimes. Droplet velocity value is near about the same for the three geometry configurations for dripping and jetting regimes. The dimensionless analysis gave a prediction of simulated non-dimensional droplet length with an average absolute error of 1.8%. These findings will help understand droplet generation under various physicochemical parameters and directly apply to the microfluidic platform-based device.

REFERENCES

1. Fu, T., Wu, Y., Ma, Y., and Li, H.Z., Droplet formation and breakup dynamics in microfluidic flow-focusing devices: From dripping to jetting, *Chemical Engineering Science*, 2012, vol. 84, no. pp. 207-217.
2. Christopher, G.F. and Anna, S.L., Microfluidic methods for generating continuous droplet streams, *Journal of Physics D: Applied Physics*, 2007, vol. 40, no. 19, pp. R319-R336.
3. Chou, W.-L., Lee, P.-Y., Yang, C.-L., Huang, W.-Y., and Lin, Y.-S., Recent Advances in Applications of Droplet Microfluidics, *Micromachines*, 2015, vol. 6, no. 9, pp. 1249-1271.
4. Ahmadi, F., Samlali, K., Vo, P.Q.N., and Shih, S.C.C., An integrated droplet-digital microfluidic system for on-demand droplet creation, mixing, incubation, and sorting, *Lab on a Chip*, 2019, vol. 19, no. 3, pp. 524-535.
5. Sahin, S., Bliznyuk, O., Rovalino Cordova, A., and Schroën, K., Microfluidic EDGE emulsification: the importance of interface interactions on droplet formation and pressure stability, *Scientific Reports*, 2016, vol. 6, no. 1, pp. 26407.
6. Chen, Q., Li, J., Song, Y., Christopher, D.M., and Li, X., Modeling of Newtonian droplet formation in power-law non-Newtonian fluids in a flow-focusing device, *Heat and Mass Transfer*, 2020, vol. 56, no. 9, pp. 2711-2723.
7. Liu, Z., Chai, M., Chen, X., Hejazi, S.H., and Li, Y., Emulsification in a microfluidic flow-focusing device: Effect of the dispersed phase viscosity, *Fuel*, 2021, vol. 283, no. pp. 119229.

8. Jing, L. and Nam-Trung, N., Numerical Simulation of Droplet-Based Microfluidics - A Review, *Micro and Nanosystems*, 2010, vol. 2, no. 3, pp. 193-201.

9. Yobas, L., Martens, S., Ong, W.-L., and Ranganathan, N., High-performance flow-focusing geometry for spontaneous generation of monodispersed droplets, *Lab on a Chip*, 2006, vol. 6, no. 8, pp. 1073-1079.

10. Ong, W.-L., Hua, J., Zhang, B., Teo, T.-Y., Zhuo, J., Nguyen, N.-T., Ranganathan, N., and Yobas, L., Experimental and computational analysis of droplet formation in a high-performance flow-focusing geometry, *Sensors and Actuators A: Physical*, 2007, vol. 138, no. 1, pp. 203-212.

11. Peng, L., Yang, M., Guo, S.-s., Liu, W., and Zhao, X.-z., The effect of interfacial tension on droplet formation in flow-focusing microfluidic device, *Biomedical Microdevices*, 2011, vol. 13, no. 3, pp. 559-564.

12. Roberts, C.C., Rao, R.R., Loewenberg, M., Brooks, C.F., Galambos, P., Grillet, A.M., and Nemer, M.B., Comparison of monodisperse droplet generation in flow-focusing devices with hydrophilic and hydrophobic surfaces, *Lab on a Chip*, 2012, vol. 12, no. 8, pp. 1540-1547.

13. Lan, W., Li, S., Wang, Y., and Luo, G., CFD Simulation of Droplet Formation in Microchannels by a Modified Level Set Method, *Industrial & Engineering Chemistry Research*, 2014, vol. 53, no. 12, pp. 4913-4921.

14. Chen, X., Glawdel, T., Cui, N., and Ren, C.L., Model of droplet generation in flow focusing generators operating in the squeezing regime, *Microfluidics and Nanofluidics*, 2015, vol. 18, no. 5, pp. 1341-1353.

15. Lashkaripour, A., Abouei Mehrizi, A., Rasouli, M., and Goharimanesh, M., Numerical Study of Droplet Generation Process in a Microfluidic Flow Focusing, *Journal of Computational Applied Mechanics*, 2015, vol. 46, no. 2, pp. 167-175.

16. Teo, A.J.T., Li, K.-H.H., Nguyen, N.-T., Guo, W., Heere, N., Xi, H.-D., Tsao, C.-W., Li, W., and Tan, S.H., Negative Pressure Induced Droplet Generation in a Microfluidic Flow-Focusing Device, *Analytical Chemistry*, 2017, vol. 89, no. 8, pp. 4387-4391.

17. Chen, X. and Ren, C.L., Experimental study on droplet generation in flow focusing devices considering a stratified flow with viscosity contrast, *Chemical Engineering Science*, 2017, vol. 163, no. pp. 1-10.

18. Mastiani, M., Seo, S., Jimenez, S.M., Petrozzi, N., and Kim, M.M., Flow regime mapping of aqueous two-phase system droplets in flow-focusing geometries, *Colloids and Surfaces A: Physicochemical and Engineering Aspects*, 2017, vol. 531, no. pp. 111-120.

19. Han, W., Chen, X., Wu, Z., and Zheng, Y., Three-dimensional numerical simulation of droplet formation in a microfluidic flow-focusing device, *Journal of the Brazilian Society of Mechanical Sciences and Engineering*, 2019, vol. 41, no. 6, pp. 265.

20. Rahimi, M., Shams Khorrami, A., and Rezai, P., Effect of device geometry on droplet size in co-axial flow-focusing microfluidic droplet generation devices, *Colloids and Surfaces A: Physicochemical and Engineering Aspects*, 2019, vol. 570, no. pp. 510-517.

21. Mastiani, M., Seo, S., Riou, B., and Kim, M., High inertial microfluidics for droplet generation in a flow-focusing geometry, *Biomedical Microdevices*, 2019, vol. 21, no. 3, pp. 50.

22. Roumpea, E., Kovalchuk, N.M., Chinaud, M., Nowak, E., Simmons, M.J.H., and Angeli, P., Experimental studies on droplet formation in a flow-focusing microchannel in the presence of surfactants, *Chemical Engineering Science*, 2019, vol. 195, no. pp. 507-518.

23. Palogan, B., Kumar, R., and Bhattacharya, S., Effect of surface coating on droplet generation in flow-focusing microchannels, *Microfluidics and Nanofluidics*, 2020, vol. 24, no. 9, pp. 72.

24. Sontti, S.G. and Atta, A., Numerical Insights on Controlled Droplet Formation in a Microfluidic Flow-Focusing Device, *Industrial & Engineering Chemistry Research*, 2020, vol. 59, no. 9, pp. 3702-3716.

25. Jia, H. and Zhang, P., Bubble formation in viscous fluids by a microfluidic flow-focusing junction: a computational study, *Microfluidics and Nanofluidics*, 2020, vol. 24, no. 11, pp. 85.

26. Iqbal, S., Bashir, S., Ahsan, M., Bashir, M., and Shoukat, S., Effect of Intersection Angle and Wettability on Droplet Generation in Microfluidic Flow-Focusing Device, *Journal of Fluids Engineering*, 2020, vol. 142, no. 4, pp.

27. Rahimi, M., Yazdanparast, S., and Rezai, P., Parametric study of droplet size in an axisymmetric flow-focusing capillary device, *Chinese Journal of Chemical Engineering*, 2020, vol. 28, no. 4, pp. 1016-1022.

28. Chekifi, T., Boukraa, M., and Aissani, M., DNS using CLSVOF method of single micro-bubble breakup and dynamics in flow focusing, *Journal of Visualization*, 2021, vol. 24, no. 3, pp. 519-530.

29. Fatehifar, M., Revell, A., and Jabbari, M., Non-Newtonian Droplet Generation in a Cross-Junction Microfluidic Channel, *Polymers*, 2021, vol. 13, no. 12, pp. 1915.

30. Soroor, M., Zabetian Targhi, M., and Tabatabaei, S.A., Numerical and experimental investigation of a flow focusing droplet-based microfluidic device, *European Journal of Mechanics - B/Fluids*, 2021, vol. 89, no. pp. 289-300.

31. Desamala, A.B., Vijayan, V., Dasari, A., Dasmahapatra, A.K., and Mandal, T.K., Prediction of oil-water flow patterns, radial distribution of volume fraction, pressure and velocity during separated flows in horizontal pipe, *Journal of Hydrodynamics*, 2016, vol. 28, no. 4, pp. 658-668.

32. Cristini, V. and Tan, Y.-C., Theory and numerical simulation of droplet dynamics in complex flows—a review, *Lab on a Chip*, 2004, vol. 4, no. 4, pp. 257-264.

CHAPTER 6

TWO-DIMENSIONAL SIMULATION OF DROPLET SPLITTING IN MULTI-FURCATING MICROCHANNEL

Chapter 6 Two-dimensional simulation of droplet splitting in multi-furcating microchannel

ABSTRACT

Multiple splitting of droplets through multi-furcating microchannel, consisting five outlets, is investigated using 2D simulation. For all five multi-furcating branches, a width ratio of 0.25 (branch channel width/main channel width) is used since multiple splitting occurs at this ratio. The values of the dispersed phase velocity at which the droplets multi-furcate across the five arms of the microchannel are determined. The mechanism of droplet multi-furcation is explained. Oil fraction data were collected for five velocity combinations, with the continuous phase velocity set to greater than 0.16 m/s, causing droplets to multi-furcate along the micro channel's five arms and is compared with the homogenous model. The droplet length distribution in the branch channels with various angles (0º, ±40º, and ±90º branch channels) is performed. The droplet frequency (counts per unit time) in the branch channels (0º, ±40º, and ±90º) is determined. Variation in the area distribution ratio with the capillary number was also observed. In this study a method for droplet splitting is proposed and our findings can be used in droplet-based biological assays.

This chapter is accepted in **Fluid Dyn.**, Springer

6.1. INTRODUCTION

Microfluidics have attracted the attention of researchers for various years. Microfluidics applications consist of the food industry [1], diagnostic tests [2], cosmetics [3], supra-magnetic nanoparticle synthesis [4], single-cell ribonucleic acid/deoxyribonucleic acid (RNA/DNA) sequencing [5], droplet digital polymerase chain reaction (PCR) [6], nanoparticle synthesis [7], drug delivery [8], and drug discovery [9]. Droplets can be made by mechanical agitation but they give inconsistently sized droplets and compromise the controllability of process. Whereas, microfluidics, the study of fluid behaviour at the micro to the nanoscale, allow to control the size and the quantity of droplets produced [10]. With hundreds to thousands of droplets generated, each second increases the throughput of droplet generation [11].

In a classic application of droplet-based microfluidics, chemicals or objects are captured inside individual droplets during droplet formation. It is an example of volume addition. On the other hand, Volume removal is equally important in many application scenarios. In [12] the multi-furcation of a mother droplet into five daughter droplets through a multi-furcating channel was investigated experimentally. The need of transition between splitting regimes, between the capillary number and the dimensionless droplet length was also examined. In [13] the breakup of a bubble in a four-branched microchannel was investigated numerically based on non-Newtonian pseudo-plastic fluid using the coupled level-set and volume of fluid (CLSVOF) method. The development of bubble morphology was used to assess the regime and pattern of bubble breakdown. The effects of gas velocity, solution concentration, and sub channel width on

daughter bubble length were investigated in turn. A scaling law is also constructed to anticipate the length of the daughter bubble in a two-distanced channel.

Numerous researchers made experiments and carried out numerical simulations of flow past obstacles for volume removal. In [14] the influence of square and cylindrical obstacles on droplet dynamics in the confined geometry was studied both experimentally and computationally. Because both components of the velocity gradients are fully developed at the corner, the square obstacle, in particular, encourages thread splitting at the corner areas. For optimal wetting, low Ca droplets and appropriate cylinder spacing were required. The numerical investigation was made on the consequence of obstacle configuration for droplet splitting in a microchannel via the level-set method. The numerical results revealed that obstacle configurations in a microchannel, such as the obstacle width, length, location, and inclination affect the droplet splitting patterns with or without remerging [15]. The droplet dynamics in a partly blocked confinement in the 3D channel were investigated numerically. To explore the dynamic behavior of droplet passage across an obstacle, the effects of change in the capillary number and surface wettability, as well as the obstruction size and architecture, were studied [16]. A numerical investigation of passive droplet deformation and breakdown in a microchannel with obstacles was conducted. In the symmetric scenario, the impacts of different flow and physical factors such as the Reynolds number, contact angle, channel height, and droplet diameter were examined. In this case, increasing the height of the triangle barriers, the starting diameter of the droplet, and the contact angle increased the maximum velocity of the droplet in the narrow part [17]. In [18] disintegration of a droplet was studied numerically as it went over

an obstacle in an orthogonal cross-section. To evaluate the influence of droplet breakdown on the obstacle shape, two different obstacles shapes, namely, circular and elliptical, were investigated. The effect of the barrier size and location and the capillary number on droplet breakup was also studied.

Various researchers made volume removal through the T-junction and the junction with arbitrary angles. In [11] it was experimentally found a critical condition for breaking drops at the T-junction. This work was also extended by converting a single droplet into multiple ones by using a series of T-junctions. In [19] three breakup regimes were numerically found: i) breakup with a tunnel, ii) breakup with a discontinuous obstruction, and iii) breakup with a permanent obstruction and one non-breakup regime. Also, a critical capillary number was used to distinguish the breakup and non-breakup regimes. In [20] the asymmetric droplet breakup in two angled branches was studied both experimentally and theoretically. To fine-tune the droplet size and velocity, a diluting channel was introduced. The splitting ratio was discovered to be mostly controlled by the initial droplet length and velocity. With the aid of daughter droplets, a predictive model was built by taking into account the hydrodynamic resistance of the branches. In an asymmetric T-junction microchannel, a droplet was divided into two daughter droplets using a numerical research. There are four types of droplet breakup (primary breakup, transition breakup, bubble breakup, and non-breakups). There are two basic asymmetric breakup processes that have been identified: "breakup with permanent obstruction" and "unstable breakup." [21].

The researches performed studying on the interaction of a liquid droplet with the gas stream. In [22] two approaches to breakup of a liquid drop in gas stream were theoretically

identified. One of them was based on Rayleigh instability, and the other was due to the steady-state deformation of the droplet corresponding to aerodynamic forces which arise as the gas flows around the droplet. In [23] the droplet breakup in a gas stream behind a shock wave with a triangular gas-velocity profile was investigated experimentally. Three versions of the breakup of drop are found, namely, i) pockets; ii) droplet split into two droplets; and iii) detachment of a surface layer of liquid. In [24] the multiple splitting of a droplet in a gas stream behind a shock wave was investigated experimentally using shadow photography and a high-speed camera. It was observed that Strouhal number determines the disintegration time of drop.

There is a significant influence of wetting angle on fluid flow in narrow channels. Many researchers carried out various experiments as well as numerical studies of this effect. The investigations were performed on the capillary driven filtration in porous media under the microgravity conditions. The hydrophilic form of wettability magnifies the imbibition of the liquid in the porous media, whereas the hydrophobic type of wettability magnifies the blurring of the front [25]. The displacement of a viscous fluid from a porous media was studied numerically with reference to capillary effects. It was discovered that when hydrophobicity increases, the diffusion coefficient drops. Furthermore, when the viscosity ratio of the fluids is near to unity, the displacement is similar to that of a piston [26]. Numerical studies on various ways for improving oil recovery from host rock formations were carried out. The displacement in a homogeneous media is uniform and eventually slows down; but, in an inhomogeneous medium, the imbibition front accelerates as it transits from a more permeable to a less permeable medium [27]. The capillary-driven seepage in porous media in microgravity circumstances was

investigated numerically and experimentally. In a homogeneous material, displacement is uniform and gradually slows down. In the experiment, the speed reduces more than in the computation. This is due to the mathematical model failing to account for gravity acceleration g. The graph has a difficult form space-time dependency when crossing the boundary of zones with different permeability in an inhomogeneous material [28]. In our present work, we have used the volume of fluid (VOF) method which take care the effect of the wetting angle.

In view of the above discussion, it can be observed that there were little works on the junction having more than two outlets. In the present work, using 2D simulation, we investigate the multiple splitting of droplets through a multi-furcating microchannel having five outlets. The 2D numerical simulation was carried out using the volume of fluid (VOF) method. The width ratio of 0.25 (branch channel width/main channel width) was used for all five multi-furcating branches. The values of the dispersed phase velocity at which the droplets multi-furcate across the five arms of the microchannel are determined. The mechanism of droplet multi-furcation is explained. The oil fraction data are collected for five velocity combinations with the continuous phase velocity set to greater than 0.16 m/s, causing droplets to multi-furcate along the micro channel's five arms and is compared with the homogenous model. The study of the influence of three parameters (dimensionless droplet length, droplet frequency (counts per unit time), and area distribution ratio) is performed to understand the insight of the multi-furcation. The results revealed the splitting of a single mother droplet into five daughter droplets using 2D simulation. Splitting of a mother droplet into five daughter droplets occurs for a critical initial droplet length/main channel width (l/W_c) of 0.64. The results also show that the multi-furcation of a

single mother droplet into five daughter droplets is due to the pressure drop in the branch channels and the formation of vortices in the area around the notch between the adjacent branch channels. These findings are not reported in the literature to the present date.

6.2. COMPUTATIONAL MODEL

In this work, the VOF technique was used to model the dynamics of water (dispersed phase, w) droplet breakdown in mineral-oil (Marcol – 82) (continuous phase, o) at a multi-furcating junction of a horizontal 2D microchannel under laminar flow conditions. The fluids were considered to be Newtonian and incompressible.

6.2.1 Geometry, initial and boundary conditions

6.2.1.1 2D Geometry:

The 2D domain is made up of a series of microchannels that branch out (having five branches). Figure 6.1a depicts the details of the computational domain's geometry. The geometry is made up of two inlets (inlet length is equal to 2 mm), one main channel (length is equal to 120 mm), and five outlets at various angles (±90° branch channel - length is equal to 3 mm, the diameter is equal to 0.2 mm; 0° and ±40° branch channel - length is equal to 5 mm, the diameter is equal to 0.2 mm). The inlets and the main channel have the same diameter (0.78 mm). Figure 6.1b depicts the corresponding mesh of the multi-furcating channel.

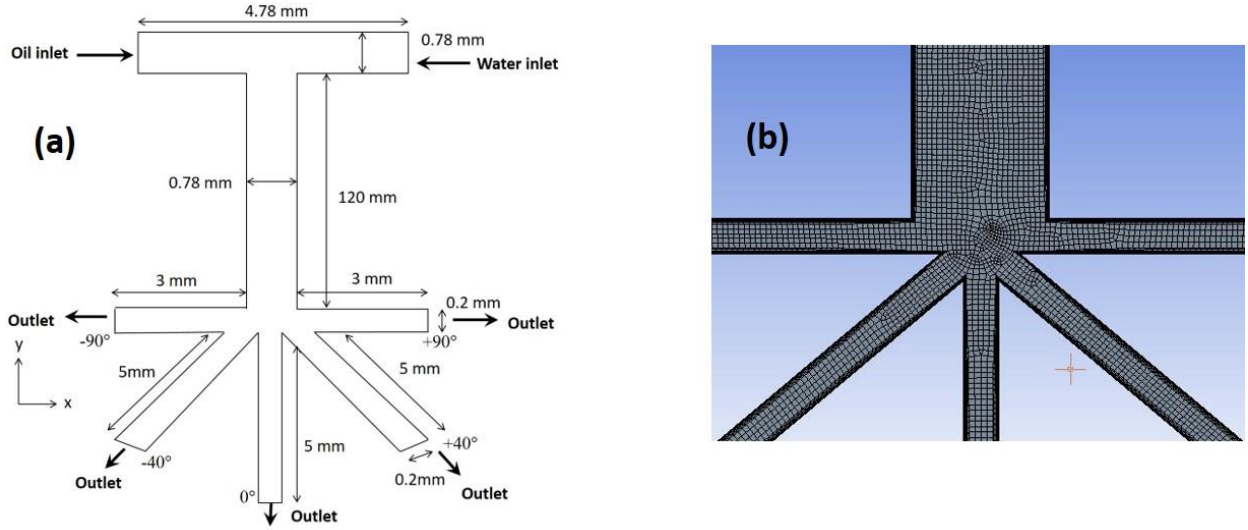

Figure 6.1. (a) 2D Computational domain; and (b) 2D mesh

In Figure 6.1a, the base is the vertical downward branch channel and considered at 0°. The horizontal branch channel is having 90° with the vertical downward branch channel. And other two branch channel is having an angle of 40° with the vertical downward branch channel.

Mineral-Oil (Marcol – 82) and water have been selected as the two liquid phases for the study, and their properties are listed below in Table 6a.1.

Table 6.1. Fluid properties

Fluids Properties	**Water**	**Mineral-Oil (Marcol - 82)**
Density (kg/m^3)	997	843

Viscosity (mPa.s)	1	30.6
Oil-water interfacial tension (N/m)	0.0301	
Calculated contact angle of oil on glass in water (^{0})	51	

6.2.1.2 Initial and boundary condition:

Initially, the channel was filled with oil (continuous phase), then water (dispersed phase), and oil ran through the inlets. The operating pressure was taken as the atmospheric pressure. No-slip and impermeable conditions were implemented on the walls. The following velocity condition were also implemented to progress the solution,

i) At the oil inlet, $u_x = V_o$ and $u_y = 0$,

ii) At the water inlet, $-u_x = V_w$ and $u_y = 0$.

Along with the above, the pressure outlet boundary condition, i.e., the gauge pressure was considered to be equal to 0 Pa at all the outlets. Time steps were meticulously calculated in order to get a consensus on the Courant number ($C = \frac{u\Delta t}{\Delta x}$).

6.2.2 Effects of wetting properties of fluids

The wettability of the fluids has been accounted through Eq. (2.2.8) as hydrodynamics of the multiphase flow is highly influenced by this property. The contact angles of mineral-oil (Marcol – 82) and water on glass are equal to 3° and 38°, respectively, which is adopted from [29]. It means that the oil is more wetting the glass surface.

6.2.3 Convergence, grid independence, code validation and verification

The residual values play an essential role in determining the convergence of the simulation. The convergence is determined by the residual values of the continuity equation and the velocity components. For the continuity equation and the *x* and *y* velocity components, the residual value was selected equal to 0.001 as reported in [30]. The convergence limit for the continuity equation was taken in the order of 10^{-3}, while the limit for the velocity components was set in the order of 10^{-5}.

The 2D simulation was validated by comparing our simulated results to the prior experimental results [29]. The grid independence investigation was carried out to get the ideal grid size from the three distinct mesh sizes for 2D simulation, as shown in Table 6.2. The table shows that the 2D simulation used 49269, 99548, and 149240 cells. After analyzing the three systems in the 2D simulation, we discovered that the system with 149240 cells had the least percentage deviation from the experimental values of C_0 among all the three. Here, $C_0 = V_{meas} / (V_w + V_o)$, and V_{meas} is the average drop/pattern velocity in the main channel, and V_w and V_o are the superficial velocity of the water and oil phases, respectively. Furthermore, the system with 149240 cells enhanced

droplet flow prediction by providing a vivid and crisp interface, particularly in the five arms of the multi-furcating channel, as depicted in Fig. 6.2. The oil (continuous phase) and the water (dispersed phase) are depicted in the pictorial representation of the volume fraction contour as red and blue, respectively. The same color terminology was used throughout the manuscript. Table 6.3. represents the variation of drop size with mesh elements in the main channel at V_w = 0.002 m/s and V_o = 0.16 m/s. The table shows that the existing grid also predicts the droplet size very well. Grid mesh (149240) gives the percentage deviation of 1.7 which is lowest among the three. For this reason, the grid mesh (149240) is used for all the 2D simulations performed in this work.

Table 6.2. Summary of the results of grid independence study performed in the main channel for C_0 values at V_w = 0.04 m/s and V_o = 0.12 m/s

Mesh elements	**Flow pattern observed**	**Experimental C_0**	**Simulated C_0**	**Percentage Deviation**
49269	Slug	1.28	1.32	3.03
99548	Slug	1.28	1.31	2.29
149240	Slug	1.28	1.29	0.78

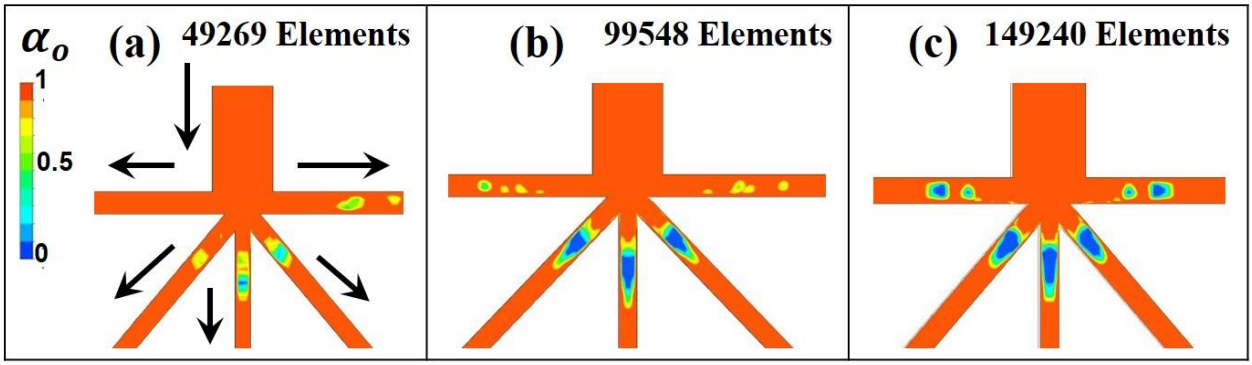

Figure 6.2. Optimization of grids by comparing the volume fraction contour at V_w = 0.002 m/s and V_o = 0.16 m/s: (a) 49269 mesh elements; (b) 99548 mesh elements; and (c) 149240 mesh elements

Table 6.3. Variation of drop size with mesh elements in the main channel at V_w = 0.002 m/s and V_o = 0.16 m/s

Mesh elements	Drop size from simulation (mm)	Drop size from Salim et al. [29] (mm)	Percentage deviation
49269	0.52	0.59	11.9
99548	0.55	0.59	6.7
149240	0.58	0.59	1.7

Same size of grids in the main channel and the branch channel has been used. The number of grids in the branch channel is less in number as compared to the main channel as the diameter of the branch channel is less than the main channel. For this reason, we have found

much diffused interface in the branch channel. The effect of wall shear and interfacial tension greatly influences the dynamics of the droplet in the smaller diameter channel. It is happening in the branch channel of the present work. Close look of Figure 6.8 tells that thickness of the continuous fluid layer between wall and droplets is much less in the branch channel as compared to the main channel. So, effect of wall shear and interfacial tension is much more crucial in the branch channel than in the main channel. To account these effects, more and more fine grids are recommended. But, it is not done in the present work as we addressed earlier. In future, I will keep this in mind.

For the code validation, we have measured the slug velocities in the main channel from our simulation and compared with Salim et al. [29], which is depicted in Figure 6.3. It is found that the results accord to each other.

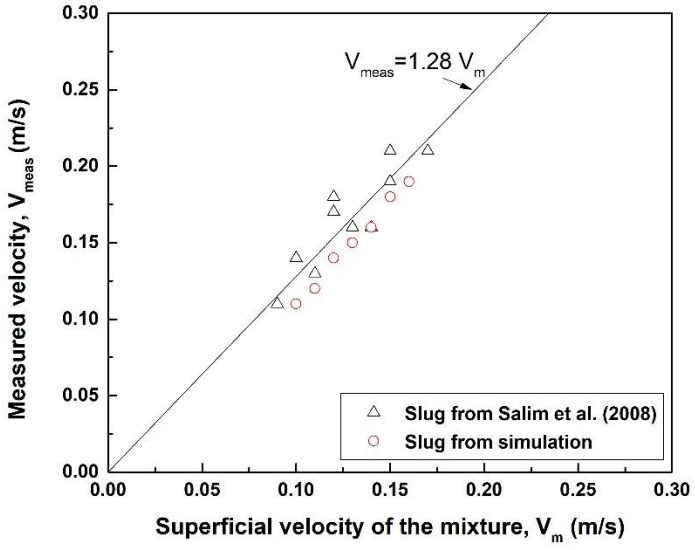

Figure 6.3. Code validation by comparing the experimental and simulated slug velocities of two-phase oil–water flow through a glass microchannel

After getting success in code validation, we have verified the code, used in the solver, with a benchmark problem as shown in Figure 6.4 and Figure 6.5. Figure 6.4 is a velocity profile at a point away from the droplet, which is located in front of the droplet. The figure shows a parabolic velocity profile, which is notably true in case of a fully developed flow. On the other hand, velocity profile at the section B-B in Figure 6.5 corresponds to a typical velocity profile of two-phase flow where a droplet passing through a conduit. Therefore, it can be said that the code used in the simulation is verified with a higher accuracy.

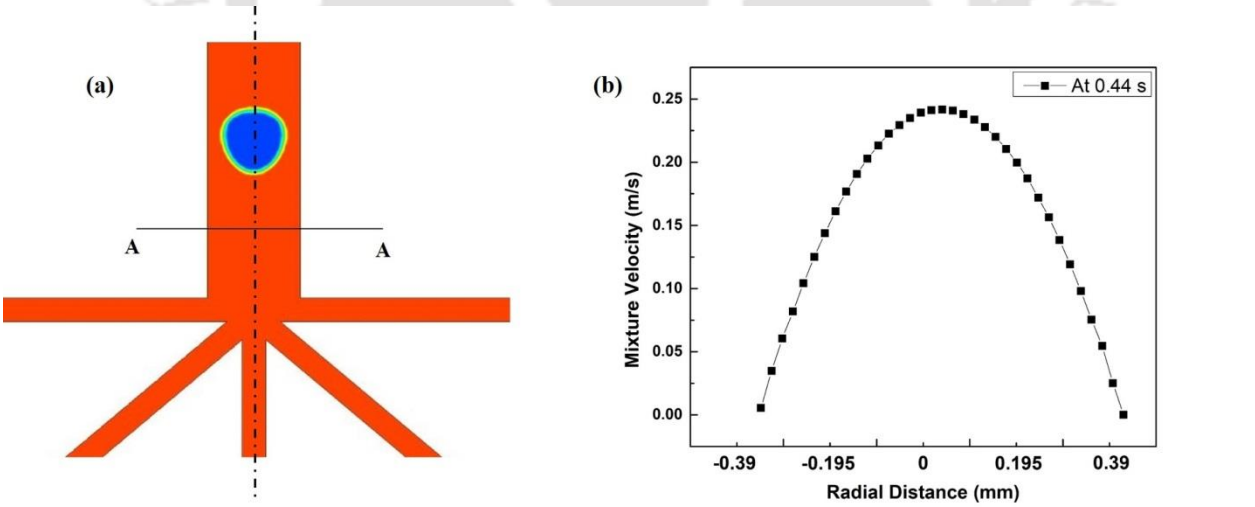

Figure 6.4. Velocity profile at the section A-A confirms the code verification. The profile has been captured at a time step of 0.44 s: (a) Sectional plane (A-A) along with volume fraction contour; and (b) Parabolic velocity profile

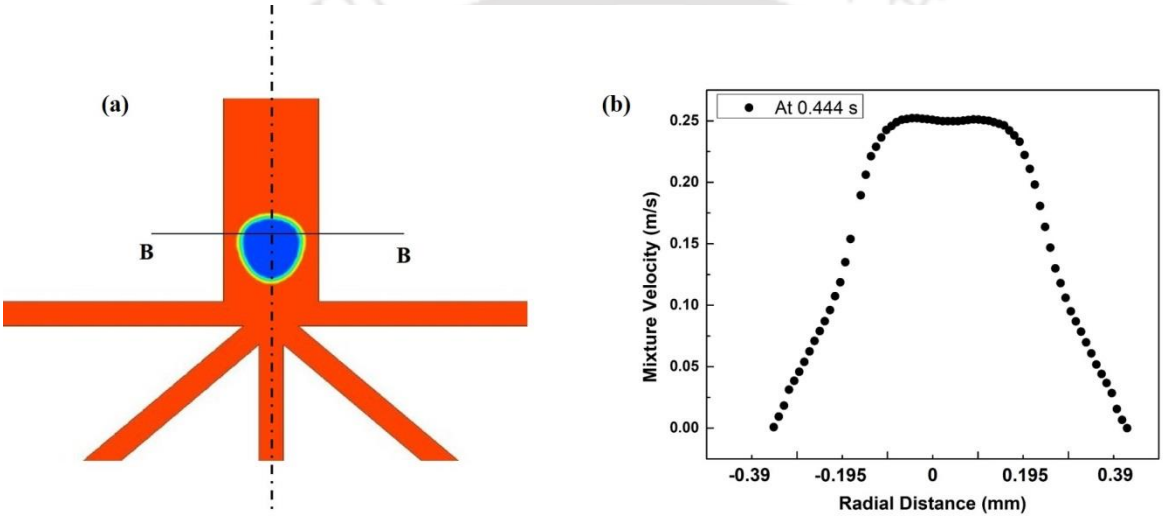

Figure 6.5. Velocity profile at the section B-B confirms the code verification. The profile has been captured at a time step of 0.444 s: (a) Sectional plane (B-B) along with volume fraction contour; and (b) Two-phase velocity profile

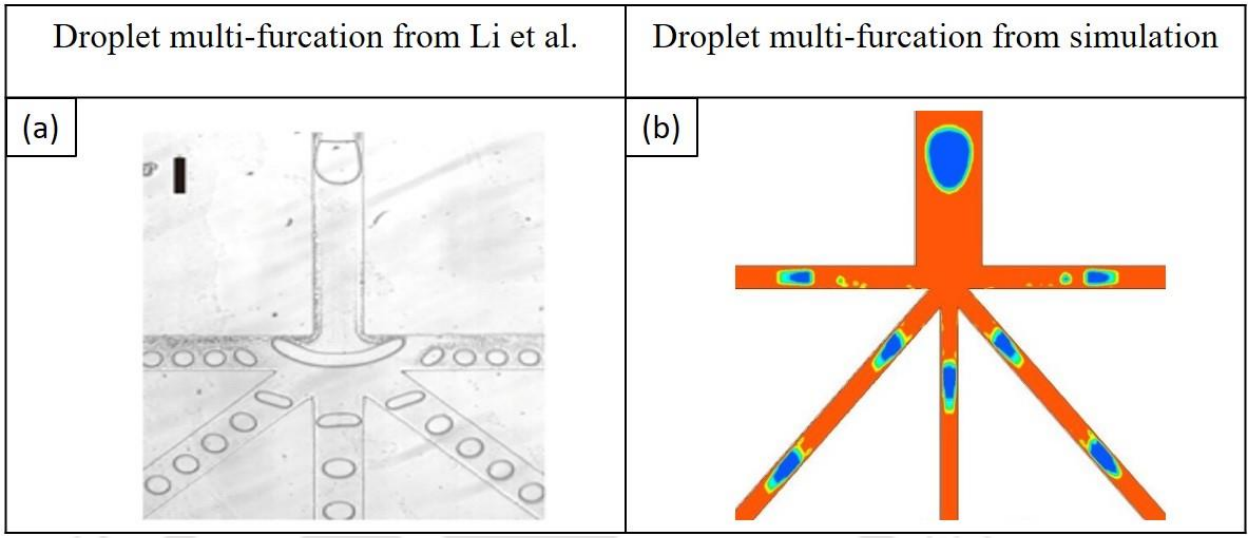

Figure 6.6. (a) Droplet multi-furcation from Li et al. [12]; and (b) Droplet multi-furcation from simulation

A qualitative (flow pattern in the channel) validation for the droplet splitting in the multi-furcating channel is incorporated by comparing the data obtained from Li et al. [12] which is represented in Figure 6.6. The above Figure tells that multi-furcation is occurring in both cases at same flow condition. However, there is a mismatch between the droplet sizes. On the other hand, droplet's character in the main channel is more or less similar in both the cases. It is due to the significant difference in channel dimension, between literature and present simulated work, especially in the main channel to branch channel ratio. The main channel to branch channel ratios are 1 and 3.9 in literature and present simulated work respectively. That is why there is a large mismatch in the length of the droplets. The analysis shows that multi-furcation is taking place in both the cases at similar flow conditions and it is considered as the basis of the validation of the present work.

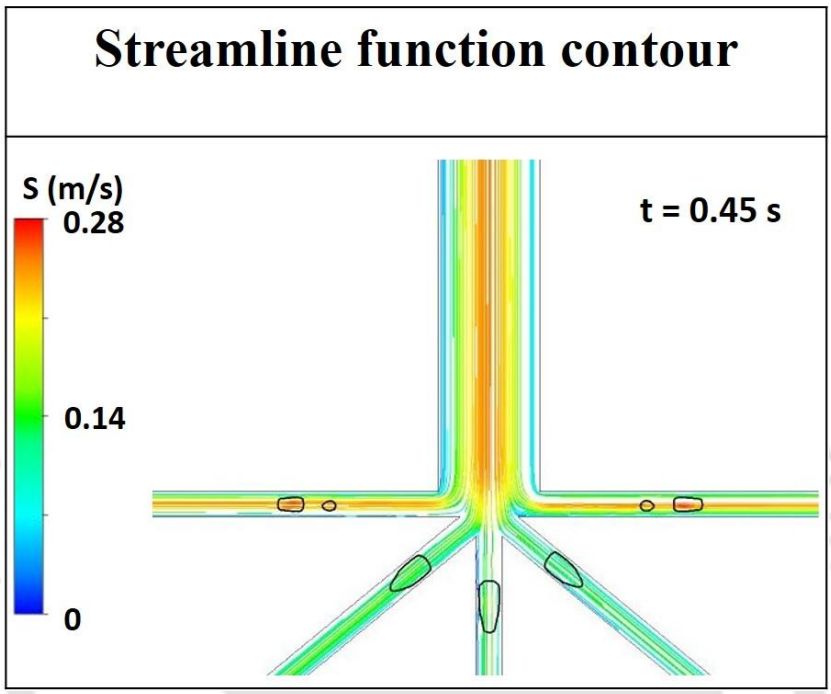

Figure 6.7. Streamline function contour at the multi-furcating junction for the continuous phase at V_w = 0.002 m/s and V_o = 0.16 m/s.

Figure 6.7 represents the Streamline profile of the multi-furcating junction at the phase velocities, V_w = 0.002 m/s and V_o = 0.16 m/s. The magnitude of the streamline function is higher in the central portion of the main channel and two branch channels at ±90°. It is gradually decreasing towards the wall. The overall magnitude of the streamline function is much lower in the branch channels at 0° and ±40° with respect to the main and ±90° branch channel.

6.3. RESULTS AND DISCUSSIONS

The present study reveals that all the flow conditions (velocity combinations) and the geometrical parameters of multi-furcated channels are not delivering five daughter droplets at a time from a single droplet. We have carried out the simulations at various oil velocities (V_o) equal to 0.12, 0.16, and 0.18 m/s and at various water velocities (V_w) ranging from 0.0001 to 0.12 m/s. It is realized that the width ratio (branch channel width/main channel width) which is equal to 0.25 is the point of onset at which five daughter droplets are generated. So, we have restricted the present discussion to this width ratio (0.25).

6.3.1 Phenomena of multi-furcation in a multi-furcating channel

In Fig. 6.8 we have illustrated the phenomena of multi-furcation of a droplet. Under the above-mentioned geometrical conditions and oil velocity, the droplet multi-furcates through the five arms of the microchannel at a low velocity of the dispersed phase, V_w = 0.002 m/s (Figs. 6.8a-6.8c). It is important to note that the sizes of daughter droplets in ±90° branched channel are smaller than that in the ±40° and 0° branched channels. However, droplets in the ±40° and 0° branched channels are comparable in size. On the other hand, the size of all daughter droplets are comparable at the higher dispersed phase velocity (V_w = 0.027 m/s), as presented in Figs. 6.8d-6.8f. These results confirm that the volume fraction of the dispersed phase can be regulated as the demand by controlling the inlet phase velocities, which is highly important in the field of mass, heat, and momentum transport and also in the domain of droplet digital PCR and drug

delivery. The droplets multi-furcate due to the pressure drop and the shear stress of the flow field. The droplets arrive at the junction and get transformed into a thin threaded necklace-like structure (Figs. 6.8b and 6.8e).

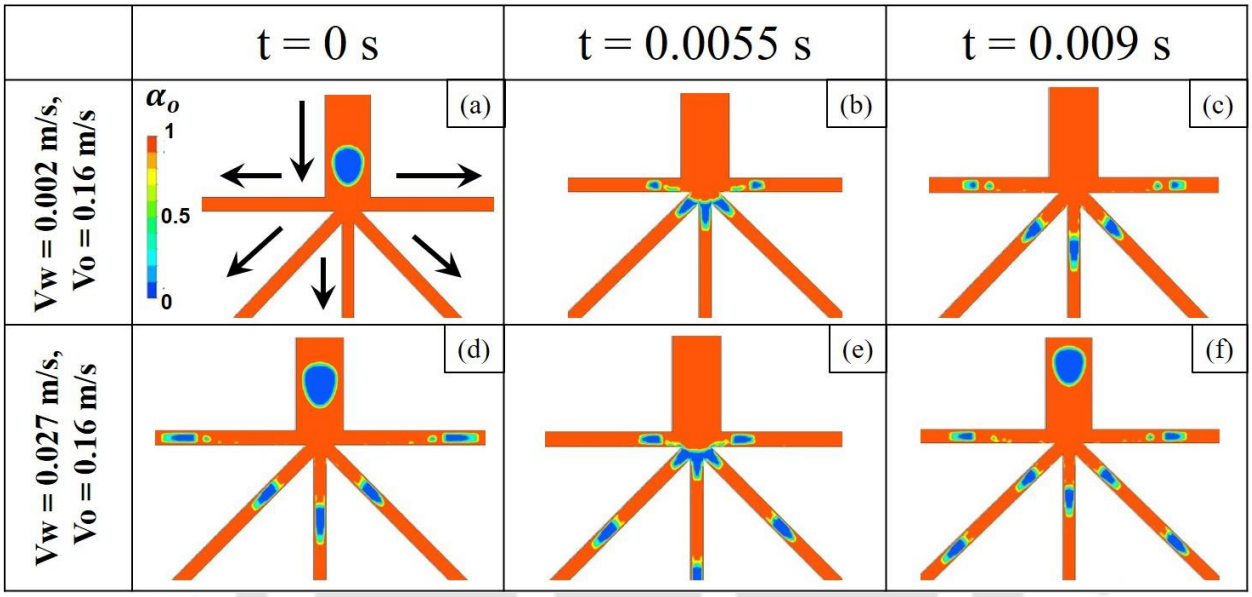

Figure 6.8. Time dependent volume fraction contour of a multi-furcation event at a fixed oil velocity (V_o = 0.16 m/s): **(**a-c) At low dispersed phase velocity; and (d-f) At high dispersed phase velocity

6.3.2 Mechanism of droplet multi-furcation phenomena

The mechanism of droplet multi-furcation is explained in this section, which is nothing but balance among the pressure field, the shear forces of the flow field, and the field of body forces (including surface tension). A set of representative results is shown in Fig. 6.9. The volume fraction contour, the dynamic pressure profile, the velocity profile, and the vorticity

profile are presented in the various columns as mentioned in the figure caption. At the time step t = 0 ms, the water droplet is approaching the junction (Fig. 6.9a). The corresponding profiles of the dynamic pressure, the velocity, and the vorticity are also depicted in Figs. 6.9b-6.9d, respectively. Figure 6.9b indicates the higher pressure field in the ±90º branch channel as compared to others (0º and ±40º branch channels). This higher pressure may forbid the entry of the water droplets into the ±90º branch channel. In other words, in this case change in the direction of the larger water droplets is not the energetically favorable process. That is why the ±90º branch channels always possess smaller droplets as compared to the others. This argument is well supported by Fig. 6.8e at the time step t = 4.5 ms and Fig. 6.9i at the time step t = 7 ms, as droplets' size in the ±90º branch channel is smaller than the other three. The row represented with the time step t = 4.5 ms, i.e., at the time of the onset of splitting a droplet into five daughter droplets, unfolds the important fundamental aspects of the splitting phenomena. At this time step, both the difference in pressure and generation of vortices make the mother droplets squeeze, leading to a thin threaded necklace-like structure (Fig. 6.9e). The red color at the junction of the ±90º branch channel (Fig. 6.9f) confirms the existence of a very strong pressure field, which is supplemented with intensive vorticity around the same region of the conduit (Fig. 6.9h). This vorticity is so strong that it enforces the snatching of a small mass from the water droplet. Probably, it is not occurring at all the velocity combination - to dig out specific conditions, a thorough analysis will be carried out in the next section.

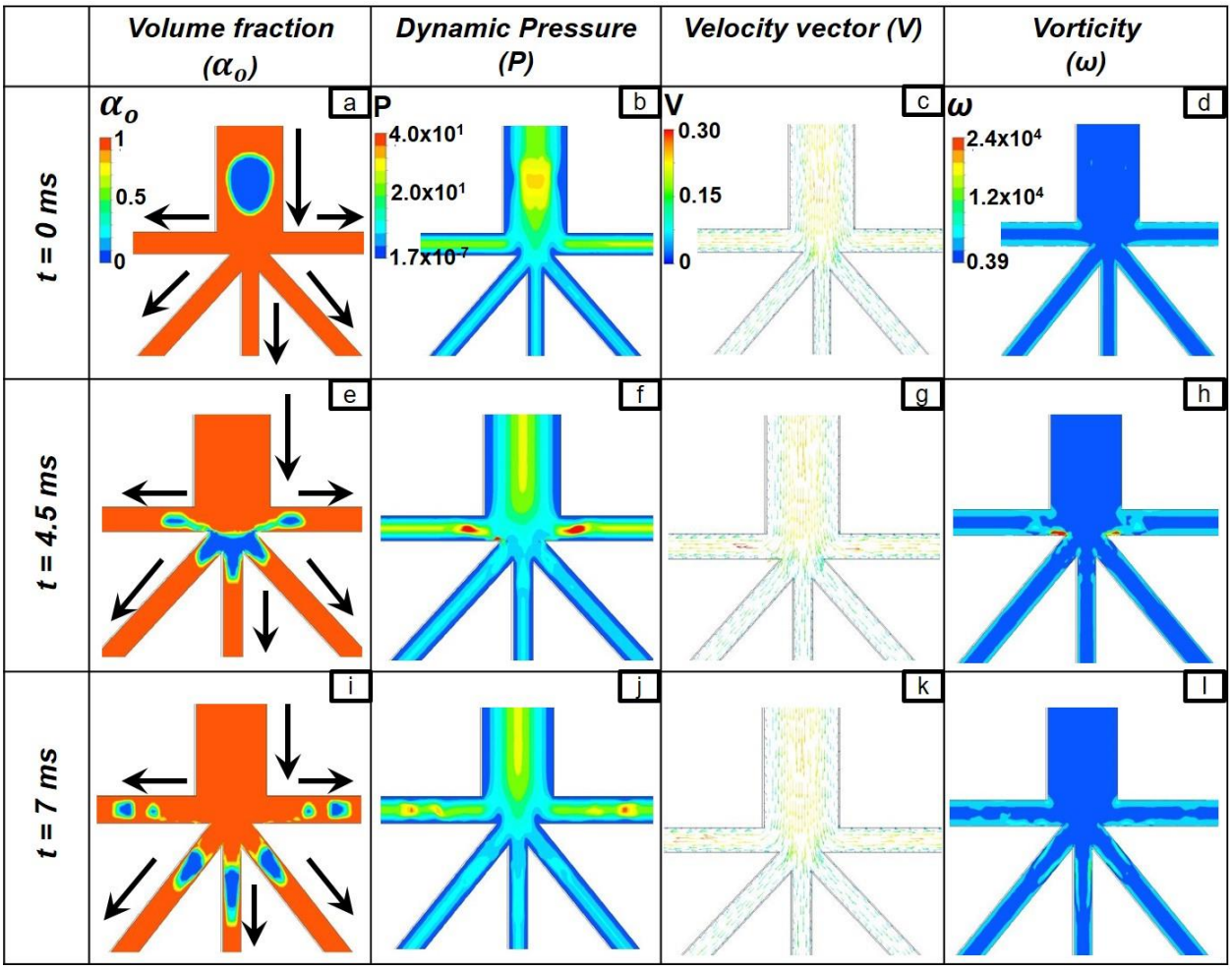

Figure 6.9. Pictorial representation of insight physics of a multi-furcation phenomena at V_w = 0.002 m/s and V_o = 0.16 m/s. 2nd column -volume fraction contour; 3rd column -dynamic pressure; 4th column -velocity vectors; and 5th column -vorticity

6.3.3 Critical mother droplet's length for multi-furcation

It is very important to establish the condition at which the specific phenomena start. This can is considered as a critical condition. We will now attempt to get the critical mother droplet's

length, which undergoes to produce at least five daughter droplets. The velocity pair at this condition and the dimensionless mother droplet's length are recorded as the critical condition in this case. Instead of all the simulated results, only the critical condition is discussed in Fig. 6.10, addressing the volume faction data. Our discussion is regulated at the width ratio equal to 0.25, as mentioned above. So, here we have concentrated our discussion on the phase velocities only.

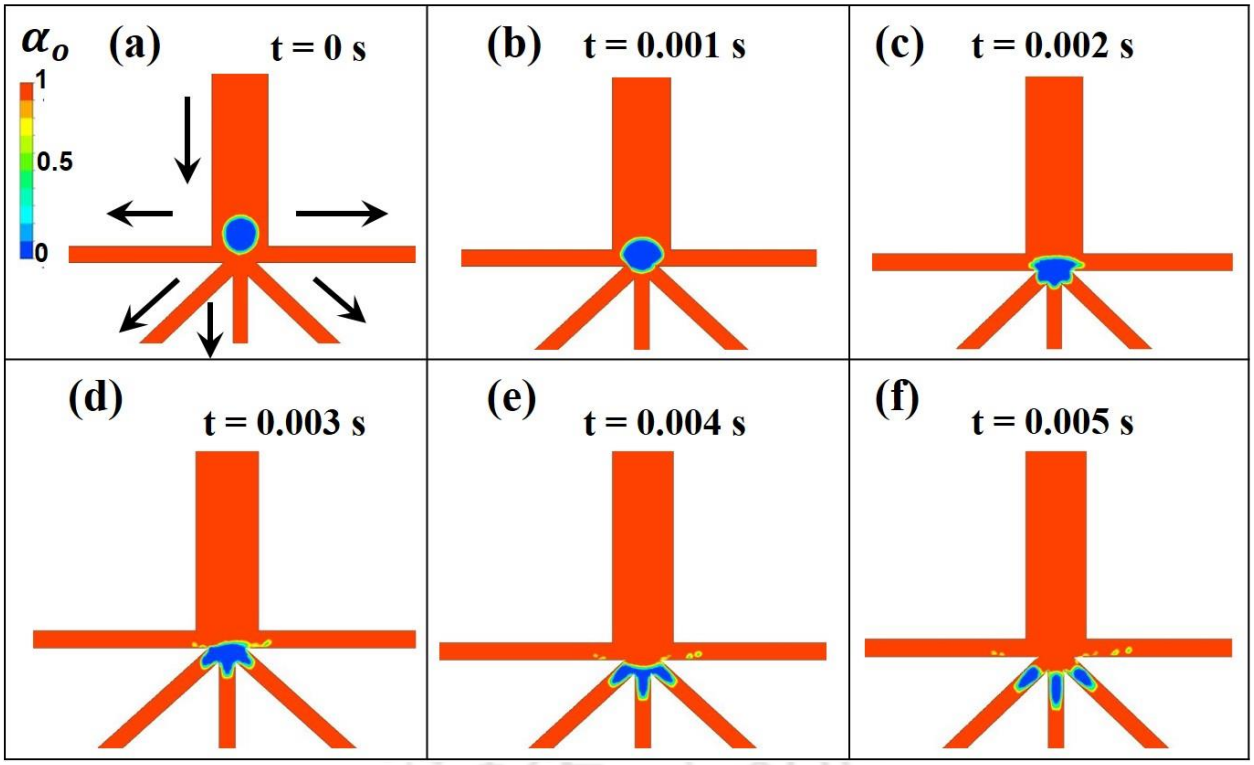

Figure 6.10. Volume fraction contour of critical mother droplet at the condition (at V_w = 0.0001 m/s and V_o = 0.16 m/s) of engendering of five daughter droplets

Figure 6.10 depicts the onset of minute droplets in the ±90° branch channel and big slugs in the 0° and ±40° branch channels. So, this flow condition, at V_w = 0.0001 m/s and V_o = 0.16

m/s, is considered as the critical velocity condition for the splitting of a mother droplet into five daughter droplets. At the flow circumstance, the dimensionless mother droplet's length becomes 0.64 (l/W_c), which is chosen as the critical (l/W_c) droplet length for a multi-furcation marvel.

6.3.4 Distribution of droplet length in branch channel (0º, ±40º and ±90º branch channel)

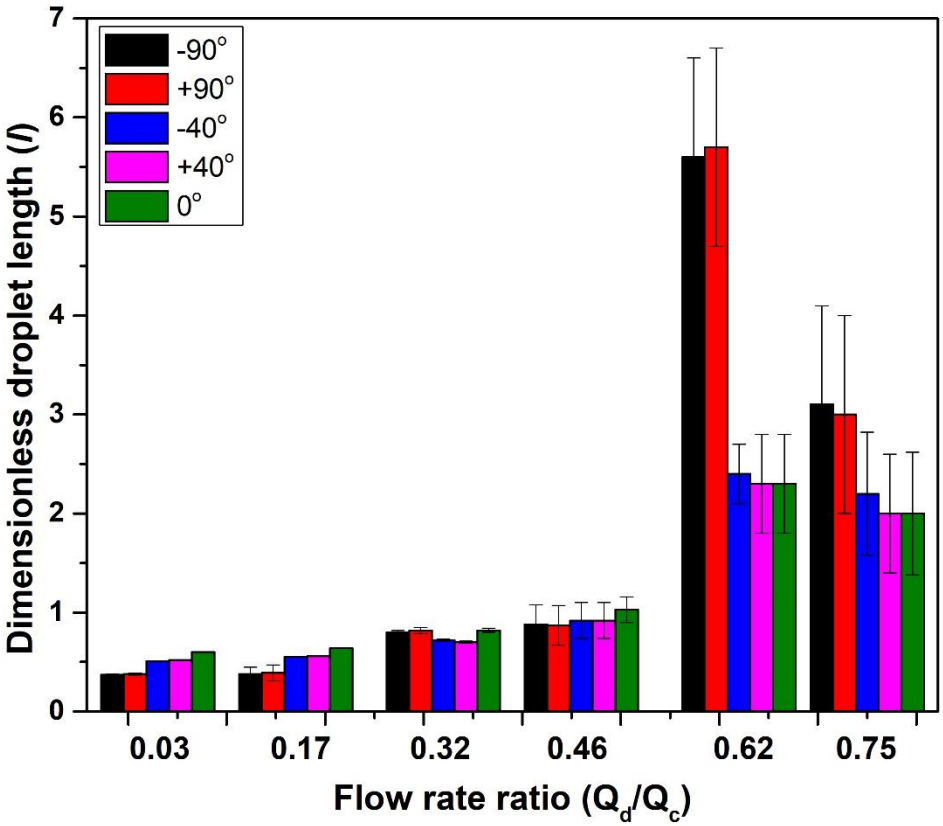

Figure 6.11. *l* Vs. Flow rate ratio for 0º, ±40º, and ±90 º branch channel

Here, the dimensionless droplet length *l* is equal to the length of the droplet in the branch channel/width of the main channel. In Fig. 6.11 it can be observed that *l* increases for all the branches up to the flow rate ratio of 0.46. At the flow rate ratios of 0.62 and 0.75, the value of *l* in the case of the 90° branch channel is more than that in the 0° and 40° branch channels. However, there is an increment in all the values of *l* for the flow rate ratio from 0.46 to 0.62 and a decrement for the flow rate ratio from 0.62 to 0.75.

Increase in the value of *l* for all the branches up to the flow rate ratio of 0.46 is due to increase in the flow rate of the dispersed phase. After reaching a certain critical flow rate ratio (0.62), there is accumulated pressure in the 0° and 40° branch channels due to the presence of droplets, so the greater droplet volume will pass through the 90° branch channel. Thus, the value of *l* for the 90° branch channel is higher than that for the 0° and 40° branch channels at the flow rate ratio of 0.62. At the flow rate ratio of 0.75, the viscous stress is comparable to the surface tension force, so more breakdown of droplets takes place. Thus, the value of *l* for all the branches at a flow rate ratio of 0.75 is less than the value of *l* for all the branches at the flow rate ratio of 0.62 due to generation of the greater number of droplets with the smaller droplet lengths, but the overall trend is similar.

6.3.5 Frequency (counts per unit time) of droplet in 0º, 40º, and 90º branch channel

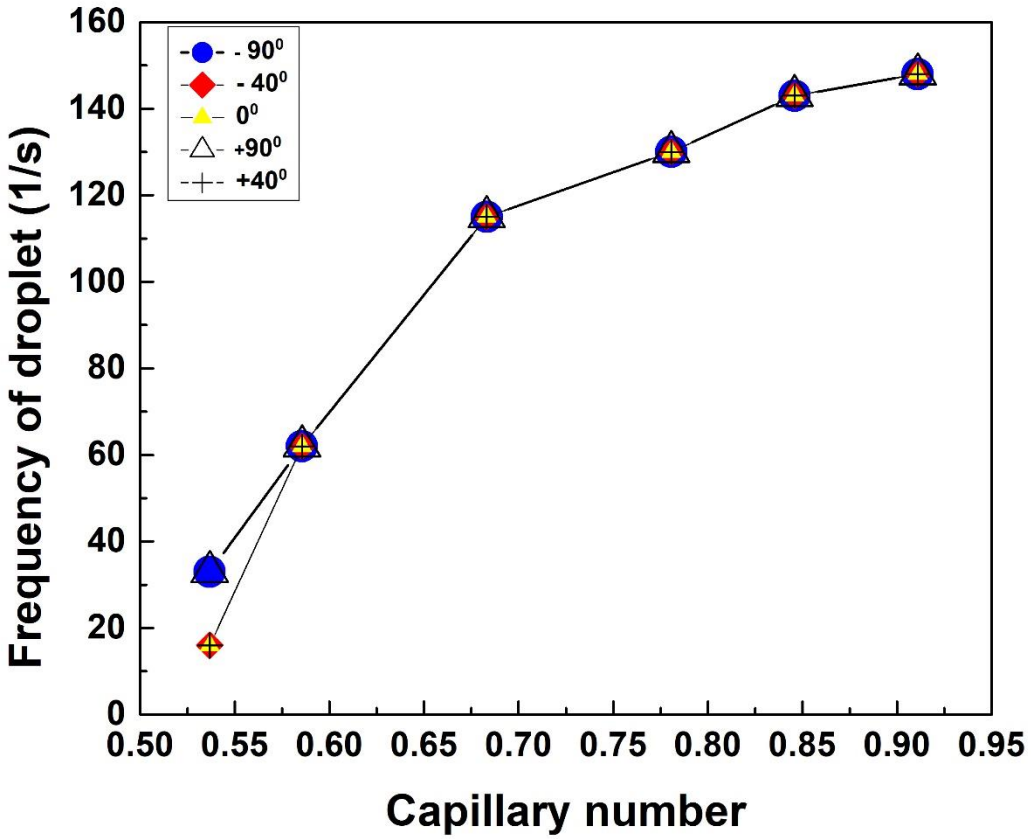

Figure 6.12. Frequency of droplet (1/s) vs. capillary number for 0º, ±40º, and ±90 º branch channel

From Fig. 6.12 it can be seen that the frequency (counts per unit time) increases with increase in the capillary number for all the branches for the regime-droplet passes through five channels. Here, the capillary number (in the branch channel) is defined as $Ca = \frac{\mu_c U}{\sigma}$, μ_c is the

viscosity of continuous phase, U is the mixer velocity, and σ is the interfacial tension. With increase in the capillary number the shear force increases, being comparable to the surface tension force. This leads to a faster breakup of dispersed thread, producing more droplets per unit time. As a result, the frequency (counts per unit time) of droplets in the branch channel increases with increase in the capillary number.

6.3.6 Area distribution ratio for 0º, ±40º, and ±90º branch channel

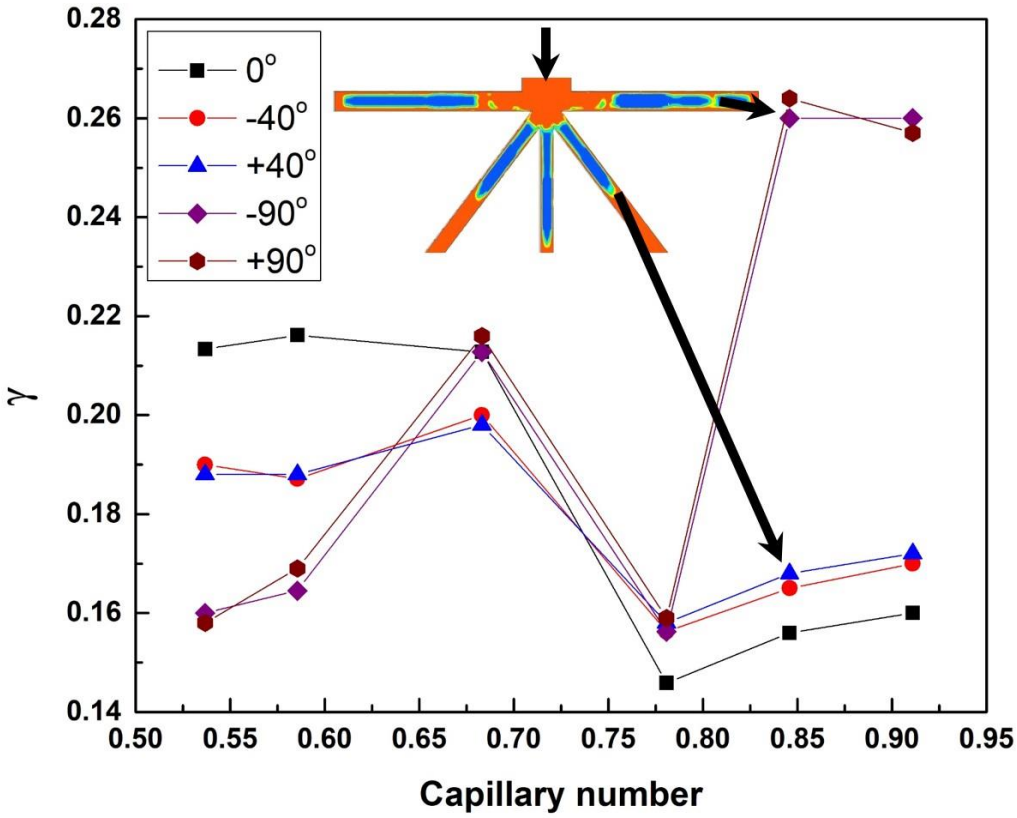

Figure 6.13. Area distribution ratio vs. capillary number for 0º, ±40º, and ±90 º branch channel

Figure 6.13 depicts the area distribution ratio as a function of the capillary number for the 0º, ±40º, and ±90 º branch channels. Here, γ is the area of the droplet in the branch channel/area of the droplet in the main channel. It has been found that for the ±40º and ±90º branch channels γ increases first for the capillary number of 0.68, then decreases for 0.78. Then again, it increases to 0.84 and goes on increasing. But for the 0º branch channel, γ decreases first for the capillary number of 0.78 then increases. The value of γ at the capillary number equal to 0.68 for the ±40º and ±90º branch channels increases due to increase in the length of the droplet in the ±40º and ±90º branch channels. Then, the value of γ decreases for the 0º, ±40º, and ±90º branch channels at the capillary number equal to 0.78, as the length of the droplet in the main channel is relatively high. Then, at last, the value of γ increases for all the branch channels due to increase in the length of the droplets in their respective branch channels. A volume fraction data representing the length of droplet at 0º, ±40º, and ±90º branch channels for the capillary number 0.85 has been presented in the Figure 6.13.

6.3.7 Two-dimensional approximation

The 2D simulations are not capable of accounting for the interfacial forces since one of the principal curvatures is equal to zero in the two-dimensional case. The 2D simulations are not suitable for the accurate estimation of the shear forces. It can give an approximate value only. Moreover, the 2D simulation is not very appropriate in the sense of accounting for the absolute values of the various forces like the surface and viscous forces, but it is significant in terms of qualitative estimate of the flow patterns, the influence of channel geometry, the velocity field, the fluid properties (except surface forces), the types of daughter branches of the channel, etc.

6.4. SUMMARY

The results of 2D simulations of multiple splitting of a mother droplet through a multi-furcating microfluidic channel are given. The mother droplet was fragmented into five daughter droplets through five arms of the multi-furcating microchannel. The grid independence test was performed for the 2D solver. The 2D models have been validated using the experimental data present in the literature (Salim et al. [29]). We have set a width ratio (branch channel/main channel) of 0.25 for all the five branches of the multi-furcating microchannel as multiple splitting occurs at this width ratio. The critical value of the dispersed phase velocity at which the droplets multi-furcate across the five arms of the microchannel is determined. The mechanism for droplet multi-furcation is explained. Simulated oil fraction data distributed across the five outlets are reported. The present simulated oil fraction data are compared with the result of the homogenous model [31]. The percentage deviation of 16.48 is found between the simulated oil fraction data and the homogenous model. The droplet length distribution in the branch channels (0^o, $\pm 40^o$, and $\pm 90^o$ branch channels) was found. It was observed that the dimensionless droplet length (l) increases first up to a certain flow rate ratio (0.62), then decreases. Variation in the frequency (counts per unit time) of droplets generated in the branch channel and the area distribution ratio with the capillary number have also been reported. This study provides knowledge about multiple splitting which can be used in the future microfluidic platform-based devices.

REFERENCES

1. Liu, Z.-M., Yang, Y., Du, Y., and Pang, Y., Advances in Droplet-Based Microfluidic Technology and Its Applications, *Chinese Journal of Analytical Chemistry*, 2017, vol. 45, no. 2, pp. 282-296.
2. Pollack, M.G., Pamula, V.K., Srinivasan, V., and Eckhardt, A.E., Applications of electrowetting-based digital microfluidics in clinical diagnostics, *Expert Review of Molecular Diagnostics*, 2011, vol. 11, no. 4, pp. 393-407.
3. Yukuyama, M.N., Ghisleni, D.D.M., Pinto, T.J.A., and Bou-Chacra, N.A., Nanoemulsion: process selection and application in cosmetics – a review, *International Journal of Cosmetic Science*, 2016, vol. 38, no. 1, pp. 13-24.
4. Zhang, Y., Fan, J., and Wang, L., Formation of Nanoliter Droplets in a Confined Microfluidic T-Shaped Junction: Formation Time and Droplet Volume, *Current Nanoscience*, 2009, vol. 5, no. 4, pp. 519-526.
5. Guo, S., Lin, W.N., Hu, Y., Sun, G., Phan, D.-T., and Chen, C.-H., Ultrahigh-throughput droplet microfluidic device for single-cell miRNA detection with isothermal amplification, *Lab on a Chip*, 2018, vol. 18, no. 13, pp. 1914-1920.
6. Perkins, G., Lu, H., Garlan, F., and Taly, V., *Chapter Three - Droplet-Based Digital PCR: Application in Cancer Research*, in *Advances in Clinical Chemistry*, G.S. Makowski, Editor. 2017, Elsevier. p. 43-91.

7. Wojnicki, M., Tokarski, T., Hessel, V., Fitzner, K., and Luty-Błocho, M., Continuous, monodisperse silver nanoparticles synthesis using microdroplets as a reactor, *Journal of Flow Chemistry*, 2019, vol. 9, no. 1, pp. 1-7.
8. Fontana, F., Ferreira, M.P.A., Correia, A., Hirvonen, J., and Santos, H.A., Microfluidics as a cutting-edge technique for drug delivery applications, *Journal of Drug Delivery Science and Technology*, 2016, vol. 34, no. pp. 76-87.
9. Dittrich, P.S. and Manz, A., Lab-on-a-chip: microfluidics in drug discovery, *Nature Reviews Drug Discovery*, 2006, vol. 5, no. 3, pp. 210-218.
10. Zhao, C.-X. and Middelberg, A.P.J., Two-phase microfluidic flows, *Chemical Engineering Science*, 2011, vol. 66, no. 7, pp. 1394-1411.
11. Link, D.R., Anna, S.L., Weitz, D.A., and Stone, H.A., Geometrically mediated breakup of drops in microfluidic devices, *Phys Rev Lett*, 2004, vol. 92, no. 5, pp. 054503.
12. Li, Z., Li, L., Liao, M., He, L., and Wu, P., Multiple splitting of droplets using multi-furcating microfluidic channels, *Biomicrofluidics*, 2019, vol. 13, no. 2, pp. 024112.
13. Du, M., Qi, T., Fan, W., and Chen, H., Numerical investigation of bubble breakup in a four-branched microchannel based on non-Newtonian pseudoplastic fluid, *Asia-Pacific Journal of Chemical Engineering*, 2020, vol. 15, no. 1, pp. e2393.
14. Chung, C., Lee, M., Char, K., Ahn, K.H., and Lee, S.J., Droplet dynamics passing through obstructions in confined microchannel flow, *Microfluidics and nanofluidics*, 2010, vol. 9, no. 6, pp. 1151-1163.
15. Lee, W. and Son, G., Numerical study of obstacle configuration for droplet splitting in a microchannel, *Computers & Fluids*, 2013, vol. 84, no. pp. 351-358.

16. Bhardwaj, S., Dalal, A., Biswas, G., and Mukherjee, P.P., Analysis of droplet dynamics in a partially obstructed confinement in a three-dimensional channel, *Physics of Fluids*, 2018, vol. 30, no. 10, pp. 102102.

17. Sipey, M.H., Delavar, M.A., and Sattari, E., Lattice Boltzmann simulation of droplet deformation and breakup due to collision with obstacles in microchannel, *Indian Journal of Physics*, 2019, vol. no. pp. 1-10.

18. Kadivar, E. and Zarei, F., Breakup a droplet passing through an obstacle in an orthogonal cross-section microchannel, *Theoretical and Computational Fluid Dynamics*, 2021, vol. 35, no. 2, pp. 249-264.

19. Chen, B., Li, G., Wang, W., and Wang, P., 3D numerical simulation of droplet passive breakup in a micro-channel T-junction using the Volume-Of-Fluid method, *Applied Thermal Engineering*, 2015, vol. 88, no. pp. 94-101.

20. Wang, X., Liu, Z., and Pang, Y., Droplet breakup in an asymmetric bifurcation with two angled branches, *Chemical Engineering Science*, 2018, vol. 188, no. pp. 11-17.

21. Cheng, W.L., Sadr, R., Dai, J., and Han, A., Prediction of microdroplet breakup regime in asymmetric t-junction microchannels, *Biomedical microdevices*, 2018, vol. 20, no. 3, pp. 1-12.

22. Gordin, K.A., Istratov, A.G., and Librovich, V.B., Kinetics of droplet deformation and breakup in a gas stream, *Fluid Dynamics*, 1969, vol. 4, no. 1, pp. 5-10.

23. Gel'fand, B.E., Gubin, S.A., Kogarko, S.M., and Komar, S.P., Breakup of liquid drops in a flow behind shock waves with a triangular gas-velocity profile, *Fluid Dynamics*, 1973, vol. 8, no. 5, pp. 724-728.

24. Belen'kii, B.M. and Evseev, G.A., Breakup of drops in the gas behind a shock wave, *Fluid Dynamics*, 1974, vol. 9, no. 2, pp. 301-303.

25. Dushin, V., Nikitin, V., Smirnov, N., Skryleva, E., and Tyurenkova, V., Microgravity investigation of capillary driven imbibition, *Microgravity Science and Technology*, 2018, vol. 30, no. 4, pp. 393-398.

26. Smirnov, N., Nikitin, V., and Gazizova, D., Evolution of a Phase Interface in the Displacement of Viscous Fluids from a Porous Medium, *Fluid Dynamics*, 2021, vol. 56, no. 1, pp. 79-92.

27. Betelin, V., Galkin, V., Shpilman, A., and Smirnov, N., DIGITAL CORE SIMULATOR-A PROMISING METHOD FOR DEVELOPMING HARD-TO-RECOVER OIL RESERVES TECHNOLOGY, *Materials Physics & Mechanics*, 2020, vol. 44, no. 2, pp.

28. Smirnov, N., Nikitin, V., and Skryleva, E., Microgravity investigation of seepage flows in porous media, *Microgravity Science and Technology*, 2019, vol. 31, no. 5, pp. 629-639.

29. Salim, A., Fourar, M., Pironon, J., and Sausse, J., Oil–water two-phase flow in microchannels: Flow patterns and pressure drop measurements, *The Canadian Journal of Chemical Engineering*, 2008, vol. 86, no. 6, pp. 978-988.

30. Desamala, A.B., Vijayan, V., Dasari, A., Dasmahapatra, A.K., and Mandal, T.K., Prediction of oil-water flow patterns, radial distribution of volume fraction, pressure and velocity during separated flows in horizontal pipe, *Journal of Hydrodynamics*, 2016, vol. 28, no. 4, pp. 658-668.

31. Gardenghi, Á.R., Filho, E.d.S., Chagas, D.G., Scagnolatto, G., Oliveira, R.M., and Tibiriçá, C.B., Overview of Void Fraction Measurement Techniques, Databases and Correlations for Two-Phase Flow in Small Diameter Channels, *Fluids*, 2020, vol. 5, no. 4, pp. 216.

CHAPTER 7

CONCLUSION AND SCOPE FOR FUTURE WORK

7.1 CONCLUSION

A detailed numerical study on droplet breakup dynamics has been done in this thesis. The thesis is initiated with computational study on phase velocity mediated droplet splitting and its mechanism at t – junction microchannel. Consequently, the effect of width ratio on droplet splitting has been shown. Both 2D and 3D numerical study on the effect of phase velocity on flow regimes in flow focusing geometry has also been done. The effect of viscous force, surface force and wettability on droplet morphology has been studied. Finally, mechanism of multi-furcation of droplet through multi-furcating channel and parametric study on multi-furcation of droplets using multi-furcating microchannel has been done. The major conclusion from each of the chapters are discussed below:

7.1.1 A COMPUTATIONAL STUDY ON PHASE VELOCITY MEDIATED DROPLET SPLITTING AND ITS MECHANISM AT T-JUNCTION MICROCHANNEL

The 2D-CFD simulation has been carried out to investigate the influence of phase velocity on droplet splitting in a T-junction microchannel. The simulated results have explored various fundamental aspects of different types of droplet splitting phenomena. The model has been validated with the previous experimental data present in the literature (Salim et al.). We have successfully simulated droplet non-breakup and droplet breakup flow regimes, changing the phase velocities of two phases. Two types of droplet breakup regimes, namely tunnel-breakup and obstructed breakup has been observed. New flow morphology, namely mixed flow pattern, transient in nature, has also been observed in a wide range of phase velocities. This transient behavior has been characterized by the alteration of the flow patterns at constant flow rates.

Different flow patterns have been presented in the form of a flow pattern map. It has been found that pressure swing phenomena at the T-junction have instigated the movement of the droplets in alternate directions. The formation of vortex flow at the front ends of the droplets is one of the critical reasons for droplet breakup with tunnel. On the other hand, the resultant effect of larger droplet volume, upstream pressure buildup, and vortex flow are found to be responsible for droplet bifurcation with obstruction. Present simulated and experimental (Salim et al.) pressure drop data have been predicted using homogeneous and drift flux model. The results show that drift flux model gives the higher accuracy in prediction. These findings will help in better understanding of droplet splitting and will have direct application in microfluidic platform based device.

7.1.2 INFLUENCE OF MICROCHANNEL GEOMETRY ON DROPLET BREAKUP DYNAMICS: A COMPUTATIONAL STUDY

The 2D-CFD simulation has been carried out to investigate the influence of width ratio and arm length ratio on droplet splitting. The model has been validated with the previous experimental data present in the literature (Salim et al.). The tunnel breakup and the obstructed breakup are mainly due to the pressure difference in the branch channel and the direction of the velocity vectors which are towards the branch's exit and the pressure swing phenomenon is the reason behind the alternate movement of the droplets. Breakup with tunnel is found in WR = 0.75, 0.5, breakup with obstruction is found in WR = 0.25 and alternate movement is found in WR = 1 for V_w = 0.01 m/s, V_o = 0.18 m/s. It has been found that breakup tendency increases as we decrease the width ratio (1, 0.75, 0.5, and 0.25) and increase the arm length ratio (0.4, 0.6,

and 0.9). Droplet breakup condition has been revealed based on initial extension. Flow pattern maps have been developed through which the mixed flow regimes and other flow regimes are displayed for all the width ratios (1, 0.75, 0.5, and 0.25). Mainly three distinct regions are found: i) Not a Ca induced region ii) Highly Ca induced region iii) May be Ca induced region. Prediction of simulated pressure gradient for width ratio = 1 has been made through Lockhart and Martinelli approach, and a percentage deviation of 52% has been found. Dimensional analysis has also been done for width ratio = 1 and 24% of average error is found between predicted and simulated pressure gradient, which is better than Lockhart and Martinelli approach.

7.1.3 2D SIMULATION OF DRIPPING AND JETTING FLOW IN A FLOW-FOCUSING GEOMETRY

2D-CFD simulations have been carried out to study the effect of flow velocity on flow regime using the VOF method. The model has been authenticated with earlier experimental data present in the literature (Fu et al.). We have effectively simulated the different flow regimes based on dispersed and continuous phase velocity. A mechanism on dripping and jetting phenomena also has been discussed. A flow pattern map has been presented identifying the dripping and jetting regimes. It has been observed that the dripping is restricted to low to moderate weber numbers of the dispersed phase and low to high capillary numbers of the continuous phase. At the same time, the jetting regime is limited to low to high capillary numbers of continuous phases and moderate to high weber number of dispersed phase. Theoretical and simulated droplet pinch-off time and jet growth time has also been calculated and compared. The confirmation of the transition between dripping and jetting has been done

through the calculation of the effective capillary number of the interface. The droplet size decreases with increase in oil-water viscosity ratio and with decrease in interfacial tension.

7.1.4 3D SIMULATION OF DRIPPING AND JETTING PHENOMENA IN A FLOW-FOCUSING GEOMETRY

3D-CFD simulations have been carried out to investigate the effect of viscosity, surface tension and wettability on droplet generation using the VOF method. The model has been authenticated with earlier experimental data present in the literature (Fu et al. [1]). We have effectively simulated droplet formation based on viscosity, surface tension and wettability. It has been observed that the droplet became smaller in size with an increase in the oil-water viscosity ratio. The frequency increases with an increase in the oil-water viscosity ratio. On the other hand, droplets became larger with the increase in the interfacial tension. The droplet is not generated at 0.002 N/m (i.e., 0 Hz frequency) as a continuous oil thread is observed. In the present simulation, droplets onset at the interfacial tension of 0.005 N/m and frequency at this condition is 60 Hz. Then, it decreases continuously with an increase in the interfacial tension. Droplet velocity decreases with an increase in the interfacial tension. The effect of wettability was studied by changing wettability angles (θ) from 0º-180º. For $\theta <= 90º$, water is the continuous phase in which droplets of PDMS were formed. For $\theta > 90$, the water became the dispersed phase in the continuous oil medium. At $\theta = 135°$ and 180º, the channel becomes super hydrophobic, which gives an annular flow configuration in the channel. Here, the oil phase warps the channel surface, and the water phase turns into a continuous thread flowing through the center of the channel. Wettability also influences the non-dimensional droplet length (L/W_c). The highest value of

L/W_c and droplet volumes are 1.25 and 220 nL, respectively, at $\theta = 100°$. The frequency increases from 18-36 Hz for a change of θ from 0°-90° respectively, and then it decreases due to a change of θ from 90°-180°. It is important to note that a water thread is formed beyond θ = 135°. That is why droplet frequency is considered 0 Hz. The droplet velocity increases from 0.045-0.050 m/s for change in θ from 0°-80° and then it decreases from 0.050-0.020 for the θ ranging from 80°-180°. Two flow regimes were identified and have been presented in the form of a phase diagram for oil-water viscosity ratio = 12, σ = 0.0118 N/m and $\theta = 40°$ (water wetting the PMMA surface in the presence of PDMS). Comparison between normal geometry and two different constricted geometry (having different orifice lengths) based on non-dimensional droplet length, frequency, droplet volume, droplet velocity has been made for both dripping and jetting regimes at oil-water viscosity ratio = 12, σ = 0.0118 N/m and $\theta = 40°$ (water wetting the PMMA surface in the presence of PDMS). It has been found that the value of non-dimensional droplet length and droplet volume is lowest in the case of constricted geometry 2 for both regimes. The frequency value is highest in the case of constricted geometry 2 for both regimes. Droplet velocity value is near about the same for the three geometry configurations for dripping and jetting regimes. The dimensionless analysis gave an excellent prediction of simulated non-dimensional droplet length with an average absolute error of 9.1%. These findings will help understand droplet generation under various physicochemical parameters and directly apply to the microfluidic platform-based device.

7.1.5 TWO-DIMENSIONAL NUMERICAL SIMULATION OF DROPLET SPLITTING IN MULTI-FURCATING MICROCHANNEL

The results of 2D simulations of multiple splitting of a mother droplet through a multi-furcating microfluidic channel are given. The mother droplet was fragmented into five daughter droplets through five arms of the multi-furcating microchannel. The grid independence test was performed for the 2D solver. The 2D models have been validated using the experimental data present in the literature (Salim et al.). We have set a width ratio (branch channel/main channel) of 0.25 for all the five branches of the multi-furcating microchannel as multiple splitting occurs at this width ratio. The critical value of the dispersed phase velocity at which the droplets multi-furcate across the five arms of the microchannel is determined. The mechanism for droplet multi-furcation is explained. Simulated oil fraction data distributed across the five outlets are reported. The present simulated oil fraction data are compared with the result of the homogenous model. The percentage deviation of 16.48 is found between the simulated oil fraction data and the homogenous model. The droplet length distribution in the branch channels (0^o, $\pm 40^o$, and $\pm 90^o$ branch channels) was found. It was observed that the dimensionless droplet length (l) increases first up to a certain flow rate ratio (0.62), then decreases. Variation in the frequency (counts per unit time) of droplets generated in the branch channel and the area distribution ratio with the capillary number have also been reported. This study provides knowledge about multiple splitting which can be used in the future microfluidic platform-based devices.

7.2 FUTURE SCOPE OF RESEARCH

The work in this thesis can be extended in many different ways. Some of the ways are remain unexplored and are mentioned below:

- Experiments or simulation on droplet breakup can be done for non-Newtonian fluids.
- Air can be used instead of oil and experiments/simulations can be done on droplet breakup.
- The effect of Mass transfer or heat transfer on droplet breakup dynamics can be observed either through simulation or experiment or both.
- Experiments or simulations on droplet breakup can be done for more complex geometry.

OUTCOMES OF THE THESIS

List of publications:

Published:

- **Biswas, S.,** Gooh Pattader, P. S., Mandal, T. K., 2021. **A computational study on phase velocity mediated droplet splitting and its mechanism at T-junction microchannel.** Journal of the Brazilian Society of Mechanical Sciences and Engineering 43, 391.
- **Biswas, S.,** Gooh Pattader, P. S., Mandal, T. K., 2022. **Two-dimensional simulation of droplet splitting in multi-furcating microchannel.** Fluid Dynamics 57,672-685.
- **Biswas, S.,** Gooh Pattader, P. S., Mandal, T. K., 2023. **Droplet splitting in multi-furcating microchannel: A three-dimensional numerical simulation study.** The Canadian Journal of Chemical Engineering, 1-15.

Paper communicated:

- **A computational study on transition mechanism of dripping to jetting flow in a flow-focusing geometry**, communicated to JTICE.
- **Influence of microchannel geometry on droplet dynamics: a computational study**, communicated to JBSMSE.
- **3D simulation of dripping and jetting phenomena in a flow-focusing geometry**, communicated to CEC.

Collaborative work:

- Nucleation and bubble formation of flow boiling in micro device

Conferences:

- **Biswas, S.**, Gooh Pattader, P. S., Mandal, T. K., 2019. The insight of the droplet splitting at the T-junction of a microchannel. ***Research Conclave 2019***, IIT Guwahati, India. (Poster)
- **Biswas, S.**, Gooh Pattader, P. S., Mandal, T. K., 2019. 2D simulation of a droplet splitting at microfluidic T-junction in oil-water two-phase flow using Volume-Of-Fluid method. ***TEQIP III Sponsored 1st National Student Conference on Advances in Chemical Engineering***, AEC, India. (Oral)
- **Biswas, S.**, Gooh Pattader, P. S., Mandal, T. K., 2020. Dynamics of droplet break-up at T-junction of a microchannel. ***International Conference on Advances in Chemical Engineering-2020 (AdChE-2020)***, UPES, Uttarakhand, India. (Oral)
- **Biswas, S.**, Gooh Pattader, P. S., Mandal, T. K., 2022. CFD simulation on flow-focusing geometry for droplet formation using VOF method. ***Advances in Chemical and Material Sciences (ACMS-2022)***, HIT Kolkata, India. (Online mode, Oral)

APPENDIX

5b.4.2 Procedure of Dimensional Analysis

There are six parameters listed i.e. "n" = 6. There are three primary parameters i.e. length (l), mass (m) and time (t) i.e. “m” = 3.

So, number of independent groups = 6-3 = 3

So, $f(\Pi_1, \Pi_2, \Pi_3) = 0$

Where, f is some function, or in an alternate expression:

$\Pi_1 = f_1(\Pi_2, \Pi_3)$

where f_1 is some function different to function f .

Taking an arbitrary choice of three parameters: ρ_m, U_m, W_c

Group 1: $\Pi_1 = \{(\rho_m)^a, (U_m)^b, (W_c)^c 2 \quad (L)$

$\{(m/l^3)^a, (l/t)^b, (l)^c\} (l) = m^0 l^0 t^0$

m: a = 0 ; l: -3a+b+c+1 = 0 ; t: -b = 0

or, a = 0 or, c = -1 or, b = 0

a = 0, b = 0, c = -1

therefore, $\Pi_1 = \{(\rho_m)^0, (U_m)^0, (W_c)^{-1}\} (L)$

$= L/ W_c$

By similar procedures the rest of the groups can be derived:

Group 2: $\Pi_2 = \{(\rho_m)^{-1}, (U_m)^{-1}, (W_c)^{-1}\}\ (\mu_m) = \mu_m / \rho_m W_c U_m$

Group 3: $\Pi_3 = \{(\rho_m)^{-1}, (U_m)^{-2}, (W_c)^{-1}\}\ (\sigma) = \sigma / \rho_m W_c U^2_m$

Therefore, we have

$$\frac{L}{W_c} = \lambda\left(\frac{\mu_m}{\rho_m U_m W_c}\right)^a \left(\frac{\sigma}{\rho_m U_m^2 W_c}\right)^b$$